

Article

Molecular Eigensolution Symmetry Analysis and Fine Structure

William G. Harter ^{1,*} and Justin C. Mitchell ²

¹ Department of Physics, University of Arkansas, Fayetteville, AR 72701, USA

² Intel Corporation, Santa Clara, CA 95054, USA; E-Mail: nanojustin@gmail.com

* Author to whom correspondence should be addressed; E-Mail: wharter@uark.edu;
Tel.: +1-479-575-6567.

Received: 3 September 2012; in revised form: 26 November 2012 / Accepted: 27 November 2012 /
Published: 4 January 2013

Abstract: Spectra of high-symmetry molecules contain fine and superfine level cluster structure related to J -tunneling between hills and valleys on rovibronic energy surfaces (RES). Such graphic visualizations help disentangle multi-level dynamics, selection rules, and state mixing effects including widespread violation of nuclear spin symmetry species. A review of RES analysis compares it to that of potential energy surfaces (PES) used in Born–Oppenheimer approximations. Both take advantage of adiabatic coupling in order to visualize Hamiltonian eigensolutions. RES of symmetric and D_2 asymmetric top rank-2-tensor Hamiltonians are compared with O_h spherical top rank-4-tensor fine-structure clusters of 6-fold and 8-fold tunneling multiplets. Then extreme 12-fold and 24-fold multiplets are analyzed by RES plots of higher rank tensor Hamiltonians. Such extreme clustering is rare in fundamental bands but prevalent in hot bands, and analysis of its superfine structure requires more efficient labeling and a more powerful group theory. This is introduced using elementary examples involving two groups of order-6 (C_6 and $D_3 \sim C_{3v}$), then applied to families of O_h clusters in SF_6 spectra and to extreme clusters.

Keywords: symmetry; molecular dynamics; tunneling; level clusters

1. Overview of Eigensolution Techniques for Symmetric Molecules

A key mathematical technique for atomic or molecular physics and quantum chemistry is matrix diagonalization for quantum eigensolution. As computers become faster and more available, more

problems of chemical physics are framed in terms of choosing bases for eigensolution of time evolution operators or Hamiltonian generator matrices. The resulting eigenvectors and eigenvalues are Fourier amplitudes and frequencies that combine to give all possible dynamics in a given basis choice.

Despite the increasing utility and power of computer diagonalization, it remains a “black box” of processes quite unlike the complex natural selection by wave interference that we imagine nature uses to arrive at its quantum states. Diagonalization uses numerical tricks to reduce each N -by- N matrix to N values and N stationary eigenstates, but the artificial processes may seem as opaque as nature itself with little or no physical insight provided by $N^2 - N$ eigenvector components. We are thus motivated to seek ways to visualize more of the physics of molecular eigensolutions and their spectra. This leads one to explore digital graphical visualization techniques that provide insight as well as increased computational power and thereby complement numerically intensive approaches [1].

Before describing tensor eigensolution techniques and rovibronic energy surfaces (RES), a brief review is given of potential energy surface (PES) to put the tensor RES in a historical and methodological context. This includes some background on semiclassical approximations of tensor algebra that help explain rotational level clustering and are used to develop the RES graphical tools. Section 2 reviews how RES apply to symmetric and asymmetric top molecules. This serves to motivate the application of RES to more complicated molecules of higher symmetry. Section 3 contains a graphical analysis of octahedral RES and an introductory review of level clusters (fine structure) having 6-fold and 8-fold quasi-degeneracy (superfine structure) due to rank-4 tensor Hamiltonians. Following this is a discussion of mixed-rank tensors that exhibit 12-fold and 24-fold monster-clusters. The latter have only recently been seen in highly excited rovibrational spectra [2] and present challenging problems of symmetry analysis to sort out a plethora of tunneling resonances and parameters for so many resonant states.

Following introductory Section 4, these problems are addressed in Sections 6–8 by redeveloping group algebraic symmetry analysis into a more physically direct and elegantly powerful approach. It uses underlying duality between internal and external symmetry states and their operations. Duality is introduced using the simplest order-6 symmetry groups C_6 and $D_3 \sim C_{3v}$ before applying it to O_h symmetric monster-clusters in Section 8. Monsters in REES-polyad bands are shown in final Section 9.

The direct approach to symmetry starts by viewing a group product table as a Hamiltonian matrix H representing an \mathbf{H} operator that is a linear combination of group operators \mathbf{g}_k with a set of ortho-complete tunneling coefficients g_k labeling each tunneling path. A main idea is that symmetry operators “know” the eigensolutions of their algebra and thus of all Hamiltonian and evolution operators made of \mathbf{g}_k 's.

1.1. Computer Graphical Techniques

Several graphical techniques and procedures exist for gaining spectral insight. One of the oldest is the Born–Oppenheimer approximate (BOA) potential energy surface (PES) that is a well-established tool for disentangling vibrational-electronic (vibronic) dynamics. While BOA-PES predate the digital age by decades, their calculation and display is made practical by computer. More recent are studies of phase portraits and wavepacket propagation techniques to follow high- ν vibrational dynamics and chemical pathways for dissociation or re-association [3,4]. This includes BOA-breakdown states in which a system evolves on multiply interfering PES paths. Dynamic Jahn–Teller–Renner effects involve

multi-BOA-PES states in molecules and solids. Examples in recent works [5,6] include coherent photo-synthesis [7].

Visualizing eigensolutions and spectra in crystalline solids is helped by bands of dispersion functions in reciprocal frequency-versus-wavevector space. Fermi-sea contours are used to analyze de Haas–van Alphen effects and more recently in understanding quantum Hall effects. Analogy between band theory of solids and molecular rovibronic clusters is made in Section 4 and 7.

Visualization of molecular rotational, rovibrational, and rovibronic eigensolutions and spectra is the subject of this work and involves the rotational energy surface (RES). As described below, an RES is a multipole expansion plot of an effective Hamiltonian in rotational momentum space. Ultra sensitivity of vibronic states to rotation lets the RES expose subtle and unexpected physics. Multi-RES or rovibronic energy eigenvalue surfaces (REES) have conical intersections analogous to Jahn–Teller PES (See Section 9).

The RES was introduced about thirty years ago [8] to analyze spectral fine structure of high resolution spectral bands in molecules of high symmetry including PH_3 [9] XDH_3 and XD_2H molecules [10], tetrahedral (P_4) [11], tetrafluorides (CF_4 and SiF_4) [12], hexafluorides (SF_6 , $Mo(CO)_6$ and UF_6) [13–16], cubane (C_8H_8), and buckyball (C_{60}) [15,16] and predicted major mixing of Herzberg rovibronic species. Recently RES have been extended to help understand the dynamics and spectra of fluxional rotors [17] or “floppy” molecules such as methyl-complexes [18] and vibrational overtones [2].

Each of the techniques and particularly the RES-based ones described below depend upon the key wave functional properties of stationary phase, adiabatic invariance, and the spacetime symmetry underlying quantum theory. Additional symmetry (point group, space group, exchange, gauge, *etc.*) of a molecular system introduces additional resonance. Symmetry tends to make graphical techniques even more useful since they help clarify resonant phenomenal dynamics and symmetry labeling [19].

1.1.1. Vibronic Born–Openheimer Approximate Potential Energy Surfaces (BOA-PES)

A BOA-PES depends on an adiabatic invariance of each electronic wavefunction to nuclear vibration. It is often said that the electrons are so much faster than nuclei that the system “sticks” to a particular PES that electrons provide. Perhaps a better criterion would be that the Fourier spectrum associated with nuclear motion does not overlap that of an electronic transition to another energy level. Nuclei often provide stable configurations that quantize electronic energy into levels separated by gaps much wider than that of low lying vibrational “phonon” states.

A BOA wavefunction is a peculiarly entangled outer product $\Psi = \eta\psi$ of a nuclear factor wavefunction $\eta_{\nu(\epsilon)}(X \dots)$ whose quantum labels $\nu(\epsilon)$ depend on electronic quantum numbers $\epsilon = nlm$, *etc.* while the electronic factor wave $\psi(x_{(X\dots)} \dots)$ is a function whose electron coordinates $x_{(X\dots)} \dots$ depend adiabatically on nuclear vibrational coordinates ($X \dots$) of PES $V_\epsilon(X \dots)$ for electron bond state ϵ .

$$\Psi_{\nu(\epsilon)}(x^{electron} \dots X^{nuclei} \dots) = \psi_\epsilon(x_{(X\dots)} \dots) \cdot \eta_{\nu(\epsilon)}(X \dots) \quad \text{BOA-Entangled Product} \quad (1a)$$

$$\begin{aligned} \Psi_{\nu,\epsilon}(x^{electron} \dots X^{nuclei} \dots) &= \\ \psi_{\epsilon}(x \dots) \cdot \eta_{\nu}(X \dots) &\quad \text{Unentangled Product} \\ = \langle x \dots | \psi_{\epsilon} \rangle \langle X \dots | \eta_{\nu} \rangle &= \langle x \dots; X \dots | \psi_{\epsilon}; \eta_{\nu} \rangle \end{aligned} \quad (1b)$$

The adiabatic convenience of a single product Equation (1a) with a vibration eigenfunction $\eta_{\nu(\epsilon)}(X \dots)$ on a single PES function $V_{\epsilon}(X \dots)$ is welcome but comes at a price; a BOA-entangled coordinate-state is not a simple bra-ket wavefunction product Equation (1b) of bra-bra $\langle x \dots | \langle X \dots |$ position and ket-ket $|\psi_{\epsilon}\rangle |\eta_{\nu}\rangle$ state. Symmetry operator product analysis of Equation (1b) is well known. Symmetry of Equation (1a) depends on rotational BOA-relativity of its parts. Vibronic BOA-PES generalize to rovibronic RES by accounting for rotational relations.

1.1.2. Rovibronic BOA Rotational Energy Surfaces (BOA-RES)

The rotational energy surface (RES) can be seen as a generalization of adiabatic BOA wave Equation (1a) to Equation (2) below that includes rotational motion. Here one treats vibronic motion as having the “fast” degrees of freedom while rotational coordinates Θ (e.g., Euler angle $(\alpha\beta\gamma)$ for semi-rigid molecules) play the “slow” semi-classical role vis-a-vis the “faster” adiabatic vibration or vibronic states.

$$\begin{aligned} \Phi_{J[\nu(\epsilon)]}(x^{elec} \dots Q^{vib} \dots \Theta^{rot}) &= \\ \psi_{\epsilon}(x(Q \dots \Theta \dots)) \cdot \eta_{\nu(\epsilon)}(Q \dots [\Theta \dots]) \cdot \rho_{J[\nu(\epsilon)]}(\Theta^{rot} \dots) \end{aligned} \quad (2)$$

In Equation (2), the wave factors of each motion are ordered fast-to-slow going left-to-right. As in Equation (1a) each wave-factor quantum number depends on quanta in “faster” wave-factors written to its left, but each coordinate has adiabatic dependence on coordinates in “slower” factors written to its right.

The Q in Equation (2) denotes vibrational normal coordinates (q_1, q_2, \dots, q_m) and ν denotes their quanta $(\nu_1, \nu_2, \dots, \nu_m)$. The number $m = 3N - 6$ of modes of an N -atom semi-rigid molecule has subtracted 3 translational and 3 rotational coordinates. Each mode q_k assumes an adiabatic BOA dependency on overall translation and rotation Θ known as the Eckart conditions. (Here we will ignore translation.)

RES are multipole expansion plots of effective BOA energy tensors for each quantum value of vibronic $\nu(\epsilon)$ and conserved total angular momentum J . Choices of effective energy tensors depend on the level of adiabatic approximation. So do the choices of spaces in which RES are plotted. Elementary examples of model BOA waves, tensors, and RES for rigid or semi-rigid molecules are discussed below.

1.2. Lab-Frame Coupling vs. Body Frame Constriction

Wave $\rho_J(\Theta^{rotation})$ for a bare rigid symmetric-top ($\psi = 1 = \eta$) molecule is a Wigner D^J -function.

$$\rho_J(\Theta) = \rho_{J,M,K}(\alpha\beta\gamma) = D_{M,K}^{J*}(\alpha\beta\gamma) \sqrt{\text{norm}} \quad \text{norm} = [J] = 2J + 1 \quad (3)$$

Total angular momentum J is $J = R$ for a bare rotor. Bare lab-frame z-component is labeled $M = m$. Its body-frame \bar{z} -component is labeled $K = \bar{M} = n$. m and n range from $+R$ to $-R$ in integral steps.

Entangled BOA product Equation (2) mates vibronic factor Equation (1a) with a rotor factor $\rho_J = \rho_{J,M,K}$ in Equation (3). Now J and $K = \bar{M}$ depend on total vibronic momentum l and its body \bar{z} -component $\bar{\mu}$ in $\Psi_{\nu(\epsilon)} = \Psi_{\bar{\mu}}^l$.

$$\Phi_{J[\nu(\epsilon)]} = \Psi_{\nu(\epsilon)}^l \cdot \rho_{J[\nu(\epsilon)]} = \Psi_{\bar{\mu}}^l \cdot \rho_{J,M,K} = \Psi_{\bar{\mu}}^l \cdot \mathcal{D}_{M,K}^{J*} \sqrt{[J]} \tag{4}$$

Disentangled product Ψ_ρ in Equation (1b) of lab-based vibronic wave Ψ_μ^l and bare rotor $\rho_{R,m,n}$ of Equation (3) is coupled by Clebsch–Gordan Coefficients $C_{\mu m M}^{l R J}$ into a wave Φ_M^J of total $J = R + l$, $R + l - 1, \dots$ or $|R - l|$ and $M = \mu + m$ by sum Equation (5) over lab z -angular bare rotor momenta m and lab vibronic μ bases.

$$\Phi_M^J = \sum_{\mu,m} C_{\mu m M}^{l R J} \psi_\mu^l \cdot \rho_m^R = \sum_{\mu,m} C_{\mu m M}^{l R J} \psi_\mu^l \cdot \mathcal{D}_{m,n}^{R*} \sqrt{[R]} \quad (M = \mu + m = \text{const.}) \tag{5}$$

A BOA-entangled wave in Equation (1a) or Equation (4) requires more serious surgery in order to survive as a viable theoretical entity. BOA vibronic waves are not merely coupled as in Equation (5) to a rotor, they are adiabatically “glued” or constricted to the intrinsic molecular rotor frame. (A rotor is “BOA-constricted” by its vibronic wave much as a boa-constrictor rides its writhing prey as the two rotate together.)

A remarkable property of quantum rotor operator algebra is that Wigner D^l -waves in Equation (3) are also transformation matrices that relate rotating body-fixed BOA $\Psi_{\bar{\mu}}^l(\text{body})$ into the lab-fixed $\Psi_\mu^l(\text{lab})$.

$$\Psi_{\bar{\mu}}^l(\text{body}) = \sum_{\mu} \Psi_\mu^l(\text{lab}) \mathcal{D}_{\bar{\mu}\mu}^l(\alpha\beta\gamma) \tag{6a}$$

$$\Psi_\mu^l(\text{lab}) = \sum_{\bar{\mu}} \Psi_{\bar{\mu}}^l(\text{body}) \mathcal{D}_{\mu\bar{\mu}}^{l*}(\alpha\beta\gamma) \tag{6b}$$

This rotational wave relativity is a subset of Lorentz–Einstein–Minkowski space-time-frame relativity that uses symmetry algebra to keep track of the invariant sub-spaces (eigensolutions). D-Matrices underlie all tensor operators, their eigenfunctions and their eigenvalues and are a non-Abelian (non-commutative) generalization of plane waves $d^{k*}(r) = \langle r|k \rangle = e^{ikr}$ underlying Fourier operator analysis. Details of this connection comprise the later Section 5.

Of particular importance to RES theory is the Wigner–Eckart factorization lemma that relates Clebsch–Gordan $C_{\mu m M}^{l R J}$ to Wigner- D ’s and transforms coupled wave Equation (5) to BOA-constricted wave Equation (4).

$$\int d(\alpha\beta\gamma) \mathcal{D}_{\mu\bar{\mu}}^{l*}(\alpha\beta\gamma) \mathcal{D}_{mn}^{R*}(\alpha\beta\gamma) \mathcal{D}_{MK}^J(\alpha\beta\gamma) = \frac{1}{[J]} C_{\mu m M}^{l R J} C_{\bar{\mu}nK}^{l R J} \tag{7a}$$

$$\sum_{\mu} \sum_{\bar{\mu}} C_{\mu m M}^{l R J'} \mathcal{D}_{\mu\bar{\mu}}^{l*}(\alpha\beta\gamma) \mathcal{D}_{mn}^{R*}(\alpha\beta\gamma) C_{\bar{\mu}nK}^{l R J} = \delta^{JJ'} \mathcal{D}_{MK}^{J*}(\alpha\beta\gamma) \tag{7b}$$

$$\sum_{\mu} C_{\mu m M}^{l R J'} \mathcal{D}_{\mu\bar{\mu}}^{l*}(\alpha\beta\gamma) \mathcal{D}_{mn}^{R*}(\alpha\beta\gamma) = \sum_{\bar{\mu}} C_{\bar{\mu}nK}^{l R J} \mathcal{D}_{MK}^{J*}(\alpha\beta\gamma) \tag{7c}$$

A more familiar form of this is the Kronecker relation of product reduction $\mathcal{D}^l \otimes \mathcal{D}^R \approx \mathcal{D}^J \oplus \mathcal{D}^{J'} \oplus \dots$. Another form is a body-to-lab coupling relation with $M = \mu + m$ and $n = K - \bar{\mu}$ fixed in the μ or $\bar{\mu}$ sums. The latter yields a sum over $\bar{\mu} = K - n$ of body-fixed BOA waves Equation (5) giving lab-based Φ_M^J wave Equation (4).

$$\Phi_M^J = \sum_{\mu} C_{\mu m M}^{l R J} \Psi_{\mu}^l(lab) \mathcal{D}_{m,n}^{R*} \sqrt{[R]} \quad (8)$$

$$\begin{aligned} \Phi_M^J &= \sum_{\mu} C_{\mu m M}^{l R J} \sum_{\bar{\mu}} \Psi_{\mu}^l(body) \mathcal{D}_{\mu\bar{\mu}}^{l*} \mathcal{D}_{m,n}^{R*}(\alpha\beta\gamma) \sqrt{[R]} \\ &= \sum_{\mu} C_{\bar{\mu} n K}^{l R J} \Psi_{\bar{\mu}}^l(body) \mathcal{D}_{M K}^{J*}(\alpha\beta\gamma) \sqrt{[R]} \\ &= \sum_{\bar{\mu}} \bar{\mu} C_{-K\bar{\mu} n}^{J l R} \Psi_{\bar{\mu}}^l(body) \mathcal{D}_{M K}^{J*}(\alpha\beta\gamma) \sqrt{[J]} \end{aligned} \quad (9)$$

$$\Phi_M^J = \sum_{\bar{\mu}} C_{-K\bar{\mu} n}^{J l R} \Psi_{\bar{\mu}}^l \rho_{J,M,K} = \sum_{\bar{\mu}} C_{-K\bar{\mu} n}^{J l R} \Phi_{J[K\nu(\epsilon)]} \quad (10a)$$

$$\Phi_{J[K\nu(\epsilon)]} = \sum_R C_{-K\mu n}^{J l R} \Phi_M^J \quad (10b)$$

Body-(un)coupling in Equation (10a) is an undoing of BOA-constriction by subtracting vibronic ($l, \bar{\mu}$) from (J, K) of BOA-wave $\Phi_{J[K\nu(\epsilon)]}$ in Equation (10b) to make lab-fixed Φ_M^J in Equation (10a) with sharp rotor quanta $R = J - l, J - l + 1 \dots$ or $J + l$. In a lab-fixed wave Φ_M^J of Equation (5) or (10a) rotor R is conserved but K and $\bar{\mu}$ are not. A BOA wave $\Phi_{J[K\nu(\epsilon)]}$ of Equation (4) or (10b) has body-fixed vibronic K and $\bar{\mu}$ that are conserved but rotor R is not.

Note the following for Equations (8)–(10b). For Equation (8) we have constant ($M = \mu + m$). Result Equation (9) is derived from Equations (6b) and (7c) with constant ($n = K - \bar{\mu}$). In Equation (10a) $K = \bar{\mu} + n$. In Equation (10b) $M = \mu + m$.

However, in both Equation (10a) and (10b) the internal bare-rotor body component $n = K - \bar{\mu}$ is conserved due to a symmetric rotor's azimuthal isotropy. This n is a basic rovibronic-species quantum number invariant to all lab based perturbation or transition operators. Like a gyro in a suitcase, no amount of external kicking of the case will slow its spin. Only internal body operations can “brake” its n .

The duality of lab *vs.* body quantum state labels and external *vs.* internal operators is an important feature of molecular and nuclear physics, and it is to be respected if we hope to take full advantage of symmetry group algebra of eigensolutions. The duality is fundamental bra-&-ket relativity. For every group of symmetry operations such as a 3D rotation group $R(3)_{lab} = \{ \dots \mathbf{R}(\alpha\beta\gamma) \dots \}$ there is a dual body group $R(3)_{body} = \{ \dots \bar{\mathbf{R}}(\alpha\beta\gamma) \dots \}$ having identical group structure but commuting with the lab group. Tensor multipole operators, discussed next, come in dual and inter-commuting sets as well. Generalized Duality is key to efficient symmetry analysis as shown beginning in Section 6.1.

1.3. Mathematical Background for Tensor Algebra

1.3.1. Unitary Multipole Functions and Operators

Spherical harmonic functions $Y_m^l(\phi\theta)$ are well know orbital angular factors in atomic and molecular physics. They are special ($n = 0$)-cases of Wigner- D^l functions Equation (3) as follows.

$$Y_m^l(\phi\theta) = \mathcal{D}_{m,0}^{l*}(\phi\theta) \sqrt{\frac{[l]}{4\pi}} \quad \text{where: } [l] = 2l + 1 \quad (11)$$

A diatomic or linear rotor must have zero body quanta ($n = 0$) and has a $Y_m^l(\phi\theta)$ rotor wave. Y_m^l -matrix elements or expectation values of a multipole potential Y_q^k are proportional to Clebsch forms of Equation (7a).

$$\int d(\phi\theta)\mathcal{D}_{m'0}^{J'}(\phi\theta)\mathcal{D}_{q0}^{k*}(\phi\theta)\mathcal{D}_{m0}^{J*}(\phi\theta) = \sqrt{\frac{(4\pi)^3}{[J][k][J]}} \int d(\phi\theta)Y_{m'}^{J*}Y_q^kY_m^J = \frac{1}{[J]}C_{qmm'}^{kJJ'}C_{000}^{kJJ'} \tag{12}$$

A multipole \mathbf{v}_q^k matrix is Equation (12) with factor $\langle J' || k || J \rangle$ depending on $\{J', k, J\}$ but not $\{m', q, m\}$.

$$\left\langle \begin{matrix} J' \\ m' \end{matrix} \middle| \mathbf{v}_q^k \middle| \begin{matrix} J \\ m \end{matrix} \right\rangle = C_{qmm'}^{kJJ'} \langle J || k || J \rangle \tag{13a}$$

Factor $\langle J' || \mathbf{v}_q^k || J \rangle$ is the reduced matrix element of \mathbf{v}_q^k and chosen by a somewhat arbitrary convention.

$$\langle J' || \mathbf{v}_q^k || J \rangle = (-1)^{k+J'-J} \sqrt{\frac{[J']}{[k]}} \tag{13b}$$

This particular choice simplifies bra-ket coupling and creation-destruction operator expressions for \mathbf{v}_q^k .

$$\begin{aligned} \mathbf{v}_q^k &= (-1)^{2J'} \sum_{\substack{m,m' \\ =q-m}} C_{m'mq}^{J'Jk} \left| \begin{matrix} J' \\ m' \end{matrix} \right\rangle \left| \begin{matrix} J^* \\ m \end{matrix} \right\rangle^\dagger \\ &= (-1)^{2J'} \sum_{\substack{m,m' \\ =q-m}} C_{m'mq}^{J'Jk} \left| \begin{matrix} J' \\ m' \end{matrix} \right\rangle \left\langle \begin{matrix} J \\ -m \end{matrix} \right| (-1)^{J-m} \\ &= \sum_{\substack{m,m' \\ =q+m}} (-1)^{J'-m'} \sqrt{[k]} \begin{pmatrix} k & J & J' \\ q & m & -m' \end{pmatrix} \bar{\mathbf{a}}_{m'}^{J'} \bar{\mathbf{a}}_m^J \end{aligned} \tag{13c}$$

Other choices rescale \mathbf{v}_q^k eigenvalues but do not affect eigenvectors of a tensor \mathbf{v}_q^k or its transformation behavior Equation (14). (By Equations (7c) and (13c), \mathbf{v}_q^k transforms like Equation (6a) for a wave function $Y_q^k(\phi\theta)$.)

$$\bar{\mathbf{v}}_q^k = \mathbf{R}(\alpha\beta\gamma)\mathbf{v}_q^k\mathbf{R}^\dagger(\alpha\beta\gamma) = \sum_{q=-k}^k \mathbf{v}_q^k \mathcal{D}_{qk}^k(\alpha\beta\gamma) \tag{14}$$

Examples of \mathbf{v}_q^k tensor matrices for $J' = J = 1$ to 3 are given in Table 1. The $J = 2$ case is given in expanded form by Table 1. (Higher-J tables are q -folded to save space. Scalar $\langle \mathbf{v}_0^0 \rangle^J = 1/\sqrt{[J]}$ is left off each J -table in Table 2)

Table 1. Tabulated \mathbf{v}_q^k values for $J = 1$.

$\langle \mathbf{v}_2^2 \rangle^{J=1} =$ $\begin{pmatrix} \cdot & \cdot & \cdot \\ \cdot & \cdot & \cdot \\ 1 & \cdot & \cdot \end{pmatrix}$	$\langle \mathbf{v}_1^2 \rangle^{J=1} =$ $\begin{pmatrix} \cdot & \cdot & \cdot \\ 1 & \cdot & \cdot \\ \cdot & -1 & \cdot \end{pmatrix} \frac{1}{\sqrt{2}}$	$\langle \mathbf{v}_0^2 \rangle^{J=1} =$ $\begin{pmatrix} 1 & \cdot & \cdot \\ \cdot & -2 & \cdot \\ \cdot & \cdot & 1 \end{pmatrix} \frac{1}{\sqrt{6}}$	$\langle \mathbf{v}_{-1}^2 \rangle^{J=1} =$ $\begin{pmatrix} \cdot & -1 & \cdot \\ \cdot & \cdot & 1 \\ \cdot & \cdot & \cdot \end{pmatrix} \frac{1}{2}$	$\langle \mathbf{v}_{-2}^2 \rangle^{J=1} =$ $\begin{pmatrix} \cdot & \cdot & 1 \\ \cdot & \cdot & \cdot \\ \cdot & \cdot & \cdot \end{pmatrix}$
	$\langle \mathbf{v}_1^1 \rangle^{J=1} =$ $\begin{pmatrix} \cdot & \cdot & \cdot \\ 1 & \cdot & \cdot \\ \cdot & 1 & \cdot \end{pmatrix} \frac{1}{\sqrt{2}}$	$\langle \mathbf{v}_0^1 \rangle^{J=1} =$ $\begin{pmatrix} 1 & \cdot & \cdot \\ \cdot & 0 & \cdot \\ \cdot & \cdot & -1 \end{pmatrix} \frac{1}{\sqrt{2}}$	$\langle \mathbf{v}_{-1}^1 \rangle^{J=1} =$ $\begin{pmatrix} \cdot & -1 & \cdot \\ \cdot & \cdot & -1 \\ \cdot & \cdot & \cdot \end{pmatrix} \frac{1}{\sqrt{2}}$	
		$\langle \mathbf{v}_0^0 \rangle^{J=1} =$ $\begin{pmatrix} 1 & \cdot & \cdot \\ \cdot & 1 & \cdot \\ \cdot & \cdot & 1 \end{pmatrix} \frac{1}{\sqrt{3}}$		

$\langle \mathbf{v}_{q=-2\dots 2}^2 \rangle^{J=1} =$ $\begin{pmatrix} 1 & -1 & 1 \\ 1 & -2 & 1 \\ 1 & -1 & 1 \end{pmatrix} \left \begin{array}{l} 1 \\ \frac{1}{\sqrt{2}} \\ \frac{1}{\sqrt{6}} \end{array} \right.$
$\langle \mathbf{v}_{q=-1\dots 1}^1 \rangle^{J=1} =$ $\begin{pmatrix} 1 & -1 & \cdot \\ 1 & 0 & -1 \\ \cdot & 1 & -1 \end{pmatrix} \left \begin{array}{l} \cdot \\ \frac{1}{\sqrt{3}} \\ \frac{1}{\sqrt{2}} \end{array} \right.$
$\langle \mathbf{v}_0^0 \rangle^{J=1} =$ $\begin{pmatrix} 1 & \cdot & \cdot \\ \cdot & 1 & \cdot \\ \cdot & \cdot & 1 \end{pmatrix} \left \begin{array}{l} \cdot \\ \cdot \\ \frac{1}{\sqrt{3}} \end{array} \right.$

Historically, spinor $J = 1/2$ tensors shown in Table 3(a) are related to four Pauli spinor matrices σ_μ and Hamilton quaternions $\{1, \mathbf{i}, \mathbf{j}, \mathbf{k}\}$ in Table 3(b) or Table 3(c). The latter appear in 1843 and are used for Stokes' polarization theory in 1867. The σ_μ are $U(2)$ algebraic basis of quantum theory for physics ranging from sub-kHz NMR to TeV hadrons and also applies to relativity. General $U(k)$ algebra has k^2 generators $\mathbf{v}_0^0, \mathbf{v}_q^1, \dots, \mathbf{v}_q^k$ with a subset of k mutually commuting diagonal ($q = 0$) labeling operators \mathbf{v}_0^k of the $U(k)$ tensor algebras. The \mathbf{v}_q^k are related to elementary creation-destruction $e_{jk} = a_j^\dagger a_k$ -operators and to their RES in the following sections.

Table 2. Unit tensor representations.

$\langle \mathbf{v}_{q=-1...1}^1 \rangle^{J=1} =$ $\begin{matrix} 1 & 1 & \cdot & \cdot \\ 1 & 0 & -1 & \frac{1}{\sqrt{3}} \\ \cdot & 1 & -1 & \frac{1}{\sqrt{2}} \end{matrix}$	$\langle \mathbf{v}_{q=-1...1}^2 \rangle^{J=2} =$ $\begin{matrix} 2 & -\sqrt{2} & \cdot & \cdot & \cdot & \cdot \\ \sqrt{2} & 1 & -\sqrt{3} & \cdot & \cdot & \cdot \\ \cdot & \sqrt{3} & 0 & -\sqrt{3} & \cdot & \cdot \\ \cdot & \cdot & \sqrt{3} & -1 & -\sqrt{2} & \frac{1}{\sqrt{10}} \\ \cdot & \cdot & \cdot & \sqrt{2} & -2 & \frac{1}{\sqrt{10}} \end{matrix}$	$\langle \mathbf{v}_{q=-1...1}^3 \rangle^{J=3} =$ $\begin{matrix} 3 & -\sqrt{3} & \cdot & \cdot & \cdot & \cdot & \cdot & \cdot \\ \sqrt{3} & 2 & -\sqrt{5} & \cdot & \cdot & \cdot & \cdot & \cdot \\ \cdot & \sqrt{5} & 1 & -\sqrt{6} & \cdot & \cdot & \cdot & \cdot \\ \cdot & \cdot & \cdot & \sqrt{6} & -1 & -\sqrt{5} & \cdot & \cdot \\ \cdot & \cdot & \cdot & \cdot & \sqrt{5} & -2 & -\sqrt{3} & \cdot \\ \cdot & \cdot & \cdot & \cdot & \cdot & \sqrt{3} & -3 & \frac{1}{\sqrt{28}} \\ \cdot & \frac{1}{\sqrt{28}} \end{matrix}$
$\langle \mathbf{v}_{q=-2...2}^2 \rangle^{J=1} =$ $\begin{matrix} 1 & -1 & 1 & \frac{1}{\sqrt{2}} \\ 1 & -2 & 1 & \frac{1}{\sqrt{2}} \\ 1 & -1 & 1 & \frac{1}{\sqrt{6}} \end{matrix}$	$\langle \mathbf{v}_{q=-2...2}^2 \rangle^{J=2} =$ $\begin{matrix} 2 & -\sqrt{6} & \sqrt{2} & \cdot & \cdot & \cdot \\ \sqrt{6} & -1 & -1 & \sqrt{3} & \cdot & \cdot \\ \sqrt{2} & 1 & -2 & 1 & \sqrt{6} & \cdot \\ \cdot & \cdot & \sqrt{2} & -\sqrt{6} & 2 & \frac{1}{\sqrt{14}} \\ \cdot & \cdot & \cdot & \cdot & \cdot & \frac{1}{\sqrt{14}} \end{matrix}$	$\langle \mathbf{v}_{q=-2...2}^3 \rangle^{J=3} =$ $\begin{matrix} 5 & -5 & \sqrt{5} & \cdot & \cdot & \cdot & \cdot & \cdot \\ 5 & 0 & -\sqrt{15} & \sqrt{10} & \cdot & \cdot & \cdot & \cdot \\ \sqrt{5} & \sqrt{15} & -3 & -\sqrt{2} & \sqrt{12} & \cdot & \cdot & \cdot \\ \cdot & \sqrt{10} & \sqrt{2} & -4 & \sqrt{2} & \sqrt{10} & \cdot & \cdot \\ \cdot & \cdot & \sqrt{12} & -\sqrt{2} & -3 & \sqrt{15} & \sqrt{5} & \frac{1}{\sqrt{42}} \\ \cdot & \cdot & \cdot & \sqrt{10} & -\sqrt{15} & 0 & 5 & \frac{1}{\sqrt{84}} \\ \cdot & \cdot & \cdot & \cdot & \sqrt{5} & -5 & 5 & \frac{1}{\sqrt{84}} \end{matrix}$
	$\langle \mathbf{v}_{q=-3...3}^3 \rangle^{J=2} =$ $\begin{matrix} 1 & \sqrt{3} & 1 & -1 & \cdot & \cdot \\ \sqrt{3} & -2 & \sqrt{2} & 0 & -1 & \frac{1}{\sqrt{2}} \\ 1 & -\sqrt{2} & 0 & \sqrt{2} & -1 & \frac{1}{\sqrt{2}} \\ 1 & 0 & -\sqrt{2} & 2 & -\sqrt{3} & \frac{1}{\sqrt{10}} \\ \cdot & 1 & -1 & \sqrt{3} & -1 & \frac{1}{\sqrt{10}} \end{matrix}$	$\langle \mathbf{v}_{q=-3...3}^3 \rangle^{J=3} =$ $\begin{matrix} 1 & -\sqrt{2} & \sqrt{2} & -1 & \cdot & \cdot & \cdot & \cdot \\ \sqrt{2} & -1 & 0 & 1 & -\sqrt{2} & \cdot & \cdot & \cdot \\ 1 & 1 & -1 & 0 & 1 & -1 & -1 & \frac{1}{\sqrt{6}} \\ \cdot & \sqrt{2} & 0 & -1 & 1 & 0 & -\sqrt{2} & \frac{1}{\sqrt{6}} \\ \cdot & \cdot & \sqrt{2} & -1 & 0 & 1 & -\sqrt{2} & \frac{1}{\sqrt{6}} \\ \cdot & \cdot & \cdot & 1 & -\sqrt{2} & \sqrt{2} & -1 & \frac{1}{\sqrt{6}} \end{matrix}$
	$\langle \mathbf{v}_{q=-4...4}^4 \rangle^{J=2} =$ $\begin{matrix} 1 & -1 & \sqrt{3} & -1 & 1 & \frac{1}{\sqrt{2}} \\ 1 & -4 & \sqrt{6} & -\sqrt{8} & 1 & \frac{1}{\sqrt{2}} \\ \sqrt{3} & -\sqrt{6} & 6 & -\sqrt{6} & \sqrt{3} & \frac{1}{\sqrt{14}} \\ 1 & -\sqrt{8} & \sqrt{6} & -4 & 1 & \frac{1}{\sqrt{14}} \\ 1 & -1 & \sqrt{3} & -1 & 1 & \frac{1}{\sqrt{70}} \end{matrix}$	$\langle \mathbf{v}_{q=-4...4}^4 \rangle^{J=3} =$ $\begin{matrix} 3 & -\sqrt{30} & \sqrt{54} & -3 & \sqrt{3} & \cdot & \cdot & \cdot \\ \sqrt{30} & -7 & \sqrt{32} & -\sqrt{3} & -\sqrt{2} & \sqrt{5} & \cdot & \frac{1}{\sqrt{2}} \\ \sqrt{54} & -\sqrt{32} & 1 & \sqrt{15} & -\sqrt{40} & \sqrt{2} & \sqrt{3} & \frac{1}{\sqrt{2}} \\ 3 & -\sqrt{3} & -\sqrt{15} & 6 & -\sqrt{15} & -\sqrt{3} & 3 & \frac{1}{\sqrt{6}} \\ \sqrt{3} & \sqrt{2} & -\sqrt{40} & \sqrt{15} & 1 & -\sqrt{32} & \sqrt{54} & \frac{1}{\sqrt{6}} \\ \cdot & \sqrt{5} & -\sqrt{2} & -\sqrt{3} & \sqrt{32} & -7 & \sqrt{30} & \frac{1}{\sqrt{84}} \\ \cdot & \cdot & \sqrt{3} & -3 & \sqrt{54} & -\sqrt{30} & 3 & \frac{1}{\sqrt{84}} \end{matrix}$
		$\langle \mathbf{v}_{q=-5...5}^5 \rangle^{J=3} =$ $\begin{matrix} 1 & -\sqrt{5} & 1 & -\sqrt{2} & 1 & -1 & \cdot & \cdot \\ \sqrt{5} & -4 & \sqrt{27} & -\sqrt{2} & 1 & 0 & -1 & \frac{1}{\sqrt{2}} \\ 1 & -\sqrt{27} & 5 & -\sqrt{10} & 0 & 1 & -1 & \frac{1}{\sqrt{2}} \\ \sqrt{2} & -\sqrt{2} & \sqrt{10} & 0 & -\sqrt{10} & \sqrt{2} & -\sqrt{2} & \frac{1}{\sqrt{6}} \\ 1 & -1 & 0 & \sqrt{10} & -5 & \sqrt{27} & -1 & \frac{1}{\sqrt{6}} \\ 1 & 0 & -1 & \sqrt{2} & -\sqrt{27} & 4 & -\sqrt{5} & \frac{1}{\sqrt{84}} \\ \cdot & 1 & -1 & \sqrt{2} & -1 & \sqrt{5} & -1 & \frac{1}{\sqrt{84}} \end{matrix}$
		$\langle \mathbf{v}_{q=-6...6}^6 \rangle^{J=3} =$ $\begin{matrix} 1 & -\sqrt{2} & 1 & -\sqrt{2} & \sqrt{5} & -1 & 1 & \frac{1}{\sqrt{2}} \\ \sqrt{2} & -6 & \sqrt{30} & -\sqrt{8} & 3 & -\sqrt{12} & 1 & \frac{1}{\sqrt{2}} \\ 1 & -\sqrt{30} & 15 & -10 & \sqrt{15} & -3 & \sqrt{5} & \frac{1}{\sqrt{22}} \\ \sqrt{2} & -\sqrt{8} & 10 & -20 & 10 & -\sqrt{8} & \sqrt{2} & \frac{1}{\sqrt{22}} \\ \sqrt{5} & -3 & \sqrt{15} & -10 & 15 & -\sqrt{30} & 1 & \frac{1}{\sqrt{33}} \\ 1 & -\sqrt{12} & 3 & -\sqrt{8} & \sqrt{30} & -6 & \sqrt{2} & \frac{1}{\sqrt{264}} \\ 1 & -1 & \sqrt{5} & -\sqrt{2} & 1 & -\sqrt{2} & 1 & \frac{1}{\sqrt{924}} \end{matrix}$

Table 3. Tabulated \mathbf{v}_q^k values and relation to quaternions. (a) Tabulated \mathbf{v}_q^k values for $J = 1/2$; (b) Simple Conversion from \mathbf{v} to σ ; (c) Conventional quaternion-spinor relations.

(a) Tabulated \mathbf{v}_q^k values for $J=1/2$

$\langle \mathbf{v}_{-1}^1 \rangle^{J=1/2} =$ $\begin{pmatrix} \cdot & \cdot \\ -1 & \cdot \end{pmatrix}$	$\langle \mathbf{v}_0^1 \rangle^{J=1/2} =$ $-\begin{pmatrix} 1 & \cdot \\ \cdot & -1 \end{pmatrix} \frac{1}{\sqrt{2}}$	$\langle \mathbf{v}_1^1 \rangle^{J=1/2} =$ $\begin{pmatrix} \cdot & 1 \\ \cdot & \cdot \end{pmatrix}$	$\langle \mathbf{v}_{-1\dots 1}^1 \rangle^{J=1/2} =$ $\begin{pmatrix} -1 & 1 \\ -1 & 1 \end{pmatrix} \Big \frac{1}{\sqrt{2}}$
	$\langle \mathbf{v}_0^0 \rangle^{J=1/2} =$ $\begin{pmatrix} -1 & \cdot \\ \cdot & -1 \end{pmatrix} \frac{1}{\sqrt{2}}$		$\langle \mathbf{v}_0^0 \rangle^{J=1/2} =$ $-\begin{pmatrix} 1 & \cdot \\ \cdot & 1 \end{pmatrix} \frac{1}{\sqrt{2}}$

(b) Simple Conversion from \mathbf{v} to σ

$\mathbf{v}_{-1}^1 = -\sigma_-$	$\mathbf{v}_0^1 = -\frac{1}{\sqrt{2}}\sigma_z$	$\mathbf{v}_{+1}^1 = +\sigma_+$	$\mathbf{v}_0^0 = +\sigma_0$
$\sigma_x = \sigma_+ + \sigma_-$ $= \begin{pmatrix} \cdot & 1 \\ 1 & \cdot \end{pmatrix}$	$\sigma_z = -\sqrt{2}\mathbf{v}_0^1$ $= \begin{pmatrix} +1 & \cdot \\ \cdot & -1 \end{pmatrix}$	$\sigma_y = -i\sigma_+ + i\sigma_-$ $= \begin{pmatrix} \cdot & -i \\ i & \cdot \end{pmatrix}$	$\sigma_0 = -\sqrt{2}\mathbf{v}_0^0$ $= \begin{pmatrix} 1 & 0 \\ 0 & 1 \end{pmatrix}$

(c) Conventional quaternion-spinor relations

$\mathbf{i} = i\sigma_x$ $= \begin{pmatrix} 0 & i \\ i & 0 \end{pmatrix}$	$\mathbf{k} = i\sigma_z$ $= \begin{pmatrix} +i & 0 \\ 0 & -i \end{pmatrix}$	$\mathbf{j} = i\sigma_y$ $= \begin{pmatrix} 0 & 1 \\ -1 & 0 \end{pmatrix}$	$\mathbf{1} = \sigma_0$ $= \begin{pmatrix} 1 & 0 \\ 0 & 1 \end{pmatrix}$
--	--	---	---

1.3.2. Tensor and Elementary Matrix Operators

Coefficient $\langle \begin{smallmatrix} J \\ m' \end{smallmatrix} | \mathbf{v}_q^k | \begin{smallmatrix} J \\ m \end{smallmatrix} \rangle$ of elementary operator $\mathbf{e}_{m',m} = \begin{smallmatrix} J \\ m' \end{smallmatrix} \rangle \langle \begin{smallmatrix} J \\ m \end{smallmatrix} |$ is the following CG or Wigner 3-j.

$$\langle \mathbf{v}_q^k \rangle^J = \sum_{m',m} \langle \begin{smallmatrix} J \\ m' \end{smallmatrix} | \mathbf{v}_q^k | \begin{smallmatrix} J \\ m \end{smallmatrix} \rangle \langle \begin{smallmatrix} J \\ m' \end{smallmatrix} \rangle \langle \begin{smallmatrix} J \\ m \end{smallmatrix} | = \sum_{m',m} \langle \begin{smallmatrix} J \\ m' \end{smallmatrix} | \mathbf{v}_q^k | \begin{smallmatrix} J \\ m \end{smallmatrix} \rangle \langle \mathbf{e}_{m'm} \rangle^J \text{ where: } q = m' - m \quad (15a)$$

$$\langle \begin{smallmatrix} J' \\ m' \end{smallmatrix} | \mathbf{v}_q^k | \begin{smallmatrix} J \\ m \end{smallmatrix} \rangle = (-1)^{J'+m'} \sqrt{[k]} \begin{pmatrix} k & J & J' \\ q & m & -m' \end{pmatrix} = (-1)^{J'+J-k} \sqrt{\frac{[k]}{[J]}} C_{qmm'}^{kJJ'} \quad (15b)$$

Each matrix $\langle \mathbf{v}_q^k \rangle^J$ for $J' = J = 1$ to 5 is displayed in compressed form by the following tensor representation Table 2.

CG-3j relation Equation (13c) implies $\langle \mathbf{v}_q^k \rangle^J$ and $\langle \mathbf{e}_{m',m} \rangle^J$ matrices have ortho-complete unit vectors of dimension $d(J, q) = [J] - q = 2J - q + 1$ along q^{th} -diagonal of each $[J]$ -by- $[J]$ matrix. For example, quadrupole \mathbf{v}_2^2 , octopole \mathbf{v}_2^3 , and 2^4 -pole \mathbf{v}_2^4 share the $q = 2$ diagonal of $J = 2$ Table 2.

$$\begin{aligned} \langle \mathbf{v}_{q=\pm 2}^2 \rangle^{J=2} &= \sqrt{\frac{2}{7}} \langle \mathbf{e}_{-2,0} \rangle^{J=2} + \sqrt{\frac{2}{7}} \langle \mathbf{e}_{-1,1} \rangle^{J=2} + \sqrt{\frac{2}{7}} \langle \mathbf{e}_{0,2} \rangle^{J=2} \\ \begin{vmatrix} \cdot & \cdot & \sqrt{\frac{2}{7}} & \cdot & \cdot \\ \cdot & \cdot & \cdot & \sqrt{\frac{3}{7}} & \cdot \\ \cdot & \cdot & \cdot & \cdot & \sqrt{\frac{2}{7}} \\ \cdot & \cdot & \cdot & \cdot & \cdot \\ \cdot & \cdot & \cdot & \cdot & \cdot \end{vmatrix} &= \sqrt{\frac{2}{7}} \begin{vmatrix} \cdot & \cdot & 1 & \cdot & \cdot \\ \cdot & \cdot & \cdot & \cdot & \cdot \\ \cdot & \cdot & \cdot & \cdot & \cdot \\ \cdot & \cdot & \cdot & \cdot & \cdot \\ \cdot & \cdot & \cdot & \cdot & \cdot \end{vmatrix} + \sqrt{\frac{3}{7}} \begin{vmatrix} \cdot & \cdot & \cdot & \cdot & \cdot \\ \cdot & \cdot & \cdot & 1 & \cdot \\ \cdot & \cdot & \cdot & \cdot & \cdot \\ \cdot & \cdot & \cdot & \cdot & \cdot \\ \cdot & \cdot & \cdot & \cdot & \cdot \end{vmatrix} + \sqrt{\frac{2}{7}} \begin{vmatrix} \cdot & \cdot & \cdot & \cdot & \cdot \\ \cdot & \cdot & \cdot & \cdot & \cdot \\ \cdot & \cdot & \cdot & \cdot & 1 \\ \cdot & \cdot & \cdot & \cdot & \cdot \\ \cdot & \cdot & \cdot & \cdot & \cdot \end{vmatrix} \end{aligned} \tag{16a}$$

$$\begin{aligned} \langle \mathbf{v}_{q=\pm 2}^3 \rangle^{J=2} &= \sqrt{\frac{1}{2}} \langle \mathbf{e}_{-2,0} \rangle^{J=2} + 0 \langle \mathbf{e}_{-1,1} \rangle^{J=2} - \sqrt{\frac{1}{2}} \langle \mathbf{e}_{0,2} \rangle^{J=2} \\ \begin{vmatrix} \cdot & \cdot & \sqrt{\frac{1}{2}} & \cdot & \cdot \\ \cdot & \cdot & \cdot & 0 & \cdot \\ \cdot & \cdot & \cdot & \cdot & -\sqrt{\frac{1}{2}} \\ \cdot & \cdot & \cdot & \cdot & \cdot \\ \cdot & \cdot & \cdot & \cdot & \cdot \end{vmatrix} &= \sqrt{\frac{1}{2}} \begin{vmatrix} \cdot & \cdot & 1 & \cdot & \cdot \\ \cdot & \cdot & \cdot & \cdot & \cdot \\ \cdot & \cdot & \cdot & \cdot & \cdot \\ \cdot & \cdot & \cdot & \cdot & \cdot \\ \cdot & \cdot & \cdot & \cdot & \cdot \end{vmatrix} + 0 \begin{vmatrix} \cdot & \cdot & \cdot & \cdot & \cdot \\ \cdot & \cdot & \cdot & 1 & \cdot \\ \cdot & \cdot & \cdot & \cdot & \cdot \\ \cdot & \cdot & \cdot & \cdot & \cdot \\ \cdot & \cdot & \cdot & \cdot & \cdot \end{vmatrix} - \sqrt{\frac{1}{2}} \begin{vmatrix} \cdot & \cdot & \cdot & \cdot & \cdot \\ \cdot & \cdot & \cdot & \cdot & \cdot \\ \cdot & \cdot & \cdot & \cdot & 1 \\ \cdot & \cdot & \cdot & \cdot & \cdot \\ \cdot & \cdot & \cdot & \cdot & \cdot \end{vmatrix} \end{aligned}$$

$$\begin{aligned} \langle \mathbf{v}_{q=\pm 2}^4 \rangle^{J=2} &= \sqrt{\frac{3}{14}} \langle \mathbf{e}_{-2,0} \rangle^{J=2} - \sqrt{\frac{8}{14}} \langle \mathbf{e}_{-1,1} \rangle^{J=2} - \sqrt{\frac{3}{14}} \langle \mathbf{e}_{0,2} \rangle^{J=2} \\ \begin{vmatrix} \cdot & \cdot & \sqrt{\frac{3}{14}} & \cdot & \cdot \\ \cdot & \cdot & \cdot & -\sqrt{\frac{8}{14}} & \cdot \\ \cdot & \cdot & \cdot & \cdot & \sqrt{\frac{3}{14}} \\ \cdot & \cdot & \cdot & \cdot & \cdot \\ \cdot & \cdot & \cdot & \cdot & \cdot \end{vmatrix} &= \sqrt{\frac{3}{14}} \begin{vmatrix} \cdot & \cdot & 1 & \cdot & \cdot \\ \cdot & \cdot & \cdot & \cdot & \cdot \\ \cdot & \cdot & \cdot & \cdot & \cdot \\ \cdot & \cdot & \cdot & \cdot & \cdot \\ \cdot & \cdot & \cdot & \cdot & \cdot \end{vmatrix} - \sqrt{\frac{8}{14}} \begin{vmatrix} \cdot & \cdot & \cdot & \cdot & \cdot \\ \cdot & \cdot & \cdot & 1 & \cdot \\ \cdot & \cdot & \cdot & \cdot & \cdot \\ \cdot & \cdot & \cdot & \cdot & \cdot \\ \cdot & \cdot & \cdot & \cdot & \cdot \end{vmatrix} + \sqrt{\frac{3}{14}} \begin{vmatrix} \cdot & \cdot & \cdot & \cdot & \cdot \\ \cdot & \cdot & \cdot & \cdot & \cdot \\ \cdot & \cdot & \cdot & \cdot & 1 \\ \cdot & \cdot & \cdot & \cdot & \cdot \\ \cdot & \cdot & \cdot & \cdot & \cdot \end{vmatrix} \end{aligned}$$

Tensor $\langle \mathbf{v}_q^k \rangle^J$ relations easily invert to $\langle \mathbf{e}_{m',m} \rangle^J$ by inspection due to their being orthonormal sets.

$$\begin{aligned} \langle \mathbf{e}_{-2,0} \rangle^{J=2} &= \sqrt{\frac{2}{7}} \langle \mathbf{v}_{q=\pm 2}^2 \rangle^{J=2} + \sqrt{\frac{1}{2}} \langle \mathbf{v}_{q=\pm 2}^3 \rangle^{J=2} + \sqrt{\frac{3}{14}} \langle \mathbf{v}_{q=\pm 2}^4 \rangle^{J=2} \\ \langle \mathbf{e}_{-1,1} \rangle^{J=2} &= \sqrt{\frac{3}{7}} \langle \mathbf{v}_{q=\pm 2}^2 \rangle^{J=2} + 0 \langle \mathbf{v}_{q=\pm 2}^3 \rangle^{J=2} - \sqrt{\frac{8}{14}} \langle \mathbf{v}_{q=\pm 2}^4 \rangle^{J=2} \\ \langle \mathbf{e}_{0,2} \rangle^{J=2} &= \sqrt{\frac{2}{7}} \langle \mathbf{v}_{q=\pm 2}^2 \rangle^{J=2} - \sqrt{\frac{1}{2}} \langle \mathbf{v}_{q=\pm 2}^3 \rangle^{J=2} + \sqrt{\frac{3}{14}} \langle \mathbf{v}_{q=\pm 2}^4 \rangle^{J=2} \end{aligned} \tag{16b}$$

Any $[J]$ -by- $[J]$ matrix is a combination of elementary $\langle \mathbf{e}_{m',m} \rangle^J$ and thus also of $\langle \mathbf{v}_q^k \rangle^J$. This leads to RES maps that approximate $[J]$ -by- $[J]$ matrix $\langle \mathbf{v}_q^k \rangle^J$ eigensolutions by plotting related combinations of $Y_q^k(\theta, \phi)$ for select θ_M^J .

1.3.3. Fano–Racah Tensor Algebra

Diagonal dipole-vector (rank $k = 1$) matrix $\langle \mathbf{v}_0^1 \rangle^J$ is seen in top row of Table 2 to be proportional to the angular momentum z -component matrix $\langle \mathbf{J}_z \rangle^J$. Diagonal 2^k -pole (rank- k) tensors $\langle \mathbf{v}_0^k \rangle^J$ are linearly related to \mathbf{J}_z powers $\mathbf{J}_z^2 = \mathbf{J}_z \mathbf{J}_z$, $\mathbf{J}_z^3 = \mathbf{J}_z \mathbf{J}_z \mathbf{J}_z, \dots$ up to the k^{th} -power \mathbf{J}_z^k . This relates $\langle \mathbf{v}_0^k \rangle^J$ -eigenvalues to powers m^p of $\langle \mathbf{J}_z \rangle$ -eigenvalues m and, in turn, leads to an RES scheme to analyze $\langle \mathbf{v}_q^k \rangle^J$ eigensolutions.

For example, matrix diagonals in Table 2 give elementary representations for $J = 2$.

$$\begin{aligned} \sqrt{5} \langle \mathbf{v}_0^0 \rangle^{(J=2)} &= \langle \mathbf{1} \rangle^{(2)} &&= \begin{pmatrix} 1 & 1 & 1 & 1 & 1 \end{pmatrix} \\ \sqrt{10} \langle \mathbf{v}_0^1 \rangle^{(J=2)} &= \langle \mathbf{J}_z \rangle^{(2)} &&= \begin{pmatrix} 2 & 1 & 0 & -1 & 2 \end{pmatrix} \end{aligned} \tag{17a}$$

$$\begin{aligned} \sqrt{14} \langle \mathbf{v}_0^2 \rangle^{(2)} &= \begin{pmatrix} 2 & -1 & -2 & -1 & 2 \end{pmatrix} \\ \sqrt{10} \langle \mathbf{v}_0^3 \rangle^{(2)} &= \begin{pmatrix} 1 & -2 & 0 & 2 & -1 \end{pmatrix} \\ \sqrt{70} \langle \mathbf{v}_0^4 \rangle^{(2)} &= \begin{pmatrix} 1 & -4 & 6 & -4 & 1 \end{pmatrix} \end{aligned} \tag{17b}$$

Powers of $\langle \mathbf{J}_z \rangle^2$ in Equation (18) are combinations of $\langle \mathbf{v}_q^k \rangle^2$ found by dot products with vectors in Equations (17a) and (17b).

$$\begin{aligned} \langle \mathbf{J}_z^0 \rangle^{(2)} &= \begin{pmatrix} 1 & 1 & 1 & 1 & 1 \end{pmatrix} = \frac{5}{\sqrt{5}} \langle \mathbf{v}_0^0 \rangle^{(2)} \\ \langle \mathbf{J}_z^1 \rangle^{(2)} &= \begin{pmatrix} 2 & 1 & 0 & -1 & -2 \end{pmatrix} = \frac{10}{\sqrt{10}} \langle \mathbf{v}_0^1 \rangle^{(2)} \\ \langle \mathbf{J}_z^2 \rangle^{(2)} &= \begin{pmatrix} 4 & 1 & 0 & 1 & 4 \end{pmatrix} = \frac{10}{\sqrt{5}} \langle \mathbf{v}_0^0 \rangle^{(2)} + \frac{14}{\sqrt{14}} \langle \mathbf{v}_0^2 \rangle^{(2)} \\ \langle \mathbf{J}_z^3 \rangle^{(2)} &= \begin{pmatrix} 8 & 1 & 0 & -1 & -8 \end{pmatrix} = \frac{34}{\sqrt{10}} \langle \mathbf{v}_0^1 \rangle^{(2)} + \frac{12}{\sqrt{10}} \langle \mathbf{v}_0^3 \rangle^{(2)} \\ \langle \mathbf{J}_z^4 \rangle^{(2)} &= \begin{pmatrix} 16 & 1 & 0 & 1 & 16 \end{pmatrix} = \frac{34}{\sqrt{5}} \langle \mathbf{v}_0^0 \rangle^{(2)} + \frac{62}{\sqrt{14}} \langle \mathbf{v}_0^2 \rangle^{(2)} + \frac{24}{\sqrt{70}} \langle \mathbf{v}_0^4 \rangle^{(2)} \end{aligned} \tag{18}$$

$$\begin{aligned} \langle \mathbf{v}_0^0 \rangle^{(2)} &= \frac{1}{\sqrt{5}} \langle \mathbf{J}_z^0 \rangle^{(2)} \\ \langle \mathbf{v}_0^1 \rangle^{(2)} &= \frac{1}{\sqrt{10}} \langle \mathbf{J}_z^1 \rangle^{(2)} \\ \langle \mathbf{v}_0^2 \rangle^{(2)} &= -\frac{2}{\sqrt{14}} \langle \mathbf{J}_z^0 \rangle^{(2)} + \frac{1}{\sqrt{14}} \langle \mathbf{J}_z^2 \rangle^{(2)} \\ \langle \mathbf{v}_0^3 \rangle^{(2)} &= -\frac{34\sqrt{10}}{120} \langle \mathbf{J}_z^1 \rangle^{(2)} + \frac{\sqrt{10}}{12} \langle \mathbf{J}_z^3 \rangle^{(2)} \\ \langle \mathbf{v}_0^4 \rangle^{(2)} &= \frac{3\sqrt{70}}{(5)(7)} \langle \mathbf{J}_z^0 \rangle^{(2)} - \frac{31\sqrt{70}}{(3)(7)(8)} \langle \mathbf{J}_z^2 \rangle^{(2)} + \frac{\sqrt{70}}{24} \langle \mathbf{J}_z^4 \rangle^{(2)} \end{aligned} \tag{19}$$

Triangle inversion of Equation (18) gives each $\langle \mathbf{v}_0^k \rangle^2$ in terms of \mathbf{J}_z powers $\langle \mathbf{J}_z^p \rangle^2 = m^p$ in Equation (19). RES plots depend on relating $\langle \mathbf{v}_0^k \rangle^J$ expansions Equation (19) in \mathbf{J}_z to Wigner (J, m)

polynomials $(-1)^{J-m} \sqrt{\frac{2k+1}{2}} \begin{pmatrix} k & J & J \\ 0 & m & -m \end{pmatrix}$ in Equation (14) and Legendre polynomials $\mathcal{D}_{00}^k(\cdot\theta\cdot) = P_k(\cos \theta)$ in Equation (11) that are also polynomials of $J_z = |J| \cos \theta$. By plotting the latter we hope to shed light on the eigensolutions of the former.

2. Tensor Eigensolution and Legendre Function RE Surfaces

Legendre polynomials occupy the central (00)-component of a Wigner- D^J matrix.

$$\mathcal{D}_{00}^k(\cdot\theta\cdot) = P_k(\cos \theta) \tag{20}$$

Examples of Legendre polynomials of $\cos \theta = J_z/|J|$ and $J_z = |J| \cos \theta$ are given below.

$$\begin{aligned} P_0 &= 1 \\ P_1(\cos \theta) &= \cos \theta \\ P_2(\cos \theta) &= -\frac{1}{2} \cos^2 \theta \\ P_3(\cos \theta) &= -\frac{3}{2} \cos \theta + \frac{5}{2} \cos^3 \theta \\ P_4(\cos \theta) &= \frac{3}{8} \cos^4 \theta - \frac{30}{8} \cos^2 \theta + \frac{35}{8} \cos^4 \theta \end{aligned} \tag{21a}$$

$$\begin{aligned} |J|^1 P_1(\cos \theta) &= J_z \\ |J|^2 P_2(\cos \theta) &= -\frac{1}{2} |J|^2 + \frac{3}{2} J_z^2 \\ |J|^3 P_3(\cos \theta) &= -\frac{3}{2} |J|^2 J_z + \frac{5}{2} J_z^3 \\ |J|^4 P_4(\cos \theta) &= \frac{3}{8} |J|^4 - \frac{30}{8} |J|^2 J_z^2 + \frac{35}{8} J_z^4 \end{aligned} \tag{21b}$$

Classical P_k functions are compared with corresponding quantized $\langle \mathbf{v}_0^k \rangle^J$ unit-tensor e -values in Table 4 that generalize examples of tensor matrix ($J=1$ to 3)-eigenvalues in Table 2 and Equation (19) to any J and $m = J, \dots, -J$. The powers of m and J in $\langle \mathbf{v}_0^k \rangle^J$, shown in Table 4 are taken to higher order in Table 5.

Norm $2^k \sqrt{\frac{k!}{(2k)!}} / \sqrt{2J+k} : -k+1$ makes each $\langle \mathbf{v}_0^k \rangle^J$ a unit vector. (Note: $A + a : b = (A + a)(A + a - 1) \dots (A + b)$.) In contrast, normalized P_k have $P_k(\cos 0) = 1$. Coefficients c_p of $\cos^p \theta$ sum to $1 = \sum c_p$. Square $|c_p|^2$ usually do not sum to 1.

Tensor values $\langle \mathbf{v}_0^0 \rangle^J, \langle \mathbf{v}_0^1 \rangle^J$, and $\langle \mathbf{v}_0^2 \rangle^J$ in [...] -braces of Table 4 equal Legendre functions P_0, P_1 , and P_2 in Equation (21b) exactly using J -expectation values Equations (22a) and (22b). However, for rank higher than $k = 2, P_k$ is only approximately equal to $\langle \mathbf{v}_0^k \rangle_m^J$ though the approximation improves with higher J .

$$\langle \mathbf{J}_z \rangle_m^L = m = \langle |J| \rangle_m^J \cos \theta_m^J \tag{22a}$$

$$\langle |J_z| \rangle = \sqrt{J(J+1)} \cong J + \frac{1}{2} \tag{22b}$$

Table 4. Forming $\langle \mathbf{v}_0^k \rangle$ from powers of J and m .

$\langle \mathbf{v}_0^k \rangle_m^J = \left\langle \begin{matrix} J \\ m \end{matrix} \middle \mathbf{v}_0^k \middle \begin{matrix} J \\ m \end{matrix} \right\rangle = (-1)^{J-m} \sqrt{[k]} \begin{pmatrix} k & J & J \\ 0 & m & -m \end{pmatrix} = (-1)^k \sqrt{\frac{[k]}{[J]}} C_{0mm}^{kJJ}$		
$\langle \mathbf{v}_0^0 \rangle_m^J =$	$\frac{1}{\sqrt{2J+1}}$	[1]
$\langle \mathbf{v}_0^1 \rangle_m^J =$	$\frac{2\sqrt{3}}{\sqrt{2J+2}}$	[m]
$\langle \mathbf{v}_0^2 \rangle_m^J =$	$\frac{2^2\sqrt{5}}{\sqrt{2J+3}}$	$[-\frac{1}{2}J(J+1) \quad +\frac{3}{2}m^2]$
$\langle \mathbf{v}_0^3 \rangle_m^J =$	$\frac{2^3\sqrt{7}}{\sqrt{2J+4}}$	$[-\frac{3}{2}(J(J+1) - \frac{2}{3}m) \quad +\frac{5}{2}m^3]$

For large- J values, the $\langle \mathbf{v}_0^k \rangle_m^J$ in Table 4 approach the P_3, P_4, \dots of Equation (21b) according to the relation: $\langle |J|^k \rangle_m^J \xrightarrow{J \gg k} [J(J+1)]^{k/2}$. However, $\langle \mathbf{v}_0^k \rangle_m^J$ differ significantly from P_k for low J . The classical P_k in Equation (21b) lack the small terms ($-2/3, -5/6, etc.$) that kill the $\langle \mathbf{v}_0^k \rangle$ in Table 4 whenever J falls below strict quantum limits such as whenever $J < |m|$ or $J < k/2$. However, the quantum “killer” terms become negligible for larger J -values ($J > k$) and this makes tensor eigenvalues converge to P_k and thus to their RES plots.

2.1. Angular Momentum Cones and RES Paths

Quantum J -magnitude Equation (22b) introduces a quantum angular momentum cone geometry with quantized angles θ_m^J given by Equation (22a) as summarized here in Equation (23a) and (23b) for lab $m = M$ and molecular body $n = K$.

$$\cos \theta_M^J = \frac{M}{\sqrt{J(J+1)}} \tag{23a}$$

$$\cos \theta_K^J = \frac{K}{\sqrt{J(J+1)}} \tag{23b}$$

An angular momentum eigenstate $\left| \begin{matrix} J \\ m, n \end{matrix} \right\rangle$ has sharp (zero-uncertainty) eigenvalue m or n on the lab or body frame z or \bar{z} axis, respectively. This sharp altitude and magnitude in Equation (22b) constrains vector \mathbf{J} to base circles of cones making half-angle θ_m^J or θ_n^J with z or \bar{z} axes, respectively. Expected \mathbf{J} -values appear in Figure 1 at intersections of quantized \mathbf{J} -cones with the RES as explained below.

Table 5. Forming $\langle \mathbf{v}_0^k \rangle$ from powers of J and m , expanded.

k	m^0	m^1	m^2	m^3	m^4	m^5	m^6	m^7
0	1							
1		1						
2	$-\frac{1}{2}J(J+1)$		$\frac{3}{2}$					
3		$-\frac{3}{2}(J(J+1) - \frac{2}{3})$		$\frac{5}{2}$				
4	$\frac{3}{8}(J+2 : -1)$		$-\frac{30}{8}(J(J+1) - \frac{5}{6})$		$\frac{35}{8}$			
5		$\frac{15}{8}(J+2 : -1) - \frac{4}{3}J(J+1) - \frac{4}{5}$		$-\frac{70}{8}(J(J+1) - \frac{3}{2})$		$\frac{63}{8}$		
6	$-\frac{5}{16}(J+3 : -2)$		$\frac{105}{16}(J+2 : -1) - 3J(J+1) + \frac{14}{5}$		$-\frac{315}{16}(J(J+1) - \frac{7}{3})$		$\frac{231}{16}$	
7		$-\frac{35}{16}(J+3 : -2) - 3(J+2 : -1) + \frac{36}{5}J(J+1) - \frac{36}{7}$		$\frac{315}{16}(J+2 : -1) - 5J(J+1) + \frac{61}{9}$		$-\frac{693}{16}(J(J+1) - \frac{10}{3})$		$\frac{429}{16}$
8	$35(J+4 : -3)$		$-\frac{1260}{128}(J+3 : -2) - \frac{13}{2}(J+2 : -1) + \frac{332}{15}J(J+1) - \frac{761}{35}$		$\frac{6930}{128}(J+2 : -1) - \frac{22}{3}J(J+1) - \frac{1871}{1386}$		$-\frac{12012}{128}(J(J+1) + \frac{9}{2})$	$\frac{6435}{128}$

RES energy level analysis begins by writing a multipole T_q^k tensor expansion Equation (24a) of a general rigid rotor or asymmetric top Hamiltonian and then plotting the resulting surface using Equation (24a)

$$\begin{aligned} H &= A(J_{\bar{x}})^2 + B(J_{\bar{y}})^2 + C(J_{\bar{z}})^2 \\ &= \frac{1}{3}(A + B + C)T_0^0 + \frac{1}{3}(2C - A - B)T_0^2 \\ &\quad + \frac{1}{\sqrt{6}}(A - B)(T_2^2 + T_{-2}^2) \end{aligned} \quad (24a)$$

$$\begin{aligned} T_0^0 &= (J_{\bar{x}})^2 + (J_{\bar{y}})^2 + (J_{\bar{z}})^2 = |\mathbf{J}|^2 \\ T_0^2 &= \frac{-1}{2}(J_{\bar{x}})^2 - \frac{1}{2}(J_{\bar{y}})^2 + (J_{\bar{z}})^2 = |\mathbf{J}|^2 \left(\frac{3}{2} \cos^2 \theta - \frac{1}{2} \right) \\ &= |\mathbf{J}|^2 P_2(\cos \theta) \\ T_2^2 + T_{-2}^2 &= -\sqrt{\frac{3}{2}}(J_{\bar{x}})^2 + \sqrt{\frac{3}{2}}(J_{\bar{y}})^2 \\ &= |\mathbf{J}|^2 \sqrt{\frac{3}{2}} \sin^2 \theta \cos 2\phi \end{aligned} \quad (24b)$$

Inertial constants ($A = 1/I_{\bar{x}}$, $B = 1/I_{\bar{y}}$, $C = 1/I_{\bar{z}}$) combine J -tensor operators T_q^k . Exact relation of $\langle \mathbf{v}_0^0 \rangle^J$ and $\langle \mathbf{v}_0^2 \rangle^J$ in Table 4 to classical P_0 and P_2 in Equation (21b) is used in Equation (24b) for T_0^0 and T_0^2 .

A rigid spherical top ($A = B = C$) has only the T_0^0 term Equation (24a). Rigid prolate ($A = B > C$) or oblate ($A = B < C$) symmetric tops have only T_0^0 and T_0^2 terms with energy eigenvalues below.

$$\begin{aligned} &\left\langle \begin{matrix} J \\ m, n \end{matrix} \middle| \mathbf{H}^{\text{SymTop}} \middle| \begin{matrix} J \\ m, n \end{matrix} \right\rangle = \\ &\left\langle \begin{matrix} J \\ m, n \end{matrix} \middle| B(\mathbf{J}_{\bar{x}})^2 + B(J_{\bar{y}})^2 + C(J_{\bar{z}})^2 \middle| \begin{matrix} J \\ m, n \end{matrix} \right\rangle \\ &= \frac{1}{3} \left\langle \begin{matrix} J \\ m, n \end{matrix} \middle| (2B + C)T_0^0 + 2(C - B)T_0^2 \middle| \begin{matrix} J \\ m, n \end{matrix} \right\rangle \\ &= \left\langle \begin{matrix} J \\ m, n \end{matrix} \middle| B|\mathbf{J}|^2 + (C - B)(J_{\bar{z}})^2 \middle| \begin{matrix} J \\ m, n \end{matrix} \right\rangle \\ &= BJ(J + 1) + (C - B)n^2 \end{aligned} \quad (25)$$

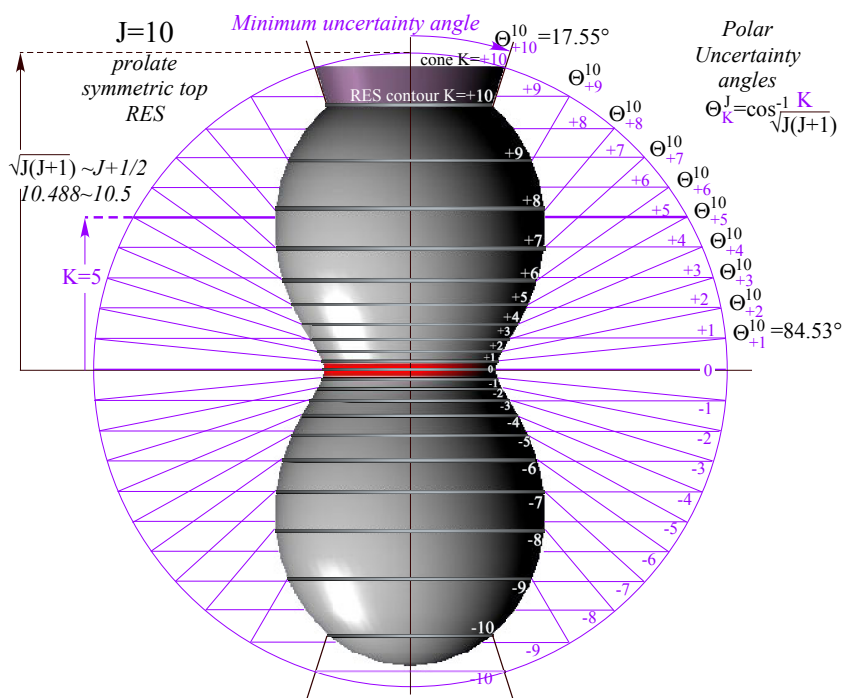
Since a rigid symmetric-top involves only T_0^0 and T_0^2 , the θ_n^J -cones define its eigenvalues exactly by \mathbf{J} -vector trajectories at angle- θ_n^J where θ_n^J -cones intersect the following T_0^2 -RES shown in Figure 1.

$$RE^{\text{SymTop}}(\theta) = \frac{1}{3}(2B + C)T_0^0(\theta) + \frac{2}{3}(C - B)T_0^2(\theta) \quad (26a)$$

Inserting quantized-body cone relation Equation (23b) yields desired eigenvalues Equation (25) exactly.

$$\begin{aligned}
 RE^{\text{SymTop}}(\theta_L^J) &= \frac{1}{3}(2B + C)J(J + 1) \\
 &+ \frac{2}{3}(C - B)J(J + 1) \left(\frac{3}{2} \cos^2 \theta_K^J - \frac{1}{2} \right) \\
 &= J(J + 1) \frac{1}{3} [(2B + C) + (C - B)(K^2 - 1)] \\
 &= J(J + 1)B + (C - B)K^2
 \end{aligned}
 \tag{26b}$$

Figure 1. J = 10 Symmetric top RES. Angular momentum cone of minimum uncertainty angle $\theta_{10}^{10}=17.55^\circ$ intersects the highest $K=J=10$ of the quantized J-path contour circles.



Cone paths in Figure 1 are constant energy contours on symmetric top RES Equations (26a) and (26b) of constant J . They may be viewed as J -phase paths on which the \mathbf{J} -vector may delocalize or “precess” on a circular θ_n^J -cone around body \bar{z} -axis. Or else one might view paths on Figure 1 as coordinate space tracks of the lab z -axis around the \bar{z} -axis by assuming \mathbf{J} lies fixed on the former. Either view describes \mathbf{J} in the body-frame by Euler polar and azimuth angles $-\beta, -\gamma$ with angle $\beta = \theta_n^J$ and $|\mathbf{J}|^2 = J(J + 1)$ fixed.

$$\mathbf{J} = (J_{\bar{x}}, J_{\bar{y}}, J_{\bar{z}}) = (-|\mathbf{J}| \cos \gamma \sin \beta, |\mathbf{J}| \sin \gamma \sin \beta, |\mathbf{J}| \cos \beta)
 \tag{27}$$

The difference between quantum solutions and semi-classical P_k solutions can be easily plotted as in Figure 2. The figure shows a slice of the semi-classical surface and the uncertainty cones for each m from J to $-J$. The orange circles indicate the intersection of the surface with the uncertainty cones and the blue circles indicate the energy of the quantum value, $\langle \mathbf{v}_0^k \rangle_m^J$, placed along the uncertainty cone.

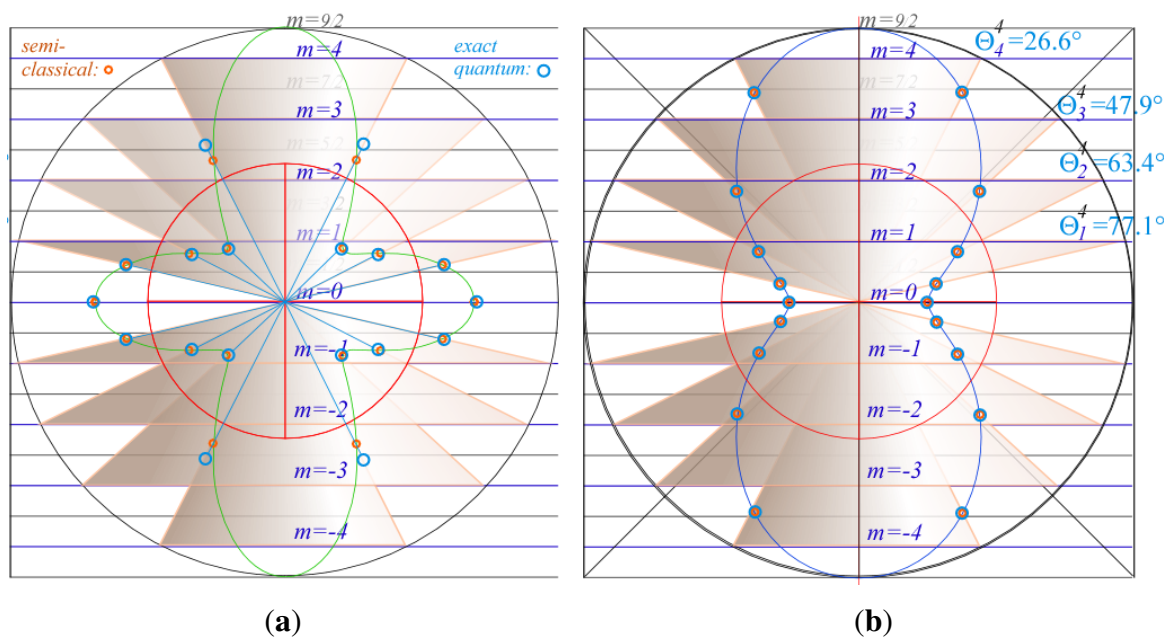
Figure 2(a) shows some divergence between quantum and semi-classical energies for $\langle v_0^4 \rangle_m^4$, while Figure 2(b) are exact for all J as in the $J = 4$ cases $\langle v_0^2 \rangle_m^4$ shown. As J and m are made larger than k then semi-classical values converge on exact eigenvalues as described below.

2.1.1. Reduced Matrix and RES Scaling

An RES is a radial plot along J direction $-\beta, -\gamma$ that has hills where energy is high and valleys where it is low, but at all points the same magnitude $|J| = \sqrt{J(J+1)}$. Origin-shift to keep RES radius positive and scaling to display hills, valleys, and saddles, may be needed to make useful RES plots.

A scalar term $s \cdot v_0^0$ added to a tensor combination $T = \sum_k t_k v_0^k$ does not affect the T -eigenvectors and neither does an overall scaling of T to cT . This is true since eigenvectors are invariant to adding a multiple $s1$ of unit matrix 1 to T or multiplying it by $c1$. (Of course, eigenvalues would, respectively, be shifted by s or scaled by c .)

Figure 2. Quantum eigenvalues (blue) compared with semi-classical cone values (orange) for multipole tensor rank (a) $k = 4$ (approximate), $\langle v_0^4 \rangle_m^4$ and $P_4(\cos \Theta_m^4)$ diverge for large m ; and (b) $k = 2$ (exact), $\langle v_0^2 \rangle_m^4$ and $P_2(\cos \Theta_m^4)$ correspond for all m .



Wigner–Racah tensor algebra defines a reduced matrix element $\langle J' || T^k || J \rangle$ to serve as a scale factor for each Clebsch–Gordan tensor matrix element having Wigner–Eckart form Equation (13a).

$$\left\langle \begin{matrix} J' \\ m' \end{matrix} \left| T_q^k \right| \begin{matrix} J \\ m \end{matrix} \right\rangle = C_{qmm'}^{kJJ'} \langle J' || T^k || J \rangle \tag{28}$$

This matrix $\left\langle \begin{matrix} J \\ m \end{matrix} \middle| T_0^2 \middle| \begin{matrix} J \\ m \end{matrix} \right\rangle$ of quadrupole- J -tensor $T_0^2 = \mathbf{J}_0^2$ in Equation (24b) reveals some key points.

$$\begin{aligned} \left\langle \begin{matrix} J \\ m \end{matrix} \middle| \left(\frac{3}{2} J_z^2 - \frac{1}{2} \mathbf{J}^2 \right) \middle| \begin{matrix} J \\ m \end{matrix} \right\rangle &= \left\langle \begin{matrix} J \\ m \end{matrix} \middle| T_0^2 \middle| \begin{matrix} J \\ m \end{matrix} \right\rangle \\ &= (C_{0mm}^{2JJ}) \cdot \langle J || T^2 || J \rangle \end{aligned} \tag{29a}$$

$$\begin{aligned} \frac{3}{2} m^2 - \frac{1}{2} J(J+1) &= \left\langle \begin{matrix} J \\ m \end{matrix} \middle| T_0^2 \middle| \begin{matrix} J \\ m \end{matrix} \right\rangle \\ &= \frac{4[J]}{\sqrt{2J+3:-1}} \left(\frac{3}{2} m^2 - \frac{1}{2} J(J+1) \right) \cdot \frac{\sqrt{2J+3:-1}}{4[J]} \end{aligned} \tag{29b}$$

Reduced matrix element $\langle J || T^2 || J \rangle$ cancels norm factor $4\sqrt{[J]}/\sqrt{2J+3:-1}$ in C_{0mm}^{2JJ} . The result is the quadratic Legendre form $|J|^2 P_2(m/|J|)$ found inside [...] -braces of Table 4 with norm $4\sqrt{[k]}/\sqrt{2J+3:-1}$ outside the braces. (The latter is just a norm in Equation (29a) and (29b) multiplied by the factor $\sqrt{[k]/[J]}$ from definition Equation (15b).)

Apparent conflicts in factors are due to having sum-of-squared-component normalization of unit \mathbf{v}^k on one hand and sum-of-component normalization of P_k on the other. Matrix elements $\left\langle \begin{matrix} J \\ m \end{matrix} \middle| T \middle| \begin{matrix} J \\ m \end{matrix} \right\rangle$ or $\left| \begin{matrix} J \\ m \end{matrix} \right\rangle \left\langle \begin{matrix} J \\ m \end{matrix} \right|$ use the former since amplitude squares give probability. However, it is *unsquared* amplitude sum $\sum c_k$ that measures anisotropy of a tensor $T = \sum c_k \cdot P_k$ since $\sum c_k$ is a maximum T -amplitude. (Each P_k contributes $P_k(0) = 1$.) Expectation values $\left\langle \begin{matrix} J \\ m \end{matrix} \middle| T \middle| \begin{matrix} J \\ m \end{matrix} \right\rangle$ scale linearly, too, but \mathbf{J}^2 tensors may have extra scale factors.

Tensor $T^2 = \mathbf{J}^2$ in Equation (29a) and (29b) scales as $|J|^2 = J(J+1)$ and $T^k = \mathbf{J}^k$ scale as $|J|^k$. Factor $4\sqrt{[J]}/\sqrt{2J+3:-1}$ of C_{0mm}^{2JJ} reduces scale $|J|^2$ to $\sqrt{2J+1} = \sqrt{[J]}$. Then the reduced factor $\langle J || T || J \rangle$ brings it back to $|J|^2$.

$$\begin{aligned} \frac{4[J]}{\sqrt{2J+3:-1}} &= \\ \frac{4(2J+1)}{\sqrt{(2J+3)(2J+2)(2J+1)(2J)(2J-1)}} & \tag{30} \\ &= \frac{\sqrt{[J]}}{\sqrt{(J+\frac{3}{2})(J+1)J(J-\frac{1}{2})}} \approx \frac{\sqrt{[J]}}{|J|^2} \end{aligned}$$

Each rank- k part has a factor $|J|^k = |J(J+1)|^{k/2}$. Anisotropy of mixed-rank \mathbf{J} -tensor $\mathbf{T} = \sum c_k \cdot \mathbf{J}^k$ is $\sum |J|^k c_k$, and thus is quite sensitive to quantum number J . So also are the RES and related eigensolutions of \mathbf{T} .

2.2. Asymmetric Top and Rank-2 RES

Plotting RES of non-diagonal Hamiltonians for the asymmetric top Equation (24a) involves 2^{nd} -rank tensors v_q^2 with reduced z-axial symmetry, nonzero q -values, and non-commuting J_a combinations. Each J_a in the quadratic expressions in Equation (24a) is replaced by its classical Euler-angle form in Equation (27).

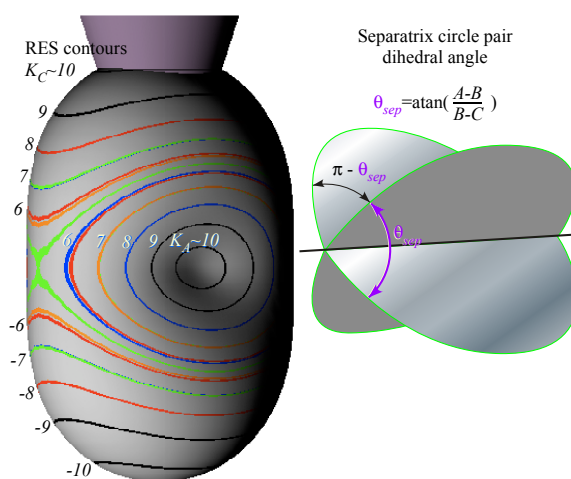
Or else, each tensor T_q^k in Equation (24a) is replaced by a multipole function $X_q^k = |J|^k \mathcal{D}_{0q}^{k*}(\cdot, \beta, \gamma)$. (Recall Equation (24b)).

$$\begin{aligned}
 H^{\text{AsymTop}} &= A (J_x)^2 + B (J_y)^2 + C (J_z)^2 \\
 \Rightarrow RES^{\text{AsymTop}} &= A (|J| \cos \gamma \sin \beta)^2 + B (|J| \sin \gamma \sin \beta)^2 + C (|J| \cos \beta)^2
 \end{aligned}
 \tag{31a}$$

$$\begin{aligned}
 H^{\text{AsymTop}} &= \frac{A + B + C}{3} T_0^0 + \frac{2C - A - B}{3} T_0^2 + \frac{A - B}{\sqrt{6}} (T_2^2 + T_{-2}^2) \\
 \Rightarrow RES^{\text{AsymTop}} &= \frac{A + B + C}{3} |J|^2 + \frac{2C - A - B}{3} X_0^2 + \frac{A - B}{\sqrt{6}} (X_2^2 + X_{-2}^2) \\
 &= |J|^2 \left[\frac{A + B}{2} + \frac{2C - A - B}{2} \cos^2 \beta + \frac{A - B}{2} \sin^2 \beta \cos 2\gamma \right]
 \end{aligned}
 \tag{31b}$$

Forms Equations (31a) and (31b) of rank- $(k = 2)$ -RES are equal and give the same plots shown in Figure 3, but tensor form Equation (31b) reveals symmetry. Terms X_0^2 and $X_{\pm 2}^2$ (Figure 1) are z -symmetric and non-zero near z -axis while $X_{\pm 2}^2$ terms are asymmetric and vary as $\sin^2 \beta$ with polar angle β between the \mathbf{J} vector and the z -axis. As β approaches $\pi/2$, $X_{\pm 2}^2$ terms grow to give equatorial valleys and saddles in Figure 3 while X_0^2 vanishes.

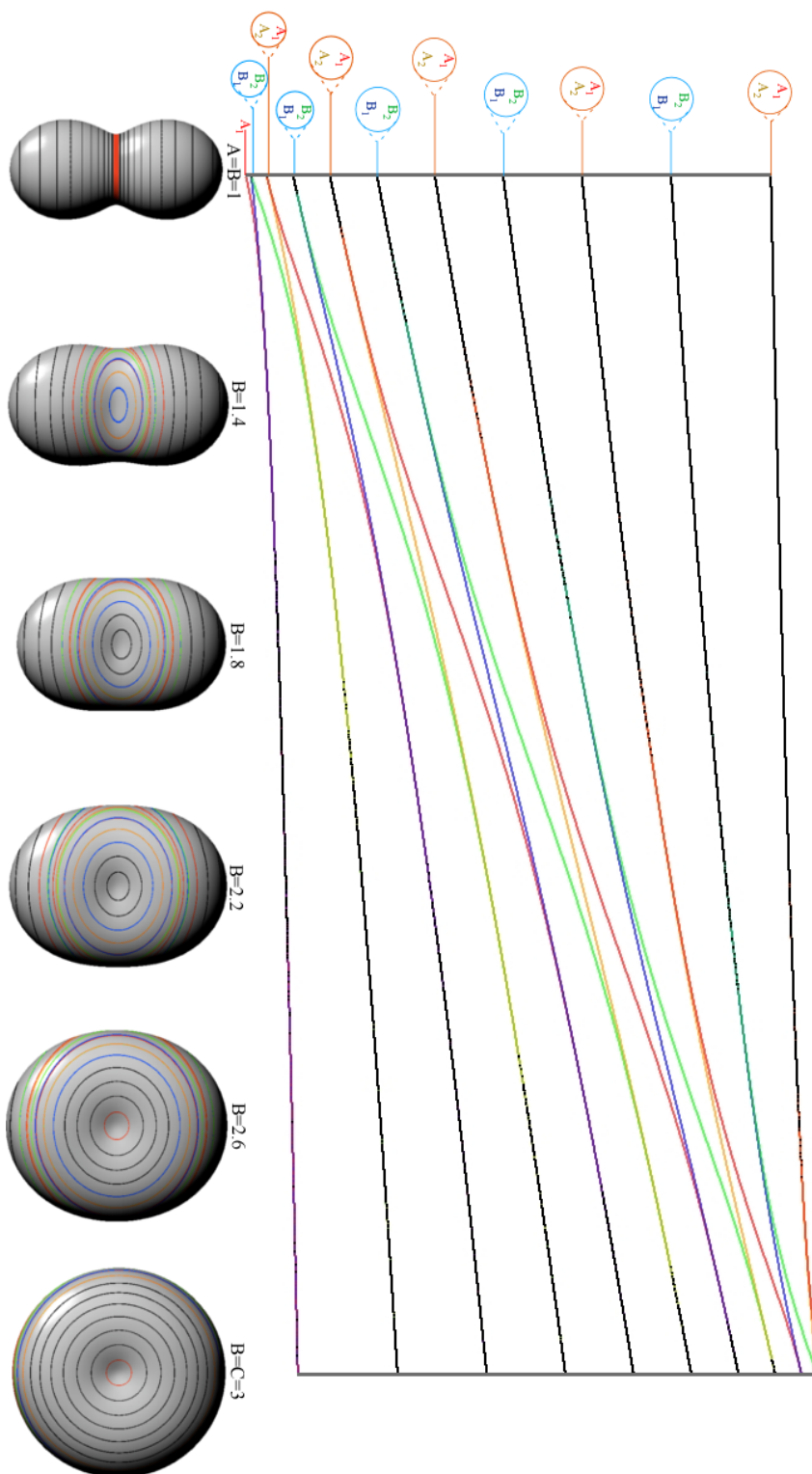
Figure 3. Asymmetric top RES $J = 10$.



Asymmetric tensor operators $T_{\pm q}^k$ are non-diagonal and do not commute with diagonal T_0^k or with each other, and so H^{AsymTop} eigenstates as well as eigenvalues vary with coefficient $(A - B)$ in Equation (31b). As $T_{\pm 2}^2$ mixes symmetric-top states $\left| \begin{smallmatrix} J \\ K \end{smallmatrix} \right\rangle$ into asymmetric-top eigenstates, θ_K^J cone circles around the z -axis of Figure 1 warp into oval-pairs squeezed by nascent ovals emerging from the

x -axis and bound by a pair of separatrix circle-planes that meet at an angle θ^{sep} on the $y(\text{or } B)$ -axis. Figure 4 shows a range of RES and levels between symmetric-prolate top ($B = A$ or $\theta^{\text{sep}} = 0$) and oblate top ($B = C$ or $\theta^{\text{sep}} = \pi$). A most-asymmetric case ($B = C$ or $\theta^{\text{sep}} = \pi/2$) is midway between the symmetric cases.

Figure 4. Asymmetric top energy levels with corresponding RES.



$$\theta^{\text{sep}} = \tan^{-1} \frac{|A - B|}{|B - C|} = \begin{cases} 0 & \text{for : } B = A \\ \pi/2 & \text{for : } B = (A + C)/2 \\ \pi & \text{for : } B = C \end{cases} \quad (32)$$

As B first differs a little from A, off-diagonal $T_{\pm 2}^2$ and asymmetric $X_{\pm 2}^2$ first “quench” degenerate $\pm K$ -momentum eigenstate pairs $\left| \begin{matrix} J \\ \pm K \end{matrix} \right\rangle$ into non-degenerate standing cos or sin-wave pairs.

$$|c_K^J\rangle = \frac{1}{\sqrt{2}} \left(\left| \begin{matrix} J \\ +K \end{matrix} \right\rangle + \left| \begin{matrix} J \\ -K \end{matrix} \right\rangle \right) \quad (33a)$$

$$|s_K^J\rangle = \frac{-i}{\sqrt{2}} \left(\left| \begin{matrix} J \\ +K \end{matrix} \right\rangle - \left| \begin{matrix} J \\ -K \end{matrix} \right\rangle \right) \quad (33b)$$

These states have nodes or anti-nodes standing on hills, saddles, or valleys of the RES topography at the principal body axes. Whether a wave is cos-like or sin-like at an axial point depends on whether it is symmetric or antisymmetric at the point and thus whether that point is an anti-node or node. Nodal location can determine whether a cos-like or sin-like wave has higher energy.

As B differs more and more from A, off-diagonal $T_{\pm 2}^2$ will mix standing waves like $|c_K^J\rangle$ with others such as $|c_{K\pm 2}^J\rangle$, $|c_{K\pm 4}^J\rangle$, and $|c_{K\pm 6}^J\rangle$ that share the same H^{AsymTop} symmetry described below.

2.3. Symmetry Labeling of Asymmetric Top Eigenstates

Throughout the range of asymmetric cases in Figure 4 the symmetry of $H^{\text{A Top}}$ in Equation (31a) and (31b) is at least orthorhombic group D_2 of 180° rotations \mathbf{R}_x , \mathbf{R}_y , and \mathbf{R}_z about inertial body axes that mutually commute ($\mathbf{R}_x\mathbf{R}_y = \mathbf{R}_z = \mathbf{R}_y\mathbf{R}_x$, etc.). Unit square ($\mathbf{R}_x^2 = 1$, etc.) \mathbf{R} -eigenvalues ± 1 label nodal symmetry (+1) or antisymmetry (−1) on each axis. D_2 is an outer product of cyclic C_2 groups for two axes, say $C_2(x)$ and $C_2(y)$. x and y values also label nodal symmetry for the z axis since $\mathbf{R}_x\mathbf{R}_y = \mathbf{R}_z$. A Cartesian 2-by-2 product of $C_2(x)$ and $C_2(y)$ symmetry character tables shown in Table 6 gives four sets of characters and four symmetry labels $[A_1, B_1, A_2, B_2]$ for $D_2 = C_2(x) \otimes C_2(y)$.

Labels (A, B) or $(1, 2)$ for (x) or (y) symmetric and anti-symmetric states follow ancient arcane conventions. We prefer a binary $(0_2, 1_2)$ notation for C_2 characters and N-ary notation $(0_N, 1_N, 2_N, \dots, (N-1)_N)$ for C_N characters $\mathcal{D}^{m_N}(R^p)$ where each label m_N denotes “ m -wave-quanta-modulo N” as in Table 7.

$$\mathcal{D}^{m_N}(\mathbf{R}^p) = e^{-im \cdot p(2\pi/N)} \quad (34)$$

This notation is used in correlation Table 8 between symmetry labels of D_2 and its subgroups $C_2(x)$, $C_2(y)$, and $C_2(z)$, respectively. Each row belongs to a D_2 species and indicates which C_2 symmetry, even (0_2) or odd (1_2), correlates to it. The Table 8(a), 8(b) and 8(c) follow respectively from the columns \mathbf{R}_x , \mathbf{R}_y , and \mathbf{R}_z of Table 6. An even (0_2) D_2 character is $\mathcal{D}^{0_2}(\mathbf{R}) = +1$ and odd (1_2) is $\mathcal{D}^{1_2}(\mathbf{R}) = -1$.

$J = 10$ H^{AsymTop} -levels in Figure 3 consist of two sets of five pairs $[(A_1, B_1) (A_2, B_2) (A_1, B_1) (A_2, B_2) (A_1, B_1)]$ and $[(B_2, A_1) (B_1, A_2) (B_2, A_1) (B_1, A_2) (B_2, A_1)]$ separated by a single (A_2) level. Each is related to RES x -valley path pairs $K_x \sim [\pm 10, \pm 9, \pm 8, \pm 7, \pm 6]$ or z -hill pairs $K_z \sim$

$[\pm 6, \pm 7, \pm 8, \pm 9, \pm 10]$ separated by a single y -path ($A_2 : K_y \sim 5$). Even- K belongs to a (0_2) column and odd- K belongs to a (1_2) column of $C_2(x)$ Table 8(a) or $C_2(z)$ Table 8(c).

Valley-pair sequence $(A_1, B_1), (A_2, B_2) \dots$ is consistent with (0_2) and (1_2) columns of the $C_2(x)$ Table 8(a), and hill-pair sequence $(B_2, A_1), (B_1, A_2) \dots$ is consistent with (0_2) and (1_2) column of the $C_2(z)$ Table 8(c). This is because lower pairs correspond to x -axial RES loops of approximate momentum $K_x \sim \pm 10, \pm 9 \dots \pm 6$ while upper pairs correspond to z -axial RES loops of approximate momentum $K_z \sim \pm 6, \pm 7 \dots \pm 10$ in Figure 3

Table 8(b) for $C_2(y)$ is not used since $\pm y$ -axes are hyperbolic saddle points on one separatrix path, unlike the disconnected pairs of elliptic RES paths that encircle $\pm x$ -axes or $\pm z$ -axes at hill or valley points. Only a single E level exists in Figure 3 at the energy E^{Sep} of the saddle points and their separatrix.

$$E^{\text{Sep}} = H^{\text{AsymTop}}(J_x, J_y, J_z) = BJ(J + 1) \text{ for } \begin{cases} J_x = 0 \\ J_y = |J|^2 \\ J_z = 0 \end{cases} \quad (35)$$

Table 6. Orthorhombic 4-group $D_2 = C_2 \times C_2$ character table construction.

$C_2(x)$		1	R_x	×	$C_2(y)$		1	R_y	=	$D_2 = C_2(x) \times C_2(y)$					
$A = (0_2)_x$	1	1	1		$1 = (0_2)_y$	1	1	1		1	$A_1 = (0_2 0_2)_{xy}$	1	1	1	1
$B = (1_2)_x$	1	-1	-1		$2 = (1_2)_y$	1	-1	1		-1	$A_2 = (0_2 1_2)_{xy}$	1	-1	1	-1
											$B_1 = (1_2 0_2)_{xy}$	1	1	-1	-1
										$B_2 = (1_2 1_2)_{xy}$	1	-1	-1	1	

Table 7. Group character tables for cyclic groups of symmetry order N. (a) N = 2; (b) N = 3: $\epsilon = e^{2\pi/3}$; (c) N = 4.

(a)			(b)				(c)				
C_2	1	R_x	C_3	1	R¹	R²	C_4	1	R¹	R²	R³
(0_2)	1	1	(0_3)	1	1	1	(0_4)	1	1	1	1
(1_2)	1	-1	(1_3)	1	ϵ^*	ϵ	(1_4)	1	$-i$	-1	i
			(2_3)	1	ϵ	ϵ^*	(2_4)	1	-1	1	-1
							$(3)_4$	1	i	-1	$-i$

Table 8. Symmetry correlation table between species of D_2 and its axial subgroups. (a) $C_2(x)$ subgroup; (b) $C_2(y)$ subgroup; (c) $C_2(z)$ subgroup.

(a)			(b)			(c)		
$D_2 \supset C_2(x)$	$(0_2)_x$	$(1_2)_x$	$D_2 \supset C_2(y)$	$(0_2)_y$	$(1_2)_y$	$D_2 \supset C_2(z)$	$(0_2)_z$	$(1_2)_z$
A_1	1	·	A_1	1	·	A_1	1	·
A_2	·	1	A_2	1	·	A_2	·	1
B_1	1	·	B_1	·	1	B_1	·	1
B_2	·	1	B_2	·	1	B_2	1	·

As symmetric H^{Sym} becomes a more asymmetric H^{AsymTop} in Figure 4, a hill or valley path bends away from its ideal single- K symmetric-top cone circle at constant polar angle θ_K^J Equations (23a) and (23b). Each H^{Sym} state $\left| \begin{matrix} J \\ K \end{matrix} \right\rangle$ turns into an H^{AsymTop} eigenstate expansion of states $\left| \begin{matrix} J \\ K \pm 2p \end{matrix} \right\rangle$ with $K \pm 2p$ above and below K , and its RES path bends from constant θ_K^J toward polar angles $\theta_{K\pm 2}^J, \theta_{K\pm 4}^J, \theta_{K\pm 6}^J \dots$ above and below angle θ_K^J . At energy near the separatrix E^{Sep} , bending of hill and valley paths become more severe as they approach separatrix asymptotes where the polar angle range Equation (32) expands to $2\theta^{\text{Sep}}$ or π and the bend becomes a kink.

It is conventional to label H^{Sep} eigenstate $|E\rangle$ by both K_x and K_z quantum values since $|E\rangle$ may use either a K_x basis or else a K_z basis. However, J_x and J_z do not commute. For energy E above E^{Sep} , a $|J, K_z\rangle$ expansion is more compact and a dominate $|K_z|$ value may label $|E\rangle$. For E below E^{Sep} , a $|J, K_x\rangle$ expansion has a meaningful $|K_x|$ label. For E near E^{Sep} , K -labels are questionable.

Table 9. Correlation tables between octahedral symmetric, O and various cyclic subgroups.

(a)					(b)			
$O \supset C_4$	0_4	1_4	2_4	3_4	$O \supset C_3$	0_3	1_3	2_3
$A_1 \downarrow C_4$	1	·	·	·	$A_1 \downarrow C_3$	1	·	·
$A_2 \downarrow C_4$	·	·	1	·	$A_2 \downarrow C_3$	1	·	·
$E \downarrow C_4$	1	·	1	·	$E \downarrow C_3$	·	1	1
$T_1 \downarrow C_4$	1	1	·	1	$T_1 \downarrow C_3$	1	1	1
$T_2 \downarrow C_4$	·	1	1	1	$T_2 \downarrow C_3$	1	1	1

(c)			(d)		
$O \supset C_2(\mathbf{i}_1)$	0_2	1_2	$O \supset C_2(\rho_z)$	0_2	1_2
$A_1 \downarrow C_2$	1	·	$A_1 \downarrow C_2$	1	·
$A_2 \downarrow C_2$	·	1	$A_2 \downarrow C_2$	1	·
$E \downarrow C_2$	1	1	$E \downarrow C_2$	2	·
$T_1 \downarrow C_2$	1	2	$T_1 \downarrow C_2$	1	2
$T_2 \downarrow C_2$	2	1	$T_2 \downarrow C_2$	1	2

Though a general form of the symmetry identification process may be unfamiliar, it may be implemented by computer. Group projectors Equation (36) can distinguish how each eigenvector splits with respect to subgroup operations. The product of these projectors and the calculated eigenvectors identifies the subgroup symmetry of each level.

$$P_{jk}^{\alpha} = \left(\frac{l^{\alpha}}{|\circ\mathcal{G}|} \right) \sum_g \mathcal{D}_{jk}^{\alpha*}(g)g \quad (36)$$

Only projectors in lower symmetry subgroups are used because they are easy to calculate and there are fewer in number. With the eigenvector projection lengths and knowledge of the correlation table between the molecular group itself and the subgroup one can start to deduce the eigenvector symmetry. As mentioned earlier, one correlation table is not enough to fully identify an eigenvector's symmetry, but using several subgroups one can assign symmetry. This process is simpler than calculating projectors of the full group, particularly if one can use a C_n subgroup and $\mathcal{D}_{jk}^{\alpha*}(g)$ in Equation (36) is found by Equation (34).

This method can be significantly simpler than a traditional block diagonalization. Block diagonalizing the Hamiltonian requires projectors of the entire molecular symmetry group rather than of the smaller subgroups.

The disadvantage of this method is that it becomes unstable when clusters are tightest. As eigenvectors become more mixed with tighter clustering the algorithm may be unable to distinguish. Some RES paths and level curves indistinguishable to numeric projector then appear black. Symmetry definitions hold for asymmetric tops where $J < 50$. Spherical tops are quite challenging as seen in Section 7.

2.4. Tunneling between RES-Path States

N-atom inversion in ammonia, NH_3 , is an example of molecular tunneling modeled by a particle whose closely paired levels (inversion doublets) lie below the barrier of a double-well PES. An RES generalization, sketched in Figure 3, shows level pairs such as (A_1, B_1) , (A_2, B_2) , etc. as rotational analogs of inversion doublets. Here the tunneling between left and right positions on a PES is replaced by an RES inversion between left-handed and right-handed rotation of an entire molecule. Instead of oscillation of expected position values $\langle \mathbf{r} \rangle$ between PES valleys there is oscillation of momentum $\langle \mathbf{J} \rangle$ between pairs of x -paths ($+K_x \leftrightarrow -K_x$) in RES valleys or else between pairs of z -paths ($+K_z \leftrightarrow -K_z$) on RES hills. Section 7 describes this phenomenon in more detail for molecules of O_h and T_d symmetry.

3. Tensor Eigensolutions for Octahedral Molecules

Section 2 has shown that asymmetric top molecules may be treated semi-classically, using only tensor operators and RES plots with a separatrix between regions of local symmetry. Spherical top molecules experience such symmetry locality, but with greater variety of local symmetry. This section focuses on the added complication and convenience of higher symmetry as well as showing novel rotational level clustering patterns related to RES paths and tunneling.

3.1. Tensor Symmetry Considerations

Theory of asymmetric top spectra in Section 2 may be generalized to a semi-classical treatment of tensor operators for T_d or O_h symmetric molecules such as CH_4 or SF_6 . The results contain level clusterings that first appeared in computer studies by Lea, Leask, and Wolf [20], Dorney and Watson [21] and followed by symmetry analyses [22,23] and others described below.

Up to fourth order, any such molecule may be treated using the Hecht Hamiltonian [24] rewritten in terms of tensor operators below in Equation (37a) and (37b) that isolates the rank-4 tensor term Equation (37c).

$$H = BJ^2 + 10t_{004}(J_x^4 + J_y^4 + J_z^4 - \frac{3}{5}J^4) \quad (37a)$$

$$H = BT_0^0 + 4t_{044}\left[T_0^4 + \sqrt{\frac{5}{14}}(T_4^4 + T_{-4}^4)\right] \quad (37b)$$

$$T^{[4]} = \sqrt{\frac{7}{12}}\left[T_0^4 + \sqrt{\frac{5}{14}}(T_4^4 + T_{-4}^4)\right] \quad (37c)$$

This is continued below to higher rank tensors with more complicated structure [14]. The coefficients of each tensor operator may be found from a spherical harmonic addition-theorem expansion of points at vertices of an octahedron. Coefficients $c_{n,m}$ are based on Equation (38), where Y_m^n is the spherical harmonic and $f(\vec{r})$ is a position of octahedral vertices (100), (010), ..., (00 - 1).

$$c_{n,m} = \int_V f(\vec{r})Y_m^n \cdot r^n d\tau \quad (38)$$

A normalized sum of these coefficients gives the rank-6 O_h tensor as follows.

$$T^{[6]} = \frac{1}{2\sqrt{2}}T_0^6 - \frac{\sqrt{7}}{4}(T_4^6 + T_{-4}^6) \quad (39)$$

The first study of RES and eigenvalue spectrum with varying rank-4 and rank-6 tensor operators [25] expressed in Equation (40) revealed intricate level cluster crossing shown below.

$$T^{[4,6]} = \cos(\theta)T^{[4]} + \sin(\theta)T^{[6]} \quad (40)$$

Later studies [26] examined rank-8 contributions such as expressed by Equation (41). Effects peculiar to combining Hamiltonian terms of rank-8 and higher include extreme clusters.

$$T^{[4,6,8]} = \cos(\phi)\left(\cos(\theta)T^{[4]} + \sin(\theta)T^{[6]}\right) + \sin(\phi)T^{[8]} \quad (41)$$

As with the asymmetric top Hamiltonian, the octahedral Hamiltonian uses non-axial operators shown in Equations (37b) and (39). Such operators involve more than Legendre functions, complicating purely semi-classical analysis. Thus, approximate solutions based on axial operators alone apply only asymptotically for high $J > 10$ and in regions away from RES separatrices. Combined powers of J and J_z do not give all levels. Tensor operators provide a sparse banded Hamiltonian matrix, but full numerical diagonalization is needed to get all levels to high precision.

Gulacsi and coworkers [26] explored how eigenvalues vary with $T^{[4]}$ and $T^{[8]}$ for $J \leq 10$ and small contributions of $T^{[6]}$. Results below agree but extend to larger J and use RES topology.

While the asymmetric top systems show clustering related to symmetry subduction from D_2 to a related C_2 subgroup, octahedral molecular clusters relate to a variety of subgroups. O_h may cluster into D_4 , D_3 , D_2 , C_4 , C_3 , C_2 or other subgroups involving reflection or inversion.

For simplicity, this discussion will focus on O rather than O_h molecules to make equations and correlation tables easier to display and interpret. Later Sections 6–7 give fuller discussions and explain the reciprocity relations that are behind correlation tables.

For D_2 -symmetric molecules, clustering patterns are described in terms of the correlation tables found in Table 8. The similar correlation tables for octahedral molecules are given for C_4 , C_3 and C_2 in Table 9. The columns of Table 9 represent the different clusters of rotational levels found within the spectra of given molecule at a given rotational transition. These clusterings are identified by their degeneracy as well as their RES location. Since symmetry labeling of octahedral group O differs from asymmetric top D_2 , a new coloring convention for O levels is defined: A_1 is red, A_2 is orange, E_2 is green, T_1 is dark blue and T_2 is light blue.

In the RES, rotationally induced deformation or symmetry breaking is seen from the shape of local regions of the RES involving a specific contour. Figure 5 shows two different RES plots, both globally octahedral, but with local regions that correspond to a subgroup symmetry of the octahedron. Figure 5(a) demonstrates a possible RES of an octahedral molecule with Hamiltonian parameters that allow for C_4 and C_3 local symmetry regions to be present. The C_4 regions are identified by their location and by their square base. Similarly, the C_3 regions are identified by their location and triangular base. In this case C_3 symmetric regions are concave while C_4 regions are convex. This is not required and is dependent on Hamiltonian fitting terms that change the relative contributions of $T^{[4]}$ and $T^{[6]}$. Likewise, Figure 5(b) shows the C_2 regions that are determined by their location and rectangular base.

Cluster degeneracy is a hallmark of a specific symmetry breaking. While a symmetric top spectra may be resolved into m_J levels, a rotationally-induced symmetry-reduced spherical top has several identical z axes. The m_J levels can then localize on a single symmetry-reduced local region. The number of these regions must equal the degeneracy of the cluster in that same region. This degeneracy, ℓ^α , is also found using the sum of the numbers in the columns of Table 9 or by Equation (42) given ${}^\circ\mathcal{G}$ is the order of the molecular symmetry group and ${}^\circ\mathcal{H}$ is the order of the subgroup.

$$\ell^\alpha = \frac{{}^\circ\mathcal{G}}{{}^\circ\mathcal{H}} \quad (42)$$

In the cases shown here cluster degeneracy ℓ^α becomes 6, 8 and 12 for C_4 , C_3 and C_2 respectively.

3.2. Numerical Assignment of Symmetry Clusters

As mentioned previously, it is possible to diagonalize the Hamiltonian and organize species by the order of each block, yet this alone will not distinguish all levels. For Hamiltonians defined by $T^{[4]}$ as Equation (37a) it is possible to analytically [25] determine the symmetry of each level. Once $T^{[6]}$ or $T^{[8]}$ terms are present, a numerical examination of eigenvectors is required to assign the symmetry of each level. Subgroup projectors are used here where the cluster degeneracy increases and the symmetry becomes challenging to distinguish. These projectors represent a simplification of the symmetry analysis of an octahedral molecule into projections onto C_4 symmetric projectors. The correlation table for $O \supset$

C_4 , shown in Table 9, and Equation (36) give the information necessary for the assignment. Moreover, when using the subgroup C_4 there are only four projectors to create and a clever choice of axis can force several of these projectors to be entirely real or entirely imaginary. Conveniently, the C_4 projectors can be used to diagnose level symmetry for clusters in any subgroup region.

3.3. Octahedral Clustering vs. RES Topography

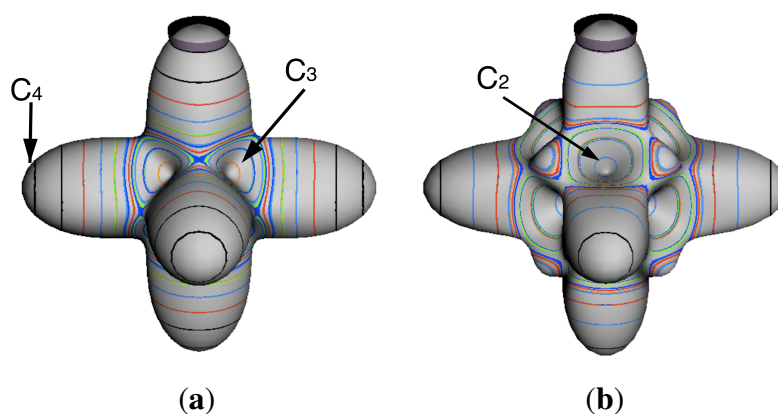
3.3.1. Variation of $T^{[4,6]}$ Topography

The Hecht Hamiltonian Equation (37a) and its higher order analogues are generic Hamiltonians. Such Hamiltonians have numerous fitting constants specific to a given molecule and a given vibronic species. To better understand all such octahedral systems, one must focus on changes in the level spectrum and RES plots with varying contributions of $T^{[4]}$, $T^{[6]}$ and $T^{[8]}$.

$T^{[4,6,8]}$ in Equation (41) has two bounded parameters θ and ϕ so several plots are required to explore this parameter space. By setting $T^{[8]}$ contributions to zero the eigenvalue spectrum for $T^{[4,6]}$ in Equation (40) can be plotted for changing values of θ , relative contributions of 4th and 6th rank tensor terms. Figure 6 plots such an eigenvalue spectrum and also places the RES plots that go along with important parts of the level diagram and, conversely, points out what spots on the level diagram correspond to important changes in the RES plot. We note $T^{[4,6]}$ RES have circular ring separatrices not unlike those on D_2 RES in Figure 3.

To understand the behavior of the level diagram in Figure 6 it is critical to inspect the changing shape of the RES plots. In particular, the clustering of levels in the eigenvalue diagram is dependent on the localized symmetry regions of the RES at each value of θ . Locally, the RES forms hills and valleys of a lower symmetry than that of the molecule. The local symmetry must also be a sub-group of the molecular symmetry. Figure 5 identifies regions of local symmetry C_4 , C_3 and C_2 whose local rotation axis lie fixed normal to the RES at the center of each region, respectively, even as θ varies from Figure 5(a) to Figure 5(b). For some θ one or two of the C_n regions may shrink out of existence as shown below in Figure 6.

Figure 5. Symmetry axes of $T^{[4,6]}$ RES for differing contributions of $T^{[4]}$ and $T^{[6]}$. (a) C_3 and C_4 local regions; (b) C_2 local region.



3.3.2. Semi-Classical Outlines vs. Quantum Eigenvalues

With this understanding of local subgroup regions it is possible to discuss more detail of Figure 6. The correspondence between the RES plots and the level diagram can also be seen by appending the eigenvalue spectrum in Figure 6 with the height of the C_4 , C_3 and C_2 axes. This serves two purposes: To confirm that the quantum spectrum sits inside the semi-classical boundaries and to see that there is a change in the eigenvalue spectrum corresponding to changes in RES topology. Figure 7 shows the same quantum spectrum as Figure 6, but also includes the height (energy) of each symmetry axis. The outlines are printed in bold and are labeled for which C_n axis they each belong.

Figure 6. $J=30$ Energy levels and RES plots for $T^{[4,6]}$ vs. $[4,6]$ mix-angle θ with $T^{[4]}$ levels above $\phi=0^\circ$ (extreme left), $T^{[6]}$ levels at $\theta=90^\circ$ (center), and $-T^{[4]}$ levels at $\theta=180^\circ$ (extreme right). C_4 local symmetry and 6-fold level clusters dominate at $\theta=17^\circ$ while C_3 type 8-fold level clusters dominate at $\theta=132^\circ$. In between these extremes are C_2 type 12-fold level clusters particularly around $\theta=80^\circ$ where a $C_3 - C_4$ level-cluster-crossing of the top 14 levels occurs.

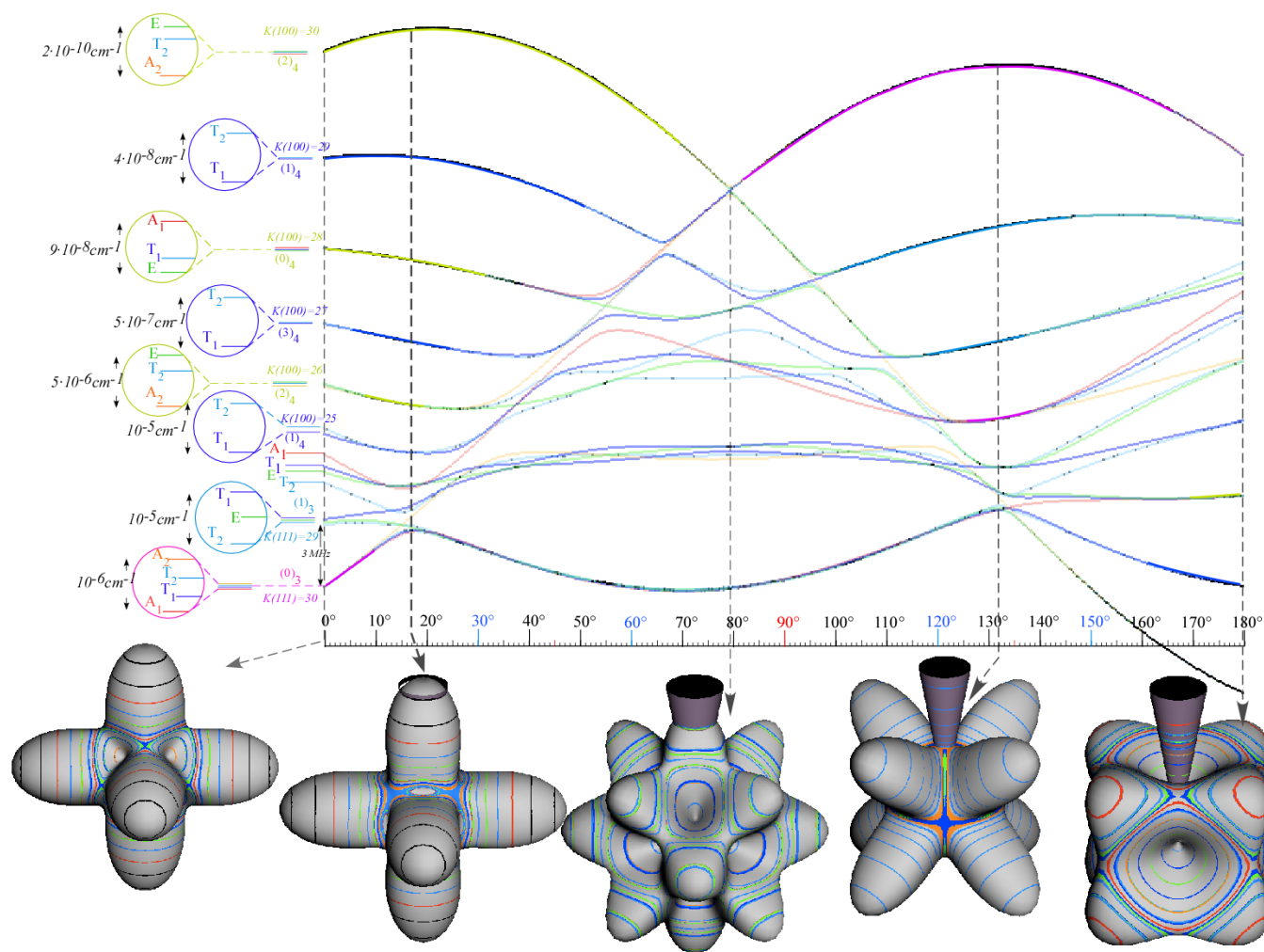
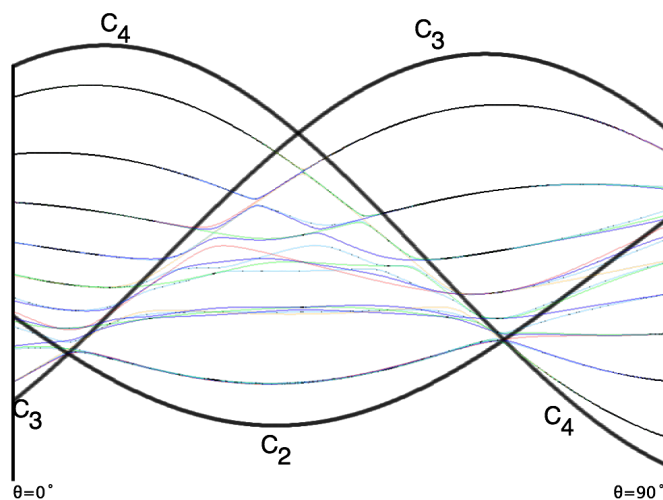


Figure 7. Quantum spectrum of octahedral Hamiltonian (Equation (40)) with changing θ . Bold lines are the energy of the classical symmetry axis labeled.



Section 2 described how to predict the error between a fully quantum mechanical calculation and a semi-classical approximation of the symmetric rotor rotational spectra. For the symmetric rotor this was done analytically. It is difficult to be as exact in calculating error for an octahedrally symmetric Hamiltonian, but a line plot can show when an RES plot fails to describe quantum mechanical behavior.

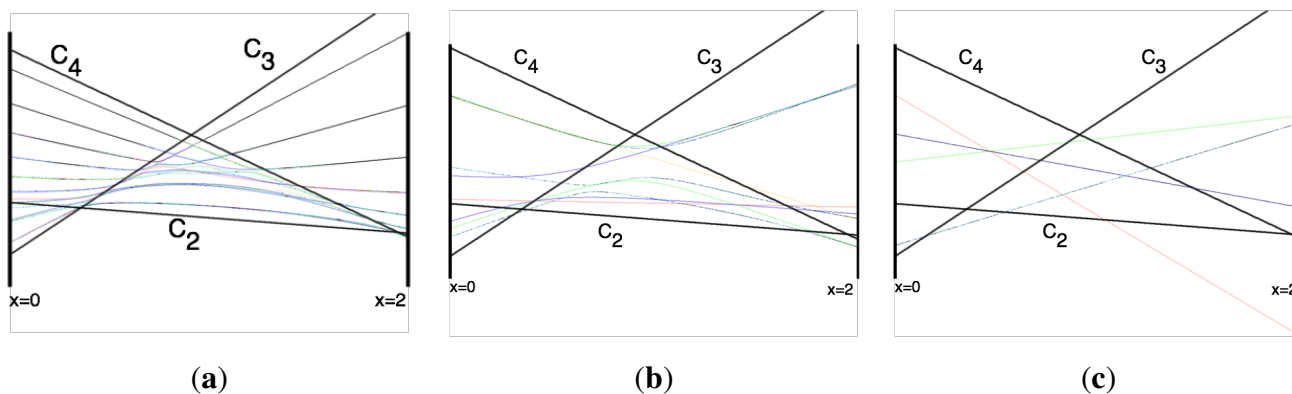
Rather than plotting the Hamiltonian as Equation (40) we will arrange it as

$$T^{[4,6]} = (1 - x)T^{[4]} + xT^{[6]} \tag{43}$$

This changes semi-classical outlines from cosines to lines and shows where quantum levels exceed semi-classical bounds and where an RES approximation fails. Also, x -line plots show by degree of avoided-crossing-curvature for each level the degree of its state mixing at x .

The three plots in Figure 8 show these spectra and semi-classical outlines for $J = 30$, $J = 10$ and $J = 4$. Figure 8(a) shows that the quantum levels fit for all values of x at $J = 30$, while Figure 8(b) shows some small disagreement near $x = 2$ for $J = 10$. Figure 8(c) shows that for low J there is strong disagreement between quantum calculations and semi-classical approximations.

Figure 8. Spectrum of Octahedral Rotor Showing Semi-Classical Boundaries Given Equation (43). (a) $J = 30$; (b) $J = 10$; (c) $J = 4$.

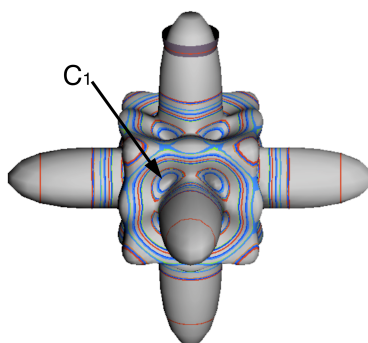


Indeed, such plots as Figure 6 have been created before, both for the RES plots and the level diagrams [25]. Next, we show such an analysis of $T^{[4,6,8]}$ and demonstrate how such a Hamiltonian can show a different type of topology than previously reported.

3.3.3. Variation of $T^{[4,6,8]}$ Topography and Level Clusters

The inclusion of eighth rank operators to the Hamiltonian dramatically changes the possible types of RES local symmetry and the related level clustering. While Figure 5 shows C_4 , C_3 and C_2 symmetric local structures for RES plots for $T^{[4,6]}$ Hamiltonians, Figure 9 shows a new kind of local $T^{[4,6,8]}$ RES path pointed out there with C_1 symmetry. (That means *no* rotational symmetry!) The path is repeated 24 times and thus belongs to a single cluster of 24 levels. As shown in Section 6.7.2. the cluster spans an *induced* representation $D^{0_1}(C_1) \uparrow O$, also known as a *regular* representation of O .

Figure 9. RES with C_1 local symmetry regions visible.



Details of the two dimensional $T^{[4,6,8]}$ parameter space appear in a figure Table 10 containing RES plots for several (θ, ϕ) points. To be consistent with Equation (41), the plots increase θ from 0 to π going left to right and ϕ from 0 to π going top to bottom. RES O levels are colored with the usual red for A_1 , orange for A_2 , green for E_2 , blue for T_1 and cyan for T_2 .

As expected from Equation (41), the top and bottom rows are opposites to one another. That is, where one RES has a hill (higher energy), the other has a crater (lower energy.) The RES at $\theta = 0, \phi = 0$ has convex C_4 and concave C_3 structure as does the RES at $\theta = \pi, \phi = \pi$, but opposite the shape of the RES at either $\theta = 0, \phi = \pi$ or $\theta = \pi, \phi = 0$. The ordering of the levels is also opposite. These two extremal rows also have no eighth order contribution, so they produce simpler shapes than the others and are incapable of producing C_1 local symmetry regions. The middle row shows a different behavior: all the diagrams are identical. Again, this follows from Equation (41) wherever $\phi = \pi/2$.

While Table 10 shows only the RES plots along the parameter space defined by Equation (41), Figure 10 shows level diagrams with RES plots placed showing the symmetry and topology present at a given point in the space. The bold vertical lines next to the RES plots indicate the spot in the level diagram that particular RES plot would exist. Again, it is clear the $\theta = \pi/2$ case would be unchanged, so it is not shown. The $\theta = \pi$ case is neglected as it is a mirror image of the $\theta = 0$ case.

Table 10. RES plots exploring the 2D parameter space.

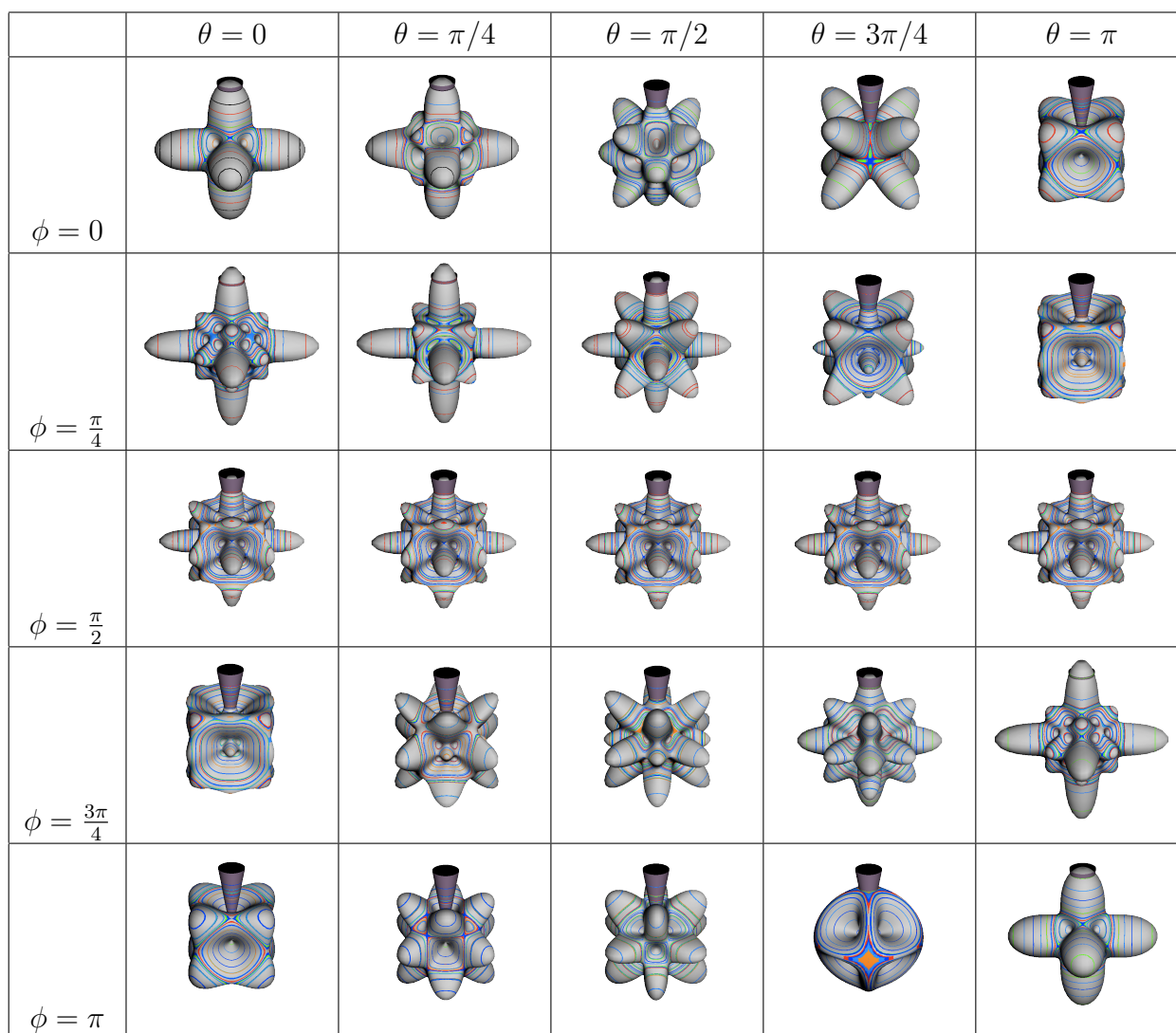
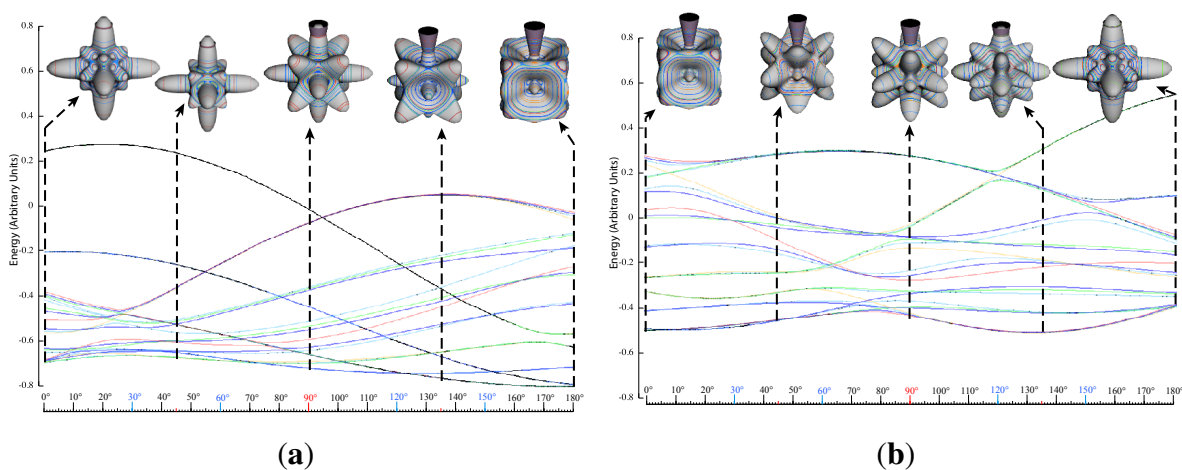


Figure 10. Level diagrams of energy vs. θ for given ϕ with RES plots at selected positions.
(a) $\phi = \pi/4$; **(b)** $\phi = 3\pi/4$.



3.4. Criteria for C_1 Level Clustering

Figures 9–11 show where the local regions of hills and valleys form on the RES depending on mixing angles ϕ and θ . Unlike the local symmetry regions known previously, the local C_1 structures associated with 24-fold level clusters have no rotation axis to locate their central maxima or minima on the RES. However, they do have bisecting reflection planes that must contain surface gradient vectors and an extreme point for which the gradient points radially. RES plots with C_1 local symmetries are shown in parts of second, third and fourth rows of Table 10 as well as parts of Figure 10(a) and 10(b). Figure 11 shows how C_1 regions lie on hills or else valleys and how they can be arranged with their neighbors into either a square or triangular pattern.

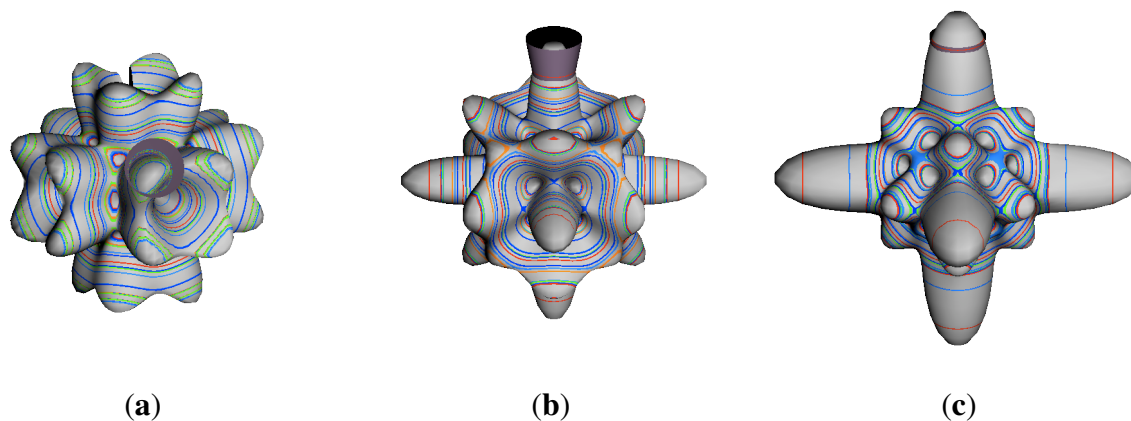
C_1 clusters require tensors of rank-8 with ϕ between π and zero as θ varies. Momentum J must be large enough for its minimum-uncertainty ($J=K$)-cone angle Θ_J^J to fit in a C_1 region.

$$\Theta_J^J = \cos^{-1}\left(\frac{J}{\sqrt{J+1}}\right) \simeq \sqrt{\frac{1}{J}} \quad (44)$$

RES with J as low as $J=4$ may have C_1 regions but fail to fit its ($2\Theta_4^4=56^\circ$)-wide cones. C_1 clusters begin to appear around $J=20$ ($2\Theta_{20}^{20}=26^\circ$) but even for $J=30$ ($2\Theta_{30}^{30}=21^\circ$) are still barely formed in Figure 11(a). There a minimum uncertainty cone appears to barely fit within a separatrix on a C_1 hill between C_3 and C_4 valleys of its ($J=30$)-RES. Others are situated more comfortably in valleys of RES shown in Figure 11(b) where they appear to encircle a C_4 axes as in Figure 10(a) where a corresponding cluster of 24 eigenvalues in 10 levels appear at the lower left hand side of the level diagram. In Figure 11(c) they surround a C_2 axis.

With higher J and O_h -tensors of greater rank than $k=8$, one expects clusters of 48-fold degeneracy corresponding to C_1 -regions centered away from O_h symmetry axes or planes. So far, these are only beginning to be explored and analyzed. To analyze such complicated tunneling effects (and better understand older ones) requires an improved symmetry analysis developed in Sections 4–7.

Figure 11. $J = 30$ RES for various rank $k=4, 6, 8$ combinations giving C_1 features. (a) C_1 hills around C_3 and C_4 ; (b) C_1 valleys near C_4 ; (c) C_1 valleys near C_3 .



4. Introducing Dual Symmetry Algebra for Tunneling and Superfine Structure

For a system to have symmetry means two or more of its parts are the same or similar and therefore subject to resonance. This can make a system particularly sensitive to internal parameters and external perturbations and give rise to interesting and useful effects. However, resonances can make it more difficult to analyze and understand a system's eigensolutions. The tensor level cluster states give rise to spectral fine structure discussed in the preceding sections and that splits further into complex *superfine* structure due to J -tunneling that is the focus of the following sections.

Fortunately, the presence of symmetry in a physical system allows algebraic or group theoretical analysis of quantum eigensolutions and their dynamics. Groups of operators (g, g', g'', \dots) leave a Hamiltonian operator H invariant ($g^\dagger H g = H$) if and only if each g commutes with it ($gH = Hg$). Then each g in the group shares a set of eigenfunctions with H . However, if (g') and (g) do not commute then the (g') and (g) sets will differ.

Hamiltonians may themselves be symmetry operators or linear expansions thereof. Multipole tensor expansions used heretofore are examples. Expanding H into operators with symmetry properties, such as $(a^\dagger a)$ or (T_q^k) , helps to analyze its eigensolutions since, in some sense, a symmetry algebra "knows" its spectral resolutions. The underlying isometry of a system's variables and states contains all the sub-algebras that are possible H -symmetries.

If H -symmetry operators (g, g', \dots) also commute with each other ($gg' = g'g, \text{etc.}$) then all g share with H a single set of eigenvectors as discussed in Section 5. Such commutative or *Abelian* symmetry analysis is just a Fourier analysis where all H are linear expansion of its symmetry elements (g, g', g'', \dots) and simultaneously diagonalized with H . Such g expansions define both Hamiltonians H and their states as described in Section 5.

However, non-commuting (non-Abelian) symmetry operators (g, g', g'', \dots) of H cannot both expand H and commute with H . This impasse is resolved in Section 6 by using a dual *local* operator group $(\bar{g}, \bar{g}', \bar{g}'', \dots)$ that mutually commutes with the original *global* group. Then local (\bar{g}) expand any H that commutes with global g , while the global g define base states and their combinations define symmetry projected states. Roughly put, one labels location while the other labels tunneling to and fro.

In Section 6, the dual group $(\bar{D}_3 \sim \bar{C}_{3v})$ of the smallest non-Abelian group $(D_3 \sim C_{3v})$ is defined. Dual symmetry-analysis is demonstrated for a trigonal tunneling system by group parametrization of all possible (D_3) -symmetric \mathbf{H} matrices and all possible eigensolutions for each. The example shows how global (g) label states while the local (\bar{g}) label tunneling paths. In this way symmetry labels processes as well as states. An added benefit is a kind of "slide-rule-lattice" to compute group products.

In Section 7, the local symmetry expansion is applied to octahedral $O \subset O_h$ tensor superfine structure. Local symmetry conditions are used to relate tunneling paths to RES topography discussed previously and predict possible energy level patterns. The $O \subset O_h$ slide-rule-lattices appear in Figures 22–24.

5. Abelian Symmetry Analysis

An introductory analysis of tunneling symmetry begins with elementary cases involving homocyclic C_n symmetry of n -fold polygonal structure. But, it applies to all Abelian (mutually commuting) groups A since all A reduce to outer products $C_p \times C_q \times \dots$ of cyclic groups of prime order.

5.1. Operator Expansion of C_n Symmetric Hamiltonian

The analysis described here and in Section 6 deviates from standard procedure [27–31]. Instead of beginning with a given quantum Hamiltonian \mathbf{H} -matrix, we start with a C_n symmetry matrix (\mathbf{r}) and build all possible C_n symmetric (\mathbf{H})-matrices by combining n powers (\mathbf{r}^p) = (\mathbf{r})^{*p*} of (\mathbf{r}) ranging from identity $\mathbf{r}^0 = \mathbf{1} = \mathbf{r}^n$ to inverse $\mathbf{r}^{n-1} = \mathbf{r}^{-1}$ [32].

$$\begin{aligned} \mathbf{H} &= r_0\mathbf{r}^0 + r_1\mathbf{r}^1 + r_2\mathbf{r}^2 + \dots + r_{n-2}\mathbf{r}^{n-2} + r_{n-1}\mathbf{r}^{n-1} \\ &= r_0\mathbf{1} + r_1\mathbf{r}^1 + r_2\mathbf{r}^2 + \dots + r_{-2}\mathbf{r}^{-2} + r_{-1}\mathbf{r}^{-1} \end{aligned} \tag{45}$$

In Equation (45) the rotation \mathbf{r} is by angle $2\pi/n$ so rotation \mathbf{r}^n is by angle $n2\pi/n = 2\pi$, that is, the identity operator $\mathbf{r}^0 = \mathbf{1} = \mathbf{r}^n$. Thus power- p indices label *modulo-n* or base- n algebras. If $n=2$, it is a *Boolean* algebra $C_1 \subset C_2$ of *parity* [+1,-1] or *classical bits* [0,1]. ($U(2)$ spin-algebras of q -bits have 4π identity but are not considered here.)

Sum rule: $p + p' = (p + p') \bmod (n)$ Product rule: $p \cdot p' = (p \cdot p') \bmod (n)$ (46)

We construct the general \mathbf{H} -matrix using C_n group-product tables shown below in a $\mathbf{g}^{-1}\mathbf{g}$ -form and a $\mathbf{g}^\dagger\mathbf{g}$ -form that is equivalent for unitary operators $\mathbf{g}^\dagger = \mathbf{g}^{-1}$. In each table the k^{th} -row label \mathbf{g}^{-1} matches k^{th} -column label \mathbf{g} so that the identity operator $\mathbf{1} = \mathbf{g}^{-1}\mathbf{g}$ resides only on the diagonal. This example is for hexagonal symmetry C_6 for which $\mathbf{r}^{-6} = \mathbf{r}^0 = \mathbf{1} = \mathbf{r}^6 = \mathbf{r}^{6\dagger}$, $\mathbf{r}^{-5} = \mathbf{r}^1 = \mathbf{r}^{5\dagger}$, $\mathbf{r}^{-4} = \mathbf{r}^2 = \mathbf{r}^{4\dagger}$, $\mathbf{r}^{-3} = \mathbf{r}^3 = \mathbf{r}^{3\dagger}$, and so forth.

$\mathbf{g}^{-1}\mathbf{g}$ <i>form</i>	$\mathbf{r}^0 \ \mathbf{r}^1 \ \mathbf{r}^2 \ \mathbf{r}^3 \ \mathbf{r}^4 \ \mathbf{r}^5$	=	$\mathbf{g}^\dagger\mathbf{g}$ <i>form</i>	$\mathbf{1} \ \mathbf{r}^{+1} \ \mathbf{r}^{+2} \ \mathbf{r}^{+3} \ \mathbf{r}^{-2} \ \mathbf{r}^{-1}$	(47)
\mathbf{r}^0	$\mathbf{r}^0 \ \mathbf{r}^1 \ \mathbf{r}^2 \ \mathbf{r}^3 \ \mathbf{r}^4 \ \mathbf{r}^5$		$\mathbf{1}$	$\mathbf{1} \ \mathbf{r}^{+1} \ \mathbf{r}^{+2} \ \mathbf{r}^{+3} \ \mathbf{r}^{-2} \ \mathbf{r}^{-1}$	
\mathbf{r}^5	$\mathbf{r}^5 \ \mathbf{r}^0 \ \mathbf{r}^1 \ \mathbf{r}^2 \ \mathbf{r}^3 \ \mathbf{r}^4$		\mathbf{r}^{-1}	$\mathbf{r}^{-1} \ \mathbf{1} \ \mathbf{r}^{+1} \ \mathbf{r}^{+2} \ \mathbf{r}^{+3} \ \mathbf{r}^{-2}$	
\mathbf{r}^4	$\mathbf{r}^4 \ \mathbf{r}^5 \ \mathbf{r}^0 \ \mathbf{r}^1 \ \mathbf{r}^2 \ \mathbf{r}^3$		\mathbf{r}^{-2}	$\mathbf{r}^{-2} \ \mathbf{r}^{-1} \ \mathbf{1} \ \mathbf{r}^{+1} \ \mathbf{r}^{+2} \ \mathbf{r}^{+3}$	
\mathbf{r}^3	$\mathbf{r}^3 \ \mathbf{r}^4 \ \mathbf{r}^5 \ \mathbf{r}^0 \ \mathbf{r}^1 \ \mathbf{r}^2$		\mathbf{r}^{+3}	$\mathbf{r}^{+3} \ \mathbf{r}^{-2} \ \mathbf{r}^{-1} \ \mathbf{1} \ \mathbf{r}^{+1} \ \mathbf{r}^{+2}$	
\mathbf{r}^2	$\mathbf{r}^2 \ \mathbf{r}^3 \ \mathbf{r}^4 \ \mathbf{r}^5 \ \mathbf{r}^0 \ \mathbf{r}^1$		\mathbf{r}^{+2}	$\mathbf{r}^{+2} \ \mathbf{r}^{+3} \ \mathbf{r}^{-2} \ \mathbf{r}^{-1} \ \mathbf{1} \ \mathbf{r}^{+1}$	
\mathbf{r}^1	$\mathbf{r}^1 \ \mathbf{r}^2 \ \mathbf{r}^3 \ \mathbf{r}^4 \ \mathbf{r}^5 \ \mathbf{r}^0$		\mathbf{r}^{+1}	$\mathbf{r}^{+1} \ \mathbf{r}^{+2} \ \mathbf{r}^{+3} \ \mathbf{r}^{-2} \ \mathbf{r}^{-1} \ \mathbf{1}$	

The $\mathbf{g}^\dagger\mathbf{g}$ -form produces a *regular representation* $R(\mathbf{g}) = (\mathbf{g})$ of each operator \mathbf{g} as shown below. Each $R(\mathbf{r}^p)$ is a zero-matrix with a 1 inserted wherever a \mathbf{r}^p appears in the $\mathbf{g}^\dagger\mathbf{g}$ -table.

$R(\mathbf{1}) =$	$R(\mathbf{r}^1) =$	$R(\mathbf{r}^2) =$	$R(\mathbf{r}^3) =$...
$\begin{pmatrix} 1 & \cdot & \cdot & \cdot & \cdot & \cdot \\ \cdot & 1 & \cdot & \cdot & \cdot & \cdot \\ \cdot & \cdot & 1 & \cdot & \cdot & \cdot \\ \cdot & \cdot & \cdot & 1 & \cdot & \cdot \\ \cdot & \cdot & \cdot & \cdot & 1 & \cdot \\ \cdot & \cdot & \cdot & \cdot & \cdot & 1 \end{pmatrix},$	$\begin{pmatrix} \cdot & 1 & \cdot & \cdot & \cdot & \cdot \\ \cdot & \cdot & 1 & \cdot & \cdot & \cdot \\ \cdot & \cdot & \cdot & 1 & \cdot & \cdot \\ \cdot & \cdot & \cdot & \cdot & 1 & \cdot \\ \cdot & \cdot & \cdot & \cdot & \cdot & 1 \\ 1 & \cdot & \cdot & \cdot & \cdot & \cdot \end{pmatrix},$	$\begin{pmatrix} \cdot & \cdot & 1 & \cdot & \cdot & \cdot \\ \cdot & \cdot & \cdot & 1 & \cdot & \cdot \\ \cdot & \cdot & \cdot & \cdot & 1 & \cdot \\ \cdot & \cdot & \cdot & \cdot & \cdot & 1 \\ 1 & \cdot & \cdot & \cdot & \cdot & \cdot \\ \cdot & 1 & \cdot & \cdot & \cdot & \cdot \end{pmatrix},$	$\begin{pmatrix} \cdot & \cdot & \cdot & 1 & \cdot & \cdot \\ \cdot & \cdot & \cdot & \cdot & 1 & \cdot \\ \cdot & \cdot & \cdot & \cdot & \cdot & 1 \\ 1 & \cdot & \cdot & \cdot & \cdot & \cdot \\ \cdot & 1 & \cdot & \cdot & \cdot & \cdot \\ \cdot & \cdot & 1 & \cdot & \cdot & \cdot \end{pmatrix}$	

(48)

The C_n Hamiltonian (\mathbf{H}) matrix has matrices from (48) inserted into expansion (45) of operator \mathbf{H} .

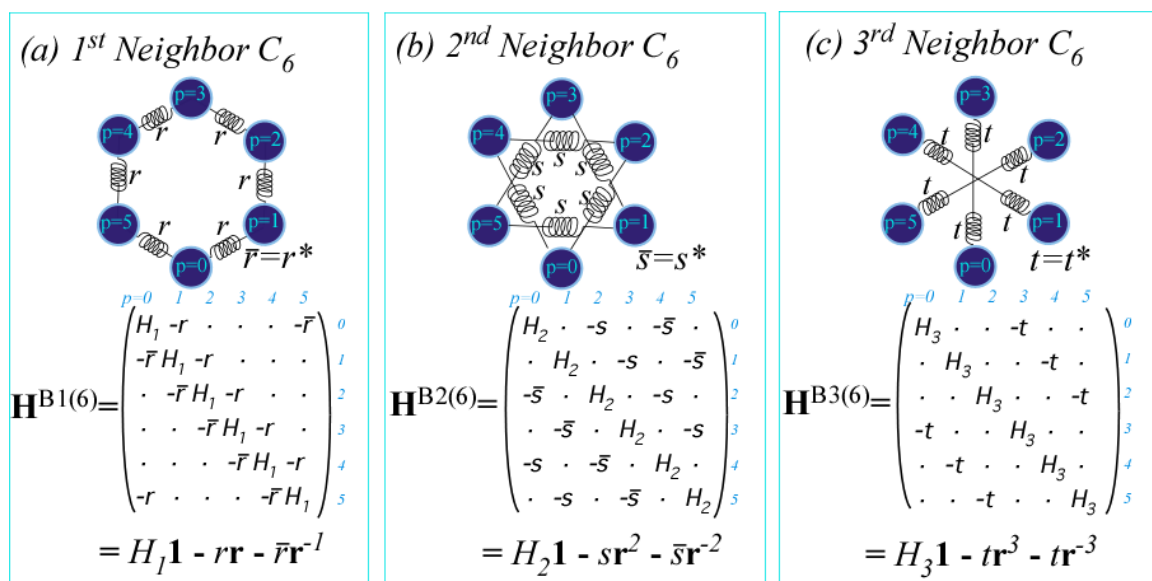
$$(\mathbf{H}) = \sum_{p=0}^{n-1} r_p (\mathbf{r}^p) = \begin{pmatrix} r_0 & r_1 & r_2 & r_3 & r_4 & r_5 \\ r_5 & r_0 & r_1 & r_2 & r_3 & r_4 \\ r_4 & r_5 & r_0 & r_1 & r_2 & r_3 \\ r_3 & r_4 & r_5 & r_0 & r_1 & r_2 \\ r_2 & r_3 & r_4 & r_5 & r_0 & r_1 \\ r_1 & r_2 & r_3 & r_4 & r_5 & r_0 \end{pmatrix} = \begin{pmatrix} r_0 & r_1 & r_2 & r_3 & r_{-2} & r_{-1} \\ r_{-1} & r_0 & r_1 & r_2 & r_3 & r_{-2} \\ r_{-2} & r_{-1} & r_0 & r_1 & r_2 & r_3 \\ r_3 & r_{-2} & r_{-1} & r_0 & r_1 & r_2 \\ r_2 & r_3 & r_{-2} & r_{-1} & r_0 & r_1 \\ r_1 & r_2 & r_3 & r_{-2} & r_{-1} & r_0 \end{pmatrix} \quad (49)$$

Matrices in Equation (49) are simply group tables Equation (47) with complex tunneling amplitude r_p replacing operator \mathbf{r}^p . Parameters $r_0 = (r_0)^*$ and $r_3 = (r_3)^*$ match self-conjugate binary subgroups $C_1 \subset C_2 = (\mathbf{1}, \mathbf{r}^3)$ related by $\mathbf{1} = (\mathbf{r}^3)^2$. Both are real if matrix (\mathbf{H}) is Hermitian self-conjugate ($H_{ab} = H_{ba}^*$).

Three distinct classes of tunneling or coupling parameters are depicted in Figure 12 using classical spring-mass analogs for quantum systems [22]. Tunneling matrices have a long history [33] going back to Wilson [34]. Here this is being revived to treat extreme J -tunneling and more recently by Ortigoso [17] and Hougen [35,36] to treat extremely floppy molecule dynamics. Both these tasks use tunneling parametrization that has so far been quite *ad.hoc*. To accomplish either of these tasks, or what will surely be needed, namely *both* tasks, we need a tighter symmetry analysis. The group operator scheme being introduced here seeks a way to achieve this.

The 1st-neighbor class has non-zero parameters $r_1=-r$ and conjugate $r_{-1}=-r^*=-\bar{r}$ coupling only nearest neighbors each with self-energy $r_0=H_1$. The 2nd-neighbor class has non-zero parameters $r_2=-s$ and conjugate $r_{-2}=-s^*=-\bar{s}$ coupling only next-nearest neighbors with self-energy $r_0=H_2$. Finally, 3rd-neighbor coupling $r_3=-t=-t^*$ is real as required for binary self-conjugacy $\mathbf{r}^3=(\mathbf{r}^3)^\dagger$.

Figure 12. Three classes of tunneling paths and parameters.



5.2. Spectral Resolution of C_n Symmetry Operators

Eigenvalues χ_p^m of each operator \mathbf{r}^p are m^{th} multiples of n^{th} -roots of unity since all C_n symmetry operators $\mathbf{g} = \mathbf{r}^p$ satisfy $\mathbf{g}^n = \mathbf{1}$ and are *characters* of C_n symmetry operators. Magnetic or *mode-wavenumber* indices m label a base- n algebra as do the power or *position-point* indices p in Equation (46). Spatial lattice points $x_p = L \cdot p$ (*meters*) are indexed by p while reciprocal- (k) -wavevector space $k_m = 2\pi m/L$ (*per meter*) is indexed by integer m .

$$\langle \mathbf{r}^p \rangle_m = \chi_p^m = e^{-i(m \cdot p)2\pi/n} = e^{-ik_m x_p} = D^{(m)}(\mathbf{r}^p) \tag{50}$$

The χ_p^m are C_n irreducible representations $D^{(m)}(\mathbf{r}^p)$ as well as C_n characters. General group characters are traces (diagonal sums) of D-matrices ($\chi^{(m)}(\mathbf{g}) = \text{trace} D^{(m)}(\mathbf{g})$). Abelian group irreducible representations are 1-dimensional due to their commutativity, and so for them characters and representations are identical. ($\chi^{(m)}(\mathbf{g}) = D^{(m)}(\mathbf{g})$) All this is generalized in subsequent Section 6. Any number of mutually commuting unitary matrices may be diagonalized by a single unitary transformation matrix. The characters in Equation (50) form a unitary transformation matrix $T_{m,p}$ that diagonalizes each C_n matrix (\mathbf{r}^p).

$$T_{m,p} = \chi_p^m / \sqrt{n} \tag{51}$$

This T is a discrete (n -by- n) Fourier transformation. A 6-by-6 example that diagonalizes all matrices in Equations (48) and (49) and in Figure 12 is shown in Figure 13 by a character table of wave phasors based on $D^{(m)}(\mathbf{r}^p)$ in Equation (50) or (51). The irreducible representations $D^{(m)}(\mathbf{r}^p)$ or *irreps* play multiple roles. They are variously eigenvalues, eigenvectors, eigenfunctions, transformation components, and Fourier components of dispersion relations. This hyper-utility centers on their role as coefficients in *spectral resolution* of operators \mathbf{r}^p into idempotent projection operators $\mathbf{P}^{(m)}$. $\mathbf{P}^{(m)}$ are like *irrep placeholders*.

$$\mathbf{r}^p = \sum_{m=0}^{n-1} \chi_p^m \mathbf{P}^{(m)} = \chi_p^0 \mathbf{P}^{(0)} + \chi_p^1 \mathbf{P}^{(1)} + \chi_p^2 \mathbf{P}^{(2)} + \chi_p^3 \mathbf{P}^{(3)} + \chi_p^4 \mathbf{P}^{(4)} + \chi_p^5 \mathbf{P}^{(5)} \tag{52}$$

Equation (52) is column- p of Figure 13. Column-0 is a *completeness* or *identity resolution* relation.

$$\mathbf{r}^0 = \sum_{m=0}^{n-1} \mathbf{P}^{(m)} = \mathbf{1} = \mathbf{P}^{(0)} + \mathbf{P}^{(1)} + \mathbf{P}^{(2)} + \mathbf{P}^{(3)} + \mathbf{P}^{(4)} + \mathbf{P}^{(5)} \tag{53}$$

Dirac notation for $\mathbf{P}^{(m)}$ is $| (m) \rangle \langle (m) |$. Its representation in its own basis (*eigenbasis*) is simply a zero matrix with a single 1 at the (m, m) -diagonal component. $\mathbf{P}^{(m)}$ -product table in Equation (54) is

equivalent through Equation (52) to g-product table in Equation (47) but the $\mathbf{P}^{(m)}$ -table given below has an orthogonal (e.g. $\mathbf{P}^{(1)}\mathbf{P}^{(2)} = \mathbf{0}$) idempotent (e.g. $\mathbf{P}^{(1)}\mathbf{P}^{(1)} = \mathbf{P}^{(1)}$) form.

$\mathbf{P}^\dagger \mathbf{P}$ <i>form</i>	$\mathbf{P}^{(0)}$	$\mathbf{P}^{(1)}$	$\mathbf{P}^{(2)}$	$\mathbf{P}^{(3)}$	$\mathbf{P}^{(4)}$	$\mathbf{P}^{(5)}$
$\mathbf{P}^{(0)}$	$\mathbf{P}^{(0)}$
$\mathbf{P}^{(1)}$.	$\mathbf{P}^{(1)}$
$\mathbf{P}^{(2)}$.	.	$\mathbf{P}^{(2)}$.	.	.
$\mathbf{P}^{(3)}$.	.	.	$\mathbf{P}^{(3)}$.	.
$\mathbf{P}^{(4)}$	$\mathbf{P}^{(4)}$.
$\mathbf{P}^{(5)}$	$\mathbf{P}^{(5)}$

$\mathbf{P}^{(m)}\mathbf{P}^{(n)} = \delta^{mn}\mathbf{P}^{(n)} \rightarrow$

$$\rightarrow (\mathbf{P}^{(2)})_{\mathbf{P}} = \begin{pmatrix} \cdot & \cdot & \cdot & \cdot & \cdot & \cdot \\ \cdot & \cdot & \cdot & \cdot & \cdot & \cdot \\ \cdot & \cdot & 1 & \cdot & \cdot & \cdot \\ \cdot & \cdot & \cdot & \cdot & \cdot & \cdot \\ \cdot & \cdot & \cdot & \cdot & \cdot & \cdot \\ \cdot & \cdot & \cdot & \cdot & \cdot & \cdot \end{pmatrix} \tag{54}$$

The location of each $\mathbf{P}^{(m)}$ in the \mathbf{P} -table is a location of a 1 in its representation as indicated in the right hand side of Equation (54) in the same way that locations in \mathbf{g} -table Equation (47) place 1's in representations Equation (48). However, idempotent self-conjugacy ($\mathbf{P}^\dagger = \mathbf{P}$) makes row labels of \mathbf{P} -table Equation (54) identical to its column labels, whereas only $\mathbf{g} = \mathbf{1}$ and $\mathbf{g} = \mathbf{r}^3$ are self-conjugate in \mathbf{g} -table Equation (47).

Character arrays such as Figure 13 represent operator eigen-products between \mathbf{r}^p and $\mathbf{P}^{(m)}$.

$$\mathbf{r}^p \mathbf{P}^{(m)} = \chi_p^m \mathbf{P}^{(m)} = \mathbf{P}^{(m)} \mathbf{r}^p \tag{55}$$

Also character χ_p^m is the scalar product *overlap* of position state bra or ket with momentum ket or bra.

Position bra: $\langle x_p | = \langle p | = \langle 0 | \mathbf{r}^{-p}$
 Position ket: $|x_p \rangle = |p \rangle = \mathbf{r}^p |0 \rangle$ (56a)

Momentum bra: $\langle k_m | = \langle (m) | = \langle 0 | \mathbf{P}^{(m)} \sqrt{n}$
 Momentum ket: $|k_m \rangle = |(m) \rangle = \mathbf{P}^{(m)} |0 \rangle \sqrt{n}$ (56b)

Momentum eigenwave $\psi_{k_m}(x_p)$ is character Equation (50) conjugated to $e^{ik_mx_p}$ and normalized by \sqrt{n} .

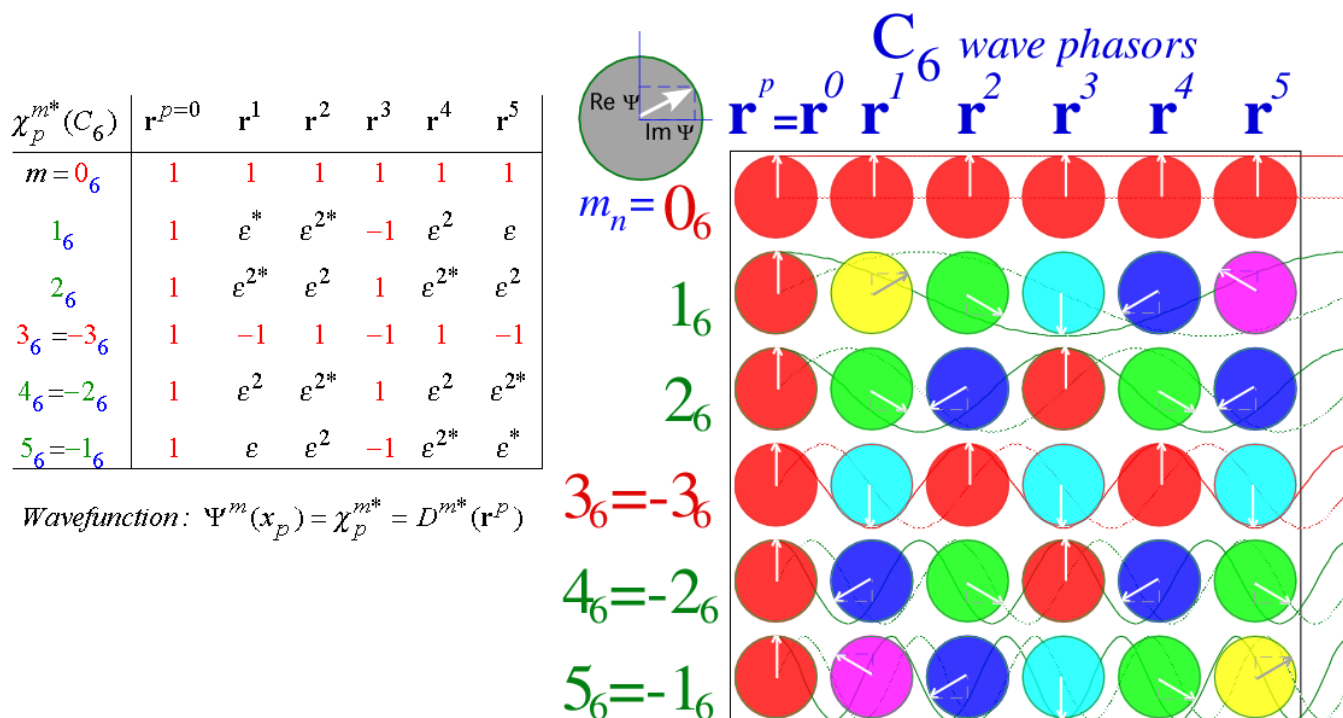
$$\begin{aligned} \psi_{k_m}(x_p) &= \langle x_p | k_m \rangle = \langle p | (m) \rangle = (\chi_p^m / \sqrt{n})^* \\ &= (\langle (m) | p \rangle)^* = e^{ik_mx_p} / \sqrt{n} \end{aligned} \tag{57}$$

Action of \mathbf{r}^p on m -ket $|(m) \rangle = |k_m \rangle$ is conjugate and inverse to action on coordinate bra $\langle x_q | = \langle q |$.

$$\begin{aligned} \psi_{k_m}(x_q - p \cdot L) &= \langle x_q | \mathbf{r}^p | k_m \rangle = \langle q | \mathbf{r}^p | (m) \rangle \\ &= \langle q - p | (m) \rangle = e^{-ik_mx_p} \langle q | (m) \rangle \end{aligned} \tag{58}$$

The same overlap results whether \mathbf{r}^p moves a (m) -wave p -points forward or moves the coordinate grid p -points backward. This C_n relativity-duality principle generalizes to non-Abelian symmetry and is key to operator labeling of coordinates, base states, Hamiltonians, and their eigensolutions.

Figure 13. C_6 characters (a) numerical table; (b) wave phasor table.



$\mathbf{P}^{(m)}$ projects m -states with conjugate characters $\phi_p^m = (\chi_p^m)^*$ with factor $1/n$ so $\mathbf{P}^{(m)}$'s are idempotent and sum to 1. ($\sum_p \mathbf{P}^{(m)} = 1$) But, $|k_m\rangle$ has ϕ_p^m with factor $1/\sqrt{n}$ to be orthonormal so its squares sum to 1. ($\sum_p |\langle x_p | k_m \rangle|^2 = 1$) Thus projection Equation (56b) of $|k_m\rangle$ by $\mathbf{P}^{(m)}$ has a factor \sqrt{n} . Inverse spectral resolution Equation (52) sums over column points p using ϕ_p^m from each row- (m) of Figure 13. Factor $1/n$ makes $\mathbf{P}^{(m)}$ complete ($\sum_m \mathbf{P}^{(m)} = 1$ in Equation (53)) and idempotent ($\mathbf{P}^{(m)} \mathbf{P}^{(m)} = \mathbf{P}^{(m)}$) in Equation (54)).

$$\mathbf{P}^{(m)} = \left(\sum_{p=0}^{n-1} \phi_p^m \mathbf{r}^p \right) / n = (\phi_0^m \mathbf{r}^0 + \phi_1^m \mathbf{r}^1 + \phi_2^m \mathbf{r}^2 + \phi_3^m \mathbf{r}^3 + \phi_4^m \mathbf{r}^4 + \phi_5^m \mathbf{r}^5) / 6 \quad (59)$$

First row ($(m)=(0)$ -row) of Figure 13 is an average, i.e., sum of all symmetry operators weighted by $1/n$.

$$\mathbf{P}^{(0)} = \left(\sum_{p=0}^{n-1} \mathbf{r}^p \right) / n = (\mathbf{r}^0 + \mathbf{r}^1 + \mathbf{r}^2 + \mathbf{r}^3 + \mathbf{r}^4 + \mathbf{r}^5) / 6 \quad (60)$$

Thus factors $\sqrt{n} = \sqrt{6}$ in state projections in Equation (56b) give state norms $\sqrt{n}/n = 1/\sqrt{n}$ in Equation (57).

$$\mathbf{P}^{(m)} |0\rangle \sqrt{n} = \left(\sum_{p=0}^{n-1} \phi_p^m |p\rangle \right) / \sqrt{n} = (\phi_0^m |0\rangle + \phi_1^m |1\rangle + \phi_2^m |2\rangle + \phi_3^m |3\rangle + \phi_4^m |4\rangle + \phi_5^m |5\rangle) / \sqrt{6} \quad (61)$$

The (0)-momentum or *scalar* state is a sum over the (m)=(0)-row of Figure 13 normalized by $1/\sqrt{n}$.

$$\mathbf{P}^{(0)}|0\rangle\sqrt{n} = \left(\sum_{p=0}^{n-1} |p\rangle \right) / \sqrt{n} = (|0\rangle + |1\rangle + |2\rangle + |3\rangle + |4\rangle + |5\rangle) / \sqrt{6} \tag{62}$$

5.3. Spectral Resolution of C_n Symmetric Hamiltonian

Given Hamiltonian \mathbf{H} expansion in Equation (45) in operators \mathbf{r}^p and the spectral resolution in Equation (52) of \mathbf{r}^p , there follows the desired spectral resolution of \mathbf{H} . The eigenvalue coefficients $\omega^{(m)}$ of $\mathbf{P}^{(m)}$ define the dispersion function $\omega(k_m)$ of \mathbf{H} in Figure 14(a) where it is conventional to center scalar origin (m)=(0).

$$\mathbf{H} = \sum_{p=0}^{n-1} r_p \mathbf{r}^p = \sum_{p=0}^{n-1} r_p \sum_{m=0}^{n-1} \chi_p^m \mathbf{P}^{(m)} = \sum_{m=0}^{n-1} \omega^{(m)} \mathbf{P}^{(m)} \quad \text{where : } \omega^{(m)} = \sum_{p=0}^{n-1} r_p \chi_p^m = \omega(k_m) \tag{63}$$

Positive k_m -axis C_6 array [...(0), (1), (2), (3), (4), (5), ...] of Equation (54) shifts to a zone-center-array mod-6: [...(4), (5), (0), (1), (2), (3), ...]=[...(-2), (-1), (0), (1), (2), (3), ...] using Equation (46).

Examples of dispersion relations for three classes of tunneling paths in Figure 12 are shown in Figure 14. Dispersion $\omega(k_m)$ for C_6 symmetry depends sensitively on the Hamiltonian tunneling amplitudes r_p for $-3 < p \leq 3$ (or $0 \leq p < 6$) in Equation (49), and for any set of eigenvalues $\omega(k_m)$ there is a unique set of r_p found by inverting Equation (63).

$$r_p = \sum_{m=0}^{n-1} \phi_p^m \omega^{(m)} / n \quad \text{where : } \phi_p^m = (\chi_p^m)^* \tag{64}$$

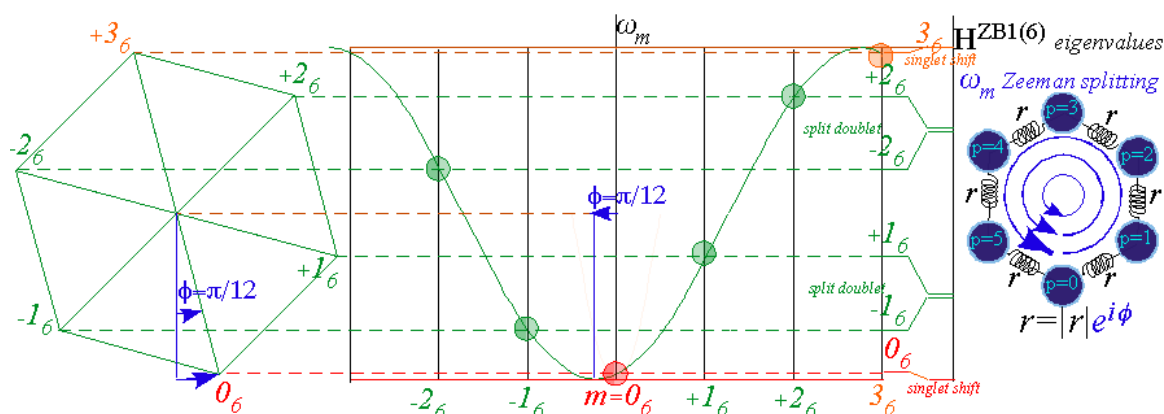
A common tunneling spectral model is the elementary Bloch 1st-neighbor $B1(6)$ -model shown in Figure 14a, much like that developed in Reference [33]. For negative values of $r_1=-r$, a $B1(6)$ spectra for C_6 consist of six points on a single inverted cosine-wave curve centered at $m=0$ with its maxima at the Brillouin-band boundaries (m)=±3. This curve applies to $B1(n)$ spectra for C_n where n equally spaced (m) points lie on the dispersion curve between $m=\pm n/2$ for even- n . The n energy eigenvalues $\omega^{(m)}$ are projections of an n -polygon. For $n=6$ that is the hexagon shown in Figure 14a projecting two doublet levels $\omega^{(\pm 1)}$ and $\omega^{(\pm 2)}$ between singlet $\omega^{(0)}$ and singlet $\omega^{(3)}$ at lowest and highest hexagonal vertices as follows from Equation (63).

$$\omega^{B1(n)}(k_m) = r_0 \chi_0^m + r_1 \chi_1^m + r_{-1} \chi_{-1}^m = H_1 - 2r \cos(2\pi m/6) \tag{65}$$

The 2nd-neighbor $B2$ -model (Figure 14b) has a two-cosine-wave dispersion curve. An equilateral triangle projects energy doublet levels [$\omega^{(0)}, \omega^{(3)}$] from its lowest vertex and a quartet [$\omega^{(\pm 1)}, \omega^{(\pm 2)}$] from its upper vertices.

$$\omega^{B2(n)}(k_m) = r_0 \chi_0^m + r_2 \chi_2^m + r_{-2} \chi_{-2}^m = H_2 - 2s \cos(4\pi m/6) \tag{66}$$

Figure 15. Zeeman shifted Bloch dispersion for complex parameter in ZB1(6) model: $r_1 = -re^{i\phi}$ with $\phi = \pi/12$.



6. Non-Abelian Symmetry Analysis

Characterization and spectral resolution in Equation (63) of a Hamiltonian $H^{Bk(6)}$ uses its expansion in Equation (45) in Abelian group C_6 . Similar spectral resolution of a Hamiltonian H by a non-Abelian group $G = [\dots g_1, g_2 \dots]$ of non-commuting symmetry operators might seem impossible. To be symmetry operators of H , elements g_1 and g_2 must commute with H , but that cannot be if H is a linear expansion of them like Equation (45). The impasse is broken by introducing operator *relativity-duality* detailed below. A D_3 -symmetric tunneling H with a 3-well potential sketched in Figure 16 is used as an example.

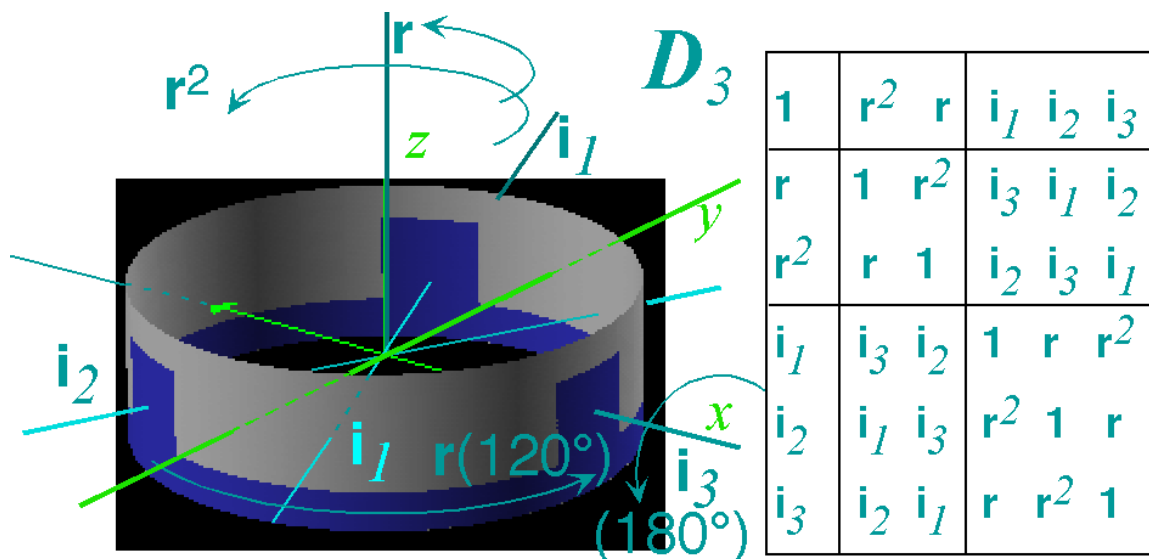
6.1. Operator Expansion of D_3 Symmetric Hamiltonian

The simplest non-Abelian group is the rotational symmetry $D_3 = [1, r^1, r^2, i_1, i_2, i_3]$ of an equilateral triangle. D_3 is used to show how to generalize C_6 operator analysis of the preceding section to any symmetry group. The D_3 analysis begins with a $g^\dagger g$ -form of group product table like Equation (47) for C_6 . However, D_3 also requires a $g g^\dagger$ -form giving the same product rules but using inverse g^\dagger ordering $[..r^2, r^1, \dots | ..r^{1\dagger}, r^{2\dagger}, \dots]$ along the top instead of down the left side as is done for the $g^\dagger g$ -form of table. (The two $\pm 120^\circ$ rotations r^1 and r^2 are the only pair ($r^{1\dagger} = r^2$) to be switched by conjugation). The three $\pm 180^\circ$ rotations are each self-conjugate ($i_p^\dagger = i_p$) as is (always) the identity $1^\dagger = 1$.

$g^\dagger g$ form	1	r^1	r^2	i_1	i_2	i_3	$g g^\dagger$ form	$\bar{1}$	\bar{r}^2	\bar{r}^1	\bar{i}_1	\bar{i}_2	\bar{i}_3
1	1	r^1	r^2	i_1	i_2	i_3	$\bar{1}$	$\bar{1}$	\bar{r}^2	\bar{r}^1	\bar{i}_1	\bar{i}_2	\bar{i}_3
r^2	r^2	1	r^1	i_2	i_3	i_1	\bar{r}^1	\bar{r}^1	$\bar{1}$	\bar{r}^2	\bar{i}_3	\bar{i}_1	\bar{i}_2
r^1	r^1	r^2	1	i_3	i_1	i_2	\bar{r}^2	\bar{r}^2	\bar{r}^1	$\bar{1}$	\bar{i}_2	\bar{i}_3	\bar{i}_1
i_1	i_1	i_2	i_3	1	r^1	r^2	\bar{i}_1	\bar{i}_1	\bar{i}_3	\bar{i}_2	$\bar{1}$	\bar{r}^1	\bar{r}^2
i_2	i_2	i_3	i_1	r^2	1	r^1	\bar{i}_2	\bar{i}_2	\bar{i}_1	\bar{i}_3	\bar{r}^2	$\bar{1}$	\bar{r}^1
i_3	i_3	i_1	i_2	r^1	r^2	1	\bar{i}_3	\bar{i}_3	\bar{i}_2	\bar{i}_1	\bar{r}^1	\bar{r}^2	$\bar{1}$

Over-bar notation is used for *dual-group* $\bar{D}_3 = [\bar{1}, \bar{r}^1, \bar{r}^2, \bar{i}_1, \bar{i}_2, \bar{i}_3]$ of “body”-based operators isomorphic to “lab”-based group.

Figure 16. Rotation operators $[1, r^1, r^2, i_1, i_2, i_3]$ for a D_3 symmetric square-well potential.



Matrix representations Equation (69a) for D_3 or matrices Equation (69b) for \bar{D}_3 are given, respectively, by $g^\dagger g$ or $g g^\dagger$ -forms Equation (68) just as $g^\dagger g$ form Equation (47) for C_6 gives matrices in Equation (48).

$$\begin{aligned}
 (1) &= \begin{pmatrix} 1 & \cdot & \cdot & \cdot & \cdot & \cdot \\ \cdot & 1 & \cdot & \cdot & \cdot & \cdot \\ \cdot & \cdot & 1 & \cdot & \cdot & \cdot \\ \cdot & \cdot & \cdot & 1 & \cdot & \cdot \\ \cdot & \cdot & \cdot & \cdot & 1 & \cdot \\ \cdot & \cdot & \cdot & \cdot & \cdot & 1 \end{pmatrix} & (r^1) &= \begin{pmatrix} \cdot & 1 & \cdot & \cdot & \cdot & \cdot \\ \cdot & \cdot & 1 & \cdot & \cdot & \cdot \\ 1 & \cdot & \cdot & \cdot & \cdot & \cdot \\ \cdot & \cdot & \cdot & \cdot & 1 & \cdot \\ \cdot & \cdot & \cdot & \cdot & \cdot & 1 \\ \cdot & \cdot & \cdot & 1 & \cdot & \cdot \end{pmatrix} & (r^2) &= \begin{pmatrix} \cdot & \cdot & 1 & \cdot & \cdot & \cdot \\ 1 & \cdot & \cdot & \cdot & \cdot & \cdot \\ \cdot & 1 & \cdot & \cdot & \cdot & \cdot \\ \cdot & \cdot & \cdot & \cdot & \cdot & 1 \\ \cdot & \cdot & \cdot & 1 & \cdot & \cdot \\ \cdot & \cdot & \cdot & \cdot & 1 & \cdot \end{pmatrix} \\
 (i_1) &= \begin{pmatrix} \cdot & \cdot & \cdot & 1 & \cdot & \cdot \\ \cdot & \cdot & \cdot & \cdot & 1 & \cdot \\ \cdot & \cdot & \cdot & \cdot & \cdot & 1 \\ 1 & \cdot & \cdot & \cdot & \cdot & \cdot \\ \cdot & \cdot & 1 & \cdot & \cdot & \cdot \\ \cdot & 1 & \cdot & \cdot & \cdot & \cdot \end{pmatrix} & (i_2) &= \begin{pmatrix} \cdot & \cdot & \cdot & \cdot & 1 & \cdot \\ \cdot & \cdot & \cdot & 1 & \cdot & \cdot \\ \cdot & \cdot & \cdot & \cdot & \cdot & 1 \\ \cdot & 1 & \cdot & \cdot & \cdot & \cdot \\ 1 & \cdot & \cdot & \cdot & \cdot & \cdot \\ \cdot & \cdot & 1 & \cdot & \cdot & \cdot \end{pmatrix} & (i_3) &= \begin{pmatrix} \cdot & \cdot & \cdot & \cdot & \cdot & 1 \\ \cdot & \cdot & \cdot & \cdot & 1 & \cdot \\ \cdot & \cdot & \cdot & 1 & \cdot & \cdot \\ \cdot & 1 & \cdot & \cdot & \cdot & \cdot \\ \cdot & \cdot & 1 & \cdot & \cdot & \cdot \\ 1 & \cdot & \cdot & \cdot & \cdot & \cdot \end{pmatrix}
 \end{aligned} \tag{69a}$$

$$\begin{aligned}
 (\bar{1}) &= \begin{pmatrix} 1 & \cdot & \cdot & \cdot & \cdot & \cdot \\ \cdot & 1 & \cdot & \cdot & \cdot & \cdot \\ \cdot & \cdot & 1 & \cdot & \cdot & \cdot \\ \cdot & \cdot & \cdot & 1 & \cdot & \cdot \\ \cdot & \cdot & \cdot & \cdot & 1 & \cdot \\ \cdot & \cdot & \cdot & \cdot & \cdot & 1 \end{pmatrix} & (\bar{r}^1) &= \begin{pmatrix} \cdot & \cdot & 1 & \cdot & \cdot & \cdot \\ 1 & \cdot & \cdot & \cdot & \cdot & \cdot \\ \cdot & 1 & \cdot & \cdot & \cdot & \cdot \\ \cdot & \cdot & \cdot & \cdot & 1 & \cdot \\ \cdot & \cdot & \cdot & \cdot & \cdot & 1 \\ \cdot & \cdot & \cdot & 1 & \cdot & \cdot \end{pmatrix} & (\bar{r}^2) &= \begin{pmatrix} \cdot & 1 & \cdot & \cdot & \cdot & \cdot \\ \cdot & \cdot & 1 & \cdot & \cdot & \cdot \\ 1 & \cdot & \cdot & \cdot & \cdot & \cdot \\ \cdot & \cdot & \cdot & \cdot & \cdot & 1 \\ \cdot & \cdot & \cdot & 1 & \cdot & \cdot \\ \cdot & \cdot & \cdot & \cdot & 1 & \cdot \end{pmatrix} \\
 (\bar{i}_1) &= \begin{pmatrix} \cdot & \cdot & \cdot & 1 & \cdot & \cdot \\ \cdot & \cdot & \cdot & \cdot & 1 & \cdot \\ \cdot & \cdot & \cdot & \cdot & \cdot & 1 \\ 1 & \cdot & \cdot & \cdot & \cdot & \cdot \\ \cdot & \cdot & 1 & \cdot & \cdot & \cdot \\ \cdot & 1 & \cdot & \cdot & \cdot & \cdot \end{pmatrix} & (\bar{i}_2) &= \begin{pmatrix} \cdot & \cdot & \cdot & \cdot & 1 & \cdot \\ \cdot & \cdot & \cdot & 1 & \cdot & \cdot \\ \cdot & \cdot & \cdot & \cdot & \cdot & 1 \\ \cdot & 1 & \cdot & \cdot & \cdot & \cdot \\ 1 & \cdot & \cdot & \cdot & \cdot & \cdot \\ \cdot & \cdot & 1 & \cdot & \cdot & \cdot \end{pmatrix} & (\bar{i}_3) &= \begin{pmatrix} \cdot & \cdot & \cdot & \cdot & \cdot & 1 \\ \cdot & \cdot & \cdot & \cdot & 1 & \cdot \\ \cdot & \cdot & \cdot & 1 & \cdot & \cdot \\ \cdot & 1 & \cdot & \cdot & \cdot & \cdot \\ \cdot & \cdot & 1 & \cdot & \cdot & \cdot \\ 1 & \cdot & \cdot & \cdot & \cdot & \cdot \end{pmatrix}
 \end{aligned} \tag{69b}$$

Most pairs of resulting D_3 matrices in Equation (69a) do not commute. (For example $(\mathbf{r}^1)(\mathbf{i}_1)=(\mathbf{i}_3)$ does not equal $(\mathbf{i}_1)(\mathbf{r}^1)=(\mathbf{i}_2)$.) Identical non-commutative product rules apply to the dual bar group \bar{D}_3 matrices in Equation (69b). However, all matrices of the latter \bar{D}_3 commute with all matrices of the former D_3 . This suggests that the Hamiltonian matrix, in order to commute with its symmetry group D_3 , is constructed by linear combination of bar group operators of \bar{D}_3 [32].

$$\mathbf{H} = r_0\bar{\mathbf{I}} + r_1\bar{\mathbf{r}}^1 + r_2\bar{\mathbf{r}}^2 + i_1\bar{\mathbf{i}}_1 + i_2\bar{\mathbf{i}}_2 + i_3\bar{\mathbf{i}}_3 \tag{70}$$

D_3 symmetric (\mathbf{H}) matrix Equation (71) generalizes C_6 symmetric (\mathbf{H}) matrix Equation (49) to a non-Abelian case.

$$(\mathbf{H}) = \sum_{g=1}^{\circ G} r_g(\bar{\mathbf{g}}) = \begin{pmatrix} r_0 & r_2 & r_1 & i_1 & i_2 & i_3 \\ r_1 & r_0 & r_2 & i_3 & i_1 & i_2 \\ r_2 & r_1 & r_0 & i_2 & i_3 & i_1 \\ i_i & i_3 & i_2 & r_0 & r_1 & r_2 \\ i_2 & i_1 & i_3 & r_2 & r_0 & r_1 \\ i_3 & i_2 & i_1 & r_1 & r_2 & r_0 \end{pmatrix} \tag{71}$$

6.2. Spectral Resolution of D_3 Symmetry Operators

Spectral resolution of D_3 or any non-Abelian group $G = [\dots\mathbf{g}_1, \mathbf{g}_2\dots]$ entails more than the C_6 expansion into a unique combination of idempotent operators $\mathbf{P}^{\alpha=|\alpha\rangle}\langle\alpha|$ multiplied by eigenvalue $D^{(\alpha)}(g)$ coefficients as in Equation (52). It is not possible to diagonalize two non-commuting \mathbf{g}_1 and \mathbf{g}_2 in one basis since numbers (eigenvalues) always commute. If \mathbf{g}_1 and \mathbf{g}_2 do not commute, their collective resolution must include eigen-matrix coefficients $D_{m,n}^{\alpha}$ involving nilpotent ($\mathbf{N}^2 = 0$) operators $\mathbf{P}_{m,n}^{\alpha=|\alpha\rangle}\langle\alpha|$ as well as idempotent ($\mathbf{I}^2 = \mathbf{I}$) operators $\mathbf{P}_{m,m}^{\alpha=|\alpha\rangle}\langle\alpha|$ seen in Equation (52).

Unlike a commutative algebra of C_n idempotents, which are shown in Equation (54) and uniquely defined by Equation (59), a non-Abelian algebra yields a panoply of equivalent choices of \mathbf{P} operators that resolve it. The number and types of these \mathbf{P} 's is uniquely determined by size and structure of certain key commuting sub-algebras. The key to symmetry analysis of quantum physics is to first sort out the operators and algebras that commute from those that do not. It amounts to a kind of symmetry analysis of symmetry and leads to a far greater diversity than is found in commutative Abelian systems.

6.2.1. Sorting Commuting Subalgebras: Rank and Commuting Observables

The rank $\rho(G)$ of a G -algebra is the maximal number of mutually-commuting operators available by linearly combining the ${}^{\circ}G$ operators \mathbf{g}_k of symmetry group G . $\rho(G)$ is also the greatest number of orthogonal idempotents \mathbf{P}^m that can resolve the G -identity $\mathbf{1}$ as in Equation (53). (${}^{\circ}G$ is total number or order of G . Here ${}^{\circ}D_3$ and ${}^{\circ}C_6$ both equal 6.)

C_6 rank is obviously equal to its order ($\rho(C_6) = 6$), but the rank of D_3 turns out to be only four ($\rho(D_3) = 4$). As shown below, D_3 can have no more than four \mathbf{P} -operators that mutually commute though there exist quite different sets of them. On the other hand, D_3 has just three linearly independent \mathbf{P}^{α} -operators that commute with all of D_3 , and there is but one invariant set of them just as there is but one set of $\mathbf{P}^{(m)}$ for C_6 in Equation (59).

Rank is a key quantum concept since it is the total number of commuting observables, the operators that label and define eigenstates. Of primary importance are *G*-invariant labeling operators \mathbf{I}_G that commute with *all* \mathbf{g} and not just with other labeling operators. \mathbf{I}_G are uniquely defined within their group *G* and invariant to all \mathbf{g} . ($\mathbf{g}\mathbf{I}_G\mathbf{g}^{-1}=\mathbf{I}_G$) For example, total angular momentum \mathbf{J}^2 and e-values $J(J + 1)$ are *R*(3)-invariant .

Next in importance are labeling operators $[\mathbf{I}_{H_{n-1}}, \mathbf{I}_{H_{n-2}}, \dots, \mathbf{I}_{H_1}]$ belonging to nested subgroups of $G=H_n$ in a *subgroup chain* $G \supset H_{n-1} \supset H_{n-2} \supset \dots H_1$. Multiple choices of chains exists since each subgroup link H_k is not uniquely determined by the H_{k+1} that contains it, but each \mathbf{I}_{H_k} is invariant to all possible $H_{j \leq k}$ at level-*k* or below.

For example, the *z*-axial momentum \mathbf{J}_z and its e-values m_z belong to a 2nd link in chain- $R(3) \supset R(2_z) \supset C_6(z)$. Given *R*(3) there are an infinity of *R*(2) subgroups besides the one for *z*-axis of quantization. \mathbf{J}_x or \mathbf{J}_y are just two of an infinite number of possible alternatives to \mathbf{J}_z . Each *R*(2_{*ζ*}) has an infinite number of cyclic $C_n(\zeta)$ sub-subgroups.

6.2.2. Sorting Commuting Subalgebras: Centrum and Class Invariants

The *centrum* $\kappa(G)$ of a *G*-algebra is the number of *all-commuting* operators available by combining \mathbf{g}_k . It is also the number of *G*-invariant \mathbf{P}^α -operators. Students of group theory know $\kappa(G)$ as the number of equivalence *classes* of group *G*. D_3 elements in Figure 16 are separated into three classes of elements $[\mathbf{1}], [\mathbf{r}^1, \mathbf{r}^2]$, and $[\mathbf{i}_1, \mathbf{i}_2, \mathbf{i}_3]$. ($\kappa(D_3) = 3$)

Elements in each class are related through transformation $\mathbf{g}_1 = \mathbf{g}_t \mathbf{g}_2 \mathbf{g}_t^{-1}$ by \mathbf{g}_t in group *G*. Sum κ_k of ${}^o C_k$ elements in \mathbf{g}_k 's class is invariant to \mathbf{g}_t transformation. (It only permutes \mathbf{g}_k -terms in κ_k thus κ_k commutes with all \mathbf{g}_t in *G*.)

$$\mathbf{g}_t \kappa_k \mathbf{g}_t^{-1} = \kappa_k \text{ where: } \kappa_k = \sum_{j=1}^{j={}^o C_k} \mathbf{g}_j = 1/{}^o s_k \sum_{t=1}^{t={}^o G} \mathbf{g}_t \mathbf{g}_k \mathbf{g}_t^{-1} \tag{72}$$

The product table for D_3 class algebra [$\kappa_1 = \mathbf{1}$, $\kappa_2 = \mathbf{r}^1 + \mathbf{r}^2$, $\kappa_3 = \mathbf{i}_1 + \mathbf{i}_2 + \mathbf{i}_3$] in Equation (73) below follows by inspecting D_3 group product tables in Figure 16 or Equation (68). It is a commutative algebra since each κ_j commutes with each κ_k as well as with each \mathbf{g}_t . This guarantees a class algebra has a unique and invariant spectral resolution.

1	r¹	r²	i₁	i₂	i₃
r²	1	r¹	i₂	i₃	i₁
r¹	r²	1	i₃	i₁	i₂
i₁	i₂	i₃	1	r¹	r²
i₂	i₃	i₁	r²	1	r¹
i₃	i₁	i₂	r¹	r²	1

 \rightarrow

$\kappa_1 = \mathbf{1}$	$\kappa_2 = \mathbf{r}^1 + \mathbf{r}^2$	$\kappa_3 = \mathbf{i}_1 + \mathbf{i}_2 + \mathbf{i}_3$
κ_2	$2\kappa_1 + \kappa_2$	$2\kappa_3$
κ_3	$2\kappa_3$	$3\kappa_1 + 3\kappa_2$

(73)

The first sum in Equation (72) is over the ${}^o C_k$ elements in \mathbf{g}_k 's class. (${}^o C_k$ is order of κ_k .) The second sum is over all ${}^o G$ group elements. The number of elements \mathbf{g}_t that commute with \mathbf{g}_k is ${}^o s_k$, the order of \mathbf{g}_k 's self-symmetry s_k . Each group operator \mathbf{g}_k has a self-symmetry group consisting of (at least) the identity $\mathbf{1}$ and powers $(\mathbf{g}_k)^p$ of itself. The order of class-*k* is the (integer) fraction ${}^o C_k = {}^o G / {}^o s_k$.

6.2.3. Resolving All-commuting Class Subalgebra: $\text{Centrum}=\kappa(D_3) = 3$

Spectral resolution gives class-sum operators $\kappa_1, \kappa_2,$ and κ_3 as combinations of three D_3 -invariant \mathbf{P}^α -operators with each of the κ_k eigenvalues as coefficients. The κ_3 characteristic equation found by Equation (73) gives three \mathbf{P}^α directly.

$$0 = \kappa_3^3 - 9\kappa_3 = (\kappa_3 - 3 \cdot \mathbf{1})(\kappa_3 + 3 \cdot \mathbf{1})(\kappa_3 + 0 \cdot \mathbf{1})$$

$$= (\kappa_3 - 3 \cdot \mathbf{1})\mathbf{P}^{A_1} = (\kappa_3 + 3 \cdot \mathbf{1})\mathbf{P}^{A_2} = (\kappa_3 - 0 \cdot \mathbf{1})\mathbf{P}^E \tag{74}$$

Standard notation $A_1, A_2,$ and E is used for the three invariant idempotents \mathbf{P}^α .

$$\begin{aligned} \kappa_1 &= 1 \cdot \mathbf{P}^{A_1} + 1 \cdot \mathbf{P}^{A_2} + 1 \cdot \mathbf{P}^E & \mathbf{P}^{A_1} &= (\kappa_1 + \kappa_2 + \kappa_3)/6 = (\mathbf{1} + \mathbf{r}^1 + \mathbf{r}^2 + \mathbf{i}_1 + \mathbf{i}_2 + \mathbf{i}_3)/6 \\ \kappa_2 &= 2 \cdot \mathbf{P}^{A_1} - 2 \cdot \mathbf{P}^{A_2} - 1 \cdot \mathbf{P}^E & \mathbf{P}^{A_2} &= (\kappa_1 + \kappa_2 - \kappa_3)/6 = (\mathbf{1} + \mathbf{r}^1 + \mathbf{r}^2 - \mathbf{i}_1 - \mathbf{i}_2 - \mathbf{i}_3)/6 \\ \kappa_3 &= 3 \cdot \mathbf{P}^{A_1} - 3 \cdot \mathbf{P}^{A_2} + 0 \cdot \mathbf{P}^E & \mathbf{P}^E &= (2\kappa_1 - \kappa_2)/3 = (2\mathbf{1} - \mathbf{r}^1 - \mathbf{r}^2)/3 \end{aligned} \tag{75}$$

Traces of D_3 matrices (\mathbf{g}_k) in Equation (69a) are zero excepting $\text{Trace}(\mathbf{1}) = 6$. Traces of (\mathbf{P}^α) then follow.

$$\text{trace}\mathbf{P}^{A_1} = 1, \quad \text{trace}\mathbf{P}^{A_2} = 1, \quad \text{trace}\mathbf{P}^E = 4 \tag{76}$$

This means (\mathbf{P}^{A_1}) and (\mathbf{P}^{A_2}) are each 1-by-1 projectors while (\mathbf{P}^E) splits into two 2-by-2 projectors. The latter splitting is not uniquely defined until subgroup chain $D_3 \supset C_3$ or a particular $D_3 \supset C_2$ chain is chosen, but relations in Equation (75) are invariant and unique. The κ_k coefficients inside parentheses of \mathbf{P}^α expansion give the D_3 character table for traces of irreducible representations (irreps). Irrep dimension ℓ^α is trace of the α^{th} -irrep of identity $\mathbf{g}_1 = \mathbf{1}$.

D_3	κ_1	κ_2	κ_3
A_1	1	1	1
A_2	1	1	-1
E	2	-1	0

$$\chi_k^\alpha = \text{Trace}D^\alpha(\mathbf{g}_k), \quad \ell^\alpha = \chi_1^\alpha = \text{Trace}D^\alpha(\mathbf{1}) \tag{77}$$

6.2.4. Resolving Maximal Mutually Commuting Subalgebra: $\text{rank} = \rho(D_3) = 4$

Completing resolution of D_3 uses a product of two completeness relations, the resolution of class identity $\kappa_1 = \mathbf{1}$ in Equation (75) with the identity resolution of a D_3 subgroup $C_3 = [\mathbf{1}, \mathbf{r}^1, \mathbf{r}^2]$ or else $C_2 = [\mathbf{1}, \mathbf{i}_3]$. In either case invariant \mathbf{P}^E splits but \mathbf{P}^{A_1} and \mathbf{P}^{A_2} do not. In Equation (78) \mathbf{P}^E is split by C_2 into plane-polarizing projectors $\mathbf{P}_{x,x}^E + \mathbf{P}_{y,y}^E = \mathbf{P}_{0_2 0_2}^E + \mathbf{P}_{1_2 1_2}^E$.

$$\left[\begin{array}{c} D_3 \text{ (class algebra)} \\ \text{completeness} \\ \mathbf{1} = \mathbf{P}^{A_1} + \mathbf{P}^{A_2} + \mathbf{P}^E \end{array} \right] \cdot \left[\begin{array}{c} C_2 \text{ (subgroup)} \\ \text{completeness} \\ \mathbf{1} = \mathbf{P}^{0_2} + \mathbf{P}^{1_2} \end{array} \right] = \left[\begin{array}{c} D_3 \text{ (group)} \\ \text{completeness} \\ \mathbf{1} = \mathbf{P}_{0_2 0_2}^{A_1} + \mathbf{P}_{1_2 1_2}^{A_2} + \mathbf{P}_{0_2 0_2}^E + \mathbf{P}_{1_2 1_2}^E \end{array} \right]$$

where :

$$\begin{aligned} \mathbf{P}^{A_1} &= \mathbf{P}_{0_2 0_2}^{A_1} = (\mathbf{1} + \mathbf{r}^1 + \mathbf{r}^2 + \mathbf{i}_1 + \mathbf{i}_2 + \mathbf{i}_3)/6 = \mathbf{P}^{A_1}\mathbf{P}^{0_2} \\ \mathbf{P}^{A_2} &= \mathbf{P}_{1_2 1_2}^{A_2} = (\mathbf{1} + \mathbf{r}^1 + \mathbf{r}^2 - \mathbf{i}_1 - \mathbf{i}_2 - \mathbf{i}_3)/6 = \mathbf{P}^{A_2}\mathbf{P}^{1_2} \quad (\text{All other } \mathbf{P}^\alpha \mathbf{P}^{m_2} = 0) \\ \mathbf{P}_{x,x}^E &= \mathbf{P}_{0_2 0_2}^E = (2\mathbf{1} - \mathbf{r}^1 - \mathbf{r}^2 - \mathbf{i}_1 - \mathbf{i}_2 + 2\mathbf{i}_3)/6 = \mathbf{P}^E\mathbf{P}^{0_2} \\ \mathbf{P}_{y,y}^E &= \mathbf{P}_{1_2 1_2}^E = (2\mathbf{1} - \mathbf{r}^1 - \mathbf{r}^2 + \mathbf{i}_1 + \mathbf{i}_2 - 2\mathbf{i}_3)/6 = \mathbf{P}^E\mathbf{P}^{1_2} \end{aligned} \tag{78}$$

In Equation (79) \mathbf{P}^E is split by C_3 into Right and Left circular-polarized projectors $\mathbf{P}_{R,R}^E + \mathbf{P}_{L,L}^E = \mathbf{P}_{1_3 1_3}^E + \mathbf{P}_{2_3 2_3}^E$.

$$\left[\begin{array}{c} D_3 \text{ (class algebra)} \\ \text{completeness} \\ \mathbf{1} = \mathbf{P}^{A_1} + \mathbf{P}^{A_2} + \mathbf{P}^E \end{array} \right] \cdot \left[\begin{array}{c} C_3 \text{ (subgroup)} \\ \text{completeness} \\ \mathbf{1} = \mathbf{P}^{0_3} + \mathbf{P}^{1_3} + \mathbf{P}^{2_3} \end{array} \right] = \left[\begin{array}{c} D_3 \text{ (group)} \\ \text{completeness} \\ \mathbf{1} = \mathbf{P}_{0_3 0_3}^{A_1} + \mathbf{P}_{0_3 0_3}^{A_2} + \mathbf{P}_{1_3 1_3}^E + \mathbf{P}_{2_3 2_3}^E \end{array} \right]$$

where :

$$\begin{aligned} \mathbf{P}^{A_1} &= \mathbf{P}_{0_3 0_3}^{A_1} = (\mathbf{1} + \mathbf{r}^1 + \mathbf{r}^2 + \mathbf{i}_1 + \mathbf{i}_2 + \mathbf{i}_3)/6 = \mathbf{P}^{A_1} \mathbf{P}^{0_3} \\ \mathbf{P}^{A_2} &= \mathbf{P}_{0_3 0_3}^{A_2} = (\mathbf{1} + \mathbf{r}^1 + \mathbf{r}^2 - \mathbf{i}_1 - \mathbf{i}_2 - \mathbf{i}_3)/6 = \mathbf{P}^{A_2} \mathbf{P}^{0_3} \\ \mathbf{P}_{R,R}^E &= \mathbf{P}_{1_3 1_3}^E = (\mathbf{1} + \varepsilon \mathbf{r}^1 + \varepsilon^* \mathbf{r}^2)/3 = \mathbf{P}^E \mathbf{P}^{1_3} \\ \mathbf{P}_{L,L}^E &= \mathbf{P}_{2_3 2_3}^E = (\mathbf{1} + \varepsilon^* \mathbf{r}^1 + \varepsilon \mathbf{r}^2)/3 = \mathbf{P}^E \mathbf{P}^{2_3} \end{aligned}$$

(All other $\mathbf{P}^\alpha \mathbf{P}^{m_3} = \mathbf{0}$)
 $\varepsilon = e^{i2\pi/3}$

(79)

In Equations (78) and (79), neither \mathbf{P}^{A_1} nor \mathbf{P}^{A_2} split or change except to acquire some C_2 or C_3 labels. The total number (four) of irreducible idempotents after either complete splitting is the same group rank noted before: $\rho(D_3)=4$. But, the RL -circularly polarized pairs $\mathbf{P}_{R,R}^E$ and $\mathbf{P}_{L,L}^E$ split-out by $C_3=[\mathbf{1}, \mathbf{r}^1, \mathbf{r}^2]$ differ from the linear xy -polarized pairs $\mathbf{P}_{x,x}^E$ and $\mathbf{P}_{y,y}^E$ split-out by $C_2=[\mathbf{1}, \mathbf{i}_3]$. $\mathbf{P}_{x,x}^E$ and $\mathbf{P}_{y,y}^E$ are, respectively, parallel (symmetric $\mathbf{i}_3 \mathbf{P}_{x,x}^E = +\mathbf{P}_{x,x}^E$) and anti-parallel (anti-symmetric $\mathbf{i}_3 \mathbf{P}_{y,y}^E = -\mathbf{P}_{y,y}^E$) to x -axial 180° rotation \mathbf{i}_3 in Figure 16 and will be used in examples.

6.2.5. Final Resolutions of Non-Commuting Algebra: ${}^o(D_3) = 6$

Mutually commuting algebras resolve into $(\mathbf{I}^2 = \mathbf{I})$ operators $\mathbf{P}_{m,m}^\alpha = |\alpha\rangle_m \langle \alpha|$ that sum to identity operator $\mathbf{1}$. They are split using the “one-equals-one-times-one” ($\mathbf{1}=\mathbf{1}\cdot\mathbf{1}$) trick in Equations (78) and (79).

Non-commuting algebras resolve into idempotents and nilpotent ($\mathbf{N}^2 = \mathbf{0}$) operators $\mathbf{P}_{m,n}^\alpha = |\alpha\rangle_m \langle \alpha|$ that are split out using the following “operator-equals-one-times-operator-times-one” ($\mathbf{g}=\mathbf{1}\cdot\mathbf{g}\cdot\mathbf{1}$) trick. It is only necessary that $\mathbf{1}$ be resolved into rank-number ρ of irreducible idempotents as in Equation (78) or (79). (Here $\rho(D_3) = 4$.)

$$\mathbf{g} = \mathbf{1} \cdot \mathbf{g} \cdot \mathbf{1} = (\mathbf{P}_{x,x}^{A_1} + \mathbf{P}_{y,y}^{A_2} + \mathbf{P}_{x,x}^E + \mathbf{P}_{y,y}^E) \cdot \mathbf{g} \cdot (\mathbf{P}_{x,x}^{A_1} + \mathbf{P}_{y,y}^{A_2} + \mathbf{P}_{x,x}^E + \mathbf{P}_{y,y}^E) \tag{80}$$

The product in Equation (80) could have sixteen terms, but only six survive due to idempotent orthogonality $\mathbf{P}_{j,j}^\alpha \mathbf{P}_{k,k}^\beta = \delta^{\alpha,\beta} \delta_{j,k} \mathbf{P}_{j,j}^\alpha$, and the fact that both \mathbf{P}^{A_1} and \mathbf{P}^{A_2} remain invariant and commute with all $\mathbf{P}_{j,j}^\alpha$ and all \mathbf{g} .

$$\begin{aligned} \mathbf{g} &= \mathbf{P}^{A_1} \cdot \mathbf{g} \cdot \mathbf{P}^{A_1} + \mathbf{P}^{A_2} \cdot \mathbf{g} \cdot \mathbf{P}^{A_2} + \mathbf{P}_{x,x}^E \cdot \mathbf{g} \cdot \mathbf{P}_{x,x}^E + \mathbf{P}_{x,x}^E \cdot \mathbf{g} \cdot \mathbf{P}_{y,y}^E \\ &\quad + \mathbf{P}_{y,y}^E \cdot \mathbf{g} \cdot \mathbf{P}_{x,x}^E + \mathbf{P}_{y,y}^E \cdot \mathbf{g} \cdot \mathbf{P}_{y,y}^E \end{aligned} \tag{81}$$

This reduces to a non-Abelian spectral resolution of D_3 that generalizes resolution Equation (52) of Abelian C_6 and includes two nilpotent projectors $\mathbf{P}_{j,k}^\alpha$ multiplied by off-diagonal irrep matrix components $D_{j,k}^\alpha$ as well as the four idempotents $\mathbf{P}_{j,j}^\alpha$ with their diagonal irrep matrix coefficients $D_{j,j}^\alpha$ that are not altogether unlike the $D^{(m)}(\mathbf{r}^p) \mathbf{P}^{(m)}$ terms in Equation (52). (Now X has matrix indices $(X_{j,k})$.)

$$\mathbf{g} = \sum_{\text{irreps } (\alpha)} \sum_{j=1}^{\ell^\alpha} \sum_{k=1}^{\ell^\alpha} D_{j,k}^\alpha(\mathbf{g}) \mathbf{P}_{j,k}^\alpha \tag{82a}$$

$$\begin{aligned}
 \mathbf{g} = & D^{A_1}(g)\mathbf{P}^{A_1} + D^{A_2}(g)\mathbf{P}^{A_2} + D_{x,x}^E(g)\mathbf{P}_{x,x}^E + D_{x,y}^E(g)\mathbf{P}_{x,y}^E \\
 & + D_{y,x}^E(g)\mathbf{P}_{y,x}^E + D_{y,y}^E(g)\mathbf{P}_{y,y}^E
 \end{aligned}
 \tag{82b}$$

$$\text{where } : \mathbf{P}_{jj}^\alpha \cdot \mathbf{g} \cdot \mathbf{P}_{jj}^\alpha = D_{jj}^\alpha(\mathbf{g})\mathbf{P}_{jj}^\alpha \quad \mathbf{P}_{jj}^\alpha \cdot \mathbf{g} \cdot \mathbf{P}_{kk}^\alpha = D_{jk}^\alpha(\mathbf{g})\mathbf{P}_{jk}^\alpha$$

Terms $(1/n)D^{(m)*}(\mathbf{r}^p)\mathbf{r}^p$ in Equation (59) of $\mathbf{P}^{(m)}$ of C_n in Equation (52) generalize here to $\mathbf{P}_{j,k}^\alpha$ and invert Equation (82a) to Equation (83).

$$\mathbf{P}_{j,k}^\alpha = (\ell^\alpha / {}^oG) \sum_{g=1}^{{}^oG} D_{j,k}^{\alpha*}(g) \mathbf{g}
 \tag{83}$$

D_3 resolution in Equation (82b) has two irreps D^{A_1} and D^{A_2} of dimension $\ell^{A_1}=1=\ell^{A_2}$ and a third irrep D^E of dimension $\ell^E=2$ as noted in the first column of the character array in Equation (77). The irrep dimensions are related to the centrum $\kappa(D_3)=3$, rank $\rho(D_3)=4$, and order ${}^oD_3=6$. The following power sums of ℓ^α apply to any finite group G .

$$\begin{aligned}
 G - \text{centrum} : \quad \kappa(G) &= \sum_{\text{irrep}(\alpha)} (\ell^\alpha)^0 = \text{Number of classes, invariants, or irrep types} \\
 G - \text{rank} : \quad \rho(G) &= \sum_{\text{irrep}(\alpha)} (\ell^\alpha)^1 = \text{Number of mutually commuting observables} \\
 G - \text{order} : \quad {}^o(G) &= \sum_{\text{irrep}(\alpha)} (\ell^\alpha)^2 = \text{Number of symmetry operators}
 \end{aligned}
 \tag{84}$$

6.3. Spectral Resolution of Dual Groups D_3 and \bar{D}_3

Spectral resolution shown in Equations (82a) and (83) of non-Abelian group G reduce $\mathbf{g}\cdot\mathbf{h}$ -product tables in Equation (68) to P -projector algebra.

$$\mathbf{P}_{jk}^\alpha \mathbf{P}_{j'k'}^\beta = \delta^{\alpha\beta} \delta_{kj'} \mathbf{P}_{jk'}^\alpha
 \tag{85}$$

Product tables in Equation (86) for D_3 projectors \mathbf{P}_{jk}^α generalize the C_6 idempotent table in Equation (54). Non-commutativity entails a pair of tables like the $\mathbf{g}^\dagger\mathbf{g}$ form and $\mathbf{g}\mathbf{g}^\dagger$ -forms in Equation (68) for “lab” \mathbf{g} and “body” $\bar{\mathbf{g}}$ operators. Tables in Equation (68) differ by switching conjugate pair \mathbf{r}^1 and \mathbf{r}^2 on side and top. ($\mathbf{r}^{1\dagger} = \mathbf{r}^2$) The rest are self conjugate. ($\mathbf{i}_1^\dagger = \mathbf{i}_1$, etc.) Similarly, tables in Equation (86) differ by switching conjugate nilpotent pair \mathbf{P}_{xy}^E and \mathbf{P}_{yx}^E . ($\mathbf{P}_{xy}^{E\dagger} = \mathbf{P}_{yx}^E$) The rest are self-conjugate. ($\mathbf{P}_{jj}^{\alpha\dagger} = \mathbf{P}_{jj}^\alpha$)

$\mathbf{p}^\dagger \mathbf{p}$ <i>form</i>	$\mathbf{P}_{xx}^{A_1}$	$\mathbf{P}_{yy}^{A_2}$	$\mathbf{P}_{xx}^{E_1}$	$\mathbf{P}_{xy}^{E_1}$	$\mathbf{P}_{yx}^{E_1}$	$\mathbf{P}_{yy}^{E_1}$
$\mathbf{P}_{xx}^{A_1}$	$\mathbf{P}_{xx}^{A_1}$
$\mathbf{P}_{yy}^{A_2}$.	$\mathbf{P}_{yy}^{A_2}$
$\mathbf{P}_{xx}^{E_1}$.	.	$\mathbf{P}_{xx}^{E_1}$	$\mathbf{P}_{xy}^{E_1}$.	.
$\mathbf{P}_{yx}^{E_1}$.	.	$\mathbf{P}_{yx}^{E_1}$	$\mathbf{P}_{yy}^{E_1}$.	.
$\mathbf{P}_{xy}^{E_1}$	$\mathbf{P}_{xx}^{E_1}$	$\mathbf{P}_{xy}^{E_1}$
$\mathbf{P}_{yy}^{E_1}$	$\mathbf{P}_{yx}^{E_1}$	$\mathbf{P}_{yy}^{E_1}$

\mathbf{pp}^\dagger <i>form</i>	$\mathbf{P}_{xx}^{A_1}$	$\mathbf{P}_{yy}^{A_2}$	$\mathbf{P}_{xx}^{E_1}$	$\mathbf{P}_{yx}^{E_1}$	$\mathbf{P}_{xy}^{E_1}$	$\mathbf{P}_{yy}^{E_1}$
$\mathbf{P}_{xx}^{A_1}$	$\mathbf{P}_{xx}^{A_1}$
$\mathbf{P}_{yy}^{A_2}$.	$\mathbf{P}_{yy}^{A_2}$
$\mathbf{P}_{xx}^{E_1}$.	.	$\mathbf{P}_{xx}^{E_1}$.	$\mathbf{P}_{xy}^{E_1}$.
$\mathbf{P}_{xy}^{E_1}$.	.	.	$\mathbf{P}_{xx}^{E_1}$.	$\mathbf{P}_{xy}^{E_1}$
$\mathbf{P}_{yx}^{E_1}$.	.	$\mathbf{P}_{yx}^{E_1}$.	$\mathbf{P}_{yy}^{E_1}$.
$\mathbf{P}_{yy}^{E_1}$.	.	.	$\mathbf{P}_{yx}^{E_1}$.	$\mathbf{P}_{yy}^{E_1}$

(86)

The $\mathbf{p}^\dagger \mathbf{p}$ and \mathbf{pp}^\dagger tables in Equation (86) give commuting representations of projector \mathbf{P}_{jk}^α just as $\mathbf{g}^\dagger \mathbf{g}$ and $\mathbf{g}\mathbf{g}^\dagger$ tables in Equation (68) give commuting $(\mathbf{g})_G$ -matrices in Equation (69a). Wherever \mathbf{P}_{jk}^α appears in a table, a “1” is put in its (\mathbf{p}) -matrix. Putting “ $D_{jk}^\alpha(g)$ ” at each \mathbf{P}_{jk}^α spot instead gives the following $\mathbf{p}^\dagger \mathbf{p}$ -representation $(\mathbf{g})_P$ of \mathbf{g} since it is a sum of $D_{jk}^\alpha(g)\mathbf{P}_{jk}^\alpha$ in Equation (82a).

$$(\mathbf{g})_P = T(\mathbf{g})_G T^\dagger = \begin{pmatrix} |\mathbf{P}_{xx}^{A_1}\rangle & |\mathbf{P}_{yy}^{A_2}\rangle & |\mathbf{P}_{xx}^{E_1}\rangle & |\mathbf{P}_{yx}^{E_1}\rangle & |\mathbf{P}_{xy}^{E_1}\rangle & |\mathbf{P}_{yy}^{E_1}\rangle \\ D^{A_1}(g) & . & . & . & . & . \\ . & D^{A_2}(g) & . & . & . & . \\ . & . & D_{xx}^{E_1}(g) & D_{xy}^{E_1}(g) & . & . \\ . & . & D_{yx}^{E_1}(g) & D_{yy}^{E_1}(g) & . & . \\ . & . & . & . & D_{xx}^{E_1}(g) & D_{xy}^{E_1}(g) \\ . & . & . & . & D_{yx}^{E_1}(g) & D_{yy}^{E_1}(g) \end{pmatrix} \tag{87}$$

Conjugate \mathbf{pp}^\dagger -representation $(\bar{\mathbf{g}})_P$ of $\bar{\mathbf{g}}$ has complex conjugate “ $D_{jk}^{\alpha*}(g)$ ” put at each \mathbf{P}_{jk}^α spot. The matrices in Equations (87) and (88) are transformations $(\mathbf{g})_P = T(\mathbf{g})_G T^\dagger$ and $(\bar{\mathbf{g}})_P = T(\bar{\mathbf{g}})_G T^\dagger$ of the respective matrices in Equations (69a) and (69b) by transformation T composed of $D_{jk}^\alpha(g)$ components. The C_6 analogy is Fourier transform Equation (51) from Equation (48) to Equation (54).

$$(\bar{\mathbf{g}})_P = T (\bar{\mathbf{g}})_G T^\dagger = \begin{pmatrix} |P_{xx}^{A_1}\rangle & |P_{yy}^{A_2}\rangle & |P_{xx}^{E_1}\rangle & |P_{yx}^{E_1}\rangle & |P_{xy}^{E_1}\rangle & |P_{yy}^{E_1}\rangle \\ \hline D^{A_1^*}(g) & \cdot & \cdot & \cdot & \cdot & \cdot \\ \cdot & D^{A_2^*}(g) & \cdot & \cdot & \cdot & \cdot \\ \hline \cdot & \cdot & D_{xx}^{E_1^*}(g) & \cdot & D_{xy}^{E_1^*}(g) & \cdot \\ \cdot & \cdot & \cdot & D_{xx}^{E_1^*}(g) & \cdot & D_{xy}^{E_1^*}(g) \\ \hline \cdot & \cdot & D_{yx}^{E_1^*}(g) & \cdot & D_{yy}^{E_1^*}(g) & \cdot \\ \cdot & \cdot & \cdot & D_{yx}^{E_1^*}(g) & \cdot & D_{yy}^{E_1^*}(g) \end{pmatrix} \tag{88}$$

Matrices ... $(\bar{\mathbf{r}}^2)_P, (\bar{\mathbf{i}}_1)_P, \dots$ defined by Equation (88) commute with every ... $(\mathbf{r}^2)_P, (\mathbf{i}_1)_P, \dots$ defined by Equation (87) while each represents identical *non-commutative* D_3 product tables in Equation (68). Both use real $[x, y]$ -based \mathbf{i}_3 -diagonal irreps $D_{jk}^\alpha(g)$ given below.

$\mathbf{g} =$	$\mathbf{1}$	\mathbf{r}	\mathbf{r}^2	\mathbf{i}_1	\mathbf{i}_2	\mathbf{i}_3
$D^{A_1}(\mathbf{g}) =$	1	1	1	1	1	1
$D^{A_2}(\mathbf{g}) =$	1	1	1	-1	-1	-1
$D_{xy}^{E_1^*}(\mathbf{g}) =$	$\begin{pmatrix} 1 & \cdot \\ \cdot & 1 \end{pmatrix}$	$\begin{pmatrix} -\frac{1}{2} & -\frac{\sqrt{3}}{2} \\ \frac{\sqrt{3}}{2} & -\frac{1}{2} \end{pmatrix}$	$\begin{pmatrix} -\frac{1}{2} & \frac{\sqrt{3}}{2} \\ -\frac{\sqrt{3}}{2} & -\frac{1}{2} \end{pmatrix}$	$\begin{pmatrix} -\frac{1}{2} & -\frac{\sqrt{3}}{2} \\ -\frac{\sqrt{3}}{2} & \frac{1}{2} \end{pmatrix}$	$\begin{pmatrix} -\frac{1}{2} & \frac{\sqrt{3}}{2} \\ \frac{\sqrt{3}}{2} & \frac{1}{2} \end{pmatrix}$	$\begin{pmatrix} 1 & \cdot \\ \cdot & -1 \end{pmatrix}$

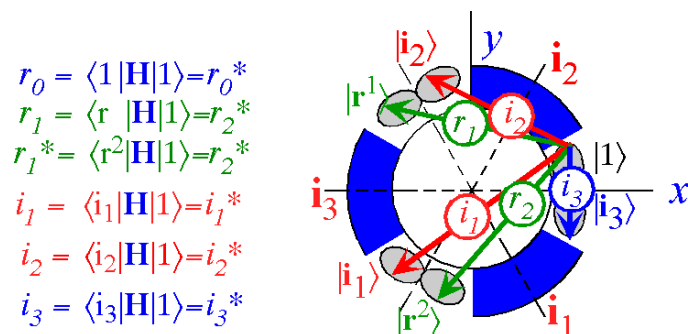
(89)

Appendix-A describes elementary derivation and visualization of $D_{jk}^\alpha(g)$ and their projectors $\mathbf{P}_{jk}^\alpha(g)$.

6.4. Spectral Resolution of D_3 Hamiltonian

Hamiltonian \mathbf{H} -matrix in Equation (71) has six parameters $[r_0, r_1, r_2, i_1, i_2, i_3]$ or coefficients of its expansion Equation (70) in terms of intrinsic \bar{D}_3 operators $[\mathbf{1} = \bar{\mathbf{r}}^0, \bar{\mathbf{r}}^1, \bar{\mathbf{r}}^2, \bar{\mathbf{i}}_1, \bar{\mathbf{i}}_2, \bar{\mathbf{i}}_3]$. The parameters are indicated in Figure 17 by tunneling paths between the first D_3 base state $|1\rangle$ and other D_3 -defined base states $|\mathbf{g}\rangle = \mathbf{g}|1\rangle$ representing potential minima.

Figure 17. D_3 -operator defined states and tunneling paths.



The resolution of \mathbf{H} -matrix then follows that of $\bar{\mathbf{g}}$ and $(\bar{\mathbf{g}})_P$ -matrices. Any reduction of all $(\bar{\mathbf{g}})_P$ -matrices, such as the $[x, y]$ -reduction in Equation (88), also reduces the $(\mathbf{H})_P$ -matrix accordingly. Row-1 of (\mathbf{H}_P) in Equation (71) has all six parameters.

$$H_{ab}^\alpha = \sum_{g=1}^{\circ G} \langle \mathbf{1} | \mathbf{H} | \mathbf{g} \rangle D_{ab}^{\alpha*}(g) = \sum_{g=1}^{\circ G} r_g D_{ab}^{\alpha*}(g) \tag{90}$$

If the P -nilpotent pair are switched to $\dots \mathbf{P}_{xy}^E, \mathbf{P}_{yx}^E \dots$, then $(\mathbf{H})_P$ and all $(\bar{\mathbf{g}})_P$ (instead of all $(\mathbf{g})_P$ as in Equation (87)) are diagonal with eigenvalues H^{A_1} and H^{A_2} or block-diagonal with a pair of identical 2×2 H^E -blocks.

$$(\mathbf{H})_P = \bar{T} (\mathbf{H})_G \bar{T}^\dagger = \begin{pmatrix} | \mathbf{P}_{xx}^{A_1} \rangle & | \mathbf{P}_{yy}^{A_2} \rangle & | \mathbf{P}_{xx}^{E_1} \rangle & | \mathbf{P}_{xy}^{E_1} \rangle & | \mathbf{P}_{yx}^{E_1} \rangle & | \mathbf{P}_{yy}^{E_1} \rangle \\ \hline H^{A_1} & \cdot & \cdot & \cdot & \cdot & \cdot \\ \cdot & H^{A_2} & \cdot & \cdot & \cdot & \cdot \\ \cdot & \cdot & H_{xx}^E & H_{xy}^E & \cdot & \cdot \\ \cdot & \cdot & H_{yx}^E & H_{yy}^E & \cdot & \cdot \\ \hline \cdot & \cdot & \cdot & \cdot & H_{xx}^E & H_{xy}^E \\ \cdot & \cdot & \cdot & \cdot & H_{yx}^E & H_{yy}^E \end{pmatrix} \tag{91}$$

The H -block matrix components follow by combining Equation (89) with Equation (90).

$$\begin{aligned} H^{A_1} &= r_0 D^{A_1*}(1) + r_1 D^{A_1*}(r^1) + r_1^* D^{A_1*}(r^2) + i_1 D^{A_1*}(i_1) + i_2 D^{A_1*}(i_2) \\ &\quad + i_3 D^{A_1*}(i_3) = r_0 + r_1 + r_1^* + i_1 + i_2 + i_3 \\ H^{A_2} &= r_0 D^{A_2*}(1) + r_1 D^{A_2*}(r^1) + r_1^* D^{A_2*}(r^2) + i_1 D^{A_2*}(i_1) + i_2 D^{A_2*}(i_2) \\ &\quad + i_3 D^{A_2*}(i_3) = r_0 + r_1 + r_1^* - i_1 - i_2 - i_3 \\ H_{xx}^E &= r_0 D_{xx}^{E*}(1) + r_1 D_{xx}^{E*}(r^1) + r_1^* D_{xx}^{E*}(r^2) + i_1 D_{xx}^{E*}(i_1) + i_2 D_{xx}^{E*}(i_2) + i_3 D_{xx}^{E*}(i_3) \\ &= (2r_0 - r_1 - r_1^* - i_1 - i_2 + 2i_3) / 2 \\ H_{xy}^E &= r_0 D_{xy}^{E*}(1) + r_1 D_{xy}^{E*}(r^1) + r_1^* D_{xy}^{E*}(r^2) + i_1 D_{xy}^{E*}(i_1) + i_2 D_{xy}^{E*}(i_2) + i_3 D_{xy}^{E*}(i_3) \\ &= \sqrt{3}(-r_1 + r_1^* - i_1 + i_2) / 2 = H_{yx}^{E*} \\ H_{yy}^E &= r_0 D_{yy}^{E*}(1) + r_1 D_{yy}^{E*}(r^1) + r_1^* D_{yy}^{E*}(r^2) + i_1 D_{yy}^{E*}(i_1) + i_2 D_{yy}^{E*}(i_2) + i_3 D_{yy}^{E*}(i_3) \\ &= (2r_0 - r_1 - r_1^* + i_1 + i_2 - 2i_3) / 2 \end{aligned} \tag{92}$$

Irrep-dimension $\ell^E = 2$ implies (at least) 2-fold degenerate E -level since eigenvalues of identical H^E -blocks must also be identical, but only certain parameter values give diagonal H^E -blocks in Equation (92), i.e., real $r_1 = r_1^*$ and equal $i_1 = i_2$.

$$\begin{aligned} \begin{pmatrix} H_{xx}^E & H_{xy}^E \\ H_{yx}^E & H_{yy}^E \end{pmatrix} &= \frac{1}{2} \begin{pmatrix} 2r_0 - r_1 - r_1^* - i_1 - i_2 + 2i_3 & \sqrt{3}(-r_1 + r_1^* - i_1 + i_2) \\ \sqrt{3}(-r_1^* + r_1 - i_1 + i_2) & 2r_0 - r_1 - r_1^* + i_1 + i_2 - 2i_3 \end{pmatrix} \\ &= \begin{pmatrix} r_0 - r_1 - i_{12} + i_3 & 0 \\ 0 & r_0 - r_1 + i_{12} - i_3 \end{pmatrix} \end{aligned} \tag{93}$$

For: $r_1 = r_1^*$ and: $i_1 = i_2 = i_{12}$

These are the values that respect the local $D_3 \supset C_2[\mathbf{1}, \mathbf{i}_3]$ subgroup chain symmetry that gave (x, y) -plane polarized splitting in Equation (78). This is broken by a complex r_1 or by unequal i_1 and i_2 . Complex

$r_1 = |r|e^{i\phi}$ gives rise to complex rotating-wave eigenstates similar to ones in Figure 15 but, unlike that ZB1 model, cannot split E -degeneracy. Unequal i_1 and i_2 shift standing-wave nodes but cannot split E -doublets either. E -levels may split if \mathbf{H} contains *external* or *lab*-based operators \mathbf{g} in addition to its *internal* or *body*-based $\bar{\mathbf{g}}$, but it thereby loses its D_3 symmetry.

6.5. Global-Lab-Relative G versus Local-Body-Relative \bar{G} Base State Definition

Non-Abelian symmetry analysis in general, and the present example of D_3 resolution in particular, involves a dual-group relativity between an *extrinsic* or *global* “lab-based” group $G=D_3$ on one hand, and an *intrinsic* or *local* “body-based” group $\bar{G}=\bar{D}_3$ on the other hand. Each $\bar{\mathbf{g}}$ in \bar{G} commutes with each \mathbf{g} in G .

In the present example, the *global* “lab-based” group $G=D_3=[\mathbf{1}, \mathbf{r}^1, \mathbf{r}^2, \mathbf{i}_1, \mathbf{i}_2, \mathbf{i}_3]$ labels equivalent locations in a potential or lab-based field and is a reference frame for an excitation wave or “body” occupying lab locations.

On the other hand, the *local* “bod-based” group $\bar{G}=\bar{D}_3=[\mathbf{1}, \bar{\mathbf{r}}^1, \bar{\mathbf{r}}^2, \bar{\mathbf{i}}_1, \bar{\mathbf{i}}_2, \bar{\mathbf{i}}_3]$ regards the excitation wave as a reference frame to define relative location of the potential or laboratory field.

Quantum waves provide the most precise space-time reference frames that are possible in any situation due to the ultra-sensitive nature of wave interferometry. This is the case for optical coherent waves or electronic and nuclear matter waves. The latter derive their space-time symmetry properties from the former, and these are deep classical and quantum mechanical rules of engagement for currently accepted Hamiltonian quantum theory.

Interference of two waves depends only on *relative* position as reflected in the following equivalent definitions of base kets for waves in a D_3 potential of Figure 16 with six localized wave bases $[|\mathbf{1}\rangle, |\mathbf{r}^1\rangle, |\mathbf{r}^2\rangle, |\mathbf{i}_1\rangle, |\mathbf{i}_2\rangle, |\mathbf{i}_3\rangle]$ in Figure 17. (We call this the “Mock-Mach Principle” of wave relativity.)

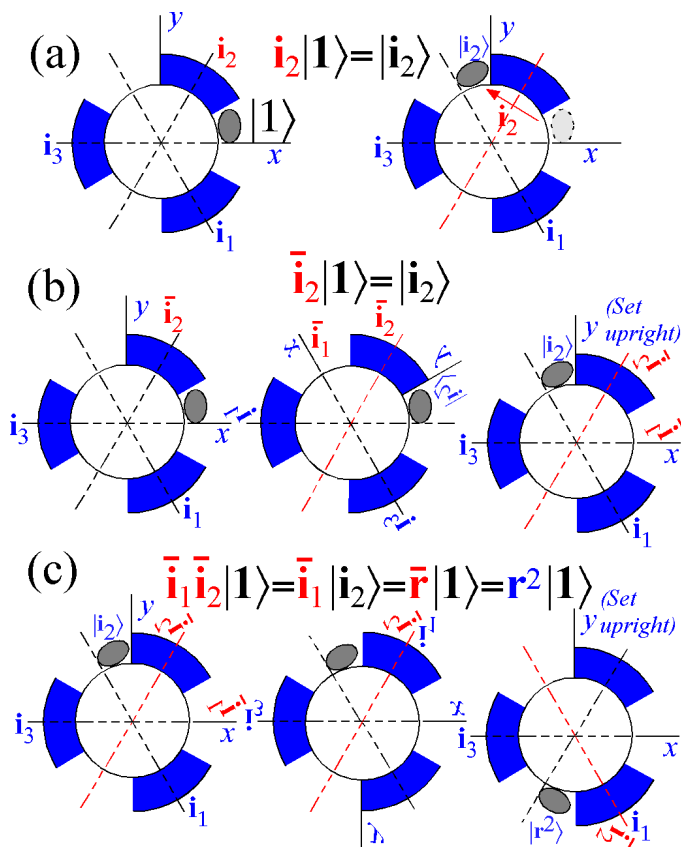
$$|\mathbf{g}_k\rangle = \mathbf{g}_k|\mathbf{1}\rangle = \bar{\mathbf{g}}_k^{-1}|\mathbf{1}\rangle \tag{94}$$

Key to this definition is the independence and *mutual commutation* of dual sets Equation (69a) and (69b).

$$\mathbf{g}_j\bar{\mathbf{g}}_k = \bar{\mathbf{g}}_k\mathbf{g}_j \tag{95}$$

Neither relation makes sense if we were to equate \mathbf{g}_k with $\bar{\mathbf{g}}_k^{-1}$. The effect of \mathbf{g}_k is equal to that of $\bar{\mathbf{g}}_k^{-1}$ *only* when acting on the origin-state $|\mathbf{1}\rangle$. The action of global \mathbf{i}_2 in Figure 18a is compared with local $\bar{\mathbf{i}}_2$ in Figure 18b that gives the same *relative* position of wave and wells. In Figure 18c product $\bar{\mathbf{i}}_1\bar{\mathbf{i}}_2=\bar{\mathbf{r}}$ has the same action as $\mathbf{i}_2\mathbf{i}_1=\mathbf{r}^{-1}=\mathbf{r}^2$ on $|\mathbf{1}\rangle$.

Figure 18. D_3 -operators compared (a) Global \mathbf{i}_2 ; (b) Local $\bar{\mathbf{i}}_2$; (c) $\bar{\mathbf{i}}_2$ followed by $\bar{\mathbf{i}}_1$.



Different points of view show how “body” $\bar{\mathbf{g}}$ operations relate to the “lab” \mathbf{g} . Starting from state $|1\rangle$, $\bar{\mathbf{r}}^1 = \bar{\mathbf{r}}$ rotates lab potential clockwise (-120°) in a view where the body “stays put”. The body wave ends up in the same well as it would if, instead, the body rotates counter-clockwise ($+120^\circ$) by $\mathbf{r} = \mathbf{r}^1$ in a lab frame that “stays put.”

In a lab view, effects of body operation $\bar{\mathbf{g}}_k$ and lab operation \mathbf{g}_k^{-1} on $|1\rangle$ are the same except that $\bar{\mathbf{g}}_k^{-1}$ also moves each body operation $\bar{\mathbf{g}}_j$ in the same way to $\bar{\mathbf{g}}_k \bar{\mathbf{g}}_j \bar{\mathbf{g}}_k^{-1}$. The lab view of a lab operation \mathbf{g}_k does not see any of lab \mathbf{g}_j axes change location. The following generalization of lab-body relativity relation Equation (94) using Equation (95) shows how $\bar{\mathbf{g}}_j$ affects arbitrary $|\mathbf{g}_k\rangle$.

$$\begin{aligned} \bar{\mathbf{g}}_j^{-1}|\mathbf{g}_k\rangle &= \bar{\mathbf{g}}_j^{-1}\mathbf{g}_k|1\rangle = \mathbf{g}_k\bar{\mathbf{g}}_j^{-1}|1\rangle \\ &= \mathbf{g}_k\bar{\mathbf{g}}_j|1\rangle = \mathbf{g}_k\bar{\mathbf{g}}_j\mathbf{g}_k^{-1}\mathbf{g}_k|1\rangle = \mathbf{g}_k\bar{\mathbf{g}}_j\mathbf{g}_k^{-1}|\mathbf{g}_k\rangle \end{aligned} \tag{96}$$

6.6. Global versus Local Eigenstate Symmetry

Applying projector \mathbf{P}_{jk}^α in Equation (83) to origin ket $|1\rangle$ gives a local-global symmetry-defined ket $|\mathbf{j}_k^\alpha\rangle$.

$$|\mathbf{j}_k^\alpha\rangle = \mathbf{P}_{jk}^\alpha|1\rangle\sqrt{oG/\ell^\alpha} = \sqrt{\ell^\alpha/oG} \sum_{g=1}^{oG} D_{j,k}^{\alpha*}(g)|\mathbf{g}\rangle \tag{97}$$

The norm-factor $N = {}^oG/\ell^\alpha$ is a non-Abelian generalization of the integral norm N for Abelian C_N eigenket projection in Equation (61). Interestingly, the non-Abelian norm is also an integer since irrep dimension ℓ^α is always a factor of its group's order oG .

A non-Abelian projection ket in Equation (97) has two independent symmetry labels j and k belonging to global-lab symmetry operators \mathbf{g} and local-body operators $\bar{\mathbf{g}}$, respectively. Application of \mathbf{g} -resolution Equation (82a) to ket Equation (97) is reduced by \mathbf{P} -product rules in Equation (85) to the following global transformation.

$$\begin{aligned} \mathbf{g} \left|_{jk}^\alpha \right\rangle &= \mathbf{g} \mathbf{P}_{jk}^\alpha |1\rangle \sqrt{N} \\ &= \sum_{j'=1}^{\ell^\alpha} \sum_{k'=1}^{\ell^\alpha} D_{j'k'}^\mu(g) \mathbf{P}_{j'k'}^\alpha \mathbf{P}_{jk}^\alpha |1\rangle \sqrt{N} = \sum_{j'=1}^{\ell^\alpha} D_{j'j}^\alpha(g) \mathbf{P}_{j'k}^\alpha |1\rangle \sqrt{N} \\ &= \sum_{j'=1}^{\ell^\alpha} D_{j'j}^\alpha(g) \left|_{j'k}^\alpha \right\rangle \end{aligned} \tag{98}$$

The corresponding local operator $\bar{\mathbf{g}}$ first commutes through \mathbf{P}_{jk}^α according to Equation (95) and is converted by Equation (94) to inverse global \mathbf{g}^{-1} on the right of \mathbf{P}_{jk}^α using Equation (82a) again. Finally, unitary irreps $D^\alpha(g^{-1}) = D^{\alpha\dagger}(g)$ are assumed.

$$\begin{aligned} \bar{\mathbf{g}} \left|_{jk}^\alpha \right\rangle &= \bar{\mathbf{g}} \mathbf{P}_{jk}^\alpha |1\rangle \sqrt{N} = \mathbf{P}_{jk}^\alpha \bar{\mathbf{g}} |1\rangle \sqrt{N} = \mathbf{P}_{jk}^\alpha \mathbf{g}^{-1} |1\rangle \sqrt{N} \\ &= \sum_{j'=1}^{\ell^\alpha} \sum_{k'=1}^{\ell^\alpha} D_{j'k'}^\mu(g^{-1}) \mathbf{P}_{jk}^\alpha \mathbf{P}_{j'k'}^\alpha |1\rangle \sqrt{N} = \sum_{j'=1}^{\ell^\alpha} D_{k'k}^\alpha(g^{-1}) \mathbf{P}_{j'k'}^\alpha |1\rangle \sqrt{N} \\ &= \sum_{j'=1}^{\ell^\alpha} D_{k'k}^\alpha(g^{-1}) \left|_{j'k'}^\alpha \right\rangle = \sum_{j'=1}^{\ell^\alpha} D_{k'k}^{\alpha*}(g) \left|_{j'k'}^\alpha \right\rangle \end{aligned} \tag{99}$$

A summary of the results is consistent with the block matrix forms in Equations (87) and (88).

$$\left\langle_{j'k}^\alpha \left| \mathbf{g} \left|_{jk}^\alpha \right\rangle \right. = D_{j'j}^\alpha(g), \quad \left\langle_{j'k'}^\alpha \left| \bar{\mathbf{g}} \left|_{jk}^\alpha \right\rangle \right. = D_{k'k}^{\alpha*}(g) \tag{100}$$

Choice of subgroup $C_2 = [1, \mathbf{i}_3]$ in Equation (78) leads to (x, y) -polarized states $(m)_2$ labeled by their \mathbf{i}_3 eigenvalues $(-1)^m$.

$$\begin{aligned} \left\langle_{j'k}^\alpha \left| \mathbf{i}_3 \left|_{jk}^\alpha \right\rangle \right. &= D_{j'j}^\alpha(i_3), & \left\langle_{j'k'}^\alpha \left| \bar{\mathbf{i}}_3 \left|_{jk}^\alpha \right\rangle \right. &= D_{k'k}^{\alpha*}(i_3). \\ = \delta_{j'j} \begin{cases} +1 \text{ for } :j=x \\ -1 \text{ for } :j=y \end{cases}, & = \delta_{k'k} \begin{cases} +1 \text{ for } :k=x \\ -1 \text{ for } :k=y \end{cases} \end{aligned} \tag{101}$$

Physical significance of these global- (j) and local- (k) values are now discussed using Figure 19.

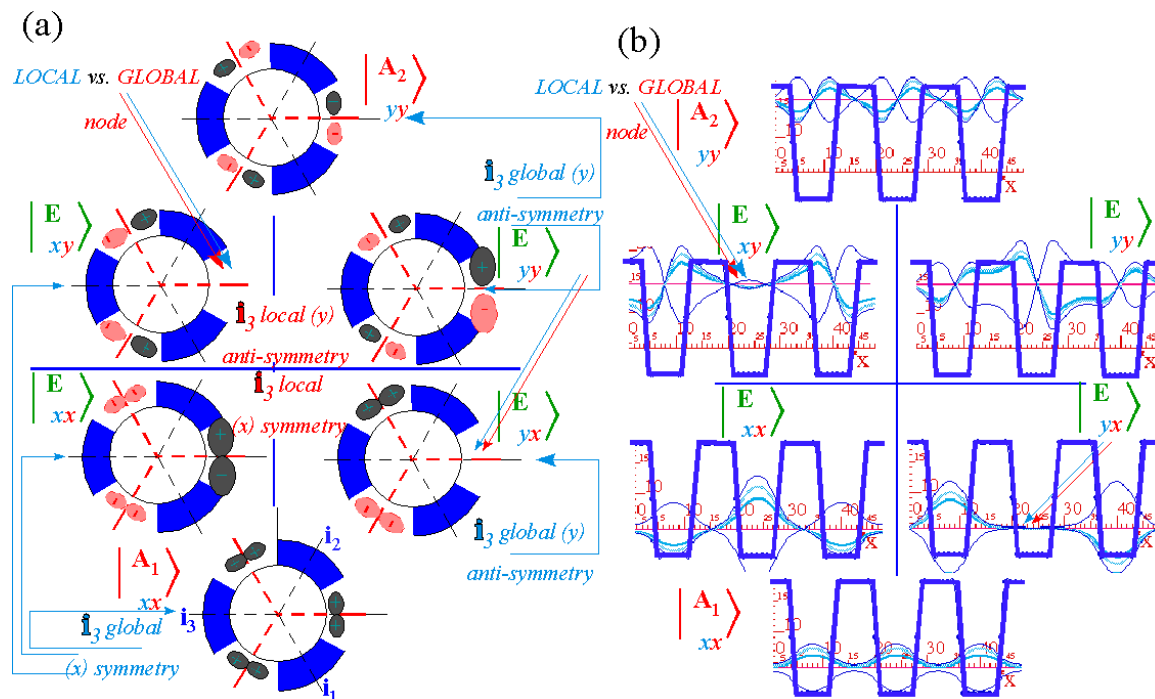
Wherever the global j is x or \mathbf{i}_3 -symmetric (0_2) , then the entire wave is symmetric to x -axial rotation by π in Figure 19a or horizontal reflection through the middle square-well in Figure 19b. Similarly, wherever the global j is y or \mathbf{i}_3 -antisymmetric (1_2) , that is seen for each overall figure, too.

However, if the local k is x or \mathbf{i}_3 -symmetric (0_2) , the local wave in each well has no node and is symmetric to its local axis of rotation by π in Figure 19a or horizontal reflection of each square-well in Figure 19b. Similarly, wherever the local k is y or \mathbf{i}_3 -antisymmetric (1_2) , that antisymmetry and one node is seen in each well, too.

Local and global symmetry clash along the \mathbf{i}_3 -axis for states projected by nilpotent \mathbf{P}_{xy}^α or \mathbf{P}_{yx}^α . The result is the x -axial wave nodes indicated by pairs of arrows in Figure 19. The $|E_{yx}\rangle$ wave in the lower

right of Figure 19b appears quite suppressed on the i_3 -axis. However, the simulation of the $|E_{xy}\rangle$ in the upper left seems to have its “node” coming unglued.

Figure 19. D_3 -symmetry waves (a) Sketch of projection; (b) 3-Well wave simulation (Compare with Figure 20).



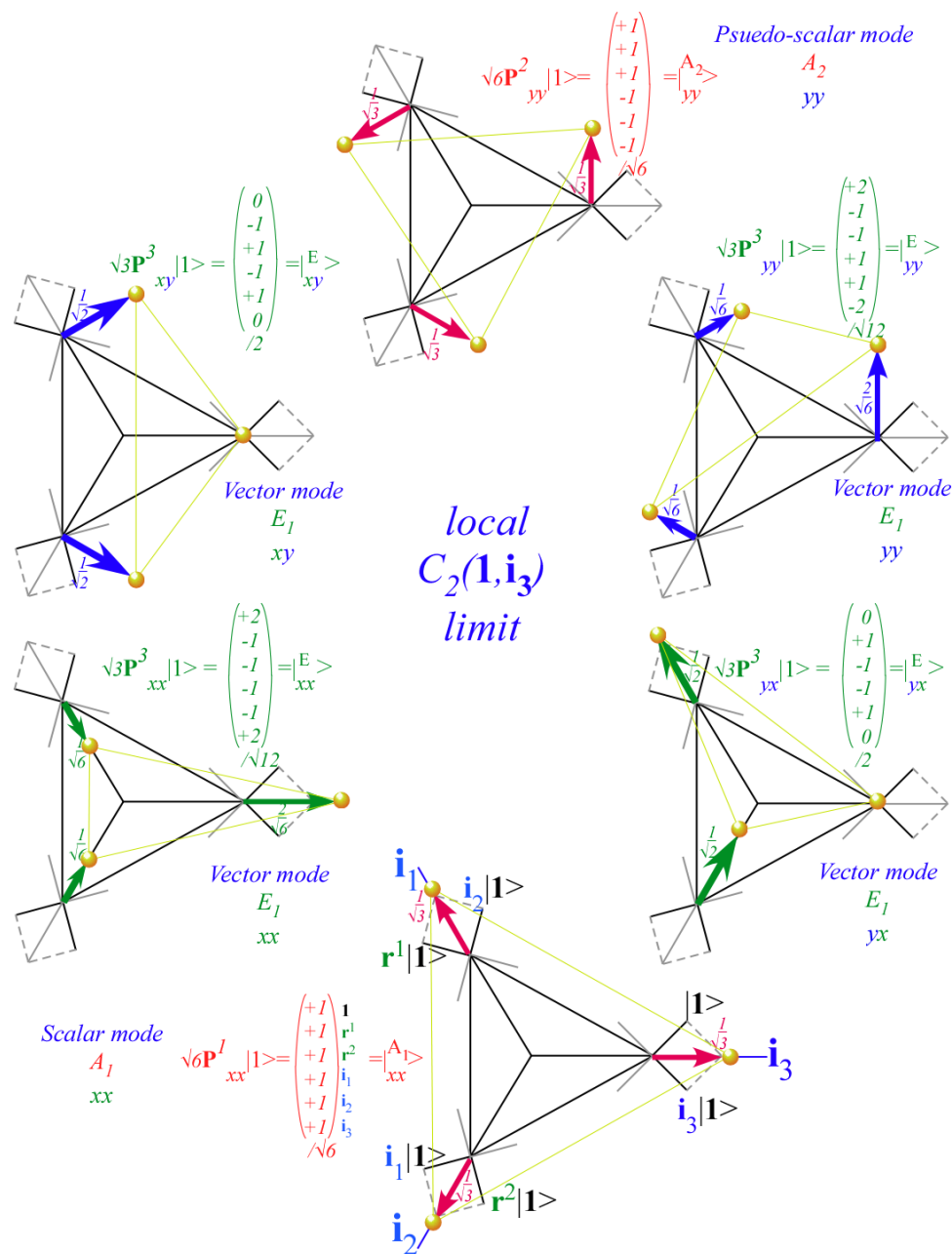
The “unglued” level ω_{xy}^E is higher than ω_{yx}^E and enjoys more tunneling. If tunneling increases so do parameters such as r_1 and r_2 in Equation (92) that do not respect x -axial local subgroup $C_2 = [1, i_3]$. This breaks x -axial nodes and i_3 local symmetry causing E -modes to be less C_2 -local and more like current-carrying above-barrier C_3 -local waves rotating on r -paths. D_3 correlation arrays in Equation (102) with C_2 or C_3 indicate level cluster structure for extremes of each case.

$D_3 \supset C_2$	0_2	1_2		$D_3 \supset C_3$	0_3	1_3	2_3		
A_1	1	.		A_1	1	.	.		(102)
A_2	.	1		A_2	1	.	.		
E	1	1		E	.	1	1		

Column 0_2 of array $D_3 \supset C_2$ in Equation (102) correlates to A_1 and E . The lower (A_1, E)-level cluster in Figure 19 has 0_2 local symmetry and lies below cluster- (A_2, E) that has local 1_2 symmetry according to the 1_2 column of Equation (102). Column 0_3 of table $D_3 \supset C_3$ indicates that A_1 and A_2 levels cluster under extreme C_3 localization, but columns 1_3 and 2_3 indicate that each E doublet level is unclustered under C_3 with no extra degeneracy beyond its own ($\ell^E = 2$).

A classical analog of quantum waves states in Figure 19 is displayed in Figure 20 in the form of vibrational modes for an X_3 molecule. A detailed description of this analogy in Appendix A includes modes of various local symmetry combinations analogous to those introduced above and in Sections 6.7.1 and 6.7.2 below.

Figure 20. $D_3 \supset C_2(i_3)$ -local symmetry modes of X_3 molecule (Compare with Figure 19).



6.7. Symmetry Correlation and Frobenius Reciprocity

The mathematical basis of correlation arrays in Equation (102) is a Frobenius reciprocity relation that exists between irreps of a group and its subgroups. This may be clarified by appealing to the physics of P_{jk}^α -projected states $|j_k^\alpha\rangle$ such as are displayed in Figure 19 and by exploiting the duality between their local and global symmetry and subgroups.

D_3 -symmetric Hamiltonian H in (71) is made only of local \bar{g} that couple $|j_k^\alpha\rangle$ -states through local k -indices by Equation (100) but leave all ℓ^α values of global j -indices unchanged. Thus α -eigenstates of H mix k -values to form ℓ^α -fold degenerate levels labeled by j -indices. (Recall $\ell^E = 2$ equal sub-matrices Equation (93) in (91).) Further degeneracy or near-degeneracy (“clustering”) occurs if

inter-and-intra local tunneling coefficients decrease exponentially with quantum numbers thus isolating equivalent local modes into nearly degenerate sets of “spontaneously” broken local symmetry.

In contrast to this clustering or “un-splitting” associated with local \bar{g} symmetry operators, global g are associated with external or “applied” symmetry reduction that causes level *splitting*. Adding global g_m to a Hamiltonian H reduces its G -symmetry to a self-symmetry subgroup $K=s_m$ consisting of operators that commute with g_m . Adding a combination of g_m and g_n reduces K to an even smaller self-symmetry intersection group $s_m \cap s_n$.

Global g couple $|j_k^\alpha\rangle$ -states through global j -indices according to Equation (98). The more global perturbations are added to a Hamiltonian H the more likely it is to split ℓ^α -fold j -degeneracy (for $\ell^\alpha \geq 2$) and/or linebreak alter eigenfunctions.

6.7.1. Global “Applied” Symmetry Reduction, Subduction, and Level Splitting

In the $G=D_3$ example, adding matrix (r^1) from Equation (69a) to (H) in Equation (71) reduces its symmetry to $K=C_3=[1, r^1, r^2]$, and adding (i_3) reduces it to $K=C_2=[1, i_3]$. Adding a combination of (r^1) and (i_3) completely reduces (H) -symmetry to intersection $C_3 \cap C_2=C_1=[1]$, which corresponds to having *no* global symmetry.

By reducing G to a subgroup $K \subset G$, each G -labeled α -level becomes relabeled by that subgroup K and split (if $\ell^\alpha \geq 2$) in precisely the way that central G -idempotent P^α is relabeled and/or split by unit resolution shown in Equation (78) or (79). The splitting in Equation (79) of D_3 idempotent P^E into C_3 -labeled $P_{1_3 1_3}^E$ plus $P_{2_3 2_3}^E$ implies the D_3 doublet level ω^E splits into C_3 -labeled singlets ω^{1_3} and ω^{2_3} . Both D_3 singlets A_1 and A_2 end up relabeled with C_3 scalar 0_3 labels.

$$\begin{array}{llll}
 D_3 \supset C_3 & \underline{P^\alpha \text{ relabel/split}} & \underline{D^\alpha \text{ relabel/reduce}} & \underline{\omega^\alpha \text{ relabel/split}} \\
 A_1 & P^{A_1} = P^{A_1} P^{0_3} = P_{0_3 0_3}^{A_1} & \Rightarrow D^{A_1} \downarrow C_3 \sim D^{0_3} & \Rightarrow \omega^{A_1} \rightarrow \omega^{0_3} \\
 A_2 & P^{A_2} = P^{A_2} P^{0_3} = P_{0_3 0_3}^{A_2} & \Rightarrow D^{A_2} \downarrow C_3 \sim D^{0_3} & \Rightarrow \omega^{A_2} \rightarrow \omega^{0_3} \\
 E & P^E = P^E P^{1_3} + P^E P^{2_3} & \Rightarrow D^E \downarrow C_3 \sim & \Rightarrow \omega^E \rightarrow \omega^{1_3} \\
 & = P_{1_3 1_3}^E + P_{2_3 2_3}^E & D^{1_3} \oplus D^{2_3} & \searrow \omega^{2_3}
 \end{array} \tag{103}$$

Global $D_3 \supset C_2$ relabeling and/or splitting is by Equation (78). Now D_3 singlets have different labels 0_2 and 1_2 .

$$\begin{array}{llll}
 D_3 \supset C_2 & \underline{P^\alpha \text{ relabel/split}} & \underline{D^\alpha \text{ relabel/reduce}} & \underline{\omega^\alpha \text{ relabel/split}} \\
 A_1 & P^{A_1} = P^{A_1} P^{0_2} = P_{0_2 0_2}^{A_1} & \Rightarrow D^{A_1} \downarrow C_2 \sim D^{0_2} & \Rightarrow \omega^{A_1} \rightarrow \omega^{0_2} \\
 A_2 & P^{A_2} = P^{A_2} P^{1_2} = P_{1_2 1_2}^{A_2} & \Rightarrow D^{A_2} \downarrow C_2 \sim D^{1_2} & \Rightarrow \omega^{A_2} \rightarrow \omega^{1_2} \\
 E & P^E = P^E P^{0_2} + P^E P^{1_2} & \Rightarrow D^E \downarrow C_2 \sim & \Rightarrow \omega^E \rightarrow \omega^{0_2} \\
 & = P_{0_2 0_2}^E + P_{1_2 1_2}^E & D^{0_2} \oplus D^{1_2} & \searrow \omega^{1_2}
 \end{array} \tag{104}$$

Center portions of splitting relations in Equations (103) and (104) use *subduction* symbols (\downarrow) to denote how each D_3 irrep- D^α reduces to subgroup C_3 or C_2 irreps under their respective global symmetry breaking. Earlier studies [34] have referred to these multiple subgroup splittings as multiple frameworks. Each α -row of Equations (103) and (104) corresponds to the row $\alpha=A_1, A_2,$ or E , of correlation array $D_3 \supset C_3$ or $D_3 \supset C_2$, respectively, in Equation (102).

6.7.2. Local “Spontaneous” Symmetry Reduction, Induction, and Level Clustering

Opposite to global $G \supset K$ symmetry irrep subduction $D^\alpha(G) \downarrow K = \dots \oplus d^a(K) \oplus d^b(K) \oplus \dots$ that predicts level-splitting is the reverse relation of local $K \subset G$ symmetry irrep induction $d^a(K) \uparrow G = \dots \oplus D^\alpha(G) \oplus D^\beta(G) \oplus \dots$ that predicts “unsplitting” or level-clustering. In the former, an ℓ^α -dimensional irrep $D^\alpha(\mathbf{k})$ of global G -symmetry is reducible to smaller ($\ell^a \leq \ell^\alpha$) block-diagonal irreps $d^a(\mathbf{k})$ of a subgroup K . In the latter, a K irrep d^a is induced (actually *projected*) kaleidoscope-like onto coset bases of a larger induced representation $d^a \uparrow G$ of G that is generally reducible to G irreps D^α .

Base states $|k \uparrow_j^\alpha\rangle$ of induced representation $d^k \uparrow G$ are each made by a G -projector \mathbf{P}_{jk}^α acting on local d^k -symmetry base state $|k\rangle = \mathbf{P}^k |k\rangle$ defined by local K -projector \mathbf{P}^k . G -projection is simpler if \mathbf{P}_{jk}^α is also based on K -projection. (It helps to stick with one framework through this!)

Of all $D_3 \supset C_2$ -projectors $\mathbf{P}_{j_2 k_2}^\alpha$ based on Equation (78), only $\mathbf{P}_{0_2 0_2}^{A_1}$, $\mathbf{P}_{0_2 0_2}^E$, and $\mathbf{P}_{1_2 0_2}^E$ have right index $k_2 = 0_2$. Only these can project induced states $|0_2 \uparrow_{j_2}^\alpha\rangle$ from local base state $|0_2\rangle$ corresponding to the 0_2 -column of $D_3 \supset C_2$ array in Equation (102) having A_1 and E . Similarly, A_2 and E in the 1_2 -column of Equation (102) correspond to $\mathbf{P}_{1_2 1_2}^{A_2}$, $\mathbf{P}_{0_2 1_2}^E$, and $\mathbf{P}_{1_2 1_2}^E$ projecting states $|1_2 \uparrow_{j_2}^\alpha\rangle$ from a local $|1_2\rangle$ state. Each projector $\mathbf{P}_{j_2 k_2}^\alpha$ in Equation (104) has a C_2 -subgroup projector \mathbf{P}^{k_2} “right-guarding” the side facing each local ℓ_2 -ket $|\ell_2\rangle = \mathbf{P}^{\ell_2} |\ell_2\rangle$ that is similarly “guarded” by its own defining projector \mathbf{P}^{ℓ_2} . C_2 -subgroup projector orthogonality then allows only $k_2 = \ell_2$, giving the projection selection rules just described.

$$\mathbf{P}_{j_2 k_2}^\alpha |\ell_2\rangle = \mathbf{P}_{j_2 k_2}^\alpha \mathbf{P}^{k_2} \mathbf{P}^{\ell_2} |\ell_2\rangle = \delta^{k_2 \ell_2} \mathbf{P}_{j_2 \ell_2}^\alpha |\ell_2\rangle = \delta^{k_2 \ell_2} |\ell_2 \uparrow_{j_2}^\alpha\rangle \tag{105}$$

Each “right guard” projector \mathbf{P}^k of \mathbf{P}_{jk}^α is part of a $G \supset K$ subgroup splitting or subduction splitting $D^\alpha(G) \downarrow K = \dots \oplus d^k(K) \oplus \dots$ as shown by $D_3 \downarrow C_2$ examples in Equation (104). (These go back to the original $D_3 \supset C_2$ subgroup chain resolution in Equation (78).) In Equation (105) each \mathbf{P}^k selects which α -type induced bases $|k \uparrow_j^\alpha\rangle$ and block-diagonal α -irreps can appear in a k -induced representation $d^k(K) \uparrow G = \dots \oplus D^\alpha(G) \oplus \dots$, and it implies a duality between induced (\uparrow) level-clustering and subduced (\downarrow) level-splitting as stated by the following *Frobenius reciprocity relation*.

$$\text{Number of } D^\alpha \text{ in } d^k(K) \uparrow G = \text{Number of } d^k \text{ in } D^\alpha(G) \downarrow K \tag{106}$$

The numbers on the left-hand side of Equation (106) would reside in the k^{th} -column of a $G \supset K$ -correlation array such as in Equation (102) while the numbers on the right-hand side of Equation (106) would reside in the α^{th} -row of the *same* array. The examples in Equation (102) have only ones $\{1\}$ and zeros $\{.\}$. A deeper correlation $D_3 \supset C_1$ to C_1 symmetry, *i.e.*, to *no* symmetry is a conflation of either the array $D_3 \supset C_2$ or the array $D_3 \supset C_3$ in Equation (102) since $C_1 = C_2 \cap C_3$ is the intersection of C_2 and C_3 .

$D_3 \supset C_1$	$0_1 = 1_1$	
A_1	1	
A_2	1	
E	2	

(107)

C_1 local symmetry base $|0_1\rangle = |1_1\rangle$ is the $|1\rangle$ in Figure 18 that contains scalar A_1 , pseudo-scalar A_2 , and two E wave states in Figure 19 consistent with a single column of $D_3 \supset C_1$ correlation array in

Equation (107). This column describes *induced* representation $D^{01}(C_1) \uparrow D_3$, also known as a *regular* representation of D_3 .

Reciprocity in Equation (106) also holds for non-Abelian subgroup irreps d^k . D_3 is the smallest non-Abelian group so it has no such subgroups, but octahedral symmetry has non-Abelian D_3 and D_4 subgroups that figure in its splitting and clustering that are described in later Section 7.

6.7.3. Coset Structure and Factored Eigensolutions

Three pairs of kets in Figure 17 relate to *left cosets* [$\mathbf{1}C_2 = (\mathbf{1}, \mathbf{i}_3)$, $\mathbf{r}C_2 = (\mathbf{r}^1, \mathbf{i}_2)$, $\mathbf{r}^2C_2 = (\mathbf{r}^2, \mathbf{i}_1)$] one at each site.

$$[(|\mathbf{1}\rangle, |\mathbf{i}_3\rangle), (|\mathbf{r}^1\rangle, |\mathbf{i}_2\rangle) = \mathbf{r}^1(|\mathbf{1}\rangle, |\mathbf{i}_3\rangle), (|\mathbf{r}^2\rangle, |\mathbf{i}_1\rangle) = \mathbf{r}^2(|\mathbf{1}\rangle, |\mathbf{i}_3\rangle)] \tag{108}$$

Conjugate bras $\langle \mathbf{g} | = \langle \mathbf{1} | \mathbf{g}^\dagger$ relate to *right cosets* [$C_2 = (\mathbf{1}, \mathbf{i}_3)$, $C_2\mathbf{r}^2 = (\mathbf{r}^2, \mathbf{i}_2)$, $C_2\mathbf{r} = (\mathbf{r}, \mathbf{i}_1)$], again, one per C_2 -well site.

$$[(\langle \mathbf{1} |, \langle \mathbf{i}_3 |), (\langle \mathbf{r}^1 |, \langle \mathbf{i}_2 |) = (\langle \mathbf{1} |, \langle \mathbf{i}_3 |) \mathbf{r}^2, (\langle \mathbf{r}^2 |, \langle \mathbf{i}_1 |) = (\langle \mathbf{1} |, \langle \mathbf{i}_3 |) \mathbf{r}^1] \tag{109}$$

C_2 projectors $\mathbf{P}^{02} = \frac{1}{2}(\mathbf{1} + \mathbf{i}_3) = \mathbf{P}^x$ and $\mathbf{P}^{12} = \frac{1}{2}(\mathbf{1} - \mathbf{i}_3) = \mathbf{P}^y$ split bra $\langle \mathbf{g} |$ into \pm -sum of bras mapped by left coset $\mathbf{g}^\dagger C_2$.

$$[\langle \mathbf{1} | \mathbf{P}^{m2} = \frac{1}{2} (\langle \mathbf{1} | \pm \langle \mathbf{i}_3 |), \langle \mathbf{r}^1 | \mathbf{P}^{m2} = \frac{1}{2} (\langle \mathbf{r}^1 | \pm \langle \mathbf{i}_2 |), \langle \mathbf{r}^2 | \mathbf{P}^{m2} = \frac{1}{2} (\langle \mathbf{r}^2 | \pm \langle \mathbf{i}_1 |)] \tag{110}$$

The same projectors split ket $|\mathbf{g}\rangle$ into bases $\mathbf{P}^{m2}|\mathbf{g}\rangle$ that are \pm -sum of kets mapped by right coset $C_2\mathbf{g}$.

$$[\mathbf{P}^{m2} |\mathbf{1}\rangle = \frac{1}{2} (|\mathbf{1}\rangle \pm |\mathbf{i}_3\rangle), \mathbf{P}^{m2} |\mathbf{r}^1\rangle = \frac{1}{2} (|\mathbf{r}^1\rangle \pm |\mathbf{i}_2\rangle), \mathbf{P}^{m2} |\mathbf{r}^2\rangle = \frac{1}{2} (|\mathbf{r}^2\rangle \pm |\mathbf{i}_1\rangle)] \tag{111}$$

g -coefficients in H -submatrix Equation (93) track C_2 cosets. Row-(bra)- x terms in $H_{x,\cdot}^E$ line up in (+)-right-coset $\mathbf{1g} + \mathbf{i}_3\mathbf{g}$ order $\dots(r_1 + i_1), (r_2 + i_2)$. Row-(bra)- y terms in $H_{y,\cdot}^E$ line up in (-)-right-coset $\mathbf{1g} - \mathbf{i}_3\mathbf{g}$ order $(r_1 - i_1), (r_2 - i_2)$. Column-(ket) (\pm)-forms $H_{\cdot,x}^E$ and $H_{\cdot,y}^E$ line up in *left-coset* order $\dots(r_1 \pm i_2), (r_2 \pm i_1)$. Either ordering gives the same matrix. Off-diagonal components $H_{x,y}^E$ and $H_{y,x}^E$ have x vs. y symmetry conflicts so coset parameters $(r^0 \pm i_3)$ vanish.

$$\begin{pmatrix} H_{[x]x}^E & H_{[x]y}^E \\ H_{[y]x}^E & H_{[y]y}^E \end{pmatrix} = \begin{pmatrix} (r_0 + i_3) - \frac{1}{2}(r_1 + i_1) - \frac{1}{2}(r_2 + i_2) & 0 \cdot (r_0 + i_3) - \frac{\sqrt{3}}{2}(r_1 + i_1) + \frac{\sqrt{3}}{2}(r_2 + i_2) \\ 0 \cdot (r_0 - i_3) + \frac{\sqrt{3}}{2}(r_1 - i_1) - \frac{\sqrt{3}}{2}(r_2 - i_2) & (r_0 - i_3) - \frac{1}{2}(r_1 - i_1) - \frac{1}{2}(r_2 - i_2) \end{pmatrix}^{bra}$$

$$\begin{pmatrix} H_{x[x]}^E & H_{x[y]}^E \\ H_{y[x]}^E & H_{y[y]}^E \end{pmatrix} = \begin{pmatrix} (r_0 + i_3) - \frac{1}{2}(r_1 + i_2) - \frac{1}{2}(r_2 + i_1) & 0 \cdot (r_0 - i_3) - \frac{\sqrt{3}}{2}(r_1 - i_2) + \frac{\sqrt{3}}{2}(r_2 - i_1) \\ 0 \cdot (r_0 + i_3) + \frac{\sqrt{3}}{2}(r_1 + i_2) - \frac{\sqrt{3}}{2}(r_2 + i_1) & (r_0 - i_3) - \frac{1}{2}(r_1 - i_2) - \frac{1}{2}(r_2 - i_1) \end{pmatrix}^{ket} \tag{112}$$

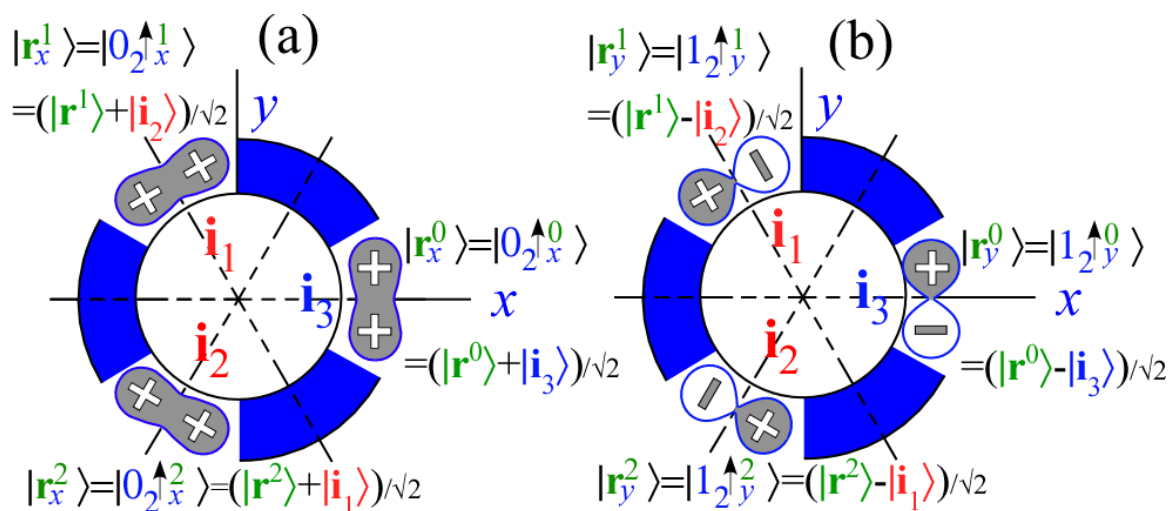
Kets $\mathbf{P}^x|\mathbf{r}^p\rangle = [\mathbf{P}^x|\mathbf{1}\rangle, \mathbf{P}^x|\mathbf{r}^1\rangle, \mathbf{P}^x|\mathbf{r}^2\rangle$ span induced representation $d^x(C_2) \uparrow D_3$, and $\mathbf{P}^y|\mathbf{r}^p\rangle$ span $d^y(C_2) \uparrow D_3$. Normalized states $\mathbf{P}^x|\mathbf{r}^p\rangle/\sqrt{2}$ and $\mathbf{P}^y|\mathbf{r}^p\rangle/\sqrt{2}$ correspond to σ -type and π -type orbitals at vertex positions $p=0, 1$, or 2 in Figure 21. D_3 table in Equation (68) is reordered in Equation (113) below to display $C_2(\mathbf{i}_3)$ body-basis right-coset representation bra-defined by $\langle \mathbf{g} | = \langle \mathbf{1} | \bar{\mathbf{g}}$ or ket-defined by

$\bar{g}^\dagger |1\rangle = |g\rangle$. The resulting H -matrix in Equation (68) is Equation (71) reordered for cosets of C_2 instead of C_3 .

D_3 body gg^\dagger form	$ 1\rangle$	$ i_3\rangle =$ $\bar{i}_3 1\rangle$	$ r^1\rangle =$ $\bar{r}^2 1\rangle$	$ i_2\rangle =$ $\bar{i}_3 \bar{r}^2 1\rangle$	$ r^2\rangle =$ $\bar{r}^1 1\rangle$	$ i_1\rangle =$ $\bar{i}_3 \bar{r}^1 1\rangle$	(113)
$\langle 1 $	1	\bar{i}_3	\bar{r}^2	\bar{i}_2	\bar{r}^1	\bar{i}_1	
$\langle i_3 = \langle 1 \bar{i}_3$	\bar{i}_3	1	\bar{i}_2	\bar{r}^2	\bar{i}_1	\bar{r}^1	
$\langle r^1 = \langle 1 \bar{r}^1$	\bar{r}^1	\bar{i}_2	1	\bar{i}_1	\bar{r}^2	\bar{i}_3	
$\langle i_2 = \langle 1 \bar{r}^1 \bar{i}_3$	\bar{i}_2	\bar{r}^1	\bar{i}_1	1	\bar{i}_3	\bar{r}^2	
$\langle r^2 = \langle 1 \bar{r}^2$	\bar{r}^2	\bar{i}_1	\bar{r}^1	\bar{i}_3	1	\bar{i}_2	
$\langle i_1 = \langle 1 \bar{r}^2 \bar{i}_3$	\bar{i}_1	\bar{r}^2	\bar{i}_3	\bar{r}^1	\bar{i}_2	1	

	$ 1\rangle$	$ i_3\rangle$	$ r^1\rangle$	$ i_2\rangle$	$ r^2\rangle$	$ i_1\rangle$
$\Rightarrow \langle H \rangle =$	r_0	i_3	r_2	i_2	r_1	i_1
	i_3	r_0	i_2	r_2	i_1	r_1
	r_1	i_2	r_0	i_1	r_2	i_3
	i_2	r_1	i_1	r_0	i_3	r_2
	r_2	i_1	r_1	i_3	r_0	i_2
	i_1	r_2	i_3	r_1	i_2	r_0

Figure 21. Induced representation $C_2 \uparrow D_3$ base wave states at vertex points $p = 0, 1,$ and 2 . (a) $0_2 \uparrow D_3$ bases $P^x |r^p\rangle \sqrt{2}$; (b) $1_2 \uparrow D_3$ bases $P^y |r^p\rangle \sqrt{2}$.



C_2 ordered products in Equation (113) help reduce H -matrix in Equation (71) to a direct sum of C_2 induced reps $(d^{0_2} \oplus d^{1_2}) \uparrow D_3$ in Equation (114). Upper (0_2) -array in Equation (114) uses σ -orbital bases $|r_x^p\rangle$ in Figure 21a while π -orbital bases $|r_y^p\rangle$ in Figure 21b span the (1_2) -array.

$$\langle H \rangle = \begin{array}{c|ccc|ccc} & |0_2 \uparrow_x^0\rangle & |0_2 \uparrow_x^1\rangle & |0_2 \uparrow_x^2\rangle & |1_2 \uparrow_y^0\rangle & |1_2 \uparrow_y^1\rangle & |1_2 \uparrow_y^2\rangle \\ \hline \langle 0_x| & r_0 + i_3 & r_2 + i_2 & r_1 + i_1 & \cdot & \cdot & \cdot \\ \langle 1_x| & r_1 + i_2 & r_0 + i_1 & r_2 + i_3 & \cdot & \cdot & \cdot \\ \langle 2_x| & r_2 + i_1 & r_1 + i_3 & r_0 + i_2 & \cdot & \cdot & \cdot \\ \hline \langle 0_y| & \cdot & \cdot & \cdot & r_0 - i_3 & r_2 - i_2 & r_1 - i_1 \\ \langle 1_y| & \cdot & \cdot & \cdot & r_1 - i_2 & r_0 - i_1 & r_2 - i_3 \\ \langle 2_y| & \cdot & \cdot & \cdot & r_2 - i_1 & r_1 - i_3 & r_0 - i_2 \end{array} \quad (114)$$

Any group component of Equation (114) or combination thereof is a possible tunneling matrix. Submatrices $d^{0_2}(\mathbf{g})\uparrow D_3$ shown for $\mathbf{g}=\mathbf{r}^1$, \mathbf{i}_1 , and \mathbf{i}_3 reflect the effect of these operators on states in Figure 21a and similarly for $d^{1_2}(\mathbf{g})\uparrow D_3$ in Figure 21b.

$$\begin{array}{c} \langle r_1 \bar{\mathbf{r}}^1 \rangle = r_1 \begin{array}{c|ccc|ccc} \cdot & \cdot & 1 & \cdot & \cdot & \cdot & \cdot \\ 1 & \cdot & \cdot & \cdot & \cdot & \cdot & \cdot \\ \cdot & 1 & \cdot & \cdot & \cdot & \cdot & \cdot \\ \hline \cdot & \cdot & \cdot & \cdot & \cdot & 1 & \cdot \\ \cdot & \cdot & \cdot & 1 & \cdot & \cdot & \cdot \\ \cdot & \cdot & \cdot & \cdot & 1 & \cdot & \cdot \end{array}, & \langle i_1 \bar{\mathbf{i}}_1 \rangle = i_1 \begin{array}{c|ccc|ccc} \cdot & \cdot & 1 & \cdot & \cdot & \cdot & \cdot \\ \cdot & 1 & \cdot & \cdot & \cdot & \cdot & \cdot \\ 1 & \cdot & \cdot & \cdot & \cdot & \cdot & \cdot \\ \hline \cdot & \cdot & \cdot & \cdot & \cdot & \cdot & -1 \\ \cdot & \cdot & \cdot & \cdot & -1 & \cdot & \cdot \\ \cdot & \cdot & \cdot & -1 & \cdot & \cdot & \cdot \end{array}, \\ \\ \langle i_3 \bar{\mathbf{i}}_3 \rangle = i_3 \begin{array}{c|ccc|ccc} 1 & \cdot & \cdot & \cdot & \cdot & \cdot & \cdot \\ \cdot & \cdot & 1 & \cdot & \cdot & \cdot & \cdot \\ \cdot & 1 & \cdot & \cdot & \cdot & \cdot & \cdot \\ \hline \cdot & \cdot & \cdot & -1 & \cdot & \cdot & \cdot \\ \cdot & \cdot & \cdot & \cdot & \cdot & -1 & \cdot \\ \cdot & \cdot & \cdot & \cdot & -1 & \cdot & \cdot \end{array} \end{array} \quad (115)$$

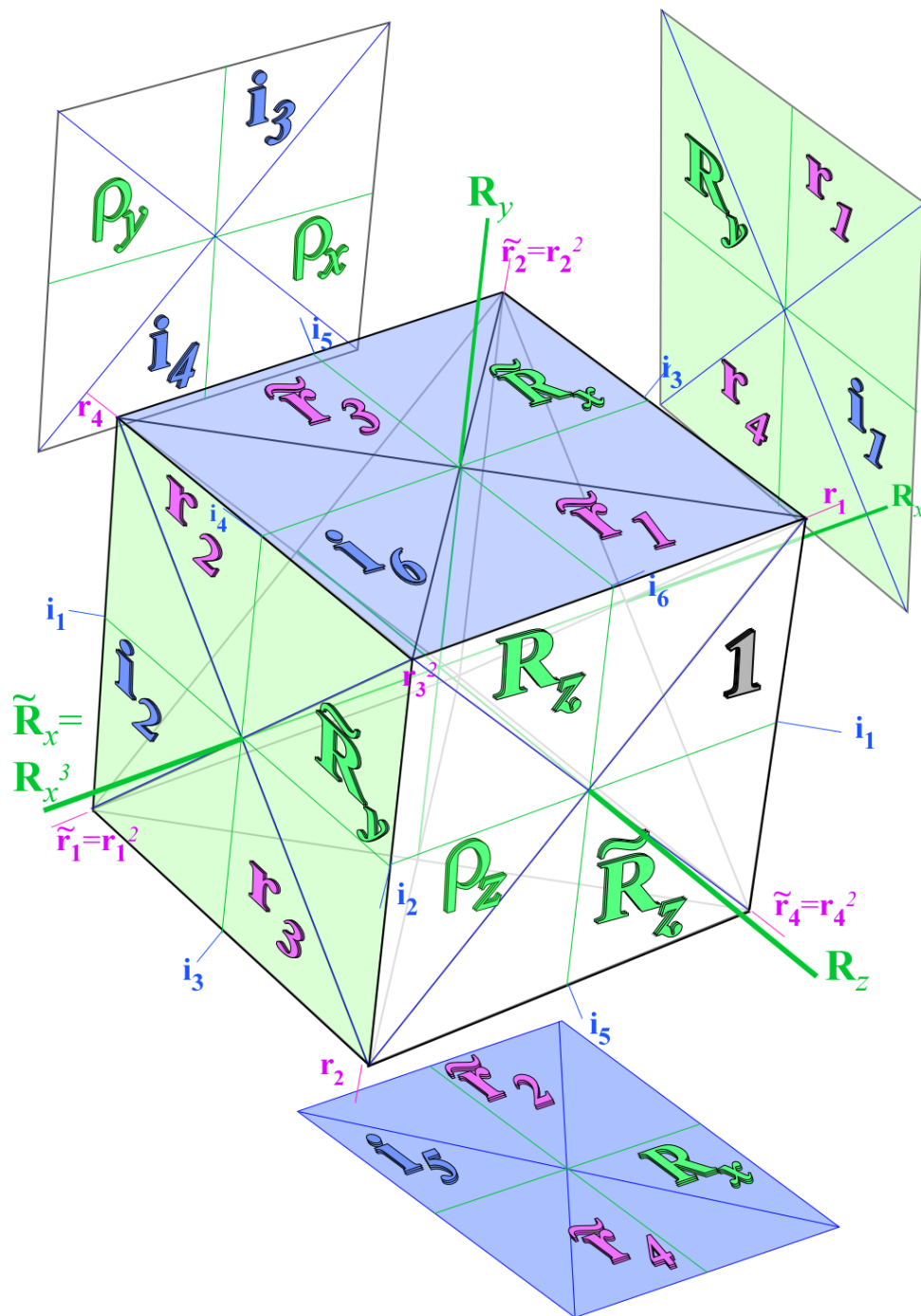
The 0_2 correlation in Equation (102) implies $d^{0_2}\uparrow D_3$ reduces further to D_3 irreps $A_1 \oplus E$ that label the lower band of Figure 19. Meanwhile $d^{1_2}\uparrow D_3$ reduces to irreps $A_2 \oplus E$ that label the upper band of Figure 19. Equation (91) shows $A_1 \oplus A_2 \oplus E \oplus E$.

7. Octahedral Symmetry Analysis

Octahedral-cubic rotational symmetry O operations are modeled in Figure 22. Rotation inversion symmetry $O_h=O \times C_i$ operations are modeled in Figure 23. In each case the larger \mathbf{g} -symbols (such as $\tilde{\mathbf{r}}_1$ on top of Figure 22) label position ket states (such as $|\tilde{\mathbf{r}}_1\rangle = \tilde{\mathbf{r}}_1|1\rangle$) while smaller \mathbf{g} -symbols label axes of rotation in O (such as i_6 on top facing edge of Figure 22 labeling that 180° rotation) or planes of reflection in O_h (such as the σ_x just above the z -axis on facing plane of Figure 23 labeling the x -plane reflection).

Figure 22 is an “ O -group slide-rule” since product $\mathbf{i}_6 \cdot \tilde{\mathbf{r}}_1$ can be viewed as operator i_6 flipping a wave in position $|\tilde{\mathbf{r}}_1\rangle$ onto position $|\mathbf{R}_z\rangle$, that is, $i_6|\tilde{\mathbf{r}}_1\rangle = |\mathbf{R}_z\rangle$ giving product $\mathbf{i}_6 \cdot \tilde{\mathbf{r}}_1 = \mathbf{R}_z$. Figure 23 is an “ O_h -group slide-rule” (that does O products, too) and just as easily gives product $\sigma_x \cdot \tilde{\mathbf{r}}_1 = \tilde{\mathbf{s}}_2$ all without knowing what $\tilde{\mathbf{r}}_1$ or $\tilde{\mathbf{s}}_2$ do. (As explained below, \mathbf{r}_1 is 120° rotation about $[111]$ axis and $\tilde{\mathbf{r}}_1$ is its inverse located on the $[\bar{1}\bar{1}\bar{1}]$ -axis while $\tilde{\mathbf{r}}_2$ is on the $[11\bar{1}]$ axis. $\tilde{\mathbf{s}}_2$ is $\tilde{\mathbf{r}}_2$ multiplied by inversion $\mathbf{I} \cdot [111] = [\bar{1}\bar{1}\bar{1}]$.)

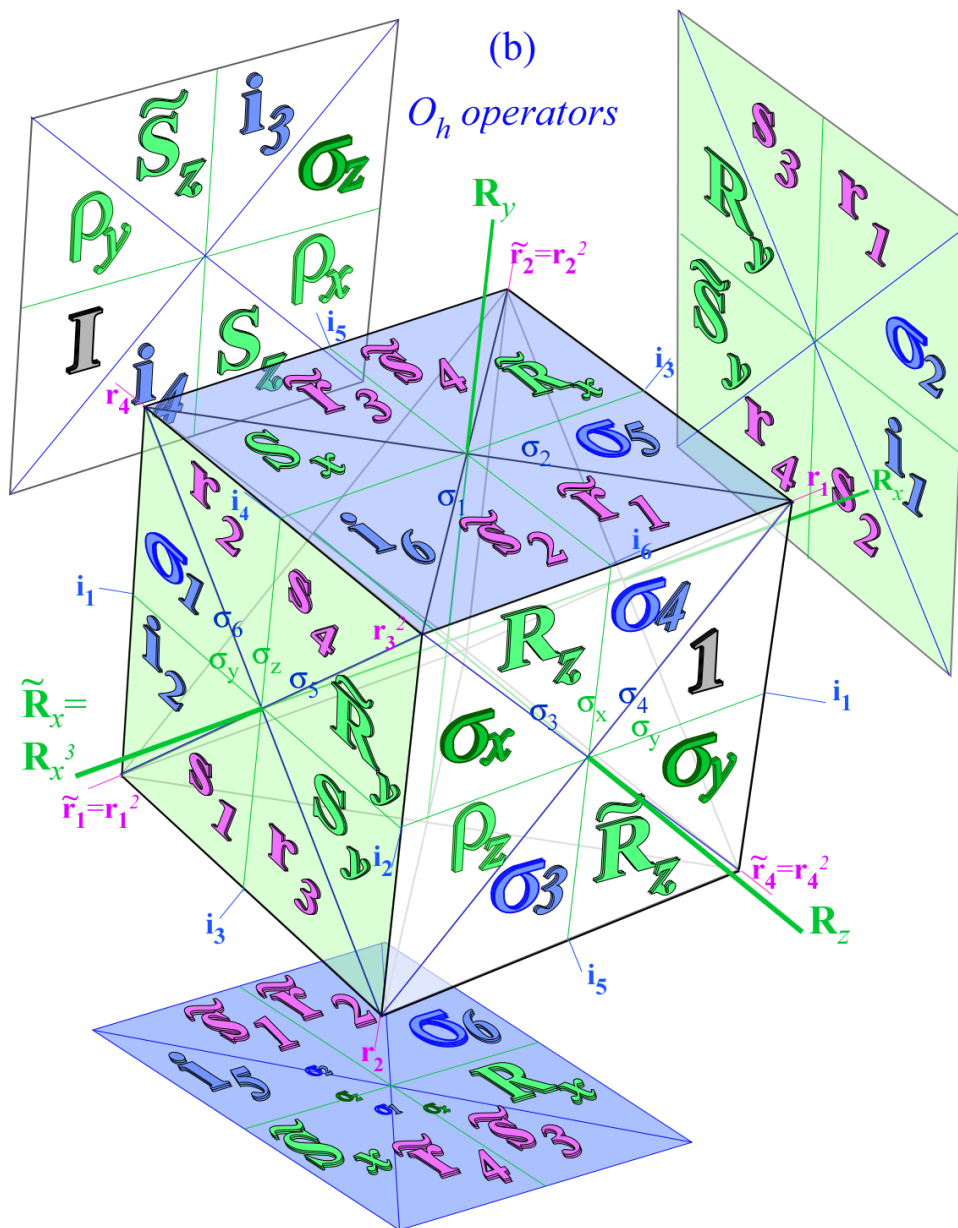
Figure 22. O operators distributed in cosets of $C_4 \supset C_2$.



Note i_6 -transform of *state* $|r_1\rangle$ (example: $i_6|r_1\rangle=|\tilde{R}_y\rangle$) differs from an i_6 -transform of *operator* r_1 (example: $i_6 \cdot r_1 \cdot i_6^{-1}=r_3^2$). The latter is divined easily by “slide-rule” as i_6 flips r_1 ’s axis onto r_3^2 ’s.

Three Cartesian C_4 axes of anti-clockwise 90° rotations R_x , R_y , and R_z define directions $[100]$, $[010]$, and $[001]$, respectively. Their inverses $\tilde{R}_x=R_x^3$, $\tilde{R}_y=R_y^3$, and $\tilde{R}_z=R_z^3$ are also 90° rotations but around negative axes $[\bar{1}00]$, $[0\bar{1}0]$, and $[00\bar{1}]$. A shorthand notation for 180° Cartesian rotations is $\rho_x=R_x^2$, $\rho_y=R_y^2$, and $\rho_z=R_z^2$. Trigonal C_3 axes of anti-clockwise 120° rotations r_1 , r_2 , r_3 , and r_4 lie along $[111]$, $[\bar{1}\bar{1}\bar{1}]$, $[\bar{1}11]$, and $[1\bar{1}\bar{1}]$, respectively, while axes of inverses $\tilde{r}_1=r_1^2$, $\tilde{r}_2=r_2^2$, $\tilde{r}_3=r_3^2$, and $\tilde{r}_4=r_4^2$ lie along the opposite directions $[\bar{1}\bar{1}\bar{1}]$, $[11\bar{1}]$, $[1\bar{1}\bar{1}]$, and $[1\bar{1}1]$, respectively.

Figure 23. O_h operators distributed in cosets of $C_{4v} \supset C_{2v}$.



There are six C_2 axes of 180° rotations $i_1, i_2, i_3, i_4, i_5,$ and i_6 located along $[101], [\bar{1}01], [110], [\bar{1}\bar{1}0], [011],$ and $[0\bar{1}1],$ respectively. This completes the five classes of O : $[1], [r_{1..4}, \tilde{r}_{1..4}], [\rho_{xyz}], [R_{xyz}, \tilde{R}_{xyz}],$ and $[i_{1..6}].$ Including the rotations with inversion I yields five more classes of O_h : $[I], [s_{1..4}, \tilde{s}_{1..4}], [\rho_{xyz}], [S_{xyz}, \tilde{S}_{xyz}],$ and $[\sigma_{1..6}]$ where $s_{1..4}=I \cdot r_{1..4}, [\sigma_{xyz}]=[I \cdot \rho_{xyz}], [S_{xyz}]=[I \cdot R_{xyz}],$ and $[\sigma_{1..6}]=[I \cdot i_{1..6}].$ σ 's are mirror-plane reflections in Figure 23.

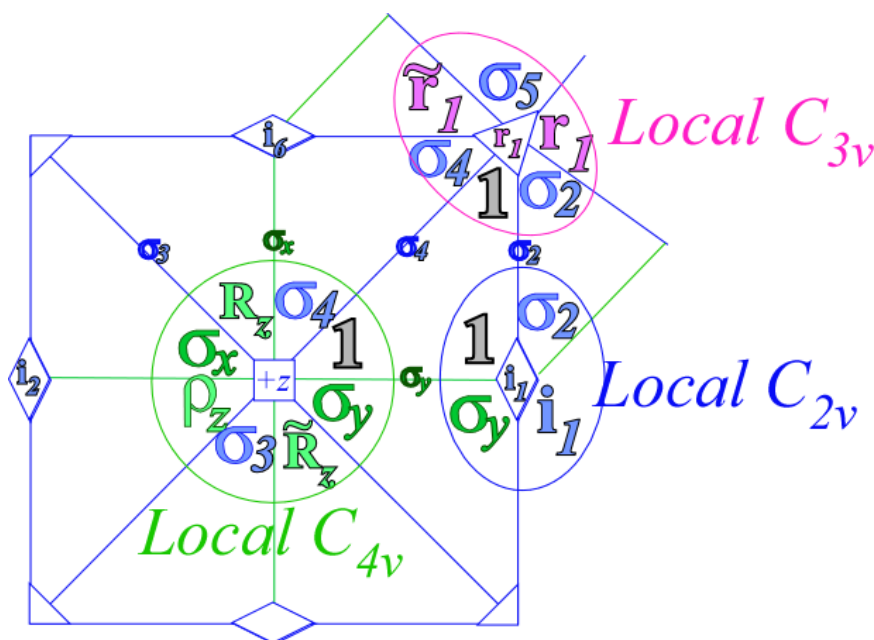
The “slide-rules” in Figures 22, 23 also help evaluate class products and construct left and right cosets of local symmetry subgroups. Three of the largest cyclic subgroups of O are tetragonal C_4 such as $C_4=[1, R_z, R_z^2=\rho_z, R_z^3=\tilde{R}_z]$ displayed on the R_z -face of the cube in Figure 22. In Figure 23 the same face displays local symmetry $C_{4v}=[1, \rho_z, R_z, \tilde{R}_z, \sigma_4, \sigma_x, \sigma_3, \sigma_y]$ that contains C_4 plus pairs of diagonal mirror reflections $[\sigma_4=I \cdot i_4, \sigma_3=I \cdot i_3]$ and Cartesian mirror reflections $[\sigma_x=I \cdot \rho_x, \sigma_y=I \cdot \rho_y].$ Each pair $[\sigma_x, \sigma_y]$ and $[\sigma_3, \sigma_4]$ is a C_{4v} class as is rotation pair $[R_z, \tilde{R}_z]$ or, singly, 1 and $\rho_z.$ The other five cube faces display cosets of the tetragonal subgroups $C_{4v} \supset C_4$ of $O_h \supset O.$

Figure 22 shows six O -cosets $g \cdot C_4$ of $C_4=[1, \mathbf{R}_z, \rho_z, \tilde{\mathbf{R}}_z]$. Opposite ρ_x -face has coset $\rho_x \cdot C_4=[\rho_x, \mathbf{i}_4, \rho_y, \mathbf{i}_3]$ in that order. The \mathbf{r}_1 -face shows coset $\mathbf{r}_1 \cdot C_4=[\mathbf{r}_1, \mathbf{i}_1, \mathbf{r}_4, \mathbf{R}_y]$ in upper right of Figure 22, and the opposite \mathbf{r}_2 -face has coset $\mathbf{r}_2 \cdot C_4=[\mathbf{r}_2, \mathbf{i}_2, \mathbf{r}_3, \tilde{\mathbf{R}}_y]$. Top and bottom faces have cosets $\tilde{\mathbf{r}}_1 \cdot C_4=[\tilde{\mathbf{r}}_1, \tilde{\mathbf{R}}_x, \tilde{\mathbf{r}}_3, \mathbf{i}_6]$ and $\tilde{\mathbf{r}}_2 \cdot C_4=[\tilde{\mathbf{r}}_2, \mathbf{R}_x, \tilde{\mathbf{r}}_4, \mathbf{i}_5]$.

Each $g \cdot C_4$ -coset element $g \cdot \mathbf{R}_z^p$ ($p = 0..3$) transforms the 1-face to the same g -face and orients it according to a C_4 element \mathbf{R}_z^p as it permutes the list of its elements accordingly. Each face may be labeled by any element $g \cdot \mathbf{R}_z^p$ in its coset. An i -class labeling by 1, \mathbf{i}_3 (or \mathbf{i}_4), \mathbf{i}_1 , \mathbf{i}_2 , \mathbf{i}_6 , and \mathbf{i}_5 of C_4 cosets in Figure 22 is as good as any other.

Figure 23 shows six O_h -cosets of C_{4v} (counting C_{4v} itself) in a geometric display that also shows eight trigonal cosets of $C_{3v} \supset C_3$ -[111] and twelve dihedral cosets of $C_{2v} \supset C_2$ -[101]. Figure 24 shows three symmetry points of Figure 23 forming a triangular cell with sides that are on reflection planes.

Figure 24. O_h local symmetry (a) C_{4v} ; (b) C_{3v} ; (c) C_{2v} .



An order-8 axial symmetry C_{4v} lies on the tetragonal- z -[001]-axis of a cube face or octahedral vertex. An order-6 C_{3v} lies on the trigonal-[111]-axis of a cube vertex or octahedral face. Finally, there is a dihedral- C_{2v} [110]-axis of a cube or octahedral edge. Lines between the axes have bilateral local reflection symmetry $C_v(y)=[1, \sigma_y]$, $C_v(2)=[1, \sigma_2]$, or $C_v(4)=[1, \sigma_4]$, fundamental symmetry operations whose products generate all others. Figure 24 is like a reduced Brillouin Zone of the O_h lattice.

Each subgroup spawns a coset space and a set of induced representations of full O_h symmetry that generalize the C_{3v} induced representations in Equation (115) and base kets sketched in Figure 21. Correlation tables between O or O_h and its subgroups $L \subset G$ tell which O or O_h irreps, states, and energy levels arise from each coset space. As local symmetry reduces and its order $^\circ L$ decreases, the coset dimension $d=^\circ G/^\circ L$ grows proportionally with a corresponding increase in number of irreps and levels in $L \uparrow G$ -induced representation cluster spaces. Examples are given below for $G=O$ and in Section 8 for $G=O_h$.

7.1. Octahedral Characters and Subgroup Correlations

Spectral class resolution of O generalizes that of D_3 in Equation (75) to give character array Equation (116).

O group $\chi_{\kappa_g}^\alpha$	$g = 1$	r_{1-4} \tilde{r}_{1-4}	ρ_{xyz}	R_{xyz} \tilde{R}_{xyz}	i_{1-6}
$\alpha = A_1$	1	1	1	1	1
A_2	1	1	1	-1	-1
E	2	-1	2	0	0
T_1	3	0	-1	1	-1
T_2	3	0	-1	-1	1

(116)

Cyclic subgroup $C_4(\mathbf{R}_z^p)$, $C_3(\mathbf{r}_1^p)$, and C_2 characters correlate to O according to arrays in Equation (117).

$O \supset C_4$	0_4	1_4	2_4	3_4	$O \supset C_3$	0_3	1_3	2_3
$A_1 \downarrow C_4$	1	·	·	·	$A_1 \downarrow C_3$	1	·	·
$A_2 \downarrow C_4$	·	·	1	·	$A_2 \downarrow C_3$	1	·	·
$E \downarrow C_4$	1	·	1	·	$E \downarrow C_3$	·	1	1
$T_1 \downarrow C_4$	1	1	·	1	$T_1 \downarrow C_3$	1	1	1
$T_2 \downarrow C_4$	·	1	1	1	$T_2 \downarrow C_3$	1	1	1

$O \supset C_2(\mathbf{i}_1)$	0_2	1_2	$O \supset C_2(\rho_z)$	0_2	1_2
$A_1 \downarrow C_2$	1	·	$A_1 \downarrow C_2$	1	·
$A_2 \downarrow C_2$	·	1	$A_2 \downarrow C_2$	1	·
$E \downarrow C_2$	1	1	$E \downarrow C_2$	2	·
$T_1 \downarrow C_2$	1	2	$T_1 \downarrow C_2$	1	2
$T_2 \downarrow C_2$	2	1	$T_2 \downarrow C_2$	1	2

(117)

Equivalent subgroup correlations $O \supset H$ and $O \supset gHg^{-1}$ share elements in the same O -classes and have one correlation array. Thus all three C_4 local symmetries have one correlation table in Equation (117), as do all four C_3 subgroups. However, $O \supset C_2(\rho_z)$ and $O \supset C_2(\mathbf{i}_1)$ correlations differ since \mathbf{i}_1 and ρ_z have different O -class and characters in Equation (116).

Projectors \mathbf{P}_{jk}^α and irreps D_{jk}^α of O depend on choice of local symmetry just as D_3 projector splitting in Equation (78) or (79) depends on choice of correlation $D_3 \supset C_2$ in Equation (104) or $D_3 \supset C_3$ in Equation (103), respectively. Sub-labels (j, k) range over C_2 values $[0_2, 1_2]$ or else C_3 values $[0_3, 1_3, 2_3]$ while a tetragonal correlation $O \supset C_4$ will use sub-labels $(j, k) = [0_4, 1_4, 2_4, 3_4]$.

The m_4 or else m_3 unambiguously defines all O states since no $O \supset C_4$ or $O \supset C_3$ correlation numbers in Equation (117) exceed unity. However, $O \supset C_2(\mathbf{i}_1)$ correlations cannot distinguish all three sub-levels of T_1 or T_2 wherever a number 2 appears, and the $O \supset C_2(\rho_z)$ correlation leaves the E sub-levels unresolved, as well. A full O_h labeling resolves the first ambiguity as shown below, but we consider the unambiguous $O \supset C_4$ case first. (C_4 resolves $C_2(\rho_z)$ ambiguities.)

7.1.1. Resolving Commuting $O \supset C_4$ Local Symmetry Subalgebra: Rank = $\rho(O) = 10$

The C_4 correlation table in Equation (117) shows how invariant class projectors \mathbf{P}^α (expanded below in terms of O characters $\chi_{\kappa_g}^\alpha$ in table shown in Equation (116)) will split into irrep projectors $\mathbf{P}_{m_4 n_4}^\alpha$ when hit by C_4 local symmetry projectors \mathbf{p}_{m_4} . The latter \mathbf{p}_m are expanded in terms of C_4 operators \mathbf{R}_z^p weighted by character eigenvalues $\phi_p^{m_4} = (\chi_p^{m_4})^*$ using Equations (57) and (59).

$$\begin{aligned}
 \mathbf{1} \cdot \mathbf{P}^\alpha &= (\mathbf{p}_{0_4} + \mathbf{p}_{1_4} + \mathbf{p}_{2_4} + \mathbf{p}_{3_4}) \cdot \mathbf{P}^\alpha \\
 \mathbf{1} \cdot \mathbf{P}^{A_1} &= \mathbf{P}_{0_4 0_4}^{A_1} + 0 + 0 + 0 \\
 \mathbf{1} \cdot \mathbf{P}^{A_2} &= 0 + 0 + \mathbf{P}_{2_4 2_4}^{A_2} + 0 \\
 \mathbf{1} \cdot \mathbf{P}^E &= \mathbf{P}_{0_4 0_4}^E + 0 + \mathbf{P}_{2_4 2_4}^E + 0 \\
 \mathbf{1} \cdot \mathbf{P}^{T_1} &= \mathbf{P}_{0_4 0_4}^{T_1} + \mathbf{P}_{1_4 1_4}^{T_1} + 0 + \mathbf{P}_{3_4 3_4}^{T_1} \\
 \mathbf{1} \cdot \mathbf{P}^{T_2} &= 0 + \mathbf{P}_{1_4 1_4}^{T_2} + \mathbf{P}_{2_4 2_4}^{T_2} + \mathbf{P}_{3_4 3_4}^{T_2}
 \end{aligned} \tag{118}$$

The five class projectors \mathbf{P}^α are O -invariant and commute with all twenty-four O -operators $(\mathbf{1}, \mathbf{r}_1, \mathbf{r}_2, \dots, \mathbf{i}_5, \mathbf{i}_6)$. So do the five class operators $(\kappa_0, \kappa_{r_k}, \kappa_{\rho_k}, \kappa_{R_k}, \kappa_{i_k})$ in which each \mathbf{P}^α is expanded as follows. (Recall D_3 classes in Equation (75).)

$$\begin{aligned}
 \mathbf{P}^\alpha &= \frac{\ell^\alpha}{\circ O} \sum_{k=0}^5 \chi_{\kappa_k}^\alpha \kappa_k = \quad \text{where: } \alpha = A_1, A_2, E, T_1, \text{ or } T_2 \\
 &= \frac{\ell^\alpha}{24} \left[\chi_0^\alpha \mathbf{1} + \chi_{\kappa_r}^\alpha (\mathbf{r}_1 + \mathbf{r}_2 + \dots + \tilde{\mathbf{r}}_4) + \chi_{\kappa_\rho}^\alpha (\rho_x + \rho_y + \rho_z) \right. \\
 &\quad \left. + \chi_{\kappa_R}^\alpha (\mathbf{R}_x + \mathbf{R}_y + \dots + \tilde{\mathbf{R}}_z) + \chi_{\kappa_i}^\alpha (\mathbf{i}_1 + \mathbf{i}_2 + \dots + \mathbf{i}_6) \right]
 \end{aligned} \tag{119}$$

Each of the ℓ^α irrep projectors $\mathbf{P}_{n_4 n_4}^\alpha$ is obtained from its invariant \mathbf{P}^α by product $\mathbf{P}^\alpha \mathbf{p}_{n_4} = \mathbf{p}_{n_4} \mathbf{P}^\alpha$ following Equation (118) with each of four C_4 local symmetry projector \mathbf{p}_{m_4} .

$$\mathbf{p}_{m_4} = \sum_{p=0}^3 \frac{e^{2\pi i m \cdot p/4}}{4} \mathbf{R}_z^p = \begin{cases} \mathbf{p}_{0_4} = (\mathbf{1} + \mathbf{R}_z + \rho_z + \tilde{\mathbf{R}}_z)/4 \\ \mathbf{p}_{1_4} = (\mathbf{1} + i\mathbf{R}_z - \rho_z - i\tilde{\mathbf{R}}_z)/4 \\ \mathbf{p}_{2_4} = (\mathbf{1} - \mathbf{R}_z + \rho_z - \tilde{\mathbf{R}}_z)/4 \\ \mathbf{p}_{3_4} = (\mathbf{1} - i\mathbf{R}_z - \rho_z + i\tilde{\mathbf{R}}_z)/4 \end{cases} \tag{120}$$

As the five (O -centrum=5) projectors \mathbf{P}^α split into ten (O -rank=10) sub-projectors $\mathbf{P}_{n_4 n_4}^\alpha$, the five O class sums κ_g split into ten C_4 -invariant sub-class sums $\mathbf{c}_k (k=1..10)$.

$$\begin{aligned}
 \frac{\circ O}{\ell^\alpha} \cdot \mathbf{P}_{n_4 n_4}^\alpha &= \sum_{k=0}^{10} D_{n_4 n_4}^{\alpha*}(g_k) \mathbf{c}_k \\
 \text{where: } D_{n_4 n_4}^\alpha(g_k) &= D_{n_4 n_4}^\alpha(R_z^\dagger g_k R_z^p)
 \end{aligned} \tag{121}$$

The resulting ten products $\frac{\circ O}{\ell^\alpha} \mathbf{P}_{n_4 n_4}^\alpha$ are listed in Equation (122) of diagonal irrep coefficients $D_{n_4 n_4}^\alpha(g_k)$ in terms of twenty-four group elements g_k that have been sorted into ten sub-classes that have $C_4(z)$ local symmetry. The ten irrep projectors $\mathbf{P}_{n_4 n_4}^\alpha$ are C_4 local-invariant, that is, they commute with four C_4 -operators $(\mathbf{1}, \mathbf{R}_z, \mathbf{R}_z^2 = \rho_z, \mathbf{R}_z^3 = \tilde{\mathbf{R}}_z)$ but not the whole O group like the \mathbf{P}^α do. The ten sub-class-sum operators \mathbf{c}_k , into which each $\mathbf{P}_{n_4 n_4}^\alpha$ is expanded in Equation (122), are each individually

invariant to \mathbf{R}_z^p , that is $\mathbf{R}_z^p \mathbf{c}_k = \mathbf{c}_k \mathbf{R}_z^p$, and $D_{n_4 n_4}^\alpha(g_k)$ is the same for all g_k in sub-class c_k . Note that a sum of ℓ^α rows belonging to $\mathbf{P}_{n_4 n_4}^\alpha$ between horizontal lines in Equation (122) yields corresponding character values $\chi_k^\alpha = \text{trace} D^\alpha(g_k)$ in O -character array Equation (116) and effectively “unsplits” the sub-classes.

$\mathbf{P}_{n_4 n_4}^{(\alpha)}(O \supset C_4)$	1	$r_1 r_2 \tilde{r}_3 \tilde{r}_4$	$\tilde{r}_1 \tilde{r}_2 r_3 r_4$	$\rho_x \rho_y$	ρ_z	$R_x \tilde{R}_x R_y \tilde{R}_y$	R_z	\tilde{R}_z	$i_1 i_2 i_5 i_6$	$i_3 i_4$
$24 \cdot \mathbf{P}_{0_4 0_4}^{A_1}$	1	1	1	1	1	1	1	1	1	1
$24 \cdot \mathbf{P}_{2_4 2_4}^{A_2}$	1	1	1	1	1	-1	-1	-1	-1	-1
$12 \cdot \mathbf{P}_{0_4 0_4}^E$	1	$-\frac{1}{2}$	$-\frac{1}{2}$	1	1	$-\frac{1}{2}$	1	1	$-\frac{1}{2}$	1
$12 \cdot \mathbf{P}_{2_4 2_4}^E$	1	$-\frac{1}{2}$	$-\frac{1}{2}$	1	1	$+\frac{1}{2}$	-1	-1	$+\frac{1}{2}$	-1
$8 \cdot \mathbf{P}_{1_4 1_4}^{T_1}$	1	$-\frac{i}{2}$	$+\frac{i}{2}$	0	-1	$+\frac{1}{2}$	$-i$	$+i$	$-\frac{1}{2}$	0
$8 \cdot \mathbf{P}_{3_4 3_4}^{T_1}$	1	$+\frac{i}{2}$	$-\frac{i}{2}$	0	-1	$+\frac{1}{2}$	$+i$	$-i$	$-\frac{1}{2}$	0
$8 \cdot \mathbf{P}_{0_4 0_4}^{T_1}$	1	0	0	-1	1	0	1	1	0	-1
$8 \cdot \mathbf{P}_{1_4 1_4}^{T_2}$	1	$+\frac{i}{2}$	$-\frac{i}{2}$	0	-1	$-\frac{1}{2}$	$-i$	$+i$	$+\frac{1}{2}$	0
$8 \cdot \mathbf{P}_{3_4 3_4}^{T_2}$	1	$-\frac{i}{2}$	$+\frac{i}{2}$	0	-1	$-\frac{1}{2}$	$+i$	$-i$	$+\frac{1}{2}$	0
$8 \cdot \mathbf{P}_{2_4 2_4}^{T_2}$	1	0	0	-1	1	0	-1	-1	0	1

(122)

Without evaluating Equation (122), one may find ten $O \supset C_4$ sub-classes by simply inspecting Figure 22 for operations in each O -class that transform into each other by C_4 operations \mathbf{R}_z^p only. The O -class of eight 120° rotations \mathbf{r}_k split into two sub-classes, one $[r_1, r_2, \tilde{r}_3, \tilde{r}_4]$ whose axes intersect four corners of the $+z$ front square, and the other $[\tilde{r}_1, \tilde{r}_2, r_3, r_4]$ whose axes similarly frame the $-z$ back square. The class of six diagonal 180° rotations \mathbf{i}_k split into a sub-class $[i_1, i_2, i_5, i_6]$ whose two-sided axes bisect edges of the xy squares, and sub-class $[i_3, i_4]$ whose axes are perpendicular to z -axis and bisect edges of xy side squares. The 180° rotational class $[\rho_x, \rho_y, \rho_z]$ splits similarly into sub-classes $[\rho_x, \rho_y]$ and $[\rho_z]$ with axes perpendicular and along, respectively, the \mathbf{R}_z axis. The 90° class splits, as indicated in the top row of Equation (122), into a sub-class of four perpendicular xy -axial rotations and separate sub-classes for R_z and \tilde{R}_z .

The inverse to Equation (121) expresses the ten subclasses in terms of the ten diagonal irrep projectors using the same (albeit, conjugated) array of $D_{n_4 n_4}^\alpha(g_k)$. However, column and row labels must switch and acquire different coefficients.

$$\frac{\mathbf{c}_k}{\circ C_k} = \sum_{k=0}^{10} D_{n_4 n_4}^\alpha(g_k) \mathbf{P}_{n_4 n_4}^\alpha = \sum_{k=0}^{10} \frac{D_{n_4 n_4}^\alpha(\mathbf{c}_k)}{\circ C_k} \mathbf{P}_{n_4 n_4}^\alpha \tag{123}$$

7.1.2. Resolving D-matrices with C_4 Local Symmetry

Off-diagonal $D_{m_4 n_4}^\alpha(g_k)$ matrices derive from products of diagonal irrep projectors in Equation (122) using Equation (82b) repeated here.

$$\mathbf{P}_{j,j}^\alpha \cdot \mathbf{g} \cdot \mathbf{P}_{k,k}^\alpha = D_{j,k}^\alpha(g) \mathbf{P}_{j,k}^\alpha \tag{124}$$

Scalar A_1 and pseudo-scalar A_2 are given first then E , T_1 , and T_2 irrep matrices for the fundamental \mathbf{i}_k -class of O .

$$\begin{aligned} D_{0_4 0_4}^{A_1}(\mathbf{i}_k \mathbf{i}_k) &= i_1 + i_2 + i_3 + i_4 + i_5 + i_6 \\ D_{2_4 2_4}^{A_2}(\mathbf{i}_k \mathbf{i}_k) &= -(i_1 + i_2 + i_3 + i_4 + i_5 + i_6) \end{aligned} \tag{125}$$

$$D^E(\mathbf{i}_k \mathbf{i}_k) = \begin{array}{c|cc|c} & 0_4 & & 2_4 \\ \hline 0_4 & -\frac{1}{2}(i_1 + i_2 + i_5 + i_6) + i_3 + i_4 & & \frac{\sqrt{3}}{2}(i_1 + i_2 - i_5 - i_6) \\ 2_4 & & h.c. & \frac{1}{2}(i_1 + i_2 + i_5 + i_6) - i_3 - i_4 \end{array} \tag{126}$$

$$D^{T_1^*}(\mathbf{i}_k \mathbf{i}_k) = \begin{array}{c|ccc|c} & 1_4 & & 3_4 & & 0_4 \\ \hline 1_4 & -\frac{1}{2}(i_1 + i_2 + i_5 + i_6) & & -\frac{1}{2}(i_1 + i_2 - i_5 - i_6) & & -\frac{1}{\sqrt{2}}(i_1 - i_2) + \frac{i}{\sqrt{2}}(i_5 - i_6) \\ & & & & & -i(i_3 - i_4) \\ 3_4 & & h.c. & -\frac{1}{2}(i_1 + i_2 + i_5 + i_6) & & +\frac{1}{\sqrt{2}}(i_1 - i_2) + \frac{i}{\sqrt{2}}(i_5 - i_6) \\ 0_4 & & h.c. & & h.c. & -(i_3 + i_4) \end{array} \tag{127}$$

$$D^{T_2^*}(\mathbf{i}_k \mathbf{i}_k) = \begin{array}{c|ccc|c} & 1_4 & & 3_4 & & 2_4 \\ \hline 1_4 & +\frac{1}{2}(i_1 + i_2 + i_5 + i_6) & & +\frac{1}{2}(i_1 + i_2 - i_5 - i_6) & & +\frac{1}{\sqrt{2}}(i_1 - i_2) + \frac{i}{\sqrt{2}}(i_5 - i_6) \\ & & & & & -i(i_3 - i_4) \\ 3_4 & & h.c. & +\frac{1}{2}(i_1 + i_2 + i_5 + i_6) & & -\frac{1}{\sqrt{2}}(i_1 - i_2) + \frac{i}{\sqrt{2}}(i_5 - i_6) \\ 0_4 & & h.c. & & h.c. & +(i_3 + i_4) \end{array}$$

Symmetry of $C_4 \subset O$ subclass $[i_1, i_2, i_5, i_6]$ and $[i_3, i_4]$ would demand equality of parameters for each.

$$i_1 = i_2 = i_5 = i_6 \equiv i_{1256} \equiv i_I, \quad \text{and}, \quad i_3 = i_4 \equiv i_{34} \equiv i_{II} \tag{128}$$

Setting each parameter to the inverse of its sub-class order ($i_k=1/(\circ c_{i_k})$) reduces each matrix to diagonal form and gives the diagonal $D_{n_4 n_4}^\alpha(g_k)$ given in Equation (122). Classes r, ρ, R behave similarly.

7.1.3. Resolving Hamiltonians with C_4 Local Symmetry

An octahedral Hamiltonian $\mathbf{H} = \sum_{k=1}^{24} g_k \bar{\mathbf{g}}_k$ with local $C_4(z)$ symmetry is resolved by sorting g_k into its $C_4(z)$ sub-classes c_k and then into $\mathbf{P}_{n_4 n_4}^\alpha$ whose coefficients are the desired \mathbf{H} eigenvalues $\epsilon_{n_4}^\alpha$. Zero off-diagonal $H_{m_4 n_4}^\alpha = 0$ and C_4 -local symmetry conditions shown in Equation (128) arise from Equation (122) consistent with Figure 22. Tunneling parameter $i_{1256} = i_I$ from $+z$ -axis to its 1st-neighbor $\pm x$ or $\pm y$ axes may dominate flip-tunneling $i_{34} = i_{II}$ to 2nd neighbor- z -axis. The i -columns of Equation (122) (or matrix diagonals in Equations (125)–(127)) give i_I and i_{II} contributions to eigenvalues $\epsilon_{n_4}^\alpha$ listed in the i_n -column of Table 11. Clusters $(\epsilon_{0_4}^{A_1}, \epsilon_{0_4}^{T_1}, \epsilon_{0_4}^E)$ through $(\epsilon_{3_4}^{T_2}, \epsilon_{3_4}^{T_1})$ are plotted in Figure 25 for select values of parameters $i_I = i_{1256}$ and $i_{II} = i_{34}$.

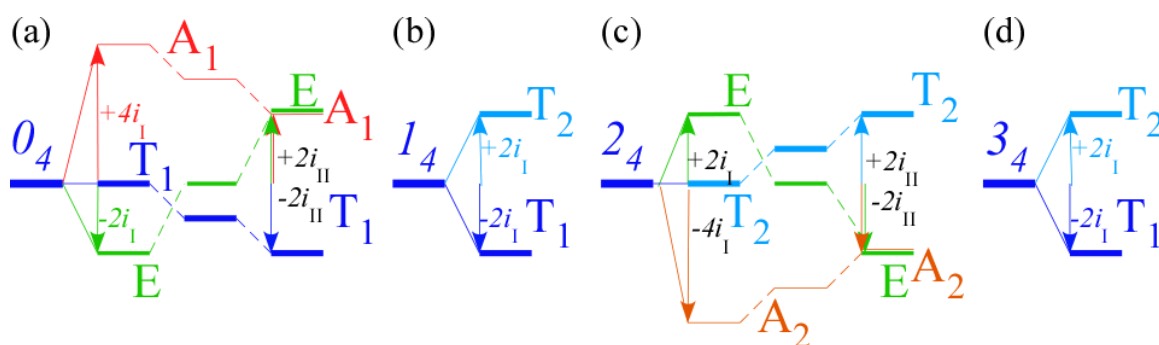
One expects the parameter i_{II} for 2nd-neighbor tunneling to be exponentially smaller than i_I for adjacent tunneling so the ($i_{II} = 0$)-cases are drawn first in Figure 25. While the i -class operations are most fundamental (all operations are generated by products of \mathbf{i}_k) other operations also generate 1st-neighbor transformation. Three class parameters $R_{xy}(90^\circ)$, $r_1(120^\circ)$, and $i_I(180^\circ)$ label 1st-neighbor

inter- C_4 axial tunneling paths that have the same i_I -level patterns and splitting ratios as ($i_{II}=0$)-cases in Figure 25 but with differing sign. (Signs differ since each sub-class eigenvalue set must be orthogonal to all others as shown below.) Level patterns in Figure 25 are reflected in spectral patterns of Figure 26 if both ground and excited vib-rotor states have similar RES-shape. However, only C_{4z} sub-class $i_I(180^\circ)$ patterns (with $i_I < 0$) exhibit spectral ordering $(A_1T_1E)(T_2T_1)(ET_2A_2)(T_2T_1)$ on the left hand side of Figure 26 that is maintained even as levels re-cluster into patterns $(T_1ET_2)(T_1ET_2)(A_2T_2T_1A_1)$ of $C_{3[111]}$ local symmetry across the separatrix break on the right-hand side of Figure 26 as analyzed below [8,37]. O -crystal-field wavefunctions for either case tend to follow a Bohr-orbital progression $s(A_1), p(T_1), d(E, T_2), f(T_1, A_2, T_2), g(E, T_1, T_2, A_1), \dots$. In general, ordering is sensitive to RES-shape and tensor rank as discussed later.

Table 11. Splittings of $O \supset C_4$ given sub-class structure.

$O \supset C_4$	0°	$r_n 120^\circ$	$\rho_n 180^\circ$	$R_n 90^\circ$	$i_n 180^\circ$
0_4	.	$r_I = \text{Re } r_{1234}$ $m_I = \text{Im } r_{1234}$.	$R_z = \text{Re } R_z$ $I_z = \text{Im } R_z$	$i_I = i_{1256}$ $i_{II} = i_{34}$
$\varepsilon_{0_4}^{A_1} =$	g_0	$+8r_I$	$+2\rho_{xy} + \rho_z$	$+4R_{xy} + 2R_z$	$+4i_I + 2i_{II}$
$\varepsilon_{0_4}^{T_1}$	g_0	0	$-2\rho_{xy} + \rho_z$	$+2R_z$	$-2i_{II}$
$\varepsilon_{0_4}^E$	g_0	$-2r_I$	$+2\rho_{xy} + \rho_z$	$-2R_{xy} - R_z$	$-2i_I + 2i_{II}$
1_4
$\varepsilon_{1_4}^{T_2}$	g_0	$+2m_I$	$-\rho_z$	$-R_{xy} - 2I_z$	$+2i_I$
$\varepsilon_{1_4}^{T_1}$	g_0	$-2m_I$	$-\rho_z$	$+R_{xy} - 2I_z$	$-2i_I$
2_4
$\varepsilon_{2_4}^E$	g_0	$-2r_I$	$+2\rho_{xy} + \rho_z$	$+2R_{xy} - R_z$	$+2i_I - 2i_{II}$
$\varepsilon_{2_4}^{T_2}$	g_0	0	$-2\rho_{xy} + \rho_z$	$-2R_z$	$+2i_{II}$
$\varepsilon_{2_4}^{A_2}$	g_0	$+8r_I$	$+2\rho_{xy} + \rho_z$	$-4R_{xy} - 2R_z$	$-4i_I - 2i_{II}$
3_4
$\varepsilon_{3_4}^{T_2}$	g_0	$-2m_I$	$-\rho_z$	$-R_{xy} + 2I_z$	$+2i_I$
$\varepsilon_{3_4}^{T_1}$	g_0	$+2m_I$	$-\rho_z$	$+R_{xy} + 2I_z$	$-2i_I$

Figure 25. O i -class level clusters of C_4 local symmetry (a) 0_4 ; (b) 1_4 ; (c) 2_4 ; (d) 3_4 .

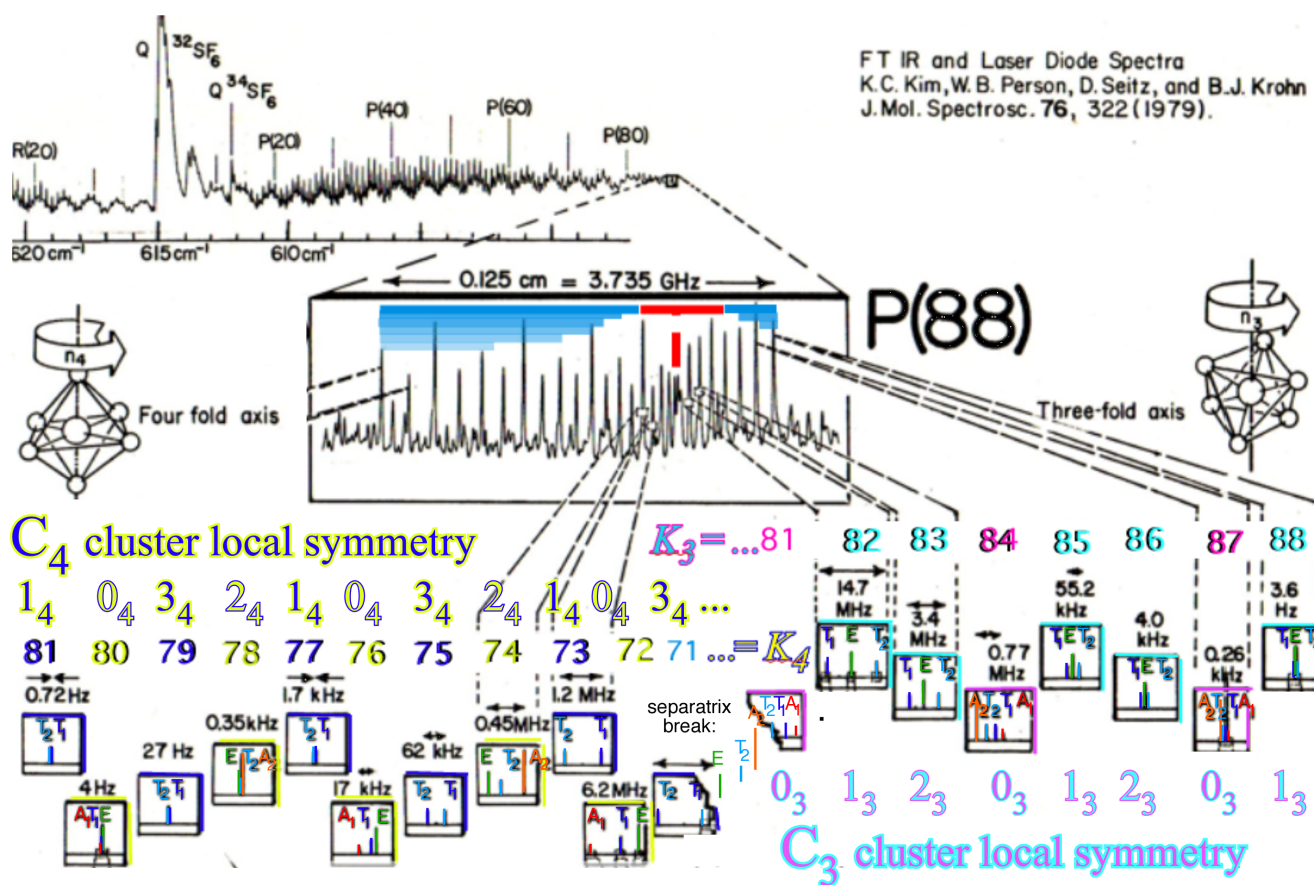


For an isolated three-level (ATE)-cluster of local symmetry 0_4 or else 2_4 the splitting pattern requires only two parameters. This could be either the $180^\circ(i_I, i_{II})$ or the $90^\circ(R_{xy}, R_z)$ class pair in Table 11. The

120°-class, lacking 180° flips, has just one real parameter r_I . Parameters i_I , R_{xy} , and r_I each split (ATE) by 2:1 ratio but differ in sign.

Local symmetry 1_4 and 3_4 each have two-level (TT) clusters that require just one splitting parameter, say i_I , or else R_{xy} . Complex parameters R_z and I_z of the $90^\circ R_n$ -class and the $\rho_n(180^\circ)$ -class in Table 11 may play minor roles in most C_4 clusters but are necessary in order that the whole set be orthonormal and complete.

Figure 26. Excerpts of $SF_6 \nu_4 P(88)$ superfine spectral cluster structure in $16\mu m$ region (Missing: $K_4=82\dots 88$).



7.1.4. Orthogonality-Completeness of Local Symmetry Parameters

Equation (122) expands $P_{nn}^{(\alpha)}$ by Equation (83) in group operators $(1, r_1, r_2, \dots, i_6)$. It acts on $|1\rangle$ to give $|_{n_4 n_4}^{(\alpha)}\rangle$ eigenkets in Equation (129).

$$\begin{aligned}
 |_{nn}^{(\alpha)}\rangle &= P_{nn}^{(\alpha)} |1\rangle \sqrt{\frac{\ell^\alpha}{\ell^\alpha}} = \sqrt{\frac{\ell^\alpha}{\ell^\alpha}} \sum_{b=1}^{\circ G} D_{nn}^{(\alpha)*}(g_b) \mathbf{g}_b |1\rangle \\
 &= \sqrt{\frac{\ell^\alpha}{\ell^\alpha}} \sum_{b=1}^{\circ G} D_{nn}^{(\alpha)*}(g_b) |g_b\rangle
 \end{aligned}
 \tag{129}$$

An O -symmetric \mathbf{H} matrix is a sum of *dual* operators $(\bar{\mathbf{1}}, \bar{r}_1, \bar{r}_2, \dots, \bar{i}_6)$ with coefficients $g_a = \epsilon_0, r_1, r_2, \dots, i_6$. Local symmetry C_4 or C_3 reduces the sum to $\rho_G = 10$ sub-class terms $\bar{c}_a = \bar{g}_a + \bar{g}'_a + \dots$ each sharing a coefficient $g_a = g'_a \dots$

$$\mathbf{H} = \sum_{a=1}^{\circ G} g_a \bar{\mathbf{g}}_a = \sum_{a=1}^{\rho_G} g_a \bar{c}_a \tag{130}$$

From these arise expansions like Table 11 of \mathbf{H} eigenvalues ϵ_n^α in terms of its coefficients g_a . Dual commutation $\mathbf{g}_j \bar{\mathbf{g}}_k = \bar{\mathbf{g}}_k \mathbf{g}_j$ makes $\mathbf{P}_{nn}^{(\alpha)}$ and \mathbf{H} commute. Duality relation in Equation (94) leads to a $D^{\alpha*}$ -weighted sum of g_a analogous to sum in Equation (129) of $|g_a\rangle$.

$$\begin{aligned} \epsilon_n^\alpha &= \langle \mathbf{1} | \mathbf{H} | \mathbf{1} \rangle = \langle \mathbf{1} | \mathbf{P}_{nn}^{(\alpha)} \mathbf{H} \mathbf{P}_{nn}^{(\alpha)} | \mathbf{1} \rangle \frac{\circ G}{\ell^\alpha} = \langle \mathbf{1} | \mathbf{H} \mathbf{P}_{nn}^{(\alpha)} | \mathbf{1} \rangle \frac{\circ G}{\ell^\alpha} = \langle \mathbf{1} | \sum_{a=0}^{\circ G} g_a \bar{\mathbf{g}}_a \sum_{b=0}^{\circ G} D_{nn}^{(\alpha)*}(g_b) \mathbf{g}_b | \mathbf{1} \rangle \\ &= \langle \mathbf{1} | \sum_{a=0}^{\circ G} g_a \sum_{b=0}^{\circ G} D_{nn}^{(\alpha)*}(g_b) \mathbf{g}_b \mathbf{g}_a^{-1} | \mathbf{1} \rangle = \sum_{a=0}^{\circ G} g_a D_{nn}^{(\alpha)*}(g_a) = \sum_{a=1}^{\rho_G} D_{nn}^{(\alpha)*}(g_a) \circ c_a g_a \end{aligned} \tag{131}$$

Each C_4 sub-class of order $\circ c_a$ has $\circ c_a$ equal terms $g_a D_{nn}^{(\alpha)*}(g_a) = g'_a D_{nn}^{(\alpha)*}(g'_a) = \dots$ expanding eigenvalue ϵ_n^α . Rank-of-group $\rho_G = 10$ is the number of eigenvalues and of expansion terms $\circ c_a g_a D_{nn}^{(\alpha)*}(g_a)$ in Equation (131) or Table 11. Each of ten eigenvalues $\epsilon_n^\alpha = (\epsilon^{A_1}, \epsilon^{A_2}, \dots, \epsilon^{T_2})$ expand to ten C_4 -local tunneling parameters $g_a = (\epsilon_0, r_1, r_2, \dots, i_6)$ and *vice-versa*.

$$\begin{aligned} g_a &= \langle \mathbf{1} | \mathbf{H} | g_a \rangle = \langle \mathbf{1} | \mathbf{H} \mathbf{g}_a | \mathbf{1} \rangle = \sum_{\alpha} \sum_j^{\ell^\alpha} \sum_k^{\ell^\alpha} D_{jk}^{(\alpha)}(g_a) \langle \mathbf{1} | \mathbf{H} \mathbf{P}_{jk}^\alpha | \mathbf{1} \rangle \\ &= \sum_{\alpha} \sum_n^{\ell^\alpha} D_{nn}^{(\alpha)}(g_a) \langle \mathbf{1} | \mathbf{H} \mathbf{P}_{nn}^\alpha | \mathbf{1} \rangle = \sum_{\alpha} \sum_n^{\ell^\alpha} D_{nn}^{(\alpha)}(g_a) \frac{\ell^\alpha}{\circ G} \epsilon_n^\alpha \end{aligned} \tag{132}$$

One might count twelve real parameters in Table 11 since both pairs (r_1, \tilde{r}_1) and (R_z, \tilde{R}_z) are complex, unlike $R_1 = \tilde{R}_1$, which are real. If H is a Hermitian array ($H = H^\dagger$) it should only require ten, the rank of O , for its ten distinct real eigenvalues and the parameter pairs must be complex conjugates.

With no conjugation symmetry, such as for a *unitary* $O \supset C_4$ -symmetric matrix, the R and r parameters may be complex and unrelated to \tilde{R} and \tilde{r} , and resulting extra real parameters are then needed. Symmetry parameter dimension matches eigensolution dimension for each local symmetry as shown in Figure 27.

7.1.5. Resolving Hamiltonians with C_3 Local Symmetry

The previous two sections have detailed of symmetry-based level clustering and cluster splitting for C_4 . In Figure 26 these are the lower energy clusters of SF_6 for $\nu_4 P(88)$. Given the previous two sections, it is possible to find the splittings of the C_3 sub-group quickly. Starting with Equation (117) and Equation (118) one can build the irreducible representations necessary to create the $\mathbf{P}_{n_3 n_3}^\alpha$ for the new sub-group. At this point, one can create a table analogous to Table 11. Such a table for C_3 is shown in Table 12. The C_3 clustering fits patterns of (A_1, A_2, T_2, T_2) and two of (E, T_1, T_2) , each with a total

degeneracy of 8. As before in Figure 25, the splittings in C_3 make different patterns depending on which tunneling parameters are active. This is demonstrated in Figure 28.

Figure 27. $O \subset L$ -local symmetry eigenmatrix parameters (a–e) $L=C_4, \dots, C_1$ (f–j) $L=O, D_4, \dots, D_2$.

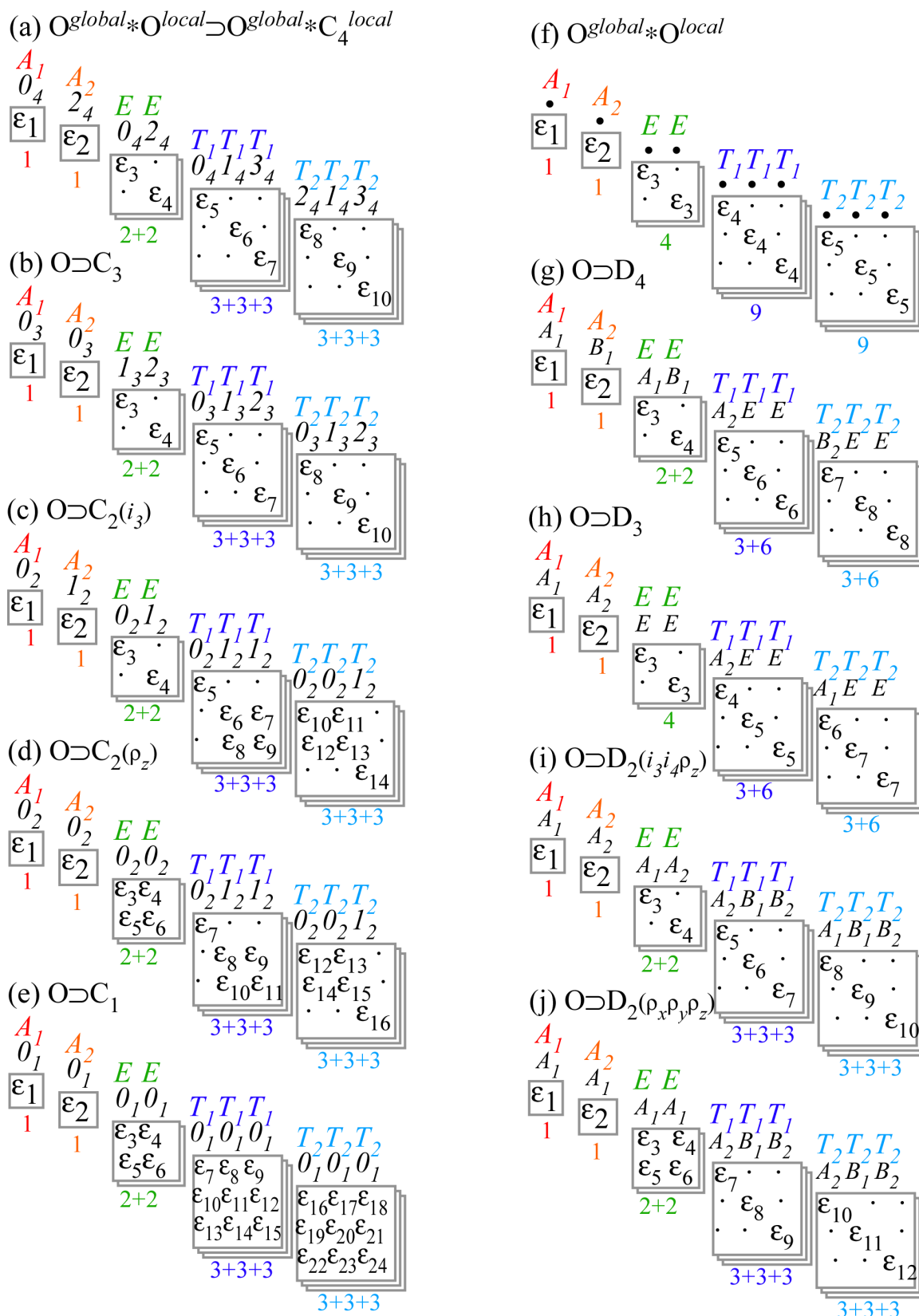
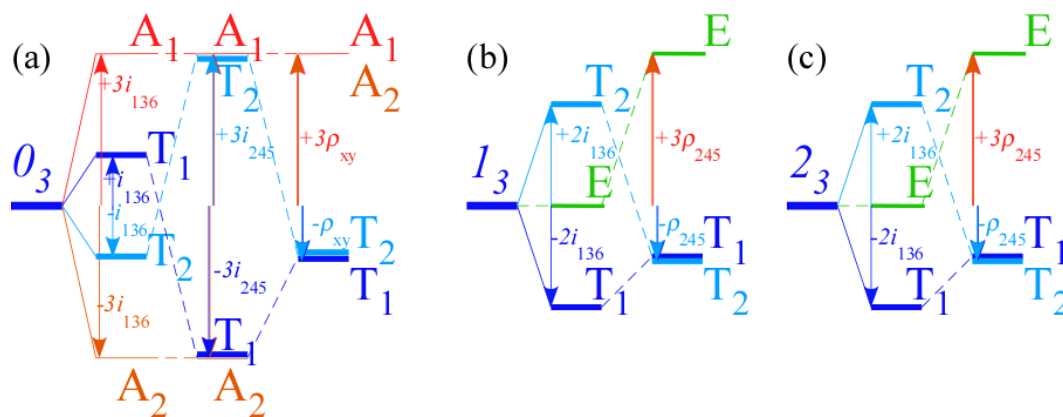


Table 12. Splittings of $O \supset C_3$ given sub-class structure.

$O \supset C_3$	0°	$r_n 120^\circ$	$\rho_n 180^\circ$	$R_n 90^\circ$	$i_n 180^\circ$
0_3	.	$r_I = Re(r_1) \quad i_I = Im(r_1)$ $r_{II} = Re(r_{234}) \quad i_{II} = Im(r_{234})$	$\rho = \rho_{xyz}$	$R_n = Re(R_{xyz})$ $I_n = Im(R_{xyz})$	$i_I = i_{136}$ $i_{II} = i_{245}$
$\varepsilon_{0_3}^{A_1}$	g_0	$2r_I + 6r_{II}$	3ρ	$6R_n$	$3i_I + 3i_{II}$
$\varepsilon_{0_3}^{A_2}$	g_0	$2r_I + 6r_{II}$	3ρ	$-6R_n$	$-3i_I - 3i_{II}$
$\varepsilon_{0_3}^{T_1}$	g_0	$2r_I - 2r_{II}$	$-\rho$	$2R_n$	$i_I - 3i_{II}$
$\varepsilon_{0_3}^{T_2}$	g_0	$2r_I - 2r_{II}$	$-\rho$	$-2R_n$	$-i_I + 3i_{II}$
1_3					
$\varepsilon_{1_3}^E$	g_0	$-r_I + \sqrt{3}i_I - 3r_{II} + 3\sqrt{3}i_{II}$	3ρ	0	0
$\varepsilon_{1_3}^{T_1}$	g_0	$-r_I + \sqrt{3}i_I + r_{II} - \sqrt{3}i_{II}$	$-\rho$	$2R_n + 2\sqrt{3}I_n$	$-2i_I$
$\varepsilon_{1_3}^{T_2}$	g_0	$-r_I + \sqrt{3}i_I + r_{II} - \sqrt{3}i_{II}$	$-\rho$	$-2R_n - 2\sqrt{3}I_n$	$2i_I$
2_3					
$\varepsilon_{2_3}^E$	g_0	$-r_I - \sqrt{3}i_I - 3r_{II} - 3\sqrt{3}i_{II}$	3ρ	0	0
$\varepsilon_{2_3}^{T_1}$	g_0	$-r_I - \sqrt{3}i_I + r_{II} + \sqrt{3}i_{II}$	$-\rho$	$2R_n - 2\sqrt{3}I_n$	$-2i_I$
$\varepsilon_{2_3}^{T_2}$	g_0	$-r_I - \sqrt{3}i_I + r_{II} + \sqrt{3}i_{II}$	$-\rho$	$-2R_n + 2\sqrt{3}I_n$	$2i_I$

Figure 28. O i -class and ρ -class level clusters of C_3 local symmetry given different tunneling parameters.



7.1.6. Octahedral Splitting for a Range of Local Symmetry $C_1 \subset C_2 \dots \subset O$

As the order $^\circ L$ of local symmetry $L \subset G$ decreases there are proportionally fewer types of local symmetry irrep $d^\lambda(L)$ and hence fewer types of energy level cluster since each cluster is defined by its induced representation $d^\lambda(L) \uparrow G$. There is a proportional increase in total number $\ell^{\lambda \uparrow G} = (\ell^\lambda)^\circ G / L$ of levels in each eigenvalue cluster. However, G -symmetry degeneracy limits the total number of *distinct* eigenvalues from all clusters to be global rank $\rho(G)$ or less, no matter what local symmetry is in effect. Octahedral rank is $\rho(O) = 10 = \ell^{A_1} + \ell^{A_2} + \ell^E + \ell^{T_1} + \ell^{T_2}$ where ℓ^α gives both the global degeneracy of each level type and the number of times it appears.

The number of H -matrix parameters equals the number of distinct eigenvalues as long as all *eigenvectors* are determined by global-local symmetry, that is, each entry is 0 or 1 in the $G \supset L$

correlation array. Diagonal eigenmatrix forms are shown in Figure 27a,b for $C_4 \subset O$ and $C_3 \subset O$ for which all bases states are distinctly labeled. Multiple correlation (≥ 2) occurs if L -symmetry is too small to determine some of the oG eigenbases. Then the H -matrix must have extra parameters that fix vectors through diagonalization.

This happens for the $C_2(\mathbf{i}_1) \subset O$ symmetry whose correlation array in Equation (117) assigns the same C_2 label to two bases of T_1 and of T_2 . (Two C_2 symmetries 0_2 and 1_2 cannot distinctly label three bases.) Figure 22 shows $C_2(\mathbf{i}_1)$ splits O into fourteen sub-classes: $(\mathbf{1})$, $(\mathbf{r}_1\tilde{\mathbf{r}}_4)$, $(\mathbf{r}_2\tilde{\mathbf{r}}_2)$, $(\mathbf{r}_3\tilde{\mathbf{r}}_3)$, $(\mathbf{r}_4\tilde{\mathbf{r}}_1)$, $(\rho_x\rho_z)$, (ρ_y) , $(\mathbf{R}_x\mathbf{R}_z)$, $(\tilde{\mathbf{R}}_x\tilde{\mathbf{R}}_z)$, $(\mathbf{R}_y\tilde{\mathbf{R}}_y)$, (\mathbf{i}_1) , (\mathbf{i}_2) , $(\mathbf{i}_3\mathbf{i}_5)$, $(\mathbf{i}_4\mathbf{i}_6)$. The $C_2 \subset O$ sub-classes form a non-commutative algebra and cannot be resolved so easily as $C_3 \subset O$ or $C_4 \subset O$ into commuting idempotent combinations like Equation (123).

Spectral resolution of fourteen $C_2(\mathbf{i}_1) \subset O$ sub-classes requires more than rank number $\rho(O)=10$ of diagonal commuting O idempotents \mathbf{P}_{nn}^α . To fully determine C_2 basis, two off-diagonal pairs $\mathbf{P}_{ab}^{T_1}=\mathbf{P}_{ba}^{T_1\dagger}$ and $\mathbf{P}_{ab}^{T_2}=\mathbf{P}_{ba}^{T_2\dagger}$ of non-commuting nilpotent projectors are needed to finish C_2 -labeling of T -triplets. Adding these four gives fourteen projectors with their fourteen parameter coefficients ϵ_ℓ shown in Figure 27c to fully define general $C_2(\mathbf{i}_1) \subset O$ H -operators. (However, only twelve of the fourteen parameters are independent for Hermitian $H_{a,b}=H_{b,a}^*$.)

The other class of C_2 symmetry has similar problems. Local $C_2(\rho_z) \subset O$ symmetry requires projector pairs $\mathbf{P}_{ab}^{T_1}=\mathbf{P}_{ba}^{T_1\dagger}$ and $\mathbf{P}_{ab}^{T_2}=\mathbf{P}_{ba}^{T_2\dagger}$, too, but then another nilpotent pair $\mathbf{P}_{ab}^E=\mathbf{P}_{ba}^{E\dagger}$ must be added to label repeated E bases in array Equation (117). This gives sixteen $C_2(\rho_z)$ sub-classes to resolve and sixteen parameters sketched in Figure 27d. (Hermitian $H=H^\dagger$ matrices for $C_2(\rho_z) \subset O$ have thirteen free parameters.)

For the lowest local symmetry $C_1=[\mathbf{1}]$ (*i.e.*, no local symmetry) sub-classes are completely split since every O -operator is invariant to $\mathbf{1}$ as C_1 provides no distinguishing labeling, and all twenty-four O -projectors ($\Sigma_\alpha(\ell^\alpha)^2=24$) are active in its resolution. The 24-parameter H -matrix resolution is sketched in Figure 27e. Each parameter ϵ_a for $a=1, \dots, 24$ is a combination of 24 products $D_{j,k}^{\alpha*}(g_p)g_p$ ($p=1, \dots, 24$) of irrep and group element coefficient g_p as given in Equation (90) or (131). (If H is Hermitian the number of free parameters reduces to $\Sigma_\alpha \ell^\alpha(\ell^\alpha+1)=17$.)

For O 's highest local symmetry, namely O itself, there is no splitting of the $\Sigma_\alpha(\ell^\alpha)^0=5$ invariant idempotents \mathbf{P}^α that resolve the five O classes. Then H has five independent parameters and five eigenvalues of degeneracy $(\ell^\alpha)^2$. This 5-parameter resolution is sketched in Figure 27f. Total level degeneracy for sub-matrix eigenvalues are listed below each one, and show less splitting than Abelian cases listed in Figure 27a–e.

Any non-Abelian local symmetry such as $L = D_4$ also fails to split \mathbf{P}^α into a full number ℓ^α of components \mathbf{P}_{nn}^α if O irrep- (α) correlates with multi-dimensional L -irreps. By splitting out less than the full rank number $\rho(O)=10$ of idempotent projectors \mathbf{P}_{nn}^α , the resulting number of independent H matrix parameters reduces accordingly. The 8-parameter resolution for an H -matrix with $D_4 \subset O$ is sketched in Figure 27g and similarly for $D_3 \subset O$ in Figure 27h. Two kinds of $D_2 \subset O$ in Figure 27i,j share degeneracy sums with the Abelian cases.

Each matrix display lists *exact* degeneracy ℓ^α due to *global* symmetry O but not the cluster *quasi*-degeneracy $\ell^{\lambda \uparrow G}$ due to *local* symmetry induced representation $d^\lambda(L) \uparrow G$. The latter is found

by summing global degeneracy ℓ^α of all states $|\alpha_{a,\lambda}\rangle$ with the same local symmetry λ as per Frobenius reciprocity in Equation (106). The result is integer $\ell^{\lambda \uparrow G} = (\ell^\lambda)^\circ G / L$ mentioned above.

8. Spectral Resolution of full O_h Symmetry

Including inversion **I** and reflection operations σ_n allows parity correlations between even-*g* (*gerade*) and odd-*u* (*ungerade*) states. Two classes of C_2 subgroups lie in O and appear in separate C_2 -correlations in Equation (117). In the following O_h correlations Equation (133), the two types of C_{2v} subgroups have separate tables. The first subgroup $C_{2v}^i = [\mathbf{1}, \sigma_y, \mathbf{i}_1, \sigma_2]$ is the one of the three local symmetries shown in Figure 12 while the second $C_{2v}^z = [\mathbf{1}, \rho_z, \sigma_y, \sigma_x]$ is just a subgroup of local symmetry C_{4v} as would be $C_{2v}^{34} = [\mathbf{1}, \rho_z, \sigma_3, \sigma_4]$.

$O_h \downarrow C_{4v}$	A'	B'	A''	B''	E	C_{3v}	A'	A''	E	
$A_{1g} \downarrow C_{4v}$	1	A_{1g}	1	.	.	
$A_{2g} \downarrow C_{4v}$.	1	.	.	.	A_{2g}	.	1	.	
$E_g \downarrow C_{4v}$	1	1	.	.	.	E_g	.	.	1	
$T_{1g} \downarrow C_{4v}$.	.	1	.	1	T_{1g}	.	1	1	
$T_{2g} \downarrow C_{4v}$.	.	.	1	1	T_{2g}	1	.	1	
$A_{1u} \downarrow C_{4v}$.	.	1	.	.	A_{1u}	.	1	.	
$A_{2u} \downarrow C_{4v}$.	.	.	1	.	A_{2u}	1	.	.	
$E_u \downarrow C_{4v}$.	.	1	1	.	E_u	.	.	1	
$T_{1u} \downarrow C_{4v}$	1	.	.	.	1	T_{1u}	1	.	1	
$T_{2u} \downarrow C_{4v}$.	1	.	.	1	T_{2u}	.	1	1	
C_{2v}^i	A'	B'	A''	B''		C_{2v}^z	A'	B'	A''	B''
A_{1g}	1	.	.	.		A_{1g}	1	.	.	.
A_{2g}	.	1	.	.		A_{2g}	1	.	.	.
E_g	1	1	.	.		E_g	2	.	.	.
T_{1g}	.	1	1	1		T_{1g}	.	1	1	1
T_{2g}	1	.	1	1		T_{2g}	.	1	1	1
A_{1u}	.	.	1	.		A_{1u}	.	.	1	.
A_{2u}	.	.	.	1		A_{2u}	.	.	1	.
E_u	.	.	1	1		E_u	.	.	2	.
T_{1u}	1	1	.	1		T_{1u}	1	1	.	1
T_{2u}	1	1	1	.		T_{2u}	1	1	.	1

(133)

The local symmetry $C_{2v}^i \subset O_h$ unambiguously defines all states in its correlation array while the other C_{2v} symmetries fail to split the E_g and E_u sub-species. The former lead to complete eigenvalue formulae. The latter may not.

8.1. Resolving Hamiltonians with C_{2v} Local Symmetry

As the order of the local sub-group symmetry goes down, the degeneracy and complexity of the rotational cluster must increase. $O_h \supset C_{2v}$ clusters are 12 fold degenerate and come in 4 cluster species.

Matrices describing this system are larger, but $O \supset C_2$ will show many of the same effects. To actually resolve the doubled T_1 or T_2 triplets of $O \supset C_2$ requires distinguishing the u and g versions of each. The C_2 clusters are 12 fold degenerate, but they are also easily displayed.

As noted earlier, $O \supset D_3 \supset C_2$ and $O \supset D_4 \supset C_2$ local symmetries give identical cluster degeneracies and groupings, but with cluster splittings and structure dependent on the sub-group chain. Though it neglects inversion, Figure 27 indicates that there are several different types of $O \supset C_2$ (and, thus $O_h \supset C_{2v}$ local sub-group symmetries). Examples given here involve the $O \supset D_4 \supset C_2(i_4)$ sub-group chain.

Compared with $O \supset C_4$ and $O \supset C_3$, the splittings of $O \supset C_2$ are relatively simple to calculate since the terms in Equation (131) will be real. Creating splitting tables for C_2 is done in the same way as for Tables 11 and 12. It is shown in Table 13.

Table 13. Splittings of $O \supset C_2(i_4)$ given sub-class structure.

$O \supset D_4$ $\supset C_2(i_4)$	0°	$r_n 120^\circ$	$\rho_n 180^\circ$	$R_n 90^\circ$	$i_n 180^\circ$
0_2					
$\varepsilon_{0_2}^{A_1}$	g_0	$4r_{12} + 4r_{34}$	$2\rho_{xy} + \rho_z$	$4R_{xy} + 2R_z$	$4i_{1256} + i_3 + i_4$
$\varepsilon_{0_2}^E$	g_0	$-2r_{12} - 2r_{34}$	$2\rho_{xy} + \rho_z$	$-2R_{xy} + 2R_z$	$-2i_{1256} + i_3 + i_4$
$\varepsilon_{0_2}^{T_1}$	g_0	$-2r_{12} + 2r_{34}$	$-\rho_z$	$2R_{xy}$	$-2i_{1256} - i_3 + i_4$
$\varepsilon_{0_2}^{T_2E}$	g_0	$2r_{12} - 2r_{34}$	$-\rho_z$	$-2R_{xy}$	$2i_{1256} - i_3 + i_4$
$\varepsilon_{0_2}^{T_2A_1}$	g_0	0	$-2\rho_{xy} + \rho_z$	$-2R_z$	$i_3 + i_4$
1_2					
$\varepsilon_{1_2}^{A_2}$	g_0	$4r_{12} + 4r_{34}$	$2\rho_{xy} + \rho_z$	$-4R_{xy} - 2R_z$	$-4i_{1256} - i_3 - i_4$
$\varepsilon_{1_2}^E$	g_0	$-2r_{12} - 2r_{34}$	$2\rho_{xy} + \rho_z$	$2R_{xy} - 2R_z$	$2i_{1256} - i_3 - i_4$
$\varepsilon_{1_2}^{T_1E}$	g_0	$2r_{12} - 2r_{34}$	$-\rho_z$	$2R_z$	$-2i_{1256} + i_3 - i_4$
$\varepsilon_{1_2}^{T_1A_2}$	g_0	0	$-2\rho_{xy} + \rho_z$	$-2R_z$	$-i_3 - i_4$
$\varepsilon_{1_2}^{T_2E}$	g_0	$-2r_{12} + 2r_{34}$	$-\rho_z$	$-2R_{xy}$	$2i_{1256} + i_3 - i_4$

8.1.1. Local Sub-Group Tunneling Matrices and Their Inverse

Table 13 can be further broken apart to demonstrate how one can create an automated process to evaluate the tunneling splittings for $O \supset C_2$ local-symmetry structures. What will result is a transformation between cluster-splitting energy and tunneling parameters. The inverse of this transformation is also easily defined.

Equation (131) produces Table 13, but even after combining splittings from each subclass, repetition exists. We show the two steps to convert Table 13 into the transformation matrix just described. First we assume that only n_m levels may interact with themselves, e.g., that a 1_2 cluster may not interact with a 0_2 cluster. Second we recognize that only half of the subclasses are needed to fully define the possible splittings, the others simply repeat the same information. Table 13 shows this for the 0_2 cluster. Looking at the A_1 level in the 0_2 cluster, one can see that the subclasses $1, r_n, \rho_n$ make a vector $\{1, 4, 4, 2, 1\}$ while the R_n, i_n subclasses make a vector $\{4, 2, 4, 1, 1\}$. These vectors are reordered versions of each

other. Thus only one is needed. The A_2 level in the 1_2 cluster shows the same similarity, but the R_n, i_n now contain a negative sign.

By using only the minimum number of splitting parameters and including only a single cluster gives a condensed version of Table 13 that acts as a transformation that inputs symmetry-based tunneling values and outputs energy levels. Such a table is shown in Table 14. A simple inverse of the matrix in Table 14 will produce the transformation giving tunneling parameters for a given set of cluster energy splittings, as shown in Table 15.

Table 14. Matrix that converts tunneling strengths to cluster splitting energies.

0_2	1	r_{12}, i_{1256}	r_{34}, R_{xy}	ρ_{xy}, R_z	ρ_z, i_3
$\varepsilon_{0_2}^{A_1}$	1	4	4	2	1
$\varepsilon_{0_2}^E$	1	-2	-2	2	1
$\varepsilon_{0_2}^{T_1}$	1	-2	2	0	-1
$\varepsilon_{E,0_2}^{T_2}$	1	2	-2	0	-1
$\varepsilon_{A_1,0_2}^{T_2}$	1	0	0	-2	1

Table 15. Matrix that converts cluster splitting energies to tunneling strengths.

0_2	$\varepsilon_{0_2}^{A_1}$	$\varepsilon_{0_2}^E$	$\varepsilon_{0_2}^{T_1}$	$\varepsilon_{E,0_2}^{T_2}$	$\varepsilon_{A_1,0_2}^{T_2}$
1	$\frac{1}{12}$	$\frac{1}{6}$	$\frac{1}{4}$	$\frac{1}{4}$	$\frac{1}{4}$
r_{12}, i_{1256}	$\frac{1}{12}$	$-\frac{1}{12}$	$-\frac{1}{8}$	$\frac{1}{8}$	0
r_{34}, R_{xy}	$\frac{1}{12}$	$-\frac{1}{12}$	$\frac{1}{8}$	$-\frac{1}{8}$	0
ρ_{xy}, R_z	$\frac{1}{12}$	$\frac{1}{6}$	0	0	$-\frac{1}{4}$
ρ_z, i_3	$\frac{1}{12}$	$\frac{1}{6}$	$-\frac{1}{4}$	$-\frac{1}{4}$	$\frac{1}{4}$

There are multiple ways to use Tables 14 and 15. Among the most useful is to use the columns of Table 14 as a predictor of possible splitting patterns. Using the inverse matrix to find spectroscopic tunneling parameters from cluster splittings may also become a useful and automated process.

An example demonstrates this process for a model (4, 6)-octahedral-Hecht spherical-top Hamiltonian Equation (134) with varying spectroscopic parameters. The terms $T^{[4]}$ and $T^{[6]}$ model rotational distortions written in an octahedral basis of fourth and sixth order respectively in J . The parameter θ is varied to explore the different relative contributions of $T^{[4]}$ and $T^{[6]}$ while keeping them normalized. Because $T^{[4]}$ and $T^{[6]}$ each have octahedral symmetry, Equation (134) represents all possible octahedral pure rotational Hamiltonians up to sixth order.

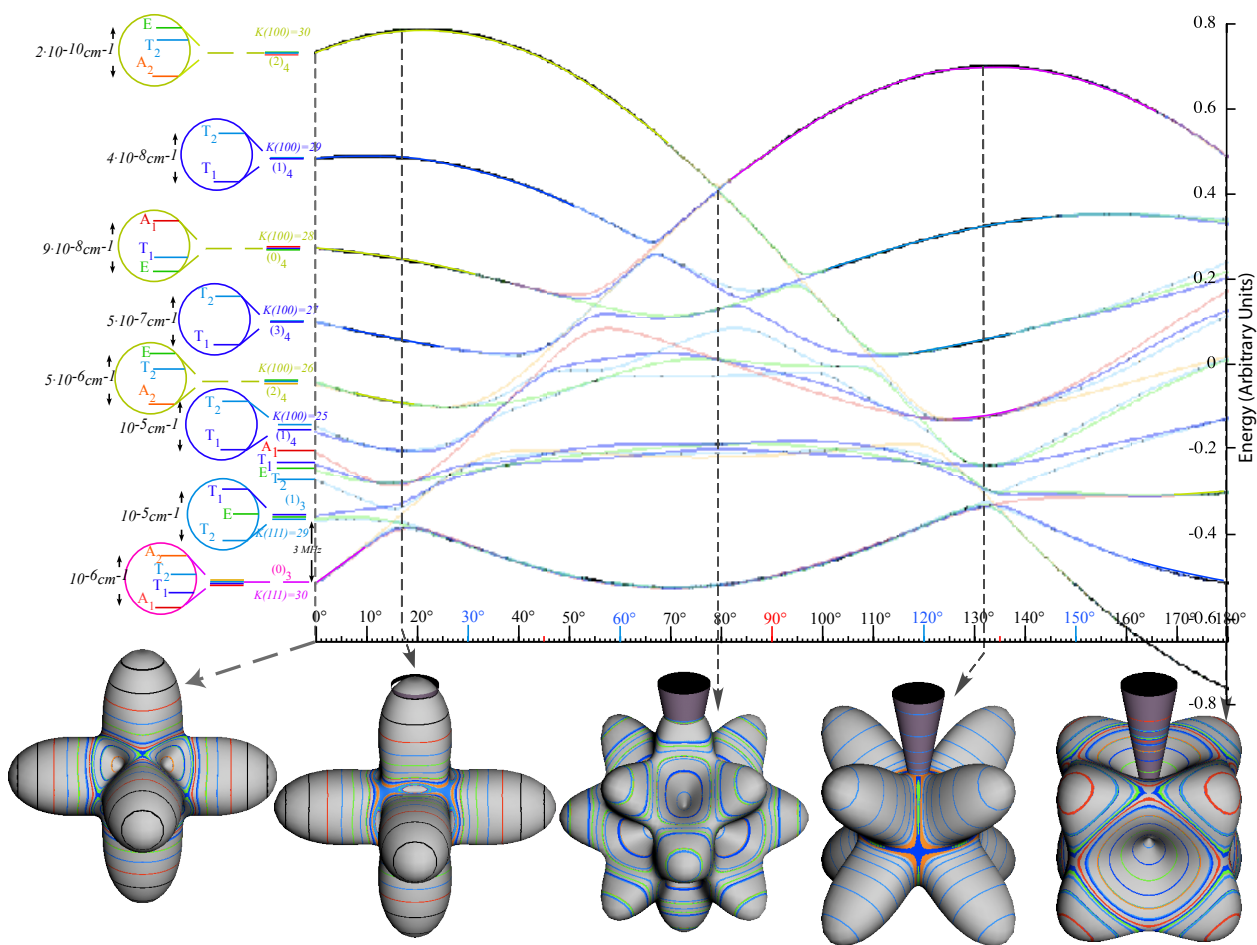
$$H = BJ^2 + \cos(\theta)T^{[4]} + \sin(\theta)T^{[6]} \tag{134}$$

As noted in Section 3 cluster structure location and the RES shape will change significantly as the Hamiltonian parameters change in Equation (134) as Figure 29 (a copy of Figure 6) shows by plotting

rotational energy levels of Equation (134) for changing θ with corresponding RES at points along the θ axis. RES plots in the figure demonstrate how the phase-space changes as θ varies.

RES diagrams in Figure 29 along with the cluster degeneracy indicate where in the parameter-space C_2 clusters exist. The lowest $0_2(C_2)\uparrow O$ cluster in Figure 29 for θ between 18° and 132° labels a kaleidoscope of 12 waves each with C_2 local symmetry. Its superfine levels are magnified about 100 times in the central inside plot of Figure 30 which has been adjusted to show level splittings but not whole cluster shifting. (The θ -dependent cluster center-of-energy is subtracted.) The locally antisymmetric $1_2(C_2)\uparrow O$ clusters contain quite similar superfine structure but with A_2 replacing A_1 and T_1 switched with T_2 .

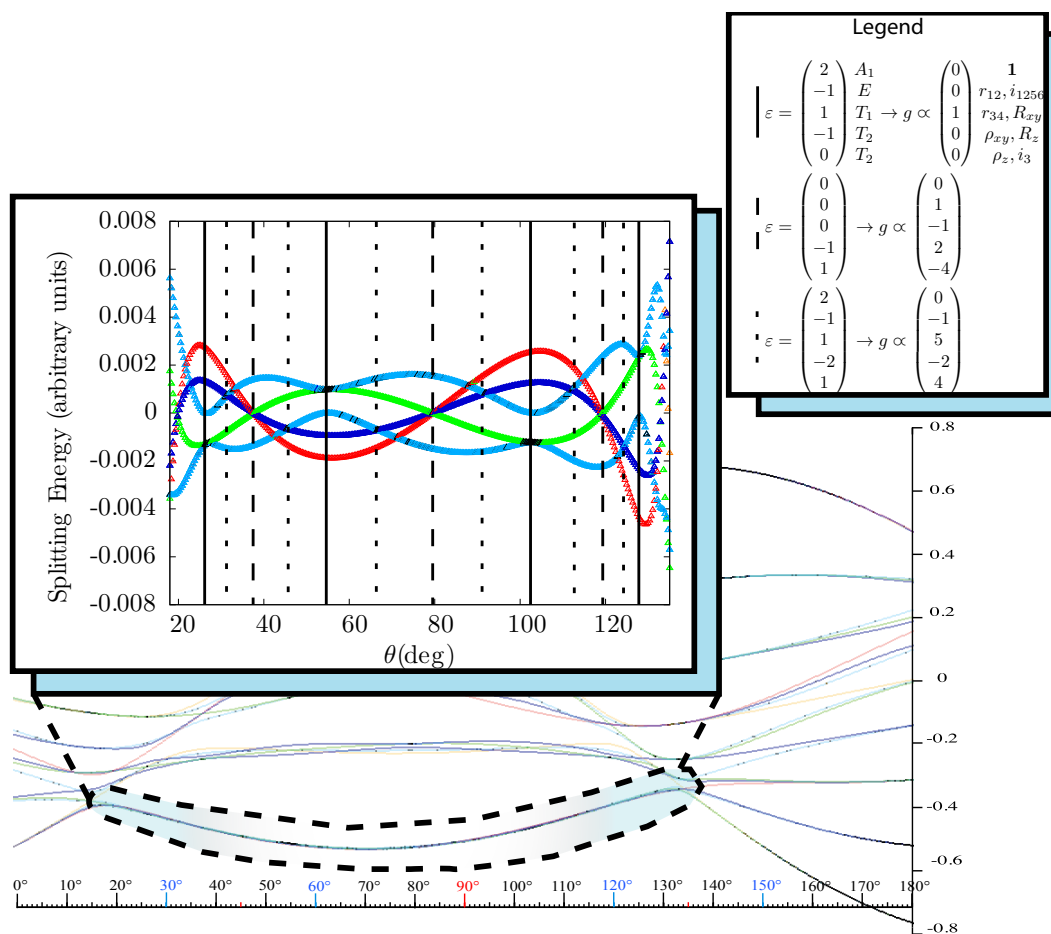
Figure 29. $J=30$ Energy levels and RES plots for $T^{[4,6]}\nu_S.[4,6]$ mix-angle θ with $T^{[4]}$ levels above $\phi=0^\circ$ (extreme left), $T^{[6]}$ levels at $\theta=90^\circ$ (center), and $-T^{[4]}$ levels at $\theta=180^\circ$ (extreme right). C_4 local symmetry and 6-fold level clusters dominate at $\theta=17^\circ$ while C_3 type 8-fold level clusters dominate at $\theta=132^\circ$. In between these extremes are C_2 type 12-fold level clusters particularly around $\theta=80^\circ$ where a $C_3 - C_4$ level-cluster-crossing of the top 14 levels occurs.



At certain θ -points in Figure 30 levels of different symmetry cross and one of three distinctive splitting patterns emerge. These points occur periodically as indicated by vertical lines that are (starting from left side) solid, dotted, dashed, dotted, solid, dotted, dashed, solid, and so forth across the

plot. The three distinctive ϵ^α -energy level patterns for species $\alpha=(A_1, E, T_1, T_2, T_2)$ are given by vectors $\epsilon_{dash}=(0, 0, 0, 1, -1)$, $\epsilon_{dot}=(2, -1, 1, 1, -1)$ and $\epsilon_{solid}=(2, -1, 1, 0, -1)$, respectively. These repetitious patterns seem to persist even outside of the marked-off sections to the very ends of the C_2 cluster region at $\theta \simeq 18^\circ$ and $\theta \simeq 132^\circ$ where they grow slightly but maintain their respective superfine ratio patterns and degeneracy. The matrix in Table 15 transforms each of the three ϵ^α -vectors in Figure 30 into a vector of O -defined sub-class tunneling amplitudes g_r . These are evaluated for clusters at several values of parameter θ used in $T^{[4,6]}$ Hamiltonian Equation (134). Proportioned values of the tunneling amplitudes g_r for the three distinctive cases are listed in the inset legend of Figure 30 based on Tables 14 and 15.

Figure 30. The plot focuses on the lowest $0_2(C_2)\uparrow O$ cluster in the previous energy plot (Figure 29) of the $T^{[4,6]}$ Hamiltonian for $J = 30$. The inside plot has been magnified 100 times. The inside diagram also centers the levels around their center-of-energy, showing only the splittings and ignoring the shifts of the cluster. Symmetry species are colored as before: A_1 : red, A_2 : orange, E_2 : green, T_1 : dark blue, and T_2 : light blue. The vertical lines on inside plot draw attention to specific clustering patterns described in the text. $1_2(C_2)\uparrow O$ clusters have similar superfine structure but with A_2 replacing A_1 and T_1 switched with T_2 .



Dotted-line and solid-line curve patterns appear alternately flipped in sign. Dotted-line patterns have a crossing (T_1, T_2) pair while the solid-line patterns have a crossing (T_2, E) pair.

Solid-line patterns appear to be centered on quasi-hyperbolic avoided-level-crossing episodes involving the pair of repeated T_2 tensor species of O . The ordering (A_1, T_1, T_2, E, T_2) of solid-line

superfine level patterns reflects Bohr-like orbital ordering (s, p, d, f, \dots) of orbital momentum and occurs only when there is just one non-zero sub-class of tunneling parameter, namely that of sub-class (r_{34} or equivalent R_{xy}) that affects tunneling between nearest-neighbor C_2 valleys.

Dashed-line pattern level curve *slopes* appear to alternate (+) and (−) signs and exhibit maximum separation of repeated T_2 -species surrounding a degenerate (A_1, T_1, E) -sextet crossing midway in between. Such triple-point crossings are quite remarkable. They appear repeatedly in Figure 30 and persist even at low- J as seen for $J=4$ in Figure 8c. Higher $1_2(C_2)\uparrow O$ clusters show similar triple points made of (A_2, T_2, E) -sextets.

Such crossings are quite ironic if we recall that it was (A_1T_1E) , (A_2T_2E) , and (T_1T_2) clusters noted by Lea, Leask, and Wolf [20] and later Dorney and Watson [21] that led to a theory involving induced representations $K_4(C_4)\uparrow O$ including $0_4(C_4)\uparrow O = A_1 \oplus T_1 \oplus E$, $2_4(C_4)\uparrow O = A_2 \oplus T_2 \oplus E$, and $\pm 1_4(C_4)\uparrow O = T_1 \oplus T_2$. (Recall C_4 columns of Equation (117) and reciprocity Equation (106)). This theory uses an inter- C_4 -axial tunneling model [22,23] with a single *ad.hoc.* tunneling parameter that predicts a 2:1-splitting ratio for (ATE) clusters. C_4 -axial tunneling cluster splitting dies exponentially as body momentum- K approaches J (Recall Figure 26) and thus $C_4(ATE)$ levels never actually cross.

However, the $C_2(ATE)$ levels in Figure 30 clearly do so and with quite the opposite 1:2-splitting ratio. It is ironic that the more elegant ortho-complete multi-path tunneling models, while useful in exposing these crossings, seem at a loss to explain them, particularly given that they were first noted by Lea, Leask, and Wolf so very long ago!

It would be easy to write off such (ATE) triple-crossings and particularly the (T_1T_2) or (ET) double-crossings as “accidental” degeneracy. Indeed, all but the latter occur for special values of a complete set of sub-class parameters. However, Figure 30 clearly shows that each type of crossing belong to a periodic structure that is unlikely to be just an accident.

Clearly there is still much to learn about multi-path tunneling models in general and the octahedral ones in particular. Here we can only offer a potentially elegant way to treat these kinds of high-symmetry cases.

9. Examples of Rovibronic Energy Eigenvalue Surfaces (REES) and J-Clusters

Semiclassical treatment of rovibronic or rovibrational states provides some insight into the transition between lab-coupled and body-coupled vibronic momentum that are related in Equation (8) through Equation (10b) of Sections 1 and 2. The first semiclassical analysis of fundamental coupling in high- J octahedral molecules was done for ν_2E [38] and ν_3T_1 [39] bands in 1978 and for overtone $\nu_2 + \nu_3$ “hot-bands” in 1979 [40].

These methods are similar in philosophy to those described in Section 2 that approximate tensor eigenvalues with Legendre formulas and thereby construct rotational energy based on a semiclassical \mathbf{J} -vector. However, the more general approach differs in that it builds an N -by- N matrix of such formulas that takes account of quantum rovibronic coupling between N vibronic (or vibrational) states, that is, a 2-by-2 matrix for the ν_2E system, a 3-by-3 matrix for the ν_3T_1 system, and a 5-by-5 matrix for the $\nu_2 + \nu_3$ system.

The resulting N eigenvalues provide points on N nested Rovibronic Energy Eigenvalue Surfaces (REES) for each direction of the semiclassical \mathbf{J} -vector. Visualization of P , Q , and R state mixing in ν_3T_1 bands by 3-sheet REES was done using the high-resolution 3D-graphics at Los Alamos in 1987 and reported in 1988 [25]. Interesting features of the ν_3T_1 REES include conical intersections that occur for zero scalar Coriolis coupling. These are analogous to well known conical intersections of Jahn–Teller PES that lend insight into BOA breakdown of single adiabatic surfaces. The following contains two examples of REES models. The first is a simplified internal rotation model involving a 2-sheet REES, and the second is an excerpt of a recent study of the $\nu_3/2\nu_4$ dyad of CF_4 that involves a 9-sheet REES.

9.1. Rotor-With-Gyro Model of Internal Rotation

A first application by Ortigosa and Hougen [17] of REES to visualize molecules with internal rotation is related to a simple rotor-with-gyro model [25,41] based on the three lowest rank tensors possible, namely the scalar (rank-0), the vector (rank-1), and the tensor (rank-2). The prolate symmetric top RES in Figure 1 is an example of a scalar-tensor combination. A vector RES lacks \mathbf{J} -inversion symmetry, that is, time reversal symmetry, so it is forbidden for normal molecules that have no intrinsic dynamic chirality such as embedded spin \mathbf{S} . We consider how to include an \mathbf{S} in a way that preserves overall T symmetry.

Total momentum $\mathbf{J}=\mathbf{R}+\mathbf{S}$ is the sum of rotor momentum \mathbf{R} and gyro spin \mathbf{S} . \mathbf{J} is conserved in lab frame but \mathbf{R} and \mathbf{S} are not. If gyro is body-frame-fixed by frictionless bearing then rotor gyro-coupling does no work and is an ignorably constant H_{RS} . \mathbf{S} and $|\mathbf{J}|$ are conserved in body frame but \mathbf{J} and \mathbf{R} are not.

$$H_{R+S(bod-fixed)} = A\mathbf{R}_x^2 + B\mathbf{R}_y^2 + C\mathbf{R}_z^2 + H_S + H_{RS} \quad (135)$$

Replacing bare-rotor momentum $\mathbf{R}=\mathbf{J}-\mathbf{S}$ gives the following with a new constant spin energy H'_{RS} .

$$\begin{aligned} H_{R,S(bod-fixed)} &= A(\mathbf{J}_x - \mathbf{S}_x)^2 + B(\mathbf{J}_y - \mathbf{S}_y)^2 + C(\mathbf{J}_z - \mathbf{S}_z)^2 + H_{RS} \\ &= A\mathbf{J}_x^2 + B\mathbf{J}_y^2 + C\mathbf{J}_z^2 - 2A\mathbf{J}_x\mathbf{S}_x - 2B\mathbf{J}_y\mathbf{S}_y - 2C\mathbf{J}_z\mathbf{S}_z + H'_{RS} \end{aligned} \quad (136)$$

The simplest classical theory of the rotor- \mathbf{R} -gyro- \mathbf{S} momentum dynamics involves superimposed RES plots, one for $+\mathbf{S}$ and one for $-\mathbf{S}$ in Figure 31; A composite RES with T symmetry. If \mathbf{J} and $+\mathbf{S}$ align (anti-align) then $|\mathbf{R}|=|\mathbf{J}-\mathbf{S}|$, rotor energy Equation (135), and rotor-gyro relative velocity are minimized (maximized) (Thus, gyro-compass alignment with Earth rotation is seen to be relativistic quantum effect!).

A quantum theory of multiple RES involves mixing extreme cases $|\mathbf{J} \pm \mathbf{S}|$. An elementary quantum gyro-spin is a two-state spin-1/2 with a 2-by-2 Hamiltonian matrix found by inserting quantum spin $\mathbf{S}=\sigma/2$ matrices into Equation (136) to give Equation (137). Gyro-rotor dynamics involves REES obtained from eigensolutions of the following 2-by-2 matrix for each body-based \mathbf{J} -vector Euler orientation (β, γ) .

$$\begin{aligned}
 H_{R,S(\text{quantized})} &= AJ_x^2 + BJ_y^2 + CJ_z^2 - AJ_x\sigma_x - BJ_y\sigma_y - CJ_z\sigma_z + \text{const.} \\
 &= \begin{pmatrix} \text{RE}_{\text{rotor}} - JC \cos \beta & -AJ \cos \gamma \sin \beta - iBJ \sin \gamma \sin \beta \\ -AJ \cos \gamma \sin \beta + iBJ \sin \gamma \sin \beta & \text{RE}_{\text{rotor}} + JC \cos \beta \end{pmatrix} \quad (137) \\
 \text{where: RE}_{\text{rotor}} &= J^2(A\cos^2\gamma\sin^2\beta + B\sin^2\gamma\sin^2\beta + C\cos^2\beta)
 \end{aligned}$$

Eigensolutions of matrix form Equation (137) transform classical RES Figure 31 into quantum REES Figure 32 that has conical intersections or avoided crossing points replacing lines of classical surface intersections in the former Figure 31. Also, individual sheets of REES have J-inversion symmetry (or *T* symmetry) that individual RES lack. Where the RES of Figure 31 are well separated their shape is not so different from that of REES in Figure 32. Differences show up near the intersection lines where the two RES approach resonance. In this resonance region the REES is deformed extremely from rank-1 or rank-2 tensor shape of the separate RES, and there arises greater mixing of the extreme $|\pm S|$ base-states.

Figure 31. Views of classical rotor-gyro RES for spin +*S* (yellow) and −*S* (gray).

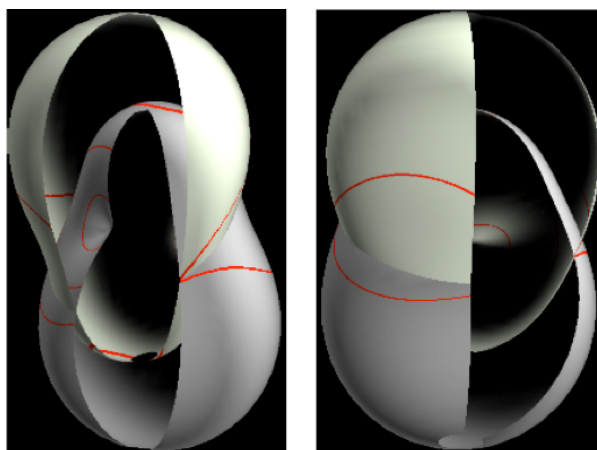
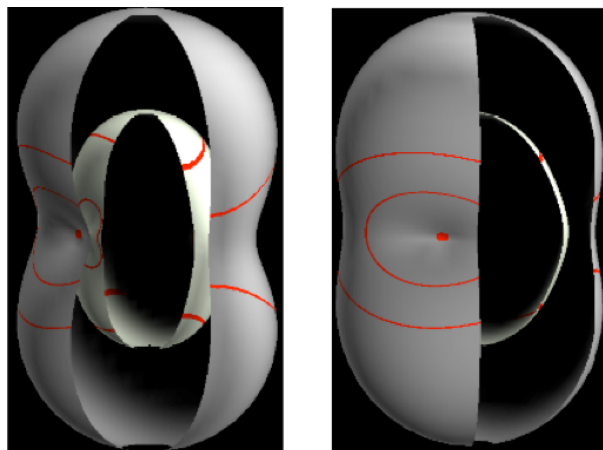


Figure 32. Same views of quantum REES for rotor with gyro spin operator $S=\sigma/2$.

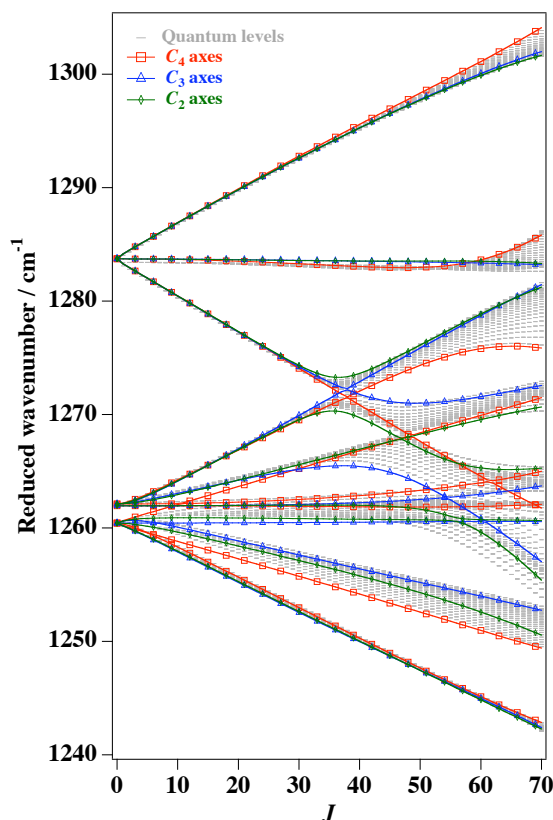


9.2. REES of CF_4 in $\nu_3/2\nu_4$ Dyad

The first practical REES application includes 9-sheet displays of the $\nu_3/2\nu_4$ dyad of CF_4 recently shown by Boudon *et al.* [2]. This large scale numerical analysis may be summarized by a revealing plot of dyad eigenlevels as a function of $J = 0$ to 70 in Figure 33. This includes colored lines representing the REES values for J located on C_4 axes (shaded red), C_3 axes (shaded blue), or C_2 axes (shaded green).

Each of the symmetry axes may take turns as central loci for clusters of their type of local symmetry C_2 , C_3 , or C_4 , or else, they may sit on a REES separatrix or saddle point between two or more different types of clusters. A third option involves C_1 clusters that have no rotation axis point but are likely to belong to vertical xyz -plane reflection symmetry $C_v = [1, \rho_z]$ or diagonal-plane reflection symmetry $C_d = [1, i_3]$. These label clusters of 24 levels associated with 24 equivalent REES hills or valleys.

Figure 33. (After Boudon *et al.* [2].) ($J \leq 70$) rotational levels of $\nu_3/2\nu_4$.



A final option involves true- C_1 clusters with no local symmetry whatsoever and 48 REES hills or valleys. So far this extreme type has not been identified, but one may speculate that it may actually become most common at extremely high J .

A common ordering noted before on the left hand side of Figure 29 (pure $T^{[4]}$) and in Figure 26 (16μ region of SF_6) is (C_3 -valley \rightarrow C_2 -saddle \rightarrow C_4 -hill). It is present in the lowest REES band of Figure 33. An inverted version of the common ordering appears clearly in the 2nd band whose REES is cubic in Figure 34.

A cutaway view at $J = 57$ of the first five REES sheets shows glimpses of the first two REES deep inside of Figure 34. The second sheet has cubic topography similar to the inverted $T^{[4]}$ RES on the right

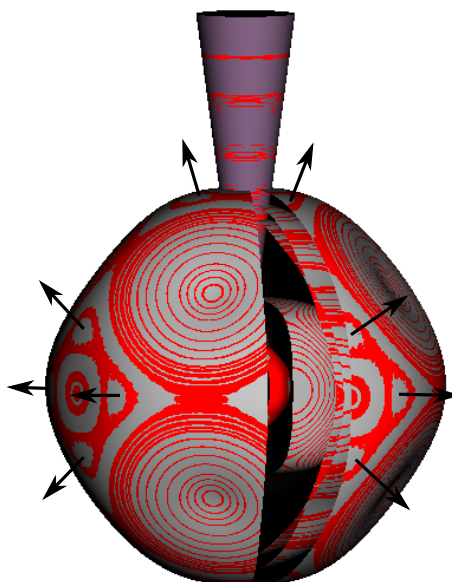
hand side of Figure 29 (pure $(-)^T^{[4]}$). However, the first and lowest REES for $J = 57$ is practically spherical with all $2J + 1 = 115$ levels and clusters crushed in Figure 33 into near degeneracy!

After the first two REES sheets the cluster topography become more complicated with multiple conical intersections and avoided crossing points.

On the 5th sheet of the $(J = 57)\nu_3/2\nu_4$ REES are found examples of C_1 -local symmetry valleys as shown in Figure 34. (The upper four sheets are made invisible.) Each C_1 loop occupies an area that is comparable to the minimum uncertainty ($J = K$)-cone shown on vertical C_4 axis of the figure and a nascent 24-level cluster of type $1_2(C_2)\uparrow O$ should be present in the level spectrum.

The symmetry details in this rovibrational spectra and the potential richness of quantum dynamics it represents should be quite evident from the few examples glimpsed here. We seem to be just scratching the surface of quantum systems of a great but potentially comprehensible complexity.

Figure 34. (After Boudon *et.al.* [2].) A rare $(J=57)1_2(C_2)\uparrow O$ structure on fifth REES.



10. Summary and Conclusions

Semiclassical methods for visualizing and analyzing rovibrational dynamics of symmetric polyatomic molecules have been reviewed. This includes improved understanding of RES and REES phase spaces and development of more powerful symmetry methods to calculate tunneling dynamics of symmetric molecules that are highly resonant. A group-table-matrix analysis of intrinsic *vs.* extrinsic symmetry duality (The “Mock-Mach-Principles” Equation (95) and Equation (94) of wave relativity.) leads to generalizing character relations between group classes and irreducible representation into sub-character relations between sub-classes and induced representations Equation (131) and (132). These provide ortho-complete parameter relations (Tables 11–15) for complex tunneling path lattices that determine molecular fine, superfine, and hyperfine spectra. The methods may be extensible to fluxional atomic and molecular systems.

Appendix

A. Classical D_3 Modes: Local C_2 and C_3 Symmetry Examples

Local symmetry theory applies to classical vibrational modes as well as to quantum tunneling. Examples of classical D_3 modes given below help clarify global-*vs*-local symmetry and geometry of group projection. For example, D_3 modes defined by local $C_2(i_3)$ in Figure 20 are to be compared with quantum waves in Figure 19. Each mode ket $|_{jk}^\alpha\rangle$ has the same coefficients $D_{jk}^{\alpha*}(\mathbf{g})$ for projections in Equation (78) as the waves do, but the mode shapes clearly display a vector geometry.

In particular, global x -vector modes $|_{xx}^{E_1}\rangle$ and $|_{xy}^{E_1}\rangle$ (left E_1 column in figure) “point” along global x -direction while y -vector modes $|_{yx}^{E_1}\rangle$ and $|_{yy}^{E_1}\rangle$ (right E_1 column) “point” along global y -direction. Each global pair $[|_{x\ell}^{E_1}\rangle, |_{y\ell}^{E_1}\rangle](\ell = x, y)$ is projected to be an i_3 -symmetric-antisymmetric pair like lab unit vectors $[|x\rangle, |y\rangle]$ (Recall Equation (78)).

$$|x\rangle = \mathbf{P}^{03} |\mathbf{1}\rangle \sqrt{2} = (|\mathbf{1}\rangle + |i_3\rangle) / \sqrt{2}, \quad |y\rangle = \mathbf{P}^{13} |\mathbf{1}\rangle \sqrt{2} = (|\mathbf{1}\rangle - |i_3\rangle) / \sqrt{2} \quad (138)$$

This exposes easy derivations of E -irrep $D_{jk}^{E_1}(\mathbf{g}) = \langle j|\mathbf{g}|k\rangle$ in Equation (89). Irreps in Equation (87) such as $D_{jk}^{E_1}(\mathbf{r})$ for 120° -rotation \mathbf{r} simply contain direction cosines $\langle j|\mathbf{r}|k\rangle = \hat{\mathbf{e}}_j \bullet \hat{\mathbf{e}}_{r.k}$ of rotated vectors $[r|x\rangle, r|y\rangle]$ relative to original $[|x\rangle, |y\rangle]$ (Note transpose of equation array to matrix array).

$$\left. \begin{array}{l} \mathbf{r} |x\rangle = -\frac{1}{2} |x\rangle + \frac{\sqrt{3}}{2} |y\rangle \\ \mathbf{r} |y\rangle = -\frac{\sqrt{3}}{2} |x\rangle - \frac{1}{2} |y\rangle \end{array} \right\} \text{implies : } \left\{ D^E(\mathbf{r}) = \begin{pmatrix} \langle x|\mathbf{r}|x\rangle & \langle x|\mathbf{r}|y\rangle \\ \langle y|\mathbf{r}|x\rangle & \langle y|\mathbf{r}|y\rangle \end{pmatrix} = \begin{pmatrix} -\frac{1}{2} & -\frac{\sqrt{3}}{2} \\ +\frac{\sqrt{3}}{2} & -\frac{1}{2} \end{pmatrix} \right. \quad (139)$$

This also fixes local transformations. Local x -vector modes $|_{xx}^{E_1}\rangle$ and $|_{yx}^{E_1}\rangle$ (lower E_1 row in figure) “point” along local x -axes that are local *radial* lines while local y -vector modes $|_{xy}^{E_1}\rangle$ and $|_{yy}^{E_1}\rangle$ (upper E_1 row) “point” along local y -axes that are local *angular* lines. If global symmetry meets local anti-symmetry as in $|_{xy}^{E_1}\rangle$ (or *vice-versa* in $|_{yx}^{E_1}\rangle$), a zero appears on the i_3 -axis in Figure 20. Singlet modes $|_{xx}^{A_1}\rangle$ and $|_{yy}^{A_2}\rangle$ avoid such conflicts by being all one or the other.

For group-defined cases like Figure 20, symmetry arguments alone determine normal modes that usually require diagonalizing a K -matrix (below) just as tunneling states (Figure 19) usually require diagonalizing an H -matrix.

A.1. Comparing K -Matrix and H -Matrix Formulation

Classical modes are eigenvectors of force-field matrix K or operator \mathbf{K} that is a linear function of spring constants (k_0 , etc. in Figure 35) for a harmonic approximate potential $V(\mathbf{x})$ that is a quadratic K -form of coordinates x_a based on six D_3 -labeled axes $\hat{\mathbf{x}}^a$ or $|a\rangle$ shown in Figure 20. Each \mathbf{K} component $K_{ab} = \langle a|\mathbf{K}|b\rangle$ is a sum over spring k -constants that connect axis- \mathbf{x}^a to axis- \mathbf{x}^b multiplied by factor $(\hat{\mathbf{k}}_a \bullet \hat{\mathbf{x}}^a)(\hat{\mathbf{k}}_b \bullet \hat{\mathbf{x}}^b)$ for projecting spring k 's end vectors $\hat{\mathbf{k}}_a$ and $\hat{\mathbf{k}}_b$ onto $\hat{\mathbf{x}}^a$ and $\hat{\mathbf{x}}^b$ at respective connections.

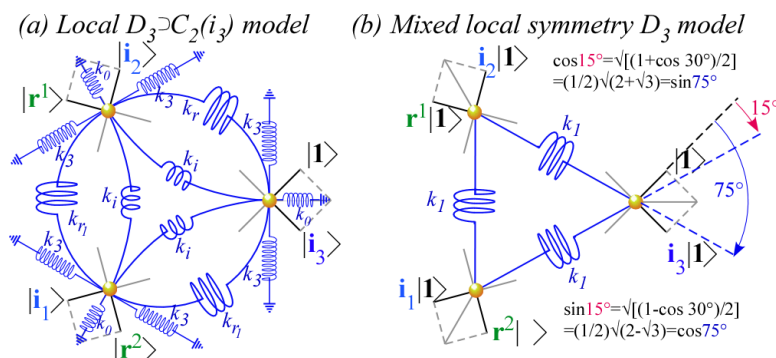
(A straight-line spring has equal $\hat{\mathbf{k}}_a=\hat{\mathbf{k}}_b$. Curvilinear springs must only have $\hat{\mathbf{k}}$ -ends with equal sense ($\rightarrow\rightarrow$) or ($\leftarrow\leftarrow$) of spring direction. Either direction gives the same K_{ab}).

$$\begin{aligned}
 V(x) &= \sum_{(k)} \frac{1}{2} \langle x | \mathbf{K} | x \rangle \quad \text{where: } |x\rangle = \sum_a x^a |a\rangle, \quad (a, b) = (1, r^1, r^2, i_1, i_2, i_3) \\
 &= \frac{1}{2} \sum_{a,b} K_{ab} x_a x_b \quad \text{where: } K_{ab} = \begin{cases} \sum_{(k)} \frac{k}{2} (\hat{\mathbf{k}}_a \cdot \hat{\mathbf{x}}^a)^2 & \text{if } : a = b \\ - \sum_{(k)} k (\hat{\mathbf{k}}_a \cdot \hat{\mathbf{x}}^a) (\hat{\mathbf{k}}_b \cdot \hat{\mathbf{x}}^b) & \text{if } : a \neq b \end{cases} \quad (140)
 \end{aligned}$$

This sum of harmonic Hooke ($kx^2/2$)-potentials has diagonal K_{aa} terms followed by off-diagonal terms ($K_{ab}=K_{ba}$).

$$\begin{aligned}
 V(x) &= \sum_{(k)} \frac{k}{2} (\Delta \ell_k)^2 = \sum_{(k)} \frac{k}{2} \sum_{a,b} (\hat{\mathbf{k}}_a \cdot \mathbf{x}^a - \hat{\mathbf{k}}_b \cdot \mathbf{x}^b)^2 \\
 &= \sum_{(k)} \frac{k}{2} \sum_a (\hat{\mathbf{k}}_a \cdot \hat{\mathbf{x}}^a)^2 x_a^2 - \sum_{(k)} k \sum_{a \neq b} (\hat{\mathbf{k}}_a \cdot \hat{\mathbf{x}}^a) (\hat{\mathbf{k}}_b \cdot \hat{\mathbf{x}}^b) x_a x_b \quad (141)
 \end{aligned}$$

Figure 35. X_3 spring models with local symmetry: (a) $D_3 \supset C_2(i_3)$; (b) Mixed.



The classical equation of coupled harmonic motion is a Newtonian $\mathbf{F} = \mathbf{M} \cdot \mathbf{a}$ relation of a n -dimensional force vector \mathbf{F} , acceleration vector \mathbf{a} , and mass operator \mathbf{M} . The latter is a unit-matrix-multiple $M \cdot \mathbf{1}$ for the D_3 -symmetric case treated here. The driving force \mathbf{F} is a (-)derivative of potential Equation (140) that becomes a \mathbf{K} -matrix expression.

$$-M \partial_t^2 x^a = \frac{\partial V}{\partial x^a} = \sum_b K_{ab} x^b \quad (142)$$

It is instructive to compare this classical equation of motion to that of Schrodinger's equation for quantum motion.

$$i\hbar \partial_t \psi^a = \sum_b H_{ab} \psi^b \quad (143)$$

Squaring quantum time generator $i\hbar \partial_t = \mathbf{H}$ yields equations having classical form Equation (142) with $K = H^2$ and $M = \hbar^2$.

$$-\hbar^2 \partial_t^2 \psi^a = \sum_b K_{ab} \psi^b \quad \text{where: } K = H^2 \quad (144)$$

The (\mathbf{H}/\hbar) -eigenvalues are quantum angular frequencies $\epsilon_m/\hbar=\omega_m$. The (\mathbf{K}/M) -eigenvalues are classical *squared* angular frequencies $k_m/M=\omega_m^2$. The former is Planck’s oscillator frequency relation $\epsilon=\hbar\omega$. The latter is Hooke’s relation $k/M=\omega^2$. Apart from normalization, eigenvectors of quantum H are identical to those of classical K and either eigenvalue set corresponds to the respective energy spectrum.

A.2. Comparing K -Matrix and H -Matrix Eigensolutions for Local $D_3\supset C_2(i_3)$

The preceding relates eigensolutions Equations (92) and (93) of quantum Hamiltonian H -matrix in (71) with those of a classical K -matrix. In particular, eigenvectors of H found using D -matrices in Equation (89) or (139) also serve as mode-eigenkets in Figure 20 that diagonalize a $D_3\supset C_2(i_3)$ -locally-symmetric K -matrix. With this symmetry, K cannot couple radial (local- x) and angular (local- y) modes and is left with just four independent real group-based parameters $g_a=r_0, r_1, i_{12}$, and i_3 allowed for $D_3\supset C_2(i_3)$ -symmetric H in Equation (93). These relate to four spring k_h -constants in Figure 35a.

Only 1st-row parameters $g_b=\langle \mathbf{1} | \mathbf{K} | g_b \rangle = K_{1b}$ of the force matrix K_{ab} are needed for the spring model in Figure 35a. That model includes k_r (angular) and k_i (radial) constants for internal connections between masses. The k_3 (angular) and k_0 (radial) constants represent external connections between each mass and an outside lab frame.

Generic group parameters $g_b=H_{1b}$, labeled $[r_0, r_1, r_2, i_1, i_2, i_3]$ for the H -matrix in Equation (71), are now applied to $g_b=K_{1b}$. The g_b are to be related to spring-constants k_j using coordinate-spring projection cosine factors $(\hat{\mathbf{k}}_1 \bullet \hat{\mathbf{x}}^1)(\hat{\mathbf{k}}_b \bullet \hat{\mathbf{x}}^b)$ in Equations (140) and (141). The usual harmonic limit assumes small vibrational amplitudes ($x_b \ll 1$) for which direction of spring end vectors $\hat{\mathbf{k}}^1$ or $\hat{\mathbf{k}}^b$ do not vary to 1st-order, and so, for lab-fixed $\hat{\mathbf{x}}^a$ the K_{ab} are constants.

$ g_b\rangle$	$ \mathbf{1}\rangle$	$ \mathbf{r}^1\rangle$	$ \mathbf{r}^2\rangle$	$ \mathbf{i}_1\rangle$	$ \mathbf{i}_2\rangle$	$ \mathbf{i}_3\rangle$	
$\langle \mathbf{1} \mathbf{K} g_b \rangle =$	$k_i/2$	$k_i/2$	$k_i/2$	$k_i/2$	$k_i/2$	$k_i/2$	
	$+k_r$	$-k_r/2$	$-k_r/2$	$+k_r/2$	$+k_r/2$	$-k_r$	(145)
	$+k_3$	$+0$	$+0$	$+0$	$+0$	$-k_3$	
	$+k_0/2$	$+0$	$+0$	$+0$	$+0$	$+k_0/2$	

One may visualize each $-K_{1b}$ as the acceleration of x_1 due to setting a (tiny) unit x_b in Equation (142). Diagonal $-K_{11}$ must be negative or else x_1 blows up. Higher order *anharmonic* terms are needed to describe effects of rotating $\hat{\mathbf{k}}^b$ or $\hat{\mathbf{x}}^b$ and such models are likely to suffer from classical stochastic (chaotic) motion.

Substitution of generic g_a from Equation (145) into reduced $D_3\supset C_2(i_3)$ -symmetric H -matrix in Equation (92) or (93) gives K -matrix eigenvalues $K_{\ell\ell}^\alpha$ due to each spring k_i, k_r, k_3 , or k_0 in Figure 35a separately or together. Modes in Figure 20 remain *eigenmodes* for all values of four spring constants k_i, k_r, k_3 , and k_0 since none can mix local x -and- y -symmetry.

$$\begin{aligned}
 K_{xx}^{A_1} &= r_0 + r_1 + r_1^* + i_1 + i_2 + i_3 &= k_0 + 3k_i \\
 K_{yy}^{A_2} &= r_0 + r_1 + r_1^* - i_1 - i_2 - i_3 &= 3k_3 \\
 \begin{pmatrix} K_{xx}^E & K_{xy}^E \\ K_{yx}^E & K_{yy}^E \end{pmatrix} &= \frac{1}{2} \begin{pmatrix} 2r_0 - r_1 - r_1^* - i_1 - i_2 + 2i_3 & \sqrt{3}(-r_1 + r_1^* - i_1 + i_2) \\ \sqrt{3}(-r_1^* + r_1 - i_1 + i_2) & 2r_0 - r_1 - r_1^* + i_1 + i_2 - 2i_3 \end{pmatrix} = \begin{pmatrix} k_0 & 0 \\ 0 & k_3 + 2k_r \end{pmatrix}
 \end{aligned}
 \tag{146}$$

Any set of four K -matrix eigenvalues k^{A_1} , k^{A_2} , k_x^E , and k_y^E is arithmetically possible by adjusting the four spring constants. However, their arrangement in Figure 20 (this was drawn to match tunneling states in Figure 19) is impossible without negative k -values that would give classical instability. As shown below, free ring molecules often have A_1 -stretching modes among the highest frequencies. In contrast, tunneling amplitudes are often negative so their A_1 states lie low. As a rule, fewer quantum nodes imply lower energy.

A.3. K -Matrix Eigensolutions for Broken Local Symmetry

In some ways the direct- k_1 -connection spring model of Figure 35b is quite the opposite of the $D_3 \supset C_2(i_3)$ model just treated since it involves maximal (50-50) mixing of x and y local symmetry. Below are recalculated generic $g_b = \langle \mathbf{1} | \mathbf{K} | g_b \rangle$ in terms of direct spring-constants k_1 using (141) with projection cosines listed in Figure 35b.

$ g_b\rangle$	$ \mathbf{1}\rangle$	$ \mathbf{r}^1\rangle$	$ \mathbf{r}^2\rangle$	$ \mathbf{i}_1\rangle$	$ \mathbf{i}_2\rangle$	$ \mathbf{i}_3\rangle$
$\langle \mathbf{1} \mathbf{K} g_b \rangle =$	$k_1(\cos^2 75^\circ + \cos^2 15^\circ)$ $= k_1$	$k_1 \cos 75^\circ \cdot \cos 15^\circ$ $= \frac{k_1}{4}$	$k_1 \cos 15^\circ \cdot \cos 75^\circ$ $= \frac{k_1}{4}$	$k_1 \cos 15^\circ \cdot \cos 15^\circ$ $= \frac{k_1(2 - \sqrt{3})}{4}$	$k_1 \cos 75^\circ \cdot \cos 75^\circ$ $= \frac{k_1(2 + \sqrt{3})}{4}$	$k_1(\cos^2 75^\circ - \cos^2 15^\circ)$ $= \frac{k_1}{2}$

(147)

Again, a substitution of generic g_a from Equation (147) into reduced H -matrix Equation (93) gives a reduced K -matrix like Equation (146), but now the E -symmetry submatrix is not diagonal.

$$\begin{aligned}
 K_{xx}^{A_1} &= 3k_1 \\
 K_{yy}^{A_2} &= 0 \\
 \begin{pmatrix} K_{xx}^E & K_{xy}^E \\ K_{yx}^E & K_{yy}^E \end{pmatrix} &= \begin{pmatrix} \frac{3k_1}{4} & \frac{3k_1}{4} \\ \frac{3k_1}{4} & \frac{3k_1}{4} \end{pmatrix}
 \end{aligned}
 \tag{148}$$

Eigenvectors of the E -submatrix are symmetric (+) and antisymmetric (−) mixtures of x and y local symmetry states.

$$\begin{aligned}
 \mathbf{K} \begin{pmatrix} E \\ g(-) \end{pmatrix} &= \mathbf{K} \left(\begin{pmatrix} E \\ gx \end{pmatrix} - \begin{pmatrix} E \\ gy \end{pmatrix} \right) \frac{1}{\sqrt{2}} = \frac{3k_1}{2} \begin{pmatrix} E \\ g(-) \end{pmatrix}, \\
 \mathbf{K} \begin{pmatrix} E \\ g(+) \end{pmatrix} &= \mathbf{K} \left(\begin{pmatrix} E \\ gx \end{pmatrix} + \begin{pmatrix} E \\ gy \end{pmatrix} \right) \frac{1}{\sqrt{2}} = 0 \begin{pmatrix} E \\ g(+) \end{pmatrix}, \quad g = (x, y).
 \end{aligned}
 \tag{149}$$

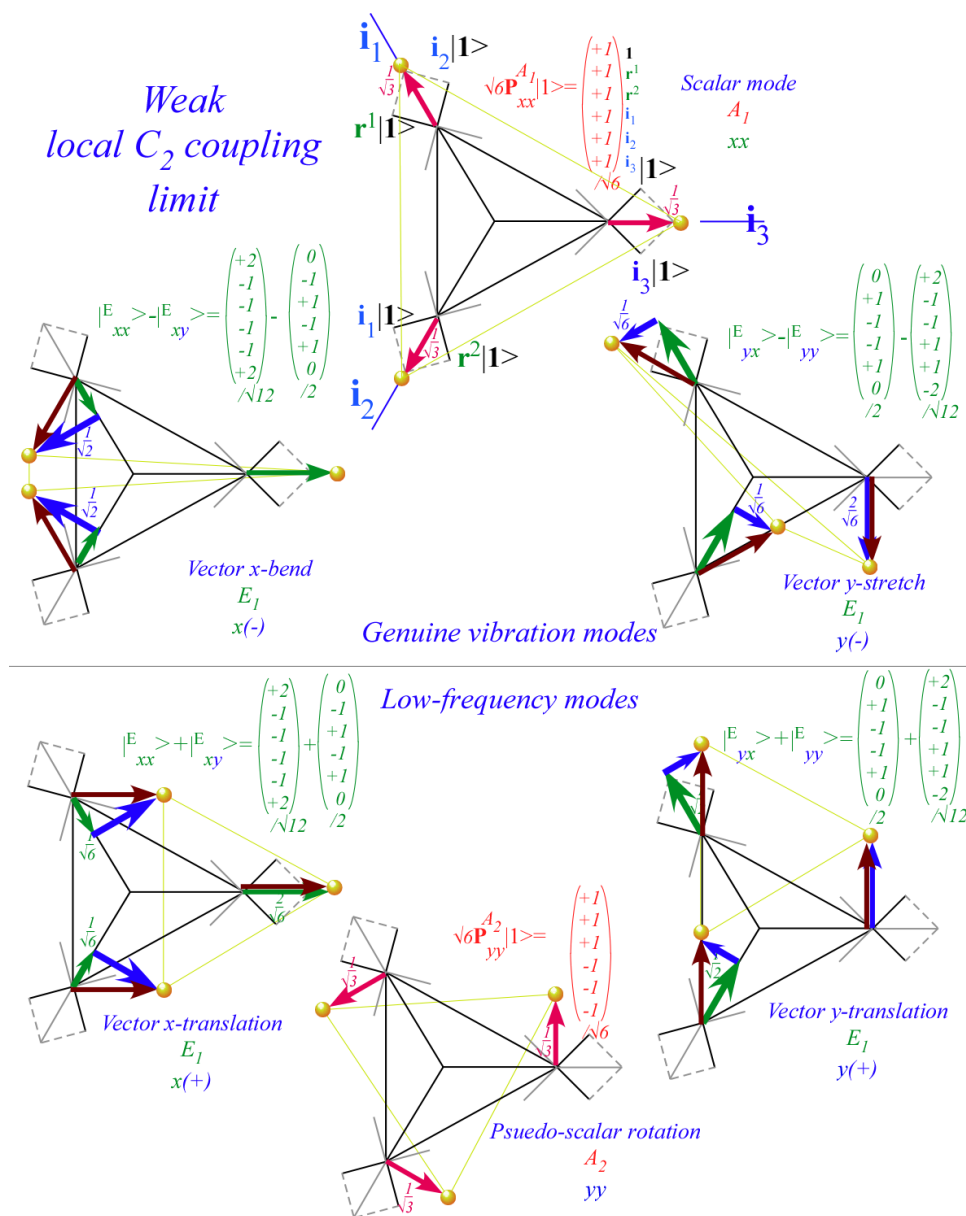
Figure 36 shows (50-50 \pm)-mixing due to k_1 . It distinguishes genuine vector modes ($|_{x,(-)}^E$) or ($|_{y,(-)}^E$) and the scalar breathing mode ($|_{x,x}^{A_1}$) from non-genuine (low or zero-frequency) vector modes of pure x or y -translation ($|_{x,(+)}^E$) or ($|_{y,(+)}^E$) and rigid rotation (pseudo-scalar $|_{y,y}^{A_2}$). The i_3 -local symmetry is wiped out by direct connection- k_1 .

In order to reestablish approximate $D_3 \supset C_2(i_3)$ -local-symmetry there needs to be a $C_2(i_3)$ -“locale” provided by lab-grounded potential springs such as those with constants k_3 and k_0 in Figure 35a. Adding these in the form of Equation (146) to Equation (148) causes a transition between the two extremes. If

the difference $(k_3 + 2k_r - k_0)$ between eigenvalues Equation (146) begins to dominate the off-diagonal component $(3k_1/4)$ of Equation (148), then mixed E -modes of Figure 36 begin to recover $D_3 \supset C_2(i_3)$ locality seen in Figure 20 .

Meanwhile the constant k_3 that determines eigenvalue $k_{y,y}^{A_2}$ does not affect locality for either of the singlet A_1 or A_2 modes. Singlet eigenvectors are non-negotiable as long as master symmetry D_3 holds.

Figure 36. Mixed-local symmetry modes of direct- k_1 -coupled X_3 model in Figure 35b.



A.4. K -Matrix Eigensolutions for $D_3 \supset C_3$ Symmetry

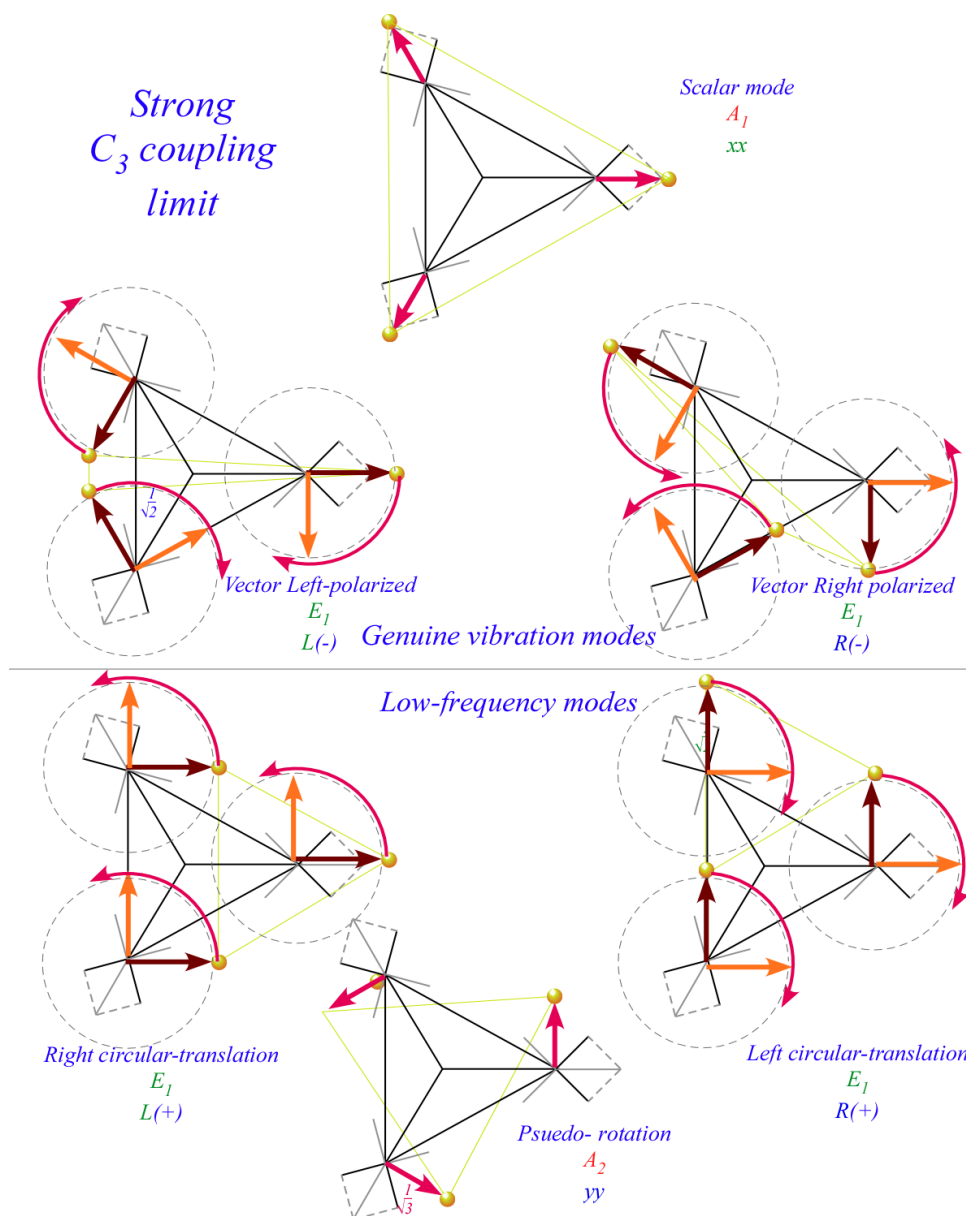
Another choice for D_3 local symmetry is the C_3 subgroup of Equation (79) corresponding to a strong chiral perturbation by internal rotation, spin, or B -field. The E -submatrix in Equation (146) with zero generic reflection parameters ($i_1=i_2=i_3=0$) may take a purely chiral C_3 form if the generic rotation

parameters r_1 and $r_2=r_1^*$ are purely imaginary corresponding to velocity dependent force ($r_1=ir$ and $r_2=-ir$. Here K is assumed Hermitian self-conjugate as was H).

$$\begin{aligned}
 K_{xx}^{A_1} &= r_0 \\
 K_{yy}^{A_2} &= r_0 \\
 \begin{pmatrix} K_{xx}^E & K_{xy}^E \\ K_{yx}^E & K_{yy}^E \end{pmatrix} &= \begin{pmatrix} r_0 & -ir\sqrt{3} \\ +ir\sqrt{3} & r_0 \end{pmatrix} \quad \begin{aligned} r_1 &= ir = -r_2^* \\ i_1 &= i_2 = i_3 = 0 \end{aligned}
 \end{aligned}
 \tag{150}$$

C_3 E -eigenvectors have local $x \pm iy=(\pm 1)_3$ combinations that exhibit purely circular right $R=(+1)_3$ and left $L=(-1)_3$ polarization orbits of C_3 symmetry shown in Figure 37 (Recall C_3 splitting in Equation (79)).

Figure 37. $D_3 \supset C_3$ -local symmetry modes of X_3 molecule.



$$\begin{aligned} \mathbf{K} \begin{vmatrix} E \\ g(+1)_3 \end{vmatrix} &= \mathbf{K} \left(\begin{vmatrix} E \\ gx \end{vmatrix} + i \begin{vmatrix} E \\ gy \end{vmatrix} \right) \frac{1}{\sqrt{2}} = +r\sqrt{3} \begin{vmatrix} E \\ g(+1)_3 \end{vmatrix}, \\ \mathbf{K} \begin{vmatrix} E \\ g(-1)_3 \end{vmatrix} &= \mathbf{K} \left(\begin{vmatrix} E \\ gx \end{vmatrix} - i \begin{vmatrix} E \\ gy \end{vmatrix} \right) \frac{1}{\sqrt{2}} = -r\sqrt{3} \begin{vmatrix} E \\ g(-1)_3 \end{vmatrix}, \quad g = (x, y). \end{aligned} \quad (151)$$

Pure C_3 symmetry is a normal subgroup and restricts $k_{x,x}^{A_1}$ and $k_{y,y}^{A_2}$ to become degenerate. Both the scalar $|_{0_3,0_3}^{A_1}\rangle$ and pseudoscalar $|_{0_3,0_3}^{A_2}\rangle$ state are both labeled equally by $(0)_3$ symmetry. Local symmetry effectively goes global in the pure C_3 -case where all internal coupling is zero.

Any internal or external parameters may split the A_1 - A_2 degeneracy and mix the C_3 states to form elliptical polarization orbits. This is most efficiently calculated using U(2) analysis similar to Equation (137).

References

1. Boudon, V.; Champion, J.; Gabard, T.; Loete, M.; Rotger, M.; Wenger, C. Spherical top theory and molecular spectra. *Wiley Handb. High Resolut. Spectrosc.* **2011**, *1*, 301.
2. Boudon, V.; Mitchell, J.; Domanskaya, A.; Maul, C.; Georges, R.; Benidar, A.; Harter, W.G. High-resolution spectroscopy and analysis of the $\nu_3/2\nu_4$ dyad of CF_4 . *Mol. Phys.* **2012**, *58*, 391–400.
3. Bowman, J.M. Beyond born-oppenheimer. *Science* **2008**, *319*, 40–41.
4. Garand, E.; Zhou, J.; Manolopoulos, D.E.; Alexander, M.H.; Neumark, D.M. Nonadiabatic interactions in the $Cl+H_2$ reaction probed by ClH_2^- and ClD_2^- photoelectron imaging. *Science* **2008**, *319*, 72–75.
5. Tsukerblat, B.; Palií, A.; Clemente-Juan, J.M.; Gaita-Arino, A.; Coronado, E. A symmetry adapted approach to the dynamic jahn-teller problem: Application to mixed-valence polyoxometalate clusters with keggin structure. *Int. J. Quantum Chem.* **2012**, *112*, 2957–2964.
6. Schnalle, R.; Schnack, J. Calculating the energy spectra of magnetic molecules: Application of real and spin-space symmetries. *Int. Rev. Phys. Chem.* **2010**, *29*, 403–452.
7. Harel, E.; Engel, G. Quantum coherence spectroscopy reveals complex dynamics in bacterial light harvesting complex 2 (LH2). *Proc. Nat. Acad. Sci.* **2012**, *109*, 706–711.
8. Harter, W.G. Theory of hyperfine and superfine levels in symmetric polyatomic molecules. II. Elementary cases in octahedral hexafluoride molecules. *Phys. Rev. A* **1981**, *24*, 192–263.
9. Yurchenko, S.N.; Thiel, W.; Patchkovskii, S.; Jensen, P. Theoretical evidence for the formation of rotational energy level clusters in the vibrational ground state of PH_3 . *Phys. Chem. Chem. Phys.* **2005**, *7*, 573–582.
10. Yurchenko, S.N.; Ovsyannikov, R.I.; Thiel, W.; Jensen, P. Rotation-vibration energy cluster formation in XH_2D and XHD_2 molecules ($X = Bi, P,$ and Sb). *J. Mol. Spectrosc.* **2009**, *256*, 119–127.
11. Van Hecke, C.; Sadovskii, D.A.; Zhilinskií, B.I.; Boudon, V. Rotational-vibrational relative equilibria and the structure of quantum energy spectrum of the tetrahedral molecule P_4 . *Eur. Phys. J. D* **2001**, *17*, 13.

12. Crogman, H.T.; Boudon, V.; Sadovskii, D.A. Local modes of silane within the framework of stretching vibrational polyads. *Eur. Phys. J. D* **2007**, *42*, 61–72.
13. Dhont, G.; Sadovskii, D.; Zhilinskiĭ, B.; Boudon, V. Analysis of the “unusual” vibrational components of triply degenerate vibrational mode ν_6 of $\text{Mo}(\text{CO})_6$ based on the classical interpretation of the effective rotation-vibration hamiltonian. *J. Mol. Spectrosc.* **2000**, *201*, 95–108.
14. Harter, W.G.; Patterson, C.W. Asymptotic eigensolutions of fourth and sixth rank octahedral tensor operators. *J. Math. Phys.* **1979**, *20*, 1453–1459.
15. Harter, W.G.; Weeks, D.E. Rotation-vibration spectra of icosahedral molecules. I. Icosahedral symmetry analysis and fine structure. *J. Chem. Phys.* **1988**, *90*, 4727.
16. Harter, W.G.; Weeks, D.E. Rovibrational spectral fine structure of icosahedral molecules. *Chem. Phys. Lett.* **1986**, *132*, 387.
17. Ortigoso, J.; Hougen, J.T. Rotational energy surfaces of molecules exhibiting internal rotation. *J. Chem. Phys.* **1994**, *101*, 2710–2719.
18. Crogman, H.T.; Boudon, V.; Harter, W.G.; Mitchell, J. Deformation of sulfur hexafluoride and floppiness of trifluoromethyl sulfur pentafluoride. *Mol. Phys.* **2006**, *104*, 2781–2790.
19. Harter, W.G. Reply to comment on RES and high-J eigenvalue structure of polyatomic molecules. *J. Chem. Phys.* **1986**, *84*, 5218–5219.
20. Lea, K.R.; Leask, M.J.M.; Wolf, W.P. Crystal field splitting and level degeneracy. *J. Chem. Phys. Solids* **1962**, *23*, 1381–1386.
21. Dorney, A.J.; Watson, J.K.G. Forbidden rotational spectra of polyatomic molecules: Stark effects and $\Delta J = 0$ transitions of T_d molecules. *J. Mol. Spectrosc.* **1972**, *42*, 135–148.
22. Harter, W.G.; Patterson, C.W. Orbital level splitting in octahedral symmetry and SF_6 rotational spectra. I. Qualitative features of high J levels. *J. Chem. Phys.* **1977**, *66*, 4872.
23. Harter, W.G. Simple model for level clusters in SF_6 . *Phys. Rev. Lett.* **1977**, *8*, 1–4.
24. Hecht, K.T. The vibration-rotation energies of tetrahedral XY_4 molecules: Part I. Theory of spherical top molecules. *J. Mol. Spectrosc.* **1961**, *5*, 355–389.
25. Harter, W.G. Computer graphical and semiclassical approaches to molecular rotations and vibrations. *Comput. Phys. Rep.* **1988**, *8*, 319–394.
26. Gulacsi, M.; Gulacsi, Z.; Tosa, V. The eigenvalue spectra of octahedral invariant tensor operator combinations up to eighth rank. *J. Mol. Spectrosc.* **1986**, *118*, 424–433.
27. Heine, V. *Group Theory in Quantum Mechanics*; Number 9 in International Series of Monographs in Pure and Applied Mathematics, The MacMillan Company: New York, NY, USA, 1960.
28. Kroto, H.W. *Molecular Rotation Spectra*; Dover Publications, Inc: New York, NY, USA, 1992.
29. Papousek, D.; Aliev, M. *Molecular Vibrational-Rotational Spectra*; Number 17 in Studies in Physical and Theoretical Chemistry, Elsevier Scientific Publishing Company: Amsterdam, The Netherlands, 1982.
30. Bright, E.; Wilson, J.; Decius, J.C.; Cross, P.C. *Molecular Vibrations: The Theory of Infrared and Raman Vibrational Spectra*; McGraw-Hill Book Company: New York, NY, USA, 1955.
31. Bunker, P.R.; Jensen, P. *Molecular Symmetry and Spectroscopy*, 2nd ed.; NRC Research Press: Ottawa, Canada, 1998.

32. Harter, W.G. *Principles of Symmetry, Dynamics, and Spectroscopy*; Wiley Interscience: New York, NY, USA, 1993.
33. Frost, A.A.; Musulin, B. A mnemonic device for molecular orbital energies. *J. Chem. Phys.* **1953**, *21*, 572–573.
34. Bright, E.; Wilson, J. Symmetry considerations concerning the splitting of vibration-rotation levels in polyatomic molecules. *J. Chem. Phys.* **1935**, *3*, 818.
35. Hougen, J.T. Hydrogen migration tunneling effects in the rotational and vibrational spectrum of protonated acetylene $C_2H_3^+$. *J. Mol. Spectrosc.* **1987**, *123*, 197–227.
36. Hougen, J.T. The Calculation of Rotational Energy Levels Using Tunneling Hamiltonians. In *Proceedings of the International Symposium on Molecular Spectroscopy*, Ohio State University, Columbus, OH, USA, 2009; Volume 64.
37. Kim, K.C.; Person, W.B.; Seitz, D.; Krohn, B.J. Analysis of the ν_4 (615cm^{-1}) region of the Fourier transform and diode laser spectra of SF_6 . *J. Mol. Spectrosc.* **1979**, *76*, 322–340.
38. Harter, W.G.; Galbraith, H.W.; Patterson, C.W. Energy level cluster analysis for $E(\nu_2)$ vibration rotation spectrum of spherical top molecules. *J. Chem. Phys.* **1978**, *69*, 4888.
39. Harter, W.G.; Patterson, C.W.; Galbraith, H.W. Centrifugal and Coriolis effects on level cluster patterns for $T(\nu_3)$ rovibrational bands in spherical top molecules. *J. Chem. Phys.* **1978**, *69*, 4896.
40. Patterson, C.W.; Galbraith, H.W.; Krohn, B.J.; Harter, W.G. Energy level clusters for $\nu_2 + \nu_3$ type combination bands of tetrahedral molecules. *J. Mol. Spectrosc.* **1979**, *77*, 457–473.
41. Harter, W.G. Molecular Symmetry. In *Handbook of Atomic, Molecular and Optical Physics*; Drake, G., Walther, H., Eds.; Springer: Berlin/Heidelberg, Germany, 2006; Chapter 32, p. 501.

© 2013 by the authors; licensee MDPI, Basel, Switzerland. This article is an open access article distributed under the terms and conditions of the Creative Commons Attribution license (<http://creativecommons.org/licenses/by/3.0/>).